

**MAPPING OF WATER QUALITY DYNAMICS DERIVED
FROM HYPERSPECTRAL EARTH OBSERVATION DATA
FOR THE TAM GIANG LAGOON IN CENTRAL VIETNAM**

MASTER'S THESIS

submitted in partial fulfillment of the requirements for the degree of
Master of Science (MSc)

PARIS-LODRON UNIVERSITY SALZBURG (PLUS)

Faculty of Digital and Analytical Sciences

Department of Geoinformatics

and

PALACKÝ UNIVERSITY OLOMOUC (UPOL)

Faculty of Science

Department of Geoinformatics

PLUS supervisor: **Zahra Dabiri**

UPOL supervisor: **Alena Vondrakova**

DLR co-supervisor: **Felix Bachofer**

submitted by

Emma Garcia Boadas

Salzburg & Olomouc, August 2024

With the support of the Erasmus+ program of the European Union. This Master's Thesis has been developed in the framework of the Erasmus Mundus Joint Master Degree (EMJMD) "Copernicus Master in Digital Earth", jointly coordinated by Paris-Lodron University Salzburg, Department of Geoinformatics, Austria together with University of South Brittany, Computer Science Department, France and Palacký University Olomouc, Department of Geoinformatics, Czech Republic. Also with the further support of the BMBF funded FloodAdaptVN project (funding no. 01LE1905A1).

ANOTATION

The primary objective is to analyse the temporal evolution of water quality in the Tam Giang, Lagoon using hyperspectral Earth Observation (EO) data and to design advanced geovisualization outcomes of these data. The aspects addressed are (1) the analysis of water quality parameters over time and (2) the visualization and cartographic representation of the derived results.

The research employs advanced hyperspectral EO sensors to assess critical water quality indicators. The student will also use Copernicus data. The lagoon is studied to understand some of the dynamic behaviour of the ecosystem; for that, a temporal analysis is used to discern patterns and dynamics in water quality parameters.

The study will assess variations in water quality indicators over time, shedding light on the lagoon's environmental changes and temporal dynamics. Innovative geospatial mapping visualization techniques will effectively illustrate these findings, clearly understanding the spatial distribution of water quality within the Tam Giang Lagoon.

The outcome of the thesis will present the analysis and advanced geovisualization of the Lagoon water quality dynamics based on a series of rasters.

KEYWORDS

Earth Observation, Remote Sensing, Hyperspectral Imaging, Geovisualization, Water Quality, Tam Giang Lagoon, Environmental Monitoring

Number of pages 103

Number of appendixes 5

This thesis has been composed by Emma Garcia Boadas for the Erasmus Mundus Joint Master's Degree Program in Copernicus Master in Digital Earth for the academic years 2022/2023 and 2023/2024 at the Department of Geoinformatics, Faculty of Natural Sciences, Paris Lodron University Salzburg, and Department of Geoinformatics, Faculty of Science, Palacký University Olomouc.

Hereby, I declare that this piece of work is entirely my own, the references cited have been acknowledged and the thesis has not been previously submitted to the fulfilment of the higher degree.

09.08.24, Olomouc



Emma Garcia Boadas

First of all, I would like to thank you, the Erasmus Mundus program, for the opportunity that has brought me this master's, personally, the supervisors of the thesis for accepting and proposing the master thesis topic. Thanks to the supervisor, Alena Vondrakova, for the complete support on the thesis planning and execution, for the insights about cartography, her unique way of sharing the thematic cartography, and for the correction of the main body of the thesis. Thank you to the co-supervisor Felix Bachofer for the interesting thesis topic, the data proportioned from the DLR and the complete support in the analytical part and the corrections of the entire text in a scientific way. Thank you to Zahra Dabiri for the corrections to the text of the thesis and planning. I want to say a special thank you to Peter Gege for the kind support during the preprocessing processing and analysis; thank you for all the explanations of WASI and support during the results operation and modeling. It has been crucial for the thesis execution. Thank you to Raquel for reprocessing the atmospheric correction of the DESIS data.

Thank you to my parents, Nuria and Antonio, for being supportive and listening to all the ups and downs of the thesis process. Thank you to Alex, who has provided support with a lot of food and coffee during this month. Thank you to my friends in Catalunya for giving support from far away: Enna, Eva, Miriam, Irene, Marta, Carlos, and Juanjo. Thank you to Adam for the support received in Olomouc. Special thank you to Maddy, who read with me to polish the thesis as a native English speaker. Thank you to Pavol for pushing me and reminding me that even though I did not have experience with water topics, it was a good idea to choose this topic. Special thank you to Agustin Lobo Aleu from GEO3BCN for giving a good basis for how to conduct scientific projects. Finally, thank you to all your colleagues for these two years of experience in Salzburg and Olomouc.

Palacký University Olomouc

Faculty of Science

Academic year: 2023/2024

ASSIGNMENT OF DIPLOMA THESIS

(project, art work, art performance)

Name and surname: Emma GARCIA BOADAS
Personal number: R220756
Study programme: N0532A330010 Geoinformatics and Cartography
Work topic: MAPPING OF WATER QUALITY DYNAMICS DERIVED FROM HYPERSPECTRAL EO DATA FOR THE TAM GIANG LAGOON IN CENTRAL VIETNAM
Assigning department: Department of Geoinformatics

Theses guidelines

The primary objective is to analyze the temporal evolution of water quality in the Tam Giang, Lagoon using hyperspectral Earth Observation (EO) data and to design advanced geovisualisation outcomes of these data. The aspects addressed are (1) the analysis of water quality parameters over time and (2) the visualization and cartographic representation of the derived results.

The research employs advanced hyperspectral EO sensors to assess critical water quality indicators. The student will also use Copernicus data. The lagoon is studied to understand some of the dynamic behavior of the ecosystem; for that, a temporal analysis is used to discern patterns and dynamics in water quality parameters.

The study will assess variations in water quality indicators over time, shedding light on the lagoon's environmental changes and temporal dynamics. Innovative geospatial mapping visualization techniques will effectively illustrate these findings, offering a clear understanding of the spatial distribution of water quality within the Tam Giang Lagoon.

The outcome of the theses will present the analysis and advanced geovisualisation of the Lagoon water quality dynamics based on a series of rasters.

Keywords: Earth Observation, Remote Sensing, Hyperspectral Imaging, Geovisualization, Water Quality, Tam Giang Lagoon, Environmental Monitoring

Extent of work report: max. 50 pages
Extent of graphics content: as needed
Form processing of diploma thesis: electronic
Language of elaboration: English

Recommended resources:

Disperati, L., & Virdis, S. G. P. (2015). Assessment of land-use and land-cover changes from 1965 to 2014 in Tam Giang-Cau Hai Lagoon, central Vietnam. *Applied Geography*, 58, 48–64. <https://doi.org/10.1016/j.apgeog.2014.12.012>

Kenneth Field,. (n.d.). *Cartography. The Definitive Guide to Making Maps | Esri Press*. ESRI Press. Retrieved 29 March 2024, from <https://www.esri.com/en-us/esri-press/browse/cartography-the-definitive-guide-to-making-maps>

Gholizadeh, M. H., Melesse, A. M., & Reddi, L. (2016a). A Comprehensive Review on Water Quality Parameters Estimation Using Remote Sensing Techniques. *Sensors*, 16(8), Article 8. <https://doi.org/10.3390/s16081298>

Gege, P. (2014). WASI-2D: A software tool for regionally optimized analysis of imaging spectrometer data from deep and shallow waters. *Computers & Geosciences*, 62, 208–215. <https://doi.org/10.1016/j.cageo.2013.07.022>

Capolupo, A., Monterisi, C., Spasiano, D., Ferraro, A., Mali, M., Fratino, U., & Tarantino, E. (2022). A WebGIS Prototype for Visualizing and Monitoring the Spatio-temporal Changes in Seawater Quality. In O. Gervasi, B. Murgante, S. Misra, A. M. A. C. Rocha, & C. Garau (Eds.), *Computational Science and Its Applications – ICCSA 2022 Workshops* (pp. 340–353). Springer International Publishing. https://doi.org/10.1007/978-3-031-10545-6_24

Supervisors of diploma thesis: **RNDr. Alena Vondráková, Ph.D.**
Department of Geoinformatics

Date of assignment of diploma thesis: **December 4, 2023**

Submission deadline of diploma thesis: **May 20, 2024**

L.S.

doc. RNDr. Martin Kubala, Ph.D.
Dean



prof. RNDr. Vilém Pechanec, Ph.D.
Head of Department

CONTENT

LIST OF ABBREVIATIONS	X
INTRODUCTION	X
INTRODUCTION	11
1 OBJECTIVES	12
2 STATE OF ART.....	13
2.1 WATER QUALITY OVERVIEW	13
2.2 TAM GIANG LAGOON	16
2.3 ENVIRONMENTAL ISSUES AND CHALLENGES IN TAM GIANG LAGOON, VIETNAM	17
2.4 HYPERSPECTRAL EARTH OBSERVATION DATA	18
2.5 WATER PROPERTIES RETRIEVAL IN HYPERSPECTRAL IMAGES EO	20
2.6 RETRIEVAL ALGORITHMS	21
2.7 UNCERTAINTIES AND CHALLENGES WATER QUALITY RETRIEVAL EO	22
2.8 WATER QUALITY ASSESSMENT IN TAM GIANG LAGOON.....	23
2.9 WATER QUALITY ASSESSMENT IN TAM GIANG LAGOON USING EO DATA...	25
2.10 SIMILAR WATER QUALITY ASSESSMENT USING INVERSION MODELS	25
2.11 METHODS OF CARTOGRAPHIC VISUALIZATION	26
2.12 MAPS OF WATER QUALITY	28
2.13 MAPS OF TAM GIANG LAGOON	30
3 METHOD	34
3.1 DATA.....	34
3.2 SOFTWARES USED.....	36
3.3 GENERAL PROCEDURE.....	36
3.4 ANALYSIS PART WASI METHOD	37
3.5 ADVANCE GEOVISUALIZATION METHOD.....	42
4 RESEARCH I THE PROCESS OF THE DATA ANALYSIS	44
4.1 DATA PREPROCESSING.....	44
4.2 DATA PROCESSING	44
4.3 DATA PREPROCESSING CHALLENGES.....	49
4.4 PROCESSING CHALLENGES.....	52
4.5 SUMMARY AND RECOMMENDATIONS	56
4.6 STATISTICAL ANALYSIS OF SATELLITE AND IN-SITU DATA FOR VALIDATION AND PARAMETER SHARED TRENDS ON TSS	57
4.6.1 Extraction satellite data for comparison with (in-situ data).....	57
4.6.2 Data plot and data selection.....	57
4.6.3 Statistical analysis of TSS, in-situ data vs satellite data TSS validation	58
4.6.4 Comparison of the in-situ parameter vs TSS	64
5 RESEARCH 2 GEOVISUALIZATION OF THE WATER QUALITY IN THE TAM LAGOON.....	67
5.1 DATA FOR GEOVISUALIZATION.....	67

5.2	THESES DATA VISUALIZATION POSSIBILITIES	68
5.3	STATIC DATA VISUALIZATION METHODOLOGY	69
5.4	ANIMATION DATA VISUALIZATION	72
6	RESULTS.....	75
6.1	RESULTS OF THE WATER QUALITY ANALYSIS.....	75
6.1.1	Water quality parameter results for EnMAP.....	76
6.1.3	Results of analysis EnMAP Model of deep water:	78
6.1.4	Results of analysis DESIS Model of deep water:.....	79
6.1.5	Results of analysis pixel statistics of every image	81
6.2	RESULTS OF THE STATISTICAL ANALYSIS TSS VALIDATION.....	83
6.2.1	Results of the comparative in-situ vs satellite TSS concentration	83
6.2.2	Results comparison of all the parameter vs TSS in in-situ data.....	89
6.3	RESULTS OF THE GEOVISUALIZATION	91
6.3.1	Static maps:.....	91
6.3.2	Map animation:.....	94
7	DISCUSSION	96
7.1	WATER QUALITY RETRIVAL ANALISIS	96
7.2	STATISTICAL ANALISIS AND TSS VALIDATION	98
7.3	GEOVISUALIZATION	100
8	CONCLUSION	103
	REFERENCES AND INFORMATION SOURCES	
	ATTACHMENTS	

LIST OF ABBREVIATIONS

Abbreviation	Meaning
AOPs	Apparent Optical Properties
BPs	Biogeochemical Parameters
CDOM	Colored Dissolved Organic Matter
Chl-a	Chlorophyll-a
CMYK	Cyan Magenta Yellow black (colour model)
COD	Chemical Oxygen Demand
DBMS	Database Management System
GIS	Geographic Information System
HDR	Header Files
IOPs	Inherent Optical Properties
PACO	Python-Based Atmospheric Correction
RGB	Red Green Blue (colour model)
Rrs	Remote Sensing Water Contribution Reflectance
SNR	Signal-to-noise ratio
TDS	Total Dissolved Solids
TSM	Total Suspended Matter
TSS	Total Suspended Solids

INTRODUCTION

Water is essential for life, and its quality is fundamental to the health and balance of the ecosystems that depend on it. Inland water bodies, in particular, are highly susceptible to changing environmental conditions such as climate change, development pressures, and shifts in land use and cover. These factors pose significant risks to water quality, impacting biodiversity, human health, and overall ecosystem sustainability (Ogashawara et al., 2017). Moreover, water quality has been identified as a critical target for the United Nations Sustainable Development Goals, underscoring its importance in global environmental and public health discourse (*Goal 6 | Department of Economic and Social Affairs, 2024*).

Satellite remote sensing offers a promising technology for monitoring water quality, particularly in inland water bodies. While this approach is well-established in ocean monitoring, its application to inland waters presents unique challenges and opportunities. The current generation of satellites dedicated to water monitoring, such as the recently launched PACE on March 2024, are primarily focused on oceanographic applications due to their larger pixel sizes, which limit their effectiveness for inland water monitoring (Dierssen et al., 2023). As a result, many studies have relied on multispectral satellites originally designed for terrestrial applications. However, the limited band resolution of these satellites often hinders precise water quality retrieval (Giardino et al., 2019).

To address these challenges, researchers have increasingly turned to hyperspectral satellite imagery, which provides detailed spectral information across a wide range of wavelengths with narrow spectral bands. This capability enables the differentiation of various water quality parameters and algae types that multispectral sensors may miss (Gholizadeh et al., 2016a). Hyperspectral sensors such as EnMAP, and DESIS have been employed in this study to retrieve detailed water quality information for the Tam Giang Lagoon.

The methods implemented for water quality retrieval in this thesis focus on physics-based models, which provide more coherent and consistent results over time compared to traditional band ratio or index methods. Specifically, the Water Colour Simulator (WASI) model is used to interpret hyperspectral data, allowing for accurate assessment of key water quality indicators such as chlorophyll-a, total suspended solids (TSS), and colored dissolved organic matter (CDOM). The WASI model leverages spectral inversion techniques to provide robust estimates of these parameters, overcoming the limitations of empirical models (Gege, 2014).

In addition to data retrieval, the visualization of water quality dynamics plays a crucial role in communicating findings and informing management decisions. This thesis explores various geovisualization techniques to represent the spatial and temporal variations in water quality effectively. Advanced cartographic visualization methods are employed to create intuitive and interactive maps, enhancing the interpretation of complex datasets (MacEachren & Kraak, 2001). By integrating geovisualization tools, the research aims to present water quality data in a way that is accessible and actionable for local authorities and stakeholders in the Hue region.

My personal interest in this topic stems from growing concerns about water resources and contamination in my local environment. I have observed firsthand the difficulties in tackling water pollution issues, flash floods, and droughts. I am motivated by the potential for this research to have a direct impact on the Hué region and the inhabitants that make a living from the Tam Giang lagoon. The results of this thesis could provide valuable insights for authorities in the Hue region and potentially offer geovisualization tools to inform and engage the local population.

1 OBJECTIVES

The primary objective of this master thesis is to **analyze the temporal evolution of water quality in the Tam Giang, Lagoon using time series hyperspectral EO data and to design advanced geovisualization techniques to better visualize the results.**

There are two aspects addressed by the thesis assignment: the analysis of water quality parameters over time, and the visualization and cartographic representation of the derived results. Therefore, there are two research parts in the thesis: the thematic analytical part presented as **Research 1** and the geovisualization part presented as **Research 2**.

The theoretical aim of the thesis is to make a comprehensive literature review focusing on the topics of water quality indicators, hyperspectral EO data, and methods of cartographic visualization of obtained results.

In the Research 1 part there are explored hyperspectral (EnMap, DESIS, PRISMA) EO sensor data to assess critical water quality indicators in the lagoon. The sub-goal of the thesis is to analyze and subsequently understand some of the dynamic behavior of the ecosystem. A temporal analysis is therefore used to discern patterns and dynamics in water quality parameters. The study has to assess variations in water quality indicators over time, shedding light on the lagoon's environmental changes and temporal dynamics.

In the Research 2 part there is an analysis of possible geovisualization of obtained results. Innovative geospatial mapping visualization techniques would effectively illustrate outcomes from the thematic part (Research 1).

The expected outcomes of the theses have to present the analysis and advanced geovisualisations of the Lagoon water quality dynamics.

2 STATE OF ART

The state of art chapter is focusing two different groups of topics that are following the content of Research 1 (subchapters 3.1, 3.2, 3.3, and 3.4) and Research 2 part (subchapter 3.5 and 3.6). The scientific databases available via university website and public articles, books and other (mostly online) information sources were used.

2.1 WATER QUALITY OVERVIEW

As mentioned, inland water bodies are susceptible to changing environments such as climate change, development pressure, land use, and land cover change, which poses a significant risk to water quality. All these changes lead to increasing temperatures, more intense precipitation and storm events, drought, deforestation, the reduction of vegetation cover, nutrient pollution. Human modification negatively impacts water; this promotes eutrophication, increased sediment and nutrient inputs, the proliferation of green-blue algae, and loss of aquatic benthos that throw off the balance of existing water systems (Ogashawara et al., 2017). The most common sources of water pollution are industrial runoff, agriculture runoff, urbanization runoff, and natural processes. Therefore, monitoring these changes and having a better understanding is crucial.

Water quality is referred to as the physical, chemical, biological, and microbiological conditions that determine the different uses of water depending on its constituents' concentrations (Chidiac et al., 2023). These conditions have been parametrized under a tool called the water quality indices (WQIs). With this parametrization, it has been easier to communicate the state of the waters (Uddin et al., 2021). There are different Indices from different institutions (the National Sanitation Foundation Model of Water Quality Index (NSFWQI), developed in the USA in 1970; the Canadian Council of Ministers of the Environment Model of Water Quality Index (CCMEWQI), created in Canada in 2001; the Horton Model of Water Quality Index (HWQI), developed in the USA in 1965, and the Tiwari and Mishra Model of Water Quality Index (TMWQI), developed in India in 1985, and others not mentioned here (Fortes, 2018; Fortes et al., 2023). Aside from these indices, there are different regulations in different countries; specifically in Vietnam, they have a regulation that provides limit values for surface water parameters used for the protection of aquatic life, drinking water, and water quality for irrigation (Circular No. 43/2011/TT-BTNMT dated December 12 of 2011 of the Minister of Natural Resources and Environment).

The **water quality parameters** of the indices and regulations are obtained by sampling the water *in situ* or laboratory analysis. The following lines detail some of the water quality parameters most used to determine water quality (Uddin et al., 2021).

- **WQI Common Water Quality parameters:**
 - Physical:
 - Temperature, Color or App., Turbidity SS, Total Solids
 - Chemical:
 - pH, DO, BOD, COD, Specific Con., Alkalinity, Cl-, NH₃-, N
 - Biological:
 - F. Coliforms, T. Coliforms
- **Additional parameters toxins:**
 - T. Phosphate, T. Sulfate Nitrates, T. hardness, Total Nitrogen
- **Toxins, pesticides, and trace metals:**
 - Cd, Mn, Zn, Cu, Hg, Pb, Phenols, Detergent, Others

There are different ways to evaluate water quality in order to monitor and forecast it. It is common to perform *in situ* measurements, as posited previously, and sample analyses, which are labor-intensive, time-consuming, and expensive. This *in situ* data collection is just representative of a point capturing the quality in a certain time and space. This technique makes monitoring big water bodies a challenge (Ritchie et al.,

2003). Remote sensing is another method to facilitate efficient planning and provides a global perspective of big surfaces. Remote sensing uses the signal reflected in different wavelengths from the water surface to determine different parameters (Yang et al., 2022). The remote sensing instruments measure the **radiance** and have the unit of a watt (steradian/square meter). Radiance is the reflectance of the proportion of radiation that is reflected from the surface (Kirk, 2010). In order to have a better understanding of the phenomena of reflectivity of the water Kirk et al describe it in a book (2010).

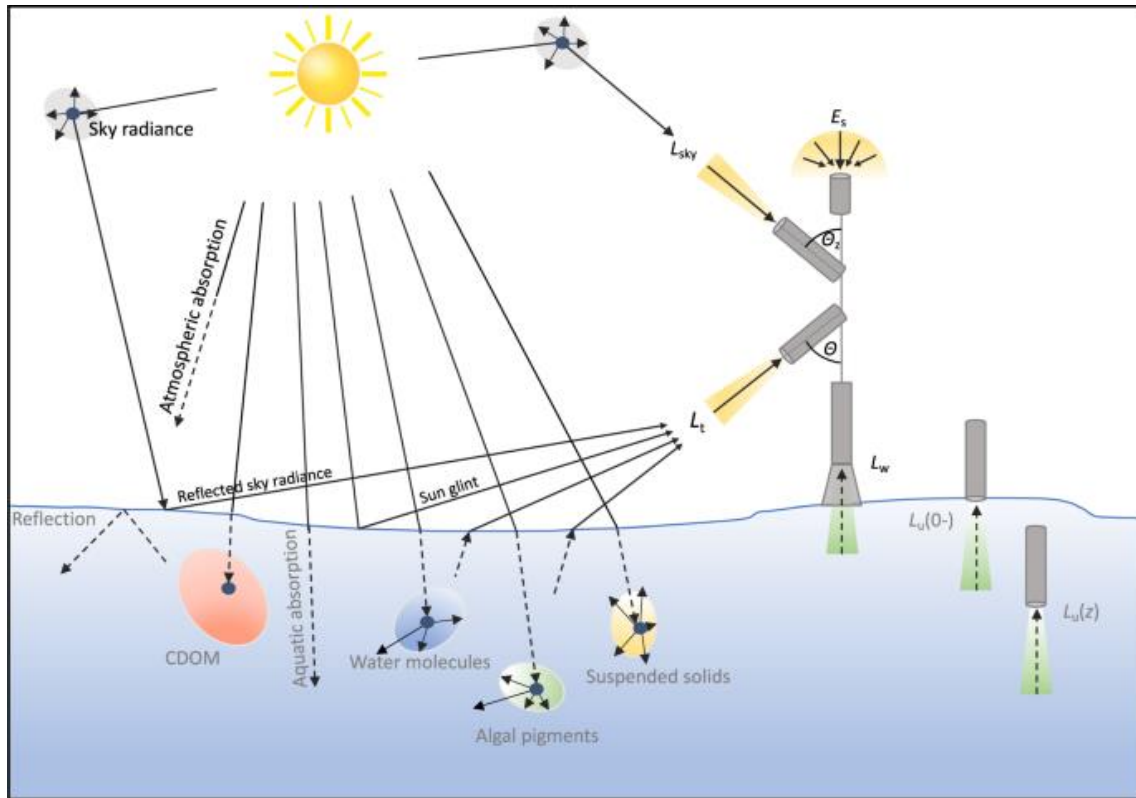


Figure 1: Spectrum transfer process between water substances and sensors (Lehmann et al., 2023).

Different parameters can be estimated with remote sensing with passive, and active sensors. The following Figure 2 lists the most commonly measured water parameters in remote sensing Figure 1.

Water Quality Parameter	Abbreviation	Units
chlorophyll-a	CHL-a	mg/L
Secchi Disk Depth	SDD	m
Temperature	T	°C
Colored Dissolved Organic Matters	CDOM	mg/L
Total Organic Carbon	TOC	mg/L
Dissolved Organic Carbon	DOC	mg/L
Total Suspended Matters	TSM	mg/L
Turbidity	TUR	NTU
Sea Surface Salinity	SSS	PSU
Total Phosphorus	TP	mg/L
Ortho-Phosphate	PO ₄	mg/L
Chemical Oxygen Demand (COD)	COD	mg/L
Biochemical Oxygen Demand	BOD	mg/L
Electrical Conductivity	EC	µs/cm
Ammonia Nitrogen	NH ₃ -N	mg/L

Figure 2: The most commonly measured parameters of water by means of remote sensing (Gholizadeh et al., 2016a)

Algae species are the base of water ecosystems. Lakes are affected by overground algal blooms and posterior eutrophication, and the Chl-a, is the pigment that is detectable with remote sensing. These blooms can produce potentially deadly toxins, posing a health risk. Additionally, blooms significantly affect water transparency, showing a correlation between the two parameters. Therefore, monitoring Chl-a is critical for assessing the impacts of eutrophication, understanding the ecological state of lakes, and evaluating the health risks from cyanobacteria blooms (Ogashawara et al., 2017).

TSM refers to organic and mineral solids suspended in the water column. This can come from surface runoff, catchment areas, rivers or coast, or be resuspended from the bottom of the water body. The TSM parameter is closely linked with water transparency/turbidity and Secchi disk depth (Niroumand-Jadidi et al., 2020). It can contain several substances and is important for water bodies management (Giardino et al., 2017); for example: high turbidity 4 NTU in drinking-water can harbour microbial pathogens and reduce the efficacy of disinfection (e.g. chlorination, ultraviolet light disinfection) (World health organization, 2024).

Coloured Dissolved Organic Matter (CDOM) is a combination of organic molecules formed during the decomposition of land vegetation, aquatic plants, phytoplankton, or bacteria. Understanding CDOM is crucial for comprehending the carbon cycle and estimating lake carbon content (Kutser et al., 2017). It is also important for monitoring drinking water quality and reacting promptly to changes in CDOM levels during water treatment processes (Kutser et al., 2017). There are different ways of calculating the CDOM, but the CDOM_{a(440)} is one of the most compatible for different types of waters used in a wide range of applications (Li et al., 2016; Nima et al., 2019).

It should be considered that other parameters are used as indicators for water pollutants, like the acidity of chemicals and pathogens. However, they cannot be directly detected by remote sensing data and methods but can be correlated with other remote sensing-derived parameters.

Some of the main **advantages** of utilising remote sensing to monitor water quality are presented in the literature (Gholizadeh et al., 2016b; Kallio, 2007), such as follows:

- Gives a synoptic view of the entire waterbody for more effective monitoring of the spatial and temporal variation.
- Makes it possible to have a synchronized view of the water quality in a group of lakes over a vast region.
- Provides a comprehensive historical record of water quality in an area and represents trends over time.
- Prioritizes sampling locations and field surveying times.

However, there are some **limitations** of using remote sensing, (Gholizadeh et al., 2016b; Kallio, 2007), such as follows:

- The parameters quantification can not be done just with remote sensing because of the boundaries of the atmosphere, atmosphere aerosol and water vapor that are unknown.
- For the calculation of the parameters, the empirical mode, physical mode, semi-empirical mode and intelligent mode are used. The empirical relationship may be established through regression analysis from samples of in-situ measurements.
- It may also be determined from the known spectral characteristics of the water quality parameter of interest. This is known as the semi-empirical approach (*Quantification of Shallow Water Quality Parameters by Means of Remote Sensing*, 2024).

2.2 TAM GIANG LAGOON

The Tam Giang Coastal Lagoon is the **largest lagoon in Southeast Asia**

Figure 3 covering an area of 216 km². It has a mean depth of 2 m and a maximum depth of 5–15 m in the inlets region caused by the water fluxes (Nghiem et al., 2007). The Lagoon has a sandbar of 66 km long and up to 20 m high; this acts as a barrier between the lagoon and the Sea. The barrier is crossed by inlets which change through time. Currently, there are two of them, called **Thuan An inlet** in the north and **Tu Hien inlet** in the south. The opening of these channels and their dynamics are closely related to the rainy season and flood season, which have led to major changes recorded for the lagoon dynamics (Tran Thanh, 2011). The lagoon system receives water from the **Huong River basin** and is the main contributor to the lagoon (Tran Thanh, 2011). The population along the lagoon is about 300,000 inhabitants, belonging to 5 districts and towns: Phong Dien, Quang Dien, Huong Tra, Phu Vang and Phu Loc (Trang et al., 2013).

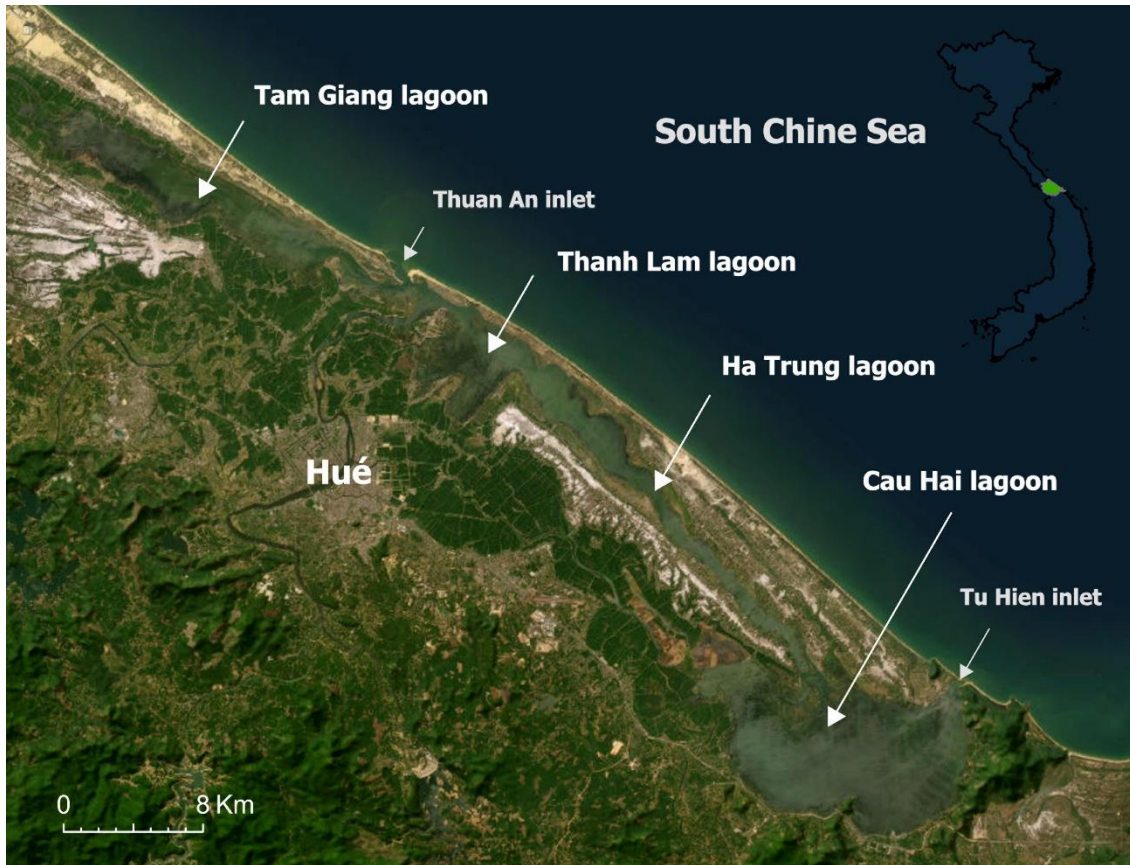


Figure 3: Tam Giang-Cau Hai lagoon area, Vietnam, Earthstar Geographics, Map powered by Esri.

During the **rainy season**, from **mid-October through February**, the lagoon experiences the main influx of water from the previously mentioned river. Moreover, another water addition in the lagoon is in the Typhoon season from early September through November, these intense precipitation episodes can occasionally lead to flooding. During these two periods more than 70% of the flow volume per year is attributed to the lagoon (Nghiem et al., 2007). This intense precipitations also causes higher turbidity in the lagoon and the decrease in the salinity (Luong et al., 2020). Most of the additions of water are discharged in the southern half of the lagoon.

The lagoons' geological context is characterized by the presence of Quaternary sedimentary rocks and Paleozoic formations, which emerged during the late-Hercynian folding of the Indochinese shield in the lower Triassic (Giuliani et al., 2011). The lagoon has mostly quaternary sediments and on the northern part, bedrock granite can be found. The quaternary sediments of the lagoon are fine sediments in general (Hirai et al., 2008). The main sediment influence is from the Huong River and the inlets. In the Cau Hai Lagoon and in the Thuy Tu Lagoon there is a mix of **silt-sandy material**, and on the strict area of Tam Giang Lagoon there is a proportion of 90% **fine sand**. The rest of the lagoon has a proportion of **silt and clay** (Giuliani et al., 2011).

2.3 ENVIRONMENTAL ISSUES AND CHALLENGES IN TAM GIANG LAGOON, VIETNAM

The lagoon has its own ecological system dependent on the water and its quality. There are three main problems that the lagoon's ecological balance and the livelihoods of local communities are facing: habitat degradation, resource exploitation, and pollution. In this study we are going to be more focused on the pollution specifically.

The pollution in Tam Giang Lagoon and Tam Giang–Cau Hai lagoon are because they receive a large amount of wastewater from five districts with various waste sources such as residences' domestic waste, agricultural runoff, aquaculture activities, livestock and industry among others (Giuliani et al., 2011; Thi Thu Trang et al., 2020). All these pollutants concentrate due to the low exchange of water through the two inlets and cause adverse effects not just in water quality, but also puts aquatic life and human health at risk.

The three key factors that contribute to the overall equilibrium, health and quality of the Tam Giang Lagoon ecosystem are **pollutants**, the organization of **aquaculture**, and the presence of **algae and seagrass**. These elements play a critical role in promoting oxygenation, the absorption of pollutants and excess nutrients, and overall oxygen levels in the lagoon. By examining each of these factors in detail, we can gain a better understanding of how they interact and impact the ecosystem as a whole.

POLLUTANTS in the lagoon:

Heavy metals (from historical industrial activities, and mining industries), Oil pollution, Nitrogen (agriculture, and anthropogenic), Organochlorine pesticides sediment, Polychlorinated Biphenyls (PCBs) in Sediments, Ammonium concentration nitrogen NH⁺, Coliform concentration (previous list references(Frignani et al., 2007) (Hằng et al., 2017) (Object, 2024)).

One of the indicators of health of the normal surface water concentration for oxygen is between 8 – 10 mg/l. If 1 mg of BOD or COD is released into the water, 1 mg of oxygen will be consumed for decay (Peters et al., 2015). In Tam Giang lagoon BOD5 concentration ranges from 0.9 to 6.1 mg/l (Hằng et al., 2017).

AQUICULTURE in Tam Gian Lagoon is abundant and it can arrive to block some of the water flow. New policies and aquiculture arrangements have been favourable to water movement inside the lagoon. Also, an advantage of aquaculture is the algae consumption and insect regulation by the fish.

ALGUE in Tam Gian Lagoon has an important ecological weight. Seagrass degradation has been a problem in the lagoon. There is a study in Luong that describes the recovery of the seagrass from an area of 1,00 hectares in 2009 and to evolution to 2,037 in 2017 (Luong et al., 2020). Moreover, in the attachments-0, there is a list of the photosynthetic live in the Lagoon. But just take into account that the lagoon has a total of 283 of phytoplankton (Hằng et al., 2017; Peters et al., 2015; Nguyen, H. Y, Tran, Đ. T., Lang, V. K. & Nguyen, T. T,2010; Ton, T. P. V& nnk, 2009).

The **ecological benefits** of having an increasing **algae population** are:

- Promote the nutrient cycle by converting water-borne nutrients like N (nitrogen) and P (phosphorus) into biomass.
- Oxygen production through photosynthesis is vital for aquatic life.
- Habitat provision for several aquatic organisms as food and shelter.
- Biodiversity + Biome diversity.

2.4 HYPERSPECTRAL EARTH OBSERVATION DATA

Hyperspectral EO data, is a passive remote sensing, non-invasive technique that provides detailed spectral information to observe the earth's surface. This technique provides more quantitative information about characteristics and real physical/chemical conditions (Zdravcheva, 2019). The principle of hyperspectral EO is spectral analysis. This spectral analysis is based on the ability of any material or object to absorb and affect electromagnetic energy in different ways (Figure 4). The

hyperspectral images permit the spectral analysis due to the hundreds to thousands of images that capture the electromagnetic spectrum having narrow spectral (contiguous) bands with a relatively high signal-to-noise ratio (SNR) (Ma et al., 2023; Rast & Painter, 2019). Hyperspectral images used to study aquatic areas are mostly airborne platforms and in situ measurements.

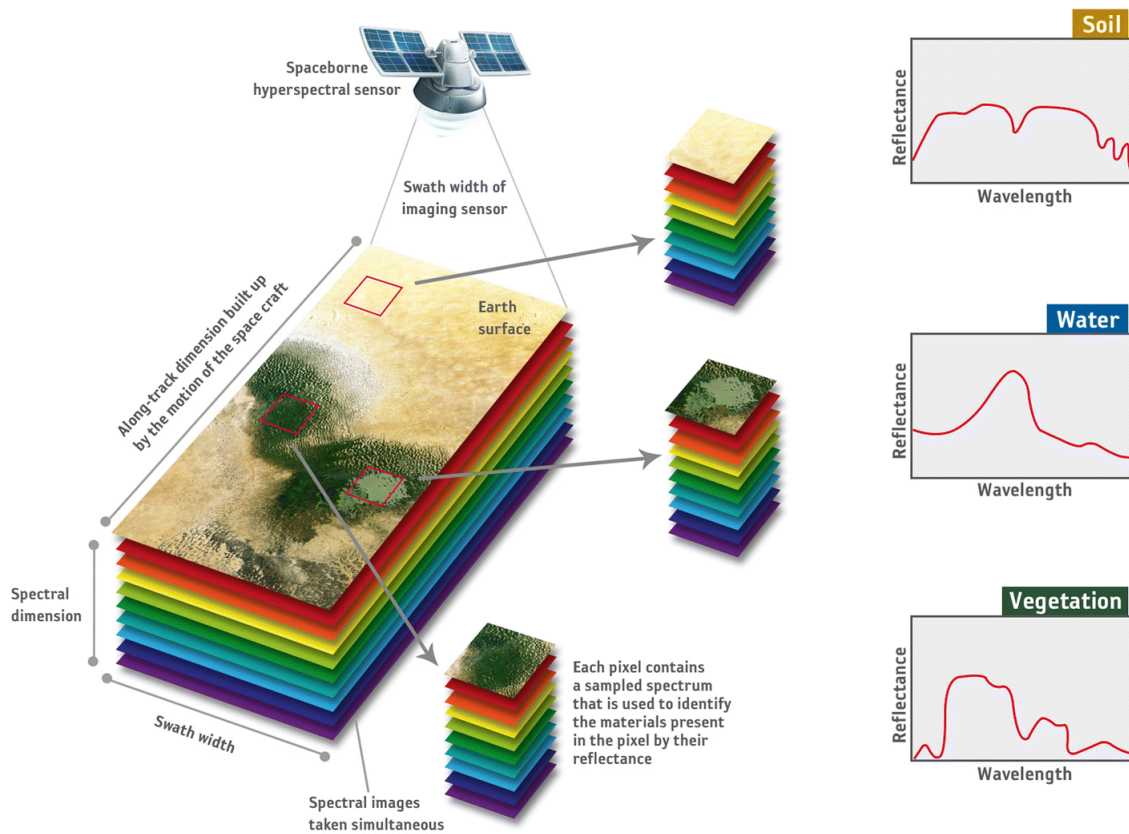


Figure 4: Principles of hyperspectral data
(Earth Observation Graphic Bureau | ReMedia, 2024)

However, hyperspectral data have a high spectral resolution with hundreds of bands but it does not have a high spatial resolution compared with any multispectral sensor (Jia et al., 2021). This **resolution tradeoff** is a handicap of the hyperspectral satellite images. It is also needed to take into account that for water applications, a narrow band of 1 to 2 nm is ideal for distinguishing between phytoplankton and other parameters. Table 1 shows the list of the most used hyperspectral satellite-based sensors.

The origin of the Satellites Imaging Spectrometry sensors are HYPERION (Earth Resources Observation And Science (EROS) Center, 2000) mission from 2000 – 2017, Compact High-Resolution Imaging Spectrometer (CHRIS) -PROBA (Barnsley et al., 2004), and Hyperspectral Imager for the Coastal Ocean (HICO) in the International Space Station (Lewis et al., 2009). These satellites have shown increasing capabilities in inland and coastal water applications (Brando & Dekker, 2003; Giardino et al., 2019; Hestir et al., 2015; Santini et al., 2010). Although their SNR might be limited in making accurate measurements of moderate changes in water quality parameters (e.g., CDOM with Hyperion in clear lakes (Brando & Dekker, 2003; Santini et al., 2010; Giardino et al., 2007) they were the promoters for the next generation of hyperspectral satellites missions.

Table 1: Hyperspectral Satellite characteristics.

Sensor	HYPERION	CHRIS-PROBA	HICO	DESI	AHSI	HISUI	PRISMA	EnMAP	PACE
Data Range	2000–2017	2001–2022	2009–2014	2018–Present	2018–Present	2020–Present	2020 - Present	2021–Present	2024–Present
Wavelengths	400–2,500 nm	400–1,050 nm	380–960 nm	400–1,000 nm	400–2,500 nm	400–2,500 nm	400–2,500 nm	420–2,450 nm	345–885 nm
Spectral Bands	220	62	128	235	335	185	239	246	107
Spatial res.	30 m	34 m	90 m	30 m (swath)	30 m	30 m	30 m	30 m	1km
Organization	NASA's Goddard Space Flight Centre (GSFC)	European Space Agency (ESA)	NASA's International Space Station (ISS)	DLR- Multi-User-System for Earth Sensing (MUSES)	Shanghai Institute of Technical Physics and Chinese Academy of Sciences	Japanese Ministry of Economy	Italian Space Agency (ASI)	German GFZ-DLR	NASA

Recently several hyperspectral satellite missions have been launched, including the Space Agency of the German Aerospace Center (DLR) Earth Sensing Imaging Spectrometer (DESI) onboard the International Space Station (ISS) (Krutz et al., 2019), China's Advanced Hyperspectral Imager (AHSI) aboard the GaoFen-5 satellite (Liu et al., 2019), and HyperScout-1, a smart hyperspectral imager for nanosatellites (Esposito & Marchi, 2019), all launched in 2018 (Braga et al., 2022). The Japanese Hyperspectral Imager SUite (HISUI) mission onboard the ISS (Matsunaga et al., 2019) and the PRecursore IperSpettrale della Missione Applicative (PRISMA) sensor by the Italian Space Agency (ASI) (Loizzo et al., 2018), were launched in 2019. The DLR Environmental Mapping and Analysis Program (EnMAP) (Guanter et al., 2015) was launched in 2022. These missions are extending the knowledge that so far has been primarily driven by Hyperion. These new missions have **increased spectral and radiometric resolution**. They will also allow progress in inland and coastal waters applications although they are being designed for a variety of applications, so they might still have some limitations in measuring the low remote sensing reflectance from water bodies (Giardino et al., 2019).

The latest American satellite is Plankton, Aerosol, Cloud, ocean Ecosystem (PACE) (Gorman et al., 2019) launched in 2024, it is specifically designed for applications in ocean and coastal waters. It has been developed to meet all the requirements for assessing biophysical parameters from space. This includes atmospheric corrections and the separation of phytoplankton and CDOM pigment separation, with a 5 nm spectral resolution between 380 and 800 nm, as well as a spectral subsampling of approximately 1 to 2 nm resolution from 655 to 710 nm for a more detailed characterization of the Chl-a sun-induced fluorescence spectrum (Giardino et al., 2019; Gorman et al., 2019). This study will be centered on DESIS, PRISMA, and EnMAP.

2.5 WATER PROPERTIES RETRIEVAL IN HYPERSPECTRAL IMAGES EO

In hyperspectral images and spectrometry, water quality retrieval has proven to be effective. Its origin comes from optical oceanography, arising from the need to monitor large areas. The inland and coastal water quality retrieval came later so it has been mostly developed in the last 30 years (Ogashawara et al., 2017). These inland and coastal aquatic ecosystems often are a **mixture of optically shallow and optically deep waters**, with gradients of clear to turbid and oligotrophic to hypertrophic productive waters and with varying bottom visibility with and without macrophytes,

macro-algae, benthic micro-algae or corals (Giardino et al., 2019). These complex aquatic systems with high optical complexity Figure 5 present a challenge for bio-optical algorithms for optical remote sensing. Therefore, there are different methodologies and different challenges associated with aquatic environments. The main bio-optical models are inherent optical properties, CDOM, phytoplankton, non-algal particles (NAP), Apparent Optical Properties (AOPs) for optically deep waters, AOPs optically deep shallow waters. The availability of new high-resolution data has allowed improvements in models based on the radiative transfer theory for assessing optical water quality parameters.

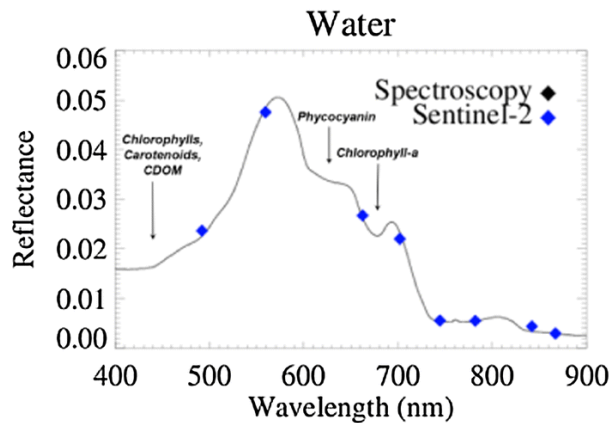


Figure 5: Sample spectrums of hyperspectral data of different materials (Earth Observation Graphic Bureau | ReMedia, 2024)

2.6 RETRIEVAL ALGORITHMS

Different methodology groups for calculating water quality retrieval were defined by Morel & Gordon (Morel & Gordon, 1980). These groups are the empirical, semi-empirical, and physical or analytical approaches. (1) Empirical methods use statistical relationships between spectral bands and water parameters. (2) Semi-empirical methods use physical and spectral information to develop algorithms. (3) Analytical approaches model water reflectance to determine constituent concentration with inherent optical characteristics. (Gholizadeh et al., 2016b)) These methods have different levels of complexity and suitability for various parameters, although the recommendation is to have complementary data from traditional sampling methods (Gholizadeh et al., 2016b). This thesis uses the analytical approach physics-based, as it does not rely on sampling. However, this approach is highly dependent on the quality of the data provided, which needs a good atmospheric correction (Brando & Dekker, 2003).

The **analytical approach** method has been developed since the 1980s. It is based on semi-analytical and quasi-analytical approaches, such as spectral inversion procedures, which rely on matching spectral data to bio-optical forward models (Giardino et al., 2017). Forward bio-optical modelling is used to demonstrate the response of water leaving reflectance (radiance reflectance) depending on the inherent optical properties of particles (Giardino et al., 2017). This model is based on **robust physical knowledge**, these spectral inversion approaches are more widely applicable than their empirical counterparts, particularly when they are coupled with methods allowing for spatial and temporal variations in water quality parameters typical of optically complex waters (Giardino et al., 2019). WASI utilizes the radiance reflectance doing and invert model, which accounts for the absorption and backscattering properties of different media that light interacts with through its travelling path, i.e., atmosphere, water surface, and column as well as the bottom substrate in optically shallow waters (less than 5m), to obtain the values of the optical properties (Giardino et al., 2019; Niroumand-Jadidi et al., 2020). The sensor signal is a composite of several

radiance components upwelling after interacting with this media (Niroumand-Jadidi et al., 2020). A detailed explanation of how WASI does that is explained in Chapter 4, justification of methods.

To have a visualization of the water quality parameter retrieval it is explained in the following lines. The image below Figure 6 represents the typical inland **water inverse remote sensing water contribution reflectance (Rrs) spectrum**. It shows distinctive spectral features, which have a high absorption in the blue spectral region due to the combined absorption by phytoplankton pigments, β -Carotene, NAP, and CDOM (Ogashawara et al., 2017). The absorption peak around 625 nm is related to the presence of phycocyanin (PC), a proxy for cyanobacteria, and another absorption peak around 675 nm is related to the absorption by Chl-a (Gurlin, 2023nd; Ogashawara et al., 2017). The complete spectrum enhances the retrieval of parameters, making hyperspectral data a key tool for water characterization.

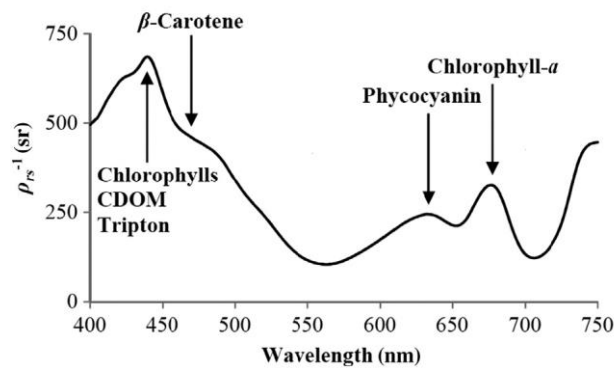


Figure 6: Typical inland waters inverse Rrs spectrum. The position of the absorption peaks by constituents , such as chl-a, PC, NAP, and CDOM are labelled (Gurlin, 2023)

2.7 UNCERTAINTIES AND CHALLENGES WATER QUALITY RETRIEVAL EO

The analytical approach faces different challenges with aquatic environments, hyperspectral fiducial reference measurements, atmospheric correction, water vapor columnar content, sun glint, the aerosol optical signal, and the signal noise ratio is always a challenge. Some sensors have their own automatic atmospheric correction levels of processing. This processing does not have the best fit for all the areas around the world due to its heavy dependence on standardized pre-processing routines and reference data of the calibration (Goyens et al., 2022). Furthermore, for ocean-observing sensors focusing on ‘Ocean Color’ variables often, a spectral sampling around 5 nm is required (Rast & Painter, 2019). Another particular challenge in shallow water is the **bottom-reflected radiance variability** that can induce challenges in the estimation of in-water constituents (Niroumand-Jadidi et al., 2020). It is important to consider that the spectral features of a specific biophysical parameter may degrade or be interfered with in the presence of other radiance components (bottom interference), especially if the desired component is not predominant (Kutser et al., 2005, 2016; Niroumand-Jadidi et al., 2019). The **presence of atmospheric effects** can significantly affect the water-leaving signal, as water bodies may only reflect up to 10% of the downwelling irradiance due to the high attenuation of light in pure water (Gege, 2014; Niroumand-Jadidi et al., 2019; Toming et al., 2016). Therefore, the SNR sensitivity of water reflectance is a critical factor in using remote sensing for aquatic applications (Braga et al., 2022; Ma et al., 2023; Niroumand-Jadidi et al., 2020; Rast & Painter, 2019). The absolute radiances at different wavelengths are not as important for empirical techniques as they are for physics-based inversion (Niroumand-Jadidi et al., 2020). This is empirically

corroborated by some studies that use top-of-atmosphere (TOA) data through regression analysis to retrieve bathymetry or in-water constituents (Toming et al., 2016). On the other hand, absolute radiances are particularly important in the analytical approach to physics-based inversion, which requires appropriate modelling of atmospheric artefacts (Dekker et al., 2011; Lee et al., 2002), and knowledge of the IOPs of the water column and substrate types/compositions in optically shallow waters, but in general are much more robust for exploring multitemporal datasets from the same area of interest (Giardino et al., 2019; Niroumand-Jadidi et al., 2020).

2.8 WATER QUALITY ASSESSMENT IN TAM GIANG LAGOON

The water quality in the Tam Gian Lagoon from the 1990s until the early 2000s was decreasing due to an increase in all types of activities and pollution. But around 2000, the authorities started to be more conscious about the state of the lagoon and the water in the region, and different initiatives started like the reporting, such as The Study on Nationwide Water Resources Development and Management in the Socialist Republic of Vietnam Final Report Volume VI Supporting Report Phase 2-1: Integrated River Basin Management Plan for the Huong River Basin (JICA 報告書 PDF 版 (JICA Report PDF), 2024). After these first actions, the lagoon had an increase in fisheries and aquaculture, which led to a big increase in the P and a decrease in oxygen. **The quantity of water and sediments in the lagoon is dependent on the water gains of fresh water from flooding and river flux.** The dynamic of the lagoon that conditions the water quality is the stratified water layer. The upper part is fresh water, and the lower part is saline water (Frignani et al., 2007). The water quality had an alteration because the increase of stake traps in Cau Hai Lagoon made it difficult for the water in the lagoon to flow and in 2008 a project integrating management of the Lagoon activities was created (GCP/VIE/029/ITA - IMOLA Project Integrated Management of Lagoon Activities in Tam Giang Cau Hai Lagoon (Thua Thien Hue Province) (Phase 1), 2008). Afterward, in 2015, the Republic of Vietnam realized the national technical regulations about surface water quality Circular No. 01/2023/TT-BTNMT (phủ, 2015)

The most recent paper about the characteristics of the lagoon and its restoration, usages of water, and quality parameters is the one done to estimate environmental carry capacity based on calculations from the Delft-3D model using three scenarios: 1) ECC following Vietnamese regulations; 2) maximum ECC or dangerous scenario (which the water body can no longer purify itself or becomes a dead water body); 3) proposed ECC for the protection of aquatic life from (Hằng et al., 2017). The data used is from 2011 and 2012, Figure 7, and Figure 8 (Trang et al., 2013). The prediction for the lagoon's carrying capacity is that it can no longer purify itself or becomes a dead water body if the pollution load discharged into the lagoon exceeds 89860 tons of BOD5, 165707 tons of COD, 13464 tons of N- (NH₄⁺⁺ NH₃), 2084 tons of N-NO₃⁻ and 30380 tons of P-PO₄³⁻ per year (Thi Thu Trang et al., 2020).

The most recent previous research has shown these values throughout the lagoon as you can see in the list:

- **Heavy Metals:** Historical industrial activities have led to the accumulation of heavy metals in the lagoon sediments (Frignani et al., 2007).
- **Oil Pollution:** Oil pollution has been documented, impacting the lagoon's water quality (Luong et al., 2020).
- **Nutrients from Agriculture:** High levels of nitrite (NO₂⁻) and ammonium (NH₄⁺) have been detected, indicating significant agricultural runoff. Nitrite levels range

from 0.08 to 0.49 mg/l, while ammonium ranges from 0.03 to 0.27 mg/l, varying between dry and rainy seasons (Hằng et al., 2017).

- **Organochlorine Pesticides:** Concentrations of DDTs and HCHs exceed both US EPA and Canadian EQG criteria, posing risks to human health and wildlife (n.d.)(Object, n.d.).
- **Chemical Oxygen Demand (COD):** COD levels range from 2.3 to 19.7 mg/l, indicating organic pollution. COD values often exceed the allowable limits set by Vietnamese standards (Hằng et al., 2017).
- **Polychlorinated Biphenyls (PCBs):** PCB levels in sediments have been studied to understand contamination trends and sources (Frignani et al., 2007).
- **Turbidity:** Turbidity ranges from 9.8 to 25.2 NTU, with higher values recorded during the rainy season (Hằng et al., 2017).
- **Dissolved Oxygen (DO):** DO levels vary from 6.2 to 7.8 mg/l, critical for aquatic life (Hằng et al., 2017).
- **Biochemical Oxygen Demand (BOD5):** BOD5 concentrations range from 0.9 to 6.1 mg/l, reflecting the organic matter present in the water (Hằng et al., 2017).
- **Coliform:** Coliform concentrations range from 600 to 6900 MPN/100 ml, with higher levels in the dry season (Hằng et al., 2017).
- **pH and Salinity:** pH values range from 6.8 to 8.2, while salinity varies from 18 to 25,950 mg/l TDS, fluctuating with seasons (Hằng et al., 2017).

Parameter	Emission coefficient (kg/person/year) ²	Current load		Forecast load	
		TG-CH area 32,983.2	The whole province	TG-CH area 45,563.2	The whole province
COD	55	14,992.4	60,450.1	20,710.5	76,549.9
THAT	25	2398.8	27,477.3	3,313.7	34,795.4
N-T	4		4,396.4		5,567.3
P-T	0,8	657,2	1,206,5	900,7	1,520,4
NO3 - +NO2 - (1)	0,04	24,0	44,0	33,1	55,7
NH4 ⁺ (1)	2,2	1,319,3	2,418,0	1,822,5	3,062,0
PO4 ³⁻ (1)	0,549	329,2	603,4	454,8	764,1
TSS	30	17,990,9	32,972,8	24,852,7	41,754,5

Figure 7: Pollution load generated in 2010 and forecast for 2020 from domestic sources in Thua Thien – Hue province figure by (Trang et al., 2013).

Parameter	Load generated throughout the province			The load is discharged directly into the lagoon		
	2010	2020	Change (%)	2010	2020	Change (%)
COD	128.455,8	173.781,9	35.29	77.292,6	96433,8	24,76
THAT	73.446,8	96.902,3	31.94	41.268,6	50419,8	22,17
N-T	35.126,4	38.940,5	10.86	18.017,5	19321,0	7,23
P-T	10.120,8	13.217,8	30.60	5.785,0	7111,7	22,93
NO3+NO2	156,57	231,56	47.89	87,4	118,00	34,98
NH4	5.139,9	7.316,6	42.35	3.115,3	4007,8	28,65
PO4	2.331,4	3.446,2	47.82	1.329,7	1764,7	32,72
TDS	2.961,0	5.033,7	70.00	1.480,5	2516,8	70,00
TSS	875.512,9	904.042,5	3.26	562.001,7	558145,0	-0,69
Grease	0,2	0,4	100.00	0,10	0,18	70,00

Figure 8: Total pollution load brought into Tam Gian – Cau Hai lagoon in 2010 and forecast for 2020 (tons/year) (Trang et al., 2013)

2.9 WATER QUALITY ASSESSMENT IN TAM GIANG LAGOON USING EO DATA

Existing research on the EO in Tam Giang Lagoon provides valuable insights. From the author's knowledge, **there are no EO water quality studies** on Tam Giang Lagoon. With that several gaps remain:

For the studies in the area no use of hyperspectral data. Most studies have relied on multispectral or traditional remote sensing methods, which lack the spectral resolution to capture detailed water quality dynamics (Aquaculture of the Tam Giang-Cau Hai Lagoon | FloodAdaptVN, n.d.-a; Disperati & Viridis, 2015; Thanh et al., 2002; Tran et al., 2001, 2006; Viridis, 2014).

2.10 SIMILAR WATER QUALITY ASSESSMENT USING INVERSION MODELS

Inversion models play a role in the assessment of water quality by utilizing the physical properties of water to retrieve information through spectral analysis. These models have evolved significantly, with early developments focusing on integrating atmospheric and hydro-optical radiative transfer models such as **MODTRAN-4** and **Hydrolight** to estimate underwater light fields. The methodology described in these models involves a matrix inversion method applied to retrieve concentrations of chlorophyll, CDOM, and Total Suspended Solids (TSS), which were then compared to field data for validation (Brando & Dekker, 2003).

The **BOOMER** model is a Bayesian framework offering a robust approach for estimating water quality parameters by incorporating uncertainty and variability in hyperspectral data. However, challenges remain with the data complexity and model calibration. Studies have demonstrated that BOOMER can effectively estimate biogeochemical parameters and inherent optical properties, reducing uncertainty and improving accuracy (O'Shea et al., 2023). Despite these advancements, modeling techniques still encounter issues of ambiguity, particularly in hyperspectral satellite imagery of inland and coastal waters. For example, the Mixture Density Networks (MDNs)—based hyperspectral framework is sensitive to uncertainties typical of hyperspectral satellite imagery for all estimations of biogeochemical parameters (BPs) and IOPs, with aCDOM and aNAP exhibiting reduced sensitivity relative to aPH (O'Shea et al., 2023).

The **Optical Water Type Guided Approach** utilizes an optical water type guided approach to estimate optical water quality parameters, demonstrating the potential of inversion models to improve accuracy in water quality assessments (Udeberg et al., 2020).

The **WASI** model has been widely used to analyze water quality parameters by simulating and inverting water-leaving radiance and reflectance for inland and coastal waters. A case study in Lake Trasimeno was conducted for water quality retrieval using inversion models. The study highlighted the advantages of high spatial resolution for characterizing water quality dynamics in optically complex waters (Niroumand-Jadidi & Bovolo, 2021). Also, Mahmoud et al. (2023) investigated the potential of remote sensing techniques in retrieving water quality parameters in urban stormwater ponds. The study utilized WASI to estimate parameters like chlorophyll-a, TSS, turbidity, and Secchi depth, demonstrating its effectiveness in urban environments (Mahmoud et al., 2023).

These studies highlight the effectiveness of inversion models in improving the accuracy and reliability of water quality assessments across various aquatic environments. However, they also point out the ongoing challenges in achieving precise

atmospheric corrections, data calibration, and the integration of multiple data sources to capture the complexities of water quality dynamics.

2.11 METHODS OF CARTOGRAPHIC VISUALIZATION

Cartographic visualization is the process of representing spatial data on a map using various techniques. Sometimes this process is also called geovisualizations. According to MacEachren and Kraak (1997), geovisualization represents a set of cartographic technologies and practices that take advantage of the ability of modern technologies. Visualization of the water quality belongs to the thematic mapping. Therefore, methods of thematic cartography were analyzed. The **thematic cartography** focuses on specific themes or subjects, using cartographic methods and techniques for empathizing the theme of the map, providing a clear visual representation of the data.

There are many cartographers presenting different classifications of the thematic cartography methods, such as (Kraak & Ormeling, 2013), (A. H. Robinson et al., 1994), (Kenneth Field, n.d.), and others. There is a way of representing these methods based on the geometric representation of the data. There, the methods are divided between point, line, and polygon.

The **point** methods involve placing symbols or markers at specific geographic locations to represent data where the geographic location is significant (Ogryzek & Ciski, 2018). Each point on the map corresponds to a specific geographic location, such as a city, a landmark, or an event. This method is particularly effective for visualizing data that is inherently point/based or for polygon/based data whose visualization is too small in the scale of the map, so these “too small” polygons are replaced by point symbols.

Point method includes:

- **Point maps** using simple points to show the location of features,
- **Proportional symbol maps** using symbol size to represent a quantitative variable,
- **Dot density maps** using symbols for quantitative visualization, as they show a good density distribution,
- **Wurman dots method**, which is similar to the graduated symbols but with a regular grid.

The **line** methods are employed to represent linear features and relationships in the landscape (Ogryzek & Ciski, 2018). This method is particularly effective for visualizing data that is inherently line/based or for polygon/based data whose visualization is too small in the scale of the map but has a linear character, so these polygons are replaced by line symbols. According to (Ogryzek & Ciski, 2018) these are effective for transportation networks, rivers, and boundaries. Line visualization is essential for understanding connectivity and flow, making it suitable for the limitation of feature flow or movement of features and network of different features and spatial relationships.

Some of the **line methods** are:

- **Route maps** showing transportation networks or movement patterns,
- **Flow maps** depicting the movement of objects, people, or data between locations,
- **Isolines map** that represents the connection of the same attribute data value on the line of the map.

Area methods involve the representation of data across defined regions or zones (Ogryzek & Ciski, 2018). This approach is particularly useful for illustrating phenomena that are distributed over larger areas, such as demographic data, land use, or environmental characteristics. Area methods can effectively represent complex information through visual regions.

Area methods using regions or polygons to visualize data, including:

- **Choropleth maps** that use shading or coloring areas based on a quantitative variable,
- **Cartograms** distort the size of areas to represent a variable.

There are also two categories of cartographic methods used to visualize spatial data: **qualitative and quantitative methods**. The qualitative methods relate to non-measurable qualities, indicating only the presence of a shown feature. On the other hand, quantitative methods show the intensity of a given phenomenon (2014).

Beyond the above methods, the following more modern approaches can be mentioned: **multivariate mapping**, that has an intern symbol encoding and combines more than one method at the same time; **bivariate/trivariate choropleth maps** that use two or three colors for the representation of the phenomena (each color for one phenomena); **multivariate Wurman dots**, combining Wurman dots method and multivariate mapping together. Other methods of multivariate mapping are not so often used and are not suitable for data visualization within this diploma thesis (such as cartotypogram, Chernoff faces, etc.).

The term **advanced cartography** is usually used for the university or online courses, where the contents of these courses include topics such as advanced thematic cartography, interactive web maps, animated maps, 3D, virtual reality, and data dashboards (*Advanced Cartography | University of Kentucky College of Arts & Sciences*, n.d.; *Information Package & Course Catalogue*, 2024) The most common terms connected to advanced cartographic methods are virtual environments, integration of big data, Machine learning and AI, collaborative visualization, real-time data visualization, and user-cantered design (Krassanakis et al., 2023; Mai et al., 2022; A. C. Robinson et al., 2023; Zhang et al., 2023). **User-Centric Design** is a growing emphasis on designing geovisualization tools that adapt to the needs of diverse users, including non-experts (A. C. Robinson et al., 2023). This trend focuses on improving usability and accessibility, ensuring that visualizations are intuitive and informative. It is the main technique that is going to be implemented in the thesis.

The mapping technique relevant to this study is the **spatiotemporal representation**. The spatiotemporal representation is a widely studied topic where geovisualization experts have been working on how to represent spatiotemporal data effectively. There are four main mapping techniques that can be used to represent spatiotemporal data (*UCGIS Bok Visualizer and Search*, n.d.):

- 1) Single static maps,
- 2) Multiple static maps,
- 3) Single dynamic maps,
- 4) Multiple dynamic maps.

For the thesis data it has been opted for two of these methods: the **multiple static maps** done as map posters and the single dynamic map as an **animation**.

The advantages of multiple static maps are they are easy to create and also allow map readers to visually compare between moments in time, even those that are not sequential. Fabrikant et al. (2008) called this **mental interactivity** by which the map reader can visually compare the spatial pattern differences between different snapshots (Irina Fabrikant et al., 2008). The main disadvantage to this method is the display size for the visualization of the data since these maps need to be simplified to be readable at a very small size.

Single dynamic maps use animation to show the changing information layers and to keep the base map static. These maps are the simplest version of animated maps and

are the easiest animated maps to create (UCGIS GIS&T Body of Knowledge, 2004). **Animated maps** provide advantages over other types of spatiotemporal visualization they are a way of having a congruent representation through time; this method uses the congruency principle (Tversky et al., 2002).

A concept of the design of animation to take into consideration on the animations is the adjustment of the dynamic variables (UN & Association, 2020). The **dynamic variables** established by DiBiase et al. (1990) are rate of change, order, and duration. DiBiase et al. (1992) describe the aspects of an animated map that can be adjusted for different effects and different representations of dynamic spatial data. The primary critique of the map animation is the cognitive limits of the map reader, which is mentioned in different literature (Battersby & Goldsberry, 2010; UCGIS GIS&T Body of Knowledge, 2024). Within this diploma thesis, the animated map (video) has been done as the introduction to the topic for the general public with an interest in the presented issue.

The choice of visualization method depends on the nature of the data, the goal of the map, and the audience (Ogryzek & Ciski, 2018). The concrete methods used for the thesis maps design are mentioned in the Research II chapter.

2.12 MAPS OF WATER QUALITY

The maps typically used for **monitoring water quality** are for scientific research purposes. According to Kiss et al. (2020), scientific visualization is known for its accurate representation of data, but it is often criticized for its lack of visual appeal. These maps serve as graphical representations of data collected by scientists and are often included in scientific papers. Scientific visualization is not limited to spatial data; it is also utilized in various other fields such as diagnostic imaging, 3D visualization of molecules, and 3D printing (Kiss et al., 2020). Kiss et al. (2020) state that information visualization and geovisualization, which focuses on spatial data, are closely related concepts, while information visualization primarily involves interactive demonstrations, aiding human cognition. However, geovisualization differs from scientific and information visualization as its main objective is to develop methods for demonstrating spatial data using maps (Kiss et al., 2020). In this study the intention is to do geovisualizations of scientific results.

The two major trends in geovisualization can be found in the study of water quality maps: **static maps** and **dynamic maps**. The classic approach of mapping is the static maps, as the maps seen in the above subchapters. Static mapping consists of creating static maps that visually represent the spatial distribution of elements, in this case, water quality indices over specific time periods, aiding in the visualization of trends and patterns in water quality data. The modern approach is a web map, a total interactive map for geo-visualization with the capacity of showing a lot of different datasets as the user wishes and near real data through API data sharing (itsupport, 2023).

Interactive mapping utilizes tools like QGIS and Google API to create interactive maps that display the spatial distribution of water quality parameters, allowing for dynamic exploration and analysis. 3D Geovisualization techniques are usually used to represent environmental data, offering a more immersive and detailed view of the spatial distribution of water quality parameters

For environmental and, specifically, **water quality map representation**, we can see that lately, a lot of platforms of web cartography have been set up and optimized for user interaction. Especially after the INSPIRE directory was implemented in the European Union. For water quality, a lot of European governments share platforms with the citizens to show the water quality of different beach areas, water bodies, piezometers, and wells. There are several examples of these platforms but some of them also offer the data download (Balla et al., 2020; Capolupo et al., 2022; Chowdary et al., 2009). An example of web cartography for seawater quality is done with an interactive

interface (Capolupo et al., 2022). Koleva et al. (2023) are presenting *IoT System for Real-Time Water Quality Measurement and Data Visualization*, Capolupo et al. (2022) are presenting *A WebGIS Prototype for Visualizing and Monitoring the Spatio-temporal Changes in Seawater Quality*, and there are more examples of such scientific presentations.

Most of the water quality maps are done with the interpolation method using points as a reference to interpolate the data (Balla et al., 2022). Another technique used is the graduated points, which can be easily used for the representation of a water parameter concentration. An example of the near real-time monitoring of water quality and hydrology management is the *4D DTE Hydrology datacube* Figure 9 (Brocca et al., 2024). All these techniques will be recurrent in the digitalization of a lot of data. However, with the digitalization of all the data, the regular public or governments and state holders normally do not have a record of all the products or facilities that are offered.

In this diploma thesis study, we have opted for a static visualization that is concise and easy to interpret and read as the decision makers normally do not spend time in the platforms analyzing the evolutions and data trends, so we face the necessity to concentrate the content of the data in that case.

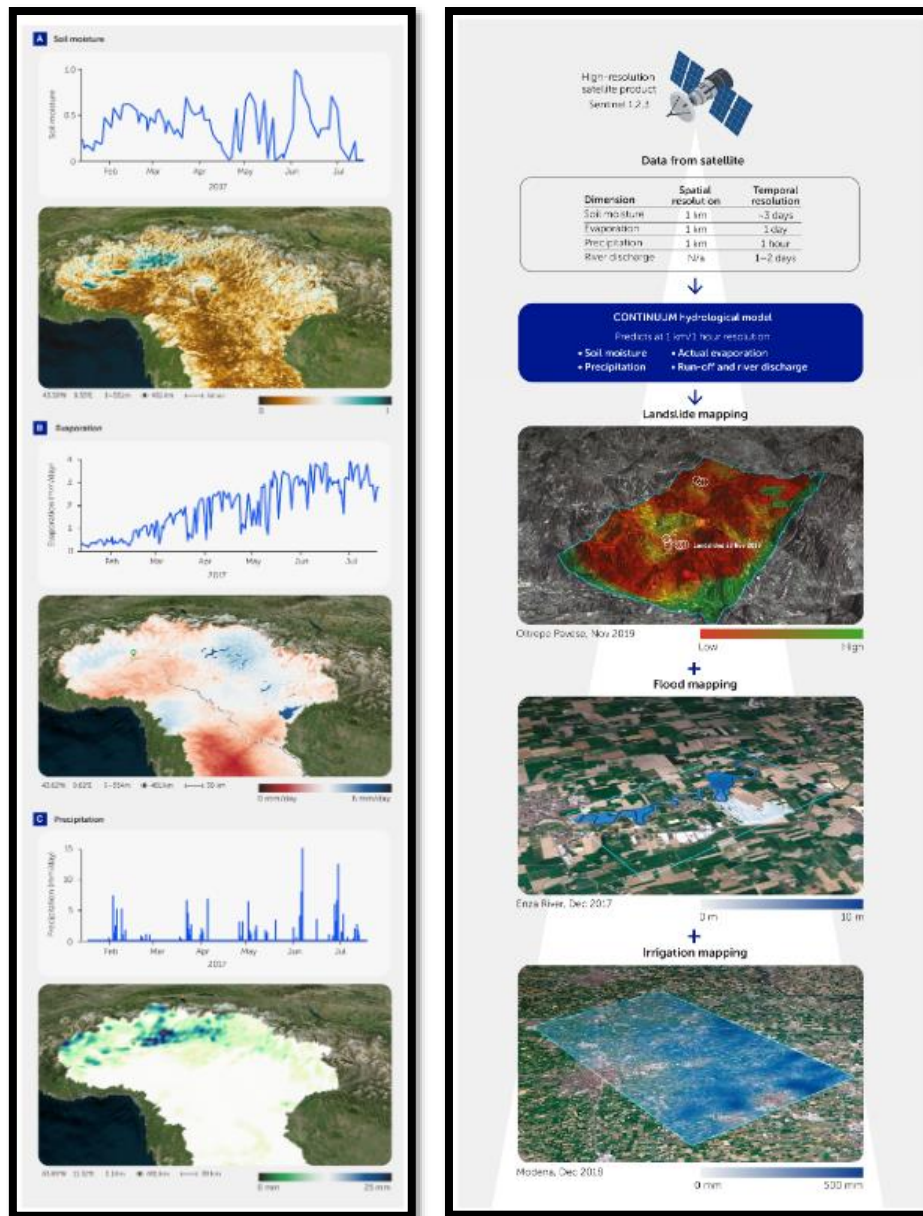


Figure 9: Digital Twin Earth (DTE) Hydrology platform (Brocca et al., 2024).

The approach that is intended in this thesis is the integration of different visualization and thematic cartography tools to enhance the representation of water quality data, providing a comprehensive view of the spatial and temporal changes in water quality parameters.

2.13 MAPS OF TAM GIANG LAGOON

The Tam Giang Lagoon lacks water quality maps from the author's knowledge. However, various maps exist, depicting the state and evolution of the ecosystems, coastal dynamics, inlets of the lagoon, bathymetries derived from morphological flux, aquaculture zones, and more. The most useful map for water quality assessment and WASI calibration is the one showing the state of the ecosystem, specifically the distribution of seagrass Figure 11.

The **orthophotomap** in Figure 10 illustrates the sites where seagrass has been collected within the Tam Giang – Cau Hai Lagoon. These sample collections promote the understanding of geographic spread and specific locations where seagrass research and

monitoring occurs. Seagrass is an important ecological indicator and plays a vital role in maintaining the health of the lagoon ecosystem as mentioned previously. This map aids in identifying areas of high ecological value and potential conservation sites.

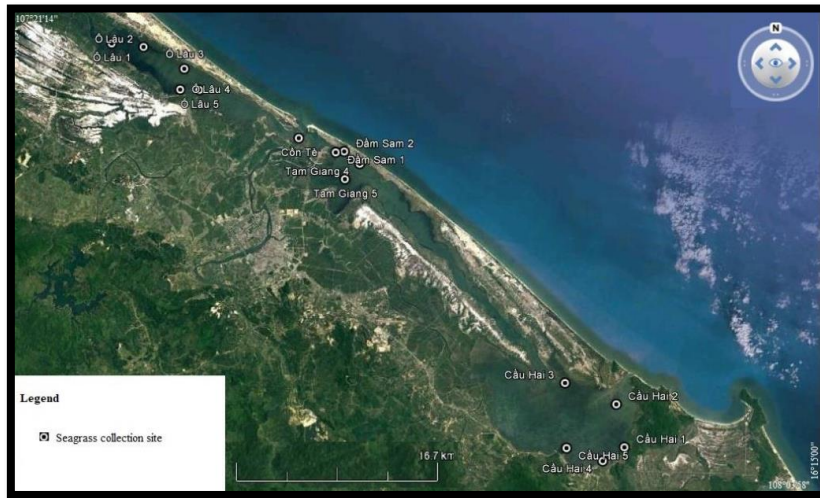


Figure 10: Image map of seagrass collection sites distribution in Tam Giang – Cau Hi Lagoon (Luong et al., 2020).

The map in Figure 11 depicts the **distribution of seagrass** throughout the lagoon, providing insight into its ecological spread and density. Understanding seagrass distribution is critical for assessing the lagoon's ecological health, and it is essential for a remote sensing shallow-water model retrieval of water quality as mentioned before.

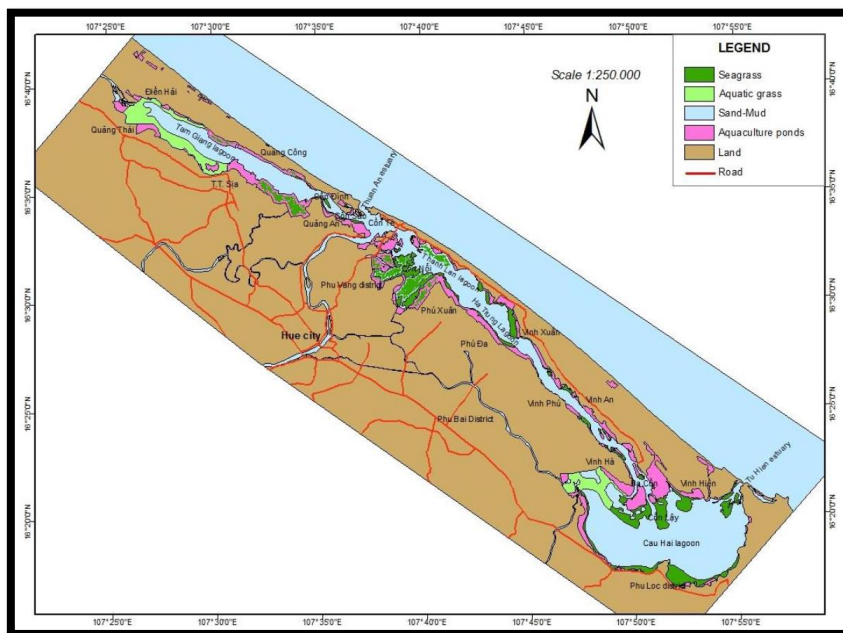


Figure 11: Map of seagrass distribution in Tam Giang – Cau Hi Lagoon(Luong et al., 2020)

The orthophotomap map (Figure 12) shows the delineation of **aquaculture activities** within the lagoon using object-based image analysis, providing insight into the spatial extent and organization of aquaculture zones. Aquaculture is a significant economic activity in the region. Having mapped its spatial distribution is vital for sustainable management.

FloodAdapt Project is the author of Figure 12. This entity has collaborated closely with the realization of this thesis.

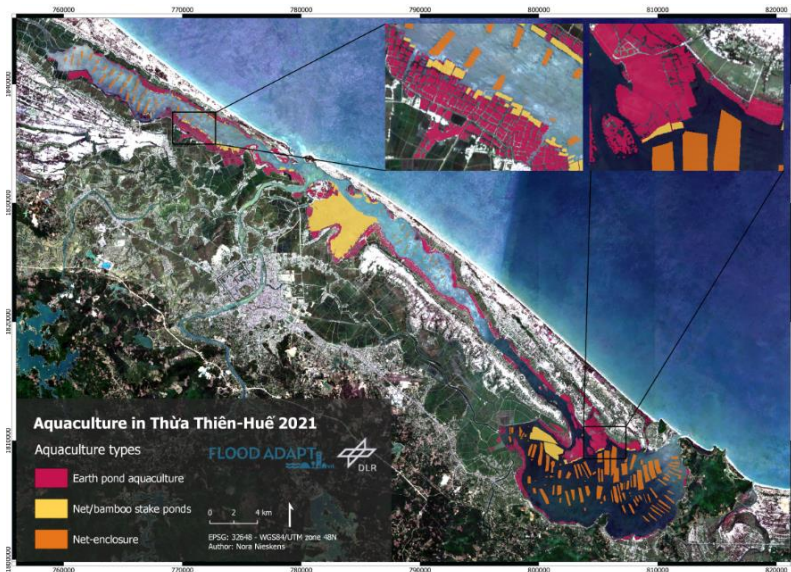


Figure 12: Aquaculture in Tam Giang lagoon delimited with Object based image analysis (Aquaculture of the Tam Giang-Cau Hai Lagoon | FloodAdaptVN, 2021).

The map in Figure 13 illustrates the project's area of intervention of the **(GCP/VIE/029/ITA - IMOLA Project Integrated Management of Lagoon Activities in Tam Giang Cau Hai Lagoon (Thua Thien Hue Province) (Phase 1)**, focusing on economic activities such as fishing, agriculture, and tourism in and around the lagoon. Identifying these areas helps understand human-lagoon interactions and informs strategies for sustainable development and conservation.

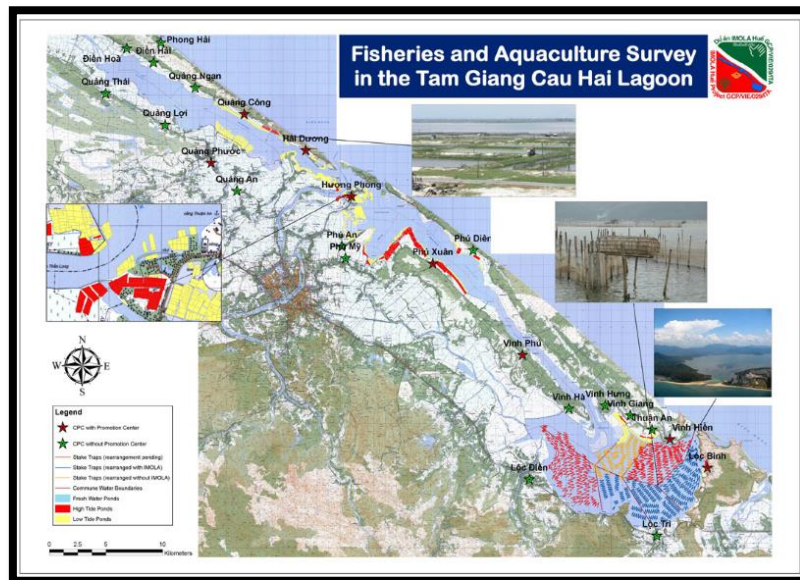


Figure 13: The project’s area of intervention and the location of some of the main economic activities carried out by people living around and in the lagoon (GCP/VIE/029/ITA - IMOLA Project Integrated Management of Lagoon Activities in Tam Giang Cau Hai Lagoon (Thua Thien Hue Province) (Phase 1), 2008).

The following Figure 14 is the showcase modifications to stake traps of the previous Figure 13 designed to improve water flow within the lagoon, an essential aspect of the ecological balance.

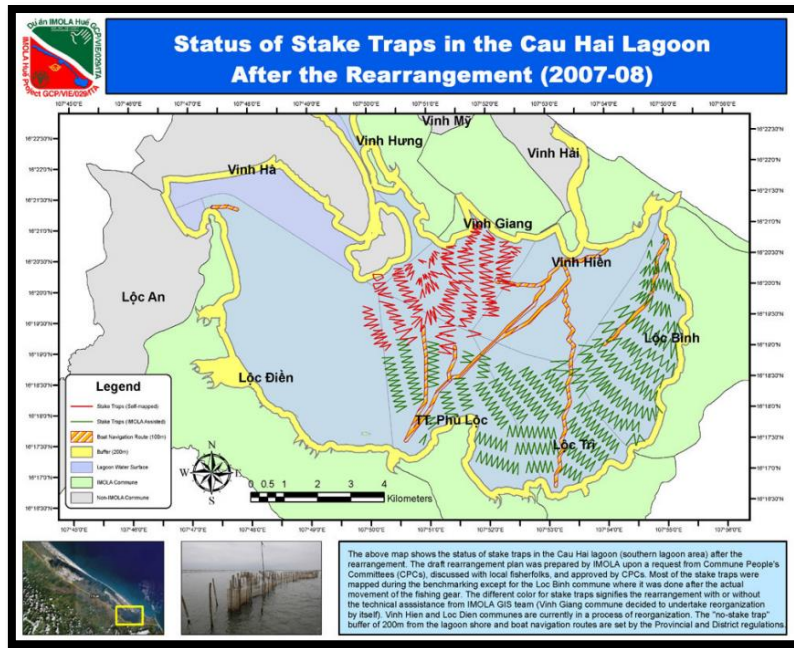


Figure 14: new status of the stake trap for a better water flow (GCP/VIE/029/ITA - IMOLA Project Integrated Management of Lagoon Activities in Tam Giang Cau Hai Lagoon (Thua Thien Hue Province) (Phase 1), 2008.

The bathymetry map in Figure 15 provides a detailed view of the lagoon's underwater topography, it is essential for understanding water flow patterns, sediment transport, and habitat distribution. **Bathymetric** data is the base for modeling hydrodynamic processes.

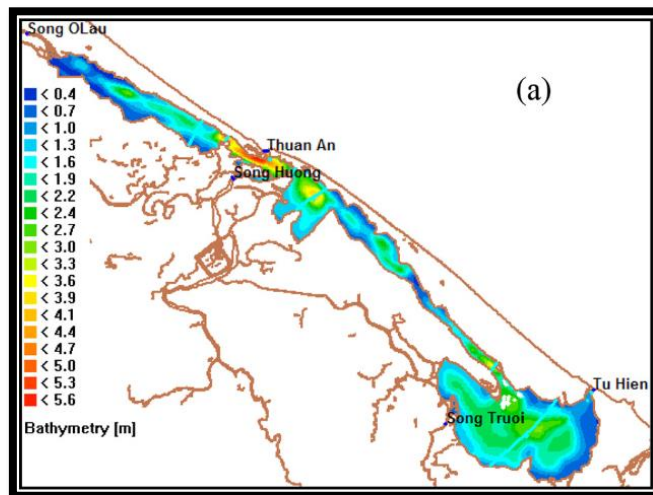


Figure 15: Bathymetry of a model from (Thi Thu Trang et al., 2020).

3 METHOD

In the initial part of the work, the following sub-chapters introduce the methods, models, technologies, and utilized datasets that were used to accomplish the set objectives. The first section provides a comprehensive list of datasets, their types as well as sources. This is followed by a brief introduction of the used software and tools. After, the conducted workflow with the most important aspects are summarized. Finally, it outlines the justification of the methods used in the analysis part and the advanced visualization.

3.1 DATA

The datasets used in the thesis are provided from the project FloodAdaptVN Project. The EO data provided was hyperspectral data from 3 different sensors. The first data provided for the analysis was with level 1 without atmospheric correction. As it is mentioned in the preprocessing challenges, the PRISMA satellite data for the analysis were discarded, and instead, level 2 of the other satellite was used. The data used in the results and the data analysis are the satellite images mentioned in Table 3, **EnMAP and DESIS images**. These images have a specific atmospheric correction appropriated for the water bodies and are described in the attachments-0. The data used for validation was **in-situ** data of water quality parameters analyzed by the laboratory from 2020–2023. The list of water parameters for in-situ data is listed in Table 4, with a total of 19.

Table 2: Hyperspectral Satellite characteristics.

Instrument	ENMAP	PRISMA	DESI
Sensor type	Hyperspectral IMG	Hyperspectral IMG	Spectrometer
Image num.	22	6	97
Dates available	08-10-2022 – 31-05-2023	12-02-2021 – 04-09-2023	12-10-2019 – 27-09-2023
Data Range	2021–Present	2020–Present	2018–Present
Spectral Bands	420–2,450 nm	400–2,500 nm	400–1,000 nm
Spatial res.	30 m	30 m	30 m (swath)
organization	German GFZ-DLR	Italian Space Agency (ASI)	DLR- Multi-User-System for Earth Sensing (MUSES)

The data used for the analysis and the results are listed in Table 3.

Table 3: Data used for the Analysis and results, EnMAP and DESIS data in level 2 of atmospheric correction.

Satellite image in L2	DATES
DESIS_002	2021-07-03
DESIS_003	2021-07-03
DESIS_004	2021-07-03
DESIS_002	2022-06-01
DESIS_001	2022-06-05
DESIS_002	2022-06-05
DESIS_002	2023-03-22
7DESIS_002	2023-05-03
DESIS_003	2023-05-03
DESIS_004	2023-05-03
EnMAP	2023-05-04
DESIS_002	2023-05-07
DESIS_003	2023-05-07
DESIS_004	2023-05-07
DESIS_002	2023-05-06
EnMAP	2023-05-31
EnMAP	2023-06-23
EnMAP	2023-07-01
DESIS_002	2023-07-06
DESIS_003	2023-07-06
EnMAP	2023-08-17
DESIS_003	2023-10-29
EnMAP	2023-11-09

Table 4: In-situ data available and analyzed at the laboratory.

In-situ Parameters	Samples Count	DATES
TSS	643	Mar-20
TEMP_oC	542	Apr-20
pH	542	Jun-20
DO	542	Aug-20
BOD5	542	Oct-20
COD	542	Mar-21
NH4+-N	541	Apr-21
NO2-	542	Jun-21
NO3-	540	Aug-21
PO43-	542	Oct-21
As	542	Feb-22
Cd	542	Apr-22
Pb	542	Jun-22
Cu	542	Aug-22
Zn	542	Oct-22
Mn	542	Nov-22
Hg	542	Dec-22
Fe	542	Feb-23
Coliform	537	Apr-23
		Jun-23

3.2 SOFTWARES USED

WASI

Versions and plugins:

WASI: simulation and inverse modeling of spectra from deep and shallow waters (Gege, 2004).

WASI-2D: inverse modeling of atmospherically corrected images (Gege, 2014).

WASI-AI: apply neural network, trained with random pixels processed with WASI-2D, to images M. Niroumand-Jadidi, P. Gege (2024): WASI-AI: Synergistic Integration of AI and Physics for Retrieving Water Quality and Benthic Parameters from Multi- and Hyperspectral Images. Submitted

Notepad++

Software Free, open-source text editor used to modify the .hdr files from the images.

SW information: (Downloads | Notepad++, 2024).

MS Excel

Microsoft Excel software was used to select and clean data. SW information: (Free Online Spreadsheet Software, 2024).

Google Colab

Google Colab is a cloud-based Jupiter notebook environment with customizable computer resources linked to the Google ecosystem used for statistical analysis.

Ecosystem documentation: (Colab.Google, 2024).

ArcGIS Pro

ArcGIS Pro is the desktop geographic information system application. This software was used for the spatial data visualization.

SW information: (*Desktop GIS Software | Mapping Analytics | ArcGIS Pro*, 2024)

Adobe Illustrator

Adobe Illustrator is a vector graphics editor software use to do the visualization compositions.

SW information: (*Vector Graphics Software – Adobe Illustrator*, 2024).

Adobe After Effects

Adobe After Effects is a digital motion graphics and compositing software application published by Adobe Systems. It is used in film and video post-production. Used for the animation.

SW information: ('Motion Graphics Efficiency and VR Features at the Core of What's New in After Effects CC', 2017).

3.3 GENERAL PROCEDURE

The workflow developed in this thesis Figure 16 starts with the data selection and preprocessing. The EnMAP and DESIS data are selected without fine clouds, Georeferenced in ArcGIS Pro, and the images are converted to a specific format file .hdr ENVI format customized in Notepad++. Following the guidance of the WASI manual and taking into account the model ambiguities, the satellite hyperspectral images from the

sensors EnMAP and DESIS with the **inversion model** for deep waters were processed, estimating three water quality parameters TSS, CDOM, and green algae content. After the water quality of the satellite data was gathered, it was compared statistically to the in-situ data; the data that was common was the TSS. From the satellite images, the information for the analysis was extracted with ArcGIS Pro, and then the **statistical analysis** was conducted with Python libraries and executed in Google Colab. Also, it was analyzed the relationship of the in-situ data, specifically the TSS vs the rest of the parameters, using Python libraries and Google Colab. With all the data and information, the data was visualized with **static maps** utilizing ArcGIS Pro and Adobe Illustrator for a customized composition. Then, an **animation** was created for better comprehensiveness of the time series using the static layers created previously and incorporating them in Adobe After Effects using the plugin ArcGIS Maps for Adobe Creative Cloud. The following section explains in more detail the methodology.

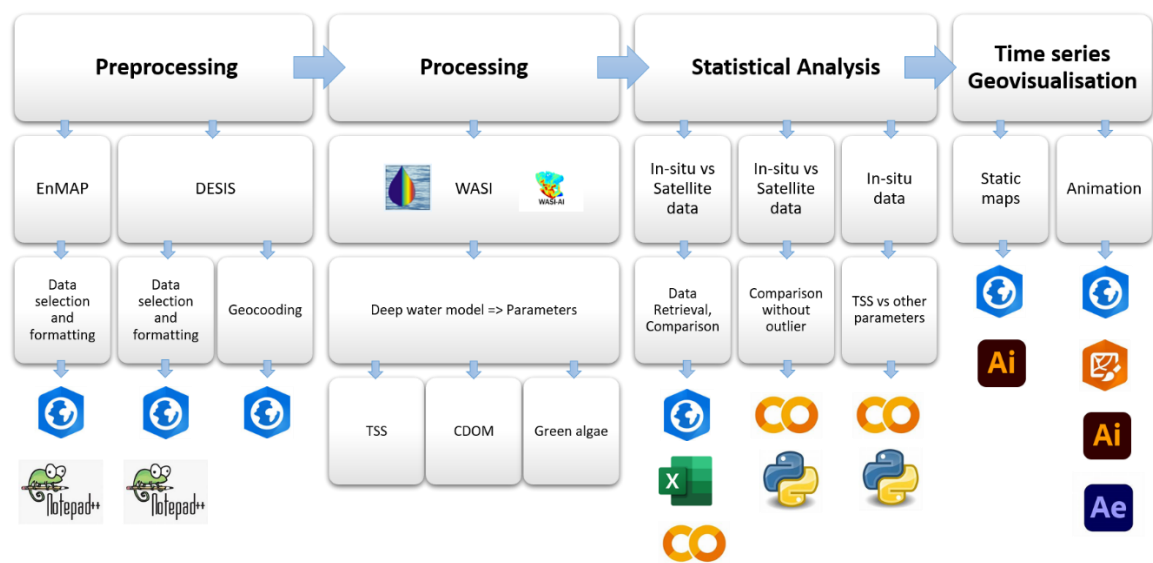


Figure 16: Thesis workflow overview.

3.4 ANALYSIS PART WASI METHOD

The main objective for this part was to extract water quality parameters. In the following lines it is explained the choice of method for this objective. The most common usage for water quality are the multispectral sensors and band ratio calculation. One of the biggest reasons is that the data is free and available without any cost. Also, EUMESAT has some products already available with water quality parameters but in a very low resolution, not suitable for inland waters, and the sensor used is multispectral image data. But in this project, we are able to use **Hyperspectral data** and have **more spectral bands** available for the analysis.

The data that was available was Hyperspectral data from different sensors (EnMAP, DESIS, PRISMA)/days/time and in-situ data (from 2020 to 2023). It is needed to take into consideration that the satellite and in-situ data do not share dates of acquisition; moreover, the acquisition and the sources are quantified with laboratory samples. These differences may affect the correlation between the concentration and may differ slightly from any satellite measurements. Due to the lack of reliable verification data, **an analytical method was implemented** to overcome the lack of data verification and the different times of image acquisitions. It is openly known that the analytical model is more reliable in different timelines and does not need any training for its effectiveness because it is based on a fiscal model. The analytical model methodology chosen can estimate different water quality parameters based on the spectrum shape of the different water quality parameters. There are many software for inverse modeling of water leaving

radiance and reflectance (*Software - IOCCG, 2024.*). The software that was adopted for the images that were processed was WASI (publicly available software and suitable for this use case). It is right to be pointed out that there are two software that could be used, WASI-2D (Gege, 2014) and BOMBER (Giardino et al., 2012) the Table 5 below is the comparison of capabilities. For this study, WASI was used as an inversion software, as the area has shallow waters and very irregular bottom substrates and WASI's proportions have 6 different options and more flexibility. Moreover, the software is available for Windows. It has to be pointed out that WASI is a model, and it is a simplification of the complex reality of the aquatic environments.

Table 5: Overview of major features of WASI-2D compared to Bomber (Gege, 2014)

Bio-optical model	WASI-2D	BOMBER
Reference	Albert and Mobley (2003), Albert (2004)	Lee et al. (1998, 1999)
Spectrum type	<ul style="list-style-type: none"> Remote sensing reflectance Upwelling radiance 	Remote sensing reflectance
No. of phytoplankton classes	6	1
No. of bottom substrate types	6	3
Specific absorption of phytoplankton	From files	From file; can be related to chlorophyll concentration
Specific absorption of gelbstoff	<ul style="list-style-type: none"> Exponential function; slope can be fit parameter From file 	Exponential function; slope can be related to gelbstoff absorption
Specific absorption of non-algal particles	From file	Exponential function; slope can be fit parameter
Specific backscattering of suspended matter	<ul style="list-style-type: none"> Power law; exponent can be fit parameter From file; can be related to suspended matter concentration 	From file
Specific backscattering of phytoplankton	From file; can be related to chlorophyll concentration	From file
Artefacts	Sun glint, sky glint	Constant offset
Software implementation		
Software environment	Windows	ENVI+IDL
Programming language	Delphi 7.0	IDL
Image format description	<ul style="list-style-type: none"> ENVI header Manual input in menu 	ENVI header
Sensor band description	<ul style="list-style-type: none"> ENVI header From ASCII files 	ENVI header
Land mask	Selectable band of image	Separate file
Inversion algorithm	Downhill Simplex	CONSTRAINED_MIN based on generalized reduced gradient method
Residual	Weighted least squares	Least squares
No. of fit parameters	<ul style="list-style-type: none"> Deep water: 21 Shallow water: 28 	<ul style="list-style-type: none"> Deep water: 4 Shallow water: 7
Fit quality measure	Residual and number of iterations	Relative error of reflectance
Test run of inversion	<ul style="list-style-type: none"> Single pixel Selected area 	Single pixel

WASI-AI functioning and model equation bases

We need to take into consideration that WASI-AI at the moment is at the beginning of the operation, and it does not have specific documentation for it. A prerequisite to processing images in WASI 2D is that since the model does not simulate the influence of the atmosphere, it needs to be calculated in advance. For the Optimization of inversion in deep water, the **most important parameters** that can be determined from irradiance reflectance spectra of deep water are the concentrations of **phytoplankton**, **CDOM**, and **NAP** (WASI manual, 57page). A study has been performed which investigated their retrieval sensitivity to errors (Gege, 2002). The results show a very small sensitivity for suspended matter, some sensitivity for CDOM, but a very high sensitivity for phytoplankton. The study suggested a procedure for initial values determination, which has been optimized by further simulations. The processing with WASI 2D supports spectral reflectance and spectral radiance. WASI uses the upwelling radiance, a radiative transfer model, to model the water characteristics. Inverse modeling determines model parameters for a given spectrum with the objective of minimizing the correspondence with the model and the curve of a given spectrum.

In this case with WASI 2D processing, it has been used the radiance reflectance Figure 17 above surface (page 64 in the WASI manual, the following chapter is based in WASI manual and the latest papers of Peter Gege (Gege, 2014).

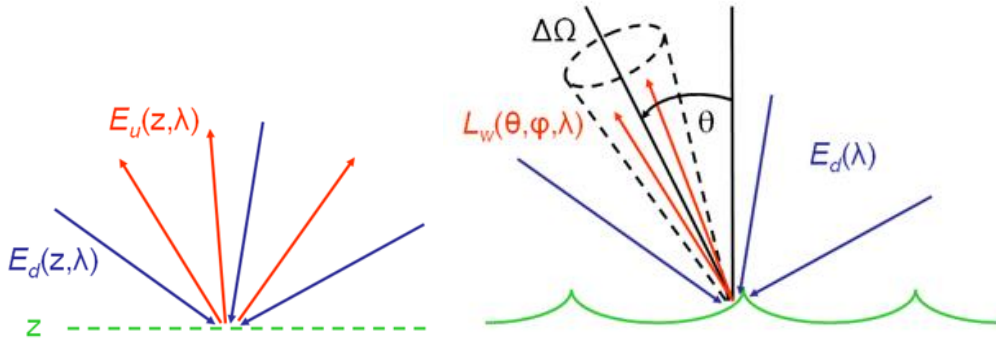


Figure 17: 1) Rays contributing to the irradiance reflectance. 2) Rays contributing to the remote-sensing reflectance(Overview :: Ocean Optics Web Book, 2024)

The **Irradiance reflectance** $R(\lambda) = E_u(\lambda) / E_d(\lambda)$, which is the ratio of upwelling irradiance to downwelling irradiance in water (Gege, 2014; Mobley, 1994). The equation 1 irradiance reflectance depends on the illumination and for deep waters, a suitable parametrization was found by Gordon et al. (1975).

$$R(\lambda) = f \cdot \omega_b(\lambda) + Q \cdot r_{rs,F}(\lambda) \quad (1)$$

F comprises the illumination dependencies(it can be treated like a constant or a parameter).

$\omega_b(\lambda)$ depends on the inherent optical properties of the water body (absorption and bac scattering).

Q, which is a measure of the anisotropy of the light field in water, is treated here as a wavelength-independent parameter with a default value of 5 sr. It depends on the geometric distribution of the upwelling and downwelling light and, thus, on the scattering and absorption properties of the water body. Consequently, **Q** depends on the wavelength.

$r_{rs,F}(\lambda)$ Is the contribution caused by the fluorescence component of radiance reflectance equation 2.

$$r_{rs,F}(\lambda) = L_F(\lambda) / E_d(\lambda) \quad (2)$$

$L_F(\lambda)$ upwelling spectral radiance

$E_d(\lambda)$ downwelling irradiance

The **Radiance reflectance** $r_{rs}(\lambda)$ equation 3 above the water surface two components of upwelling. It is the sum of the remote sensing water contribution reflectance $R_{rs}(\lambda)$ and the reflectance of the water surface $R_{rs}^{surf}(\lambda)$:

$$r_{rs}(\lambda) = R_{rs}(\lambda) + R_{rs}^{surf}(\lambda) \quad (3)$$

$r_{rs}(\lambda)$ equation 4 has 25 parameters which may be fitted and, $r_{rs}-(\lambda)$ has 15 parameters to be fitted. So, it is important to start with initial values that are not too different from the final results, for a proper fit tuning.

$$r_{rs}-(\lambda)=R(\lambda)/Q \quad (4)$$

$R_{rs}-(\lambda)$, water contribution reflectance.

$R(\lambda)$, Radiance reflectance.

Q , which is a measure of the anisotropy of the light field in water, is treated here as a wavelength-independent parameter with a default value of 5 sr. It depends on the geometric distribution of the upwelling and downwelling light and, thus, on the scattering and absorption properties of the water body. Consequently, Q depends on the wavelength.

$$r_{rs}-(\lambda)=f_{rs} \cdot \omega_b(\lambda)+r_{rs,F}(\lambda) \quad (5)$$

If a downwelling irradiance equation 5 measurement is available, the number of fit parameters for $r_{rs}(\lambda)$ can be reduced by 4 (α , β , γ , δ). In this case, the box "use Ed measurement" should be checked, and the measured spectrum must be specified.

The inherent optical properties are calculated as follows equation 6:

$$R_{rs}^{deep}(\lambda)=f_{rs}(\lambda) \cdot u(\lambda) \quad (6)$$

The factor $f_{rs}(\lambda)$ parametrize the viewing and illumination geometry in terms of the viewing angle in water, θ_v , and the sun zenith angle in water, θ_{sun} , also standars for the wind speed that can be negligible . These parameters have been based on the Hydrolight software and other prameters (Albert & Mobley, 2003; Gege, 2004; Mobley, 1994).

The factor $u(\lambda)$ function is wavelength dependent indicates the inherent optical properties of the water bodies for the absorption and backscattering and the calculation of the water constituents. The following formulas explain the relationship of the constituents equation 7.

$$u(\lambda)=b_b(\lambda) / (a(\lambda) + b_b(\lambda)) \quad (7)$$

The inherent optical proprieties of the water body are calculated as follows:

Absorption coefficients equation 8.

$$a(\lambda)=a_w(\lambda) + a_{ph}(\lambda) + a_y(\lambda) + a_d(\lambda) \quad (8)$$

Backscattering coefficients equation 9.

$$b_b(\lambda)=b_{b,w}(\lambda) + b_{b,x}(\lambda) \quad (9)$$

The absorption coefficients are constituted by the absorption of pure water $\mathbf{a_w}(\lambda)$ and, other water constituents considered (Kou et al., 1993; Pope & Fry, 1997). There are four types of water constituents considered in WASI: phytoplankton, gelbstoff, detritus and suspended particles. The first three are parameterized by their spectral absorption coefficients $\mathbf{a_{ph}}(\lambda)$, $\mathbf{a_Y}(\lambda)$ and $\mathbf{a_d}(\lambda)$, respectively; suspended particles by their spectral backscattering coefficient, $\mathbf{b_{b,x}}(\lambda)$ (Morel, A. (1974) - IOCCG, 2024.). Backscattering by phytoplankton is included in $\mathbf{b_{b,x}}(\lambda)$.

WASI water constituents' names are:

Water constituent	Parametrization	Coefficients
Phytoplankton	Spectral absorption	$a_{ph}(\lambda)$
Gelbstoff	Spectral absorption	$a_Y(\lambda)$
Detritus	Spectral absorption	$a_d(\lambda)$
Suspended particles	Spectral backscattering	$b_{b,x}(\lambda)$
Phytoplankton	Spectral backscattering	$b_{b,x}(\lambda)$

On the WASI software model, the water constituents are grouped in three with the following names for the three different spectral absorptions: CDOM, phytoplankton (phy), and non-algal particles (NAP/TSS). These constituents are the ones that are the output of processing in chapter 4. The below equations allowed us to model the spectrum and retrieve the water constituents, accurately with the condition of a preprocessed atmospheric correction. For further details on the model and the estimation of the coefficients, please look at the WASI manual, chapter 2, and (Gege, 2014).

Limitations documented that can occur in WASI:

One reason for the bad estimation results can arise since the WASI tool has been originally developed for water bodies with generally lower chlorophyll a concentrations, such as the lake Constance in Germany (Gege, 2004). It can cause differences in the results for water bodies with a high concentration of algae. The second reason for a poor result might be the bad estimation of the atmosphere and the interference in the processing incorporating noise in the model (Gege, 2004).

The work done by Marier et al has been used to provide reference of the parameters used during the processing Figure 18, and Figure 19 (Maier et al., 2021).

WASI Parameter	Range	Standard	Steps	Log Scale	Description
Chlorophyll <i>a</i>	$1 \mu\text{g L}^{-1}$ to $100 \mu\text{g L}^{-1}$	-	30	yes	concentration of chlorophyll <i>a</i>
C_X	0.1mg L^{-1} to 100mg L^{-1}	1	20	yes	concentration of non-algal particles type I
C_{Mie}	1mg L^{-1} to 20mg L^{-1}	0	20	no	concentration of non-algal particles type II
C_Y	0.1m^{-1} to 5m^{-1}	0.1	20	no	CDOM concentration
zB	1 m to 5 m	2	10	no	water depth
Sun	35° to 65°	50	10	no	sun position
FA1	0.1 to 5	0	10	no	background type sand
FA2	0.1 to 5	0	10	no	background type silt
FA5	0.1 to 3	0	10	no	background type macrophyte
g_{dd}	0Sr^{-1} to 0.5Sr^{-1}	0.02	10	no	fraction of sky radiance due to direct solar radiation
g_{dsr}	0Sr^{-1} to 1Sr^{-1}	0.318	10	no	fraction of sky radiance due to molecule scattering
g_{dsa}	0Sr^{-1} to 1Sr^{-1}	0.318	10	no	fraction of sky radiance due to aerosol scattering

Figure 18: Parameters used in WASI (Maier et al., 2021)

Table A1. Summary of the default WASI simulation parameters (see [56]).

Parameter	Standard Value	Unit	Description
C[0]	0	$\mu\text{g L}^{-1}$	Concentration of phytoplankton class 0
C[1]	0	$\mu\text{g L}^{-1}$	Concentration of phytoplankton class 1
C[2]	0	$\mu\text{g L}^{-1}$	Concentration of phytoplankton class 2
C[4]	0	$\mu\text{g L}^{-1}$	Concentration of phytoplankton class 4
fluo	0		chlorophyll a fluorescence quantum yield
S	0.014	nm^{-1}	Exponent of CDOM absorption
n	-1	-	Angström exponent of particle scattering
T_W	25	$^{\circ}\text{C}$	Water temperature
f	0.033	-	f-factor of R
Q	5	Sr^{-1}	Anisotropic factor of upwelling radiation
z	0	m	Sensor depth
view	0	$^{\circ}$	Viewing angle
bbs_phy	0.001	$\text{m}^2 \text{mg}^{-1}$	Specific backscattering coefficient of phytoplankton
f_nw	0	-	Fraction of non-water area
fA[0]	0	-	fraction of bottom type #0 (constant)
fA[3]	0	-	fraction of bottom type #3 (seagrass)
fA[4]	0	-	fraction of bottom type #4 (mussel)
f_dd	1	-	Fraction of direct downwelling irradiance
f_ds	1	-	Fraction of diffuse downwelling irradiance
H_oz	0.38	cm	Scale height of ozone
alpha	1.3170	-	Angström exponent of aerosols
beta	0.2606	-	Turbidity coefficient
WV	2.500	cm	Scale height of precipitable water in the atmosphere
rho_L	0.02006	-	Fresnel reflectance of downwelling radiance
rho_dd	0.03325	-	Reflection factor of E_{dd}
rho_ds	0.0889	-	Reflection factor of E_{ds}

Figure 19: More Parameters used in WASI (Maier et al., 2021)

3.5 ADVANCE GEOVISUALIZATION METHOD

The main objective for the following part was to create an advanced visualization product with the data extracted from the first part, water quality parameters, and supporting data. The choice of method for this objective is to use ArcGIS Pro and Adobe Illustrator to create a series of static maps and create an animation for the diffusion of the water quality in the lagoon with the software Adobe After Effects.

Static maps

For the series of static maps, ArcGIS Pro software has been used as the tool for geovisualization. The satellite images were colored according to selected color schemes, and points with corresponding colors were used for the visualization of in-situ data. The Esri basemap was used as the topographical base. The poster design was created in the Adobe Illustrator software, while the connectivity between ArcGIS Pro and Adobe Illustrator was provided by the plugin *ArcGIS Maps for Adobe Creative Cloud*.

Map animation

The map animation was created using Adobe After Effects software. Therefore, in this part, the focus is on the use of Adobe After Effects, a software renowned for its capabilities in digital visual effects and motion graphics. Adobe Illustrator is a vector-graphics editor software and was used as an intermediate step to transfer vector graphics from ArcGIS Pro to Adobe After Effects. The software's structure entails arranging layers in a timeline, providing the flexibility to manipulate properties such as position, rotation, and color, as well as the application of various effects. Primarily utilized for animating data in a timeline and vector graphics, its diverse capabilities render it valuable across industries, encompassing domains such as web design and

video post-production ('Motion Graphics Efficiency and VR Features at the Core of What's New in After Effects CC', 2017).

A lot of inspiration for the Animation creation is available at several youtube channels with tutorials like Flat Pack FX (MAP Animations - YouTube, 2024.), Boone Loves Video (Monday Maps!, 2024) and others.

For Adobe After Effects it is needed to take into consideration that it has four main panels Figure 20:

- 1- Project panel, where you can drag and drop files, and images called assets. New compositions can be created by selecting different assets and choosing composition settings.
- 2 - Layer panel is where the animation and editing of layers occur. Layer Management Controls the visibility and order of layers (e.g., top layers are visible over bottom layers)., opacity, and other effects. Editing Tools like trim, extend, or split layers act to refine the timing of the composition.
- 3- Timeline panel is the part in keyframe animation adjustment timing and transitions by setting keyframes for movement happens
- 4- Effects and Presets situated on the right side of the workspace, this panel offers a wide range of effects and presets to enhance the animation.
- 5- Output area on the center displays the composition that is created.
- 6- The top toolbar where you can create lines shapes text, and others.

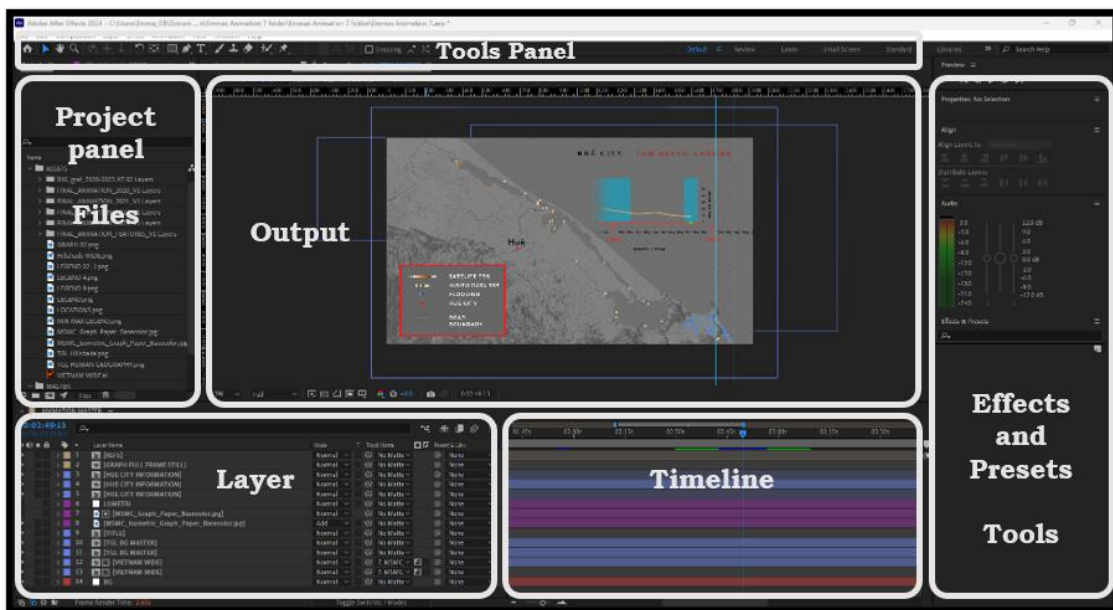


Figure 20: Adobe After Effects Interface Overview.

4 RESEARCH I

THE PROCESS OF THE DATA ANALYSIS

For the process of the data analysis, it has been an intricate step. In this chapter, it is explained how the results of water quality have been obtained from the original data, data preprocessing and data processing chapters. Also in a separate part, it has been discussed the challenges that occurred during the processing of the data and why some of the data has not been processed. After that, the statistics of the analysis data has been performed.

4.1 DATA PREPROCESSING

The following sub-chapter, data preprocessing describes the process of rearranging the data for having the proper input in the data for the processing step in WASI software.

The requirements for the data processing:

- Level2 data with good atmospheric correction (proper estimation of water vapor content).
- Proper file format .hdr (band, wavelength, and fwhm enumeration)

The data used for the processing is level 2. The EnMAP data has the MIP atmospheric correction mentioned in attachment-0. The DESIS data has a customized atmospheric correction performed by de los Reyes et al., 2024 (after realizing in several tests that the atmosphere was not properly retrieved)(de los Reyes et al., 2020).

The format of the images needed to be converted to .hdr proper format. From the original format .TIF and .bsq it is load the files in ArcGIS Pro and converted to “**ENVI .hdr**” format.

The .hdr file that is converted directly form ArcGis PRO does not contain the proper Band number, Wavelength and fwhm for that is necessary to open the .hdr file in a text editor and introduce the data manually an example of file format is in the attachments-0.

It needs to be pointed out that some of the DESIS images had geometric distortion or the geocoding was not properly done. As it is known, these images come by request and do not have a permanent orbit where the images are periodically collected. In those cases the images have been ortorectificated in ArcGIS PRO with the tool “Alignment => Georeference => Add Control Points => Save as New”.

Once this is finished we can start the processing.

4.2 DATA PROCESSING

The data processing is executed in WASI software with the objective of extracting water quality parameters from the hyperspectral images.

First of all, one must open WASI and load the image for the inversion then click in File => Load image => select the .dat file from the ENVI format image. In Options 2D it is selected the bands that you want to represent the image and the mask values for the water values depending on the image you are masking Figure 21.

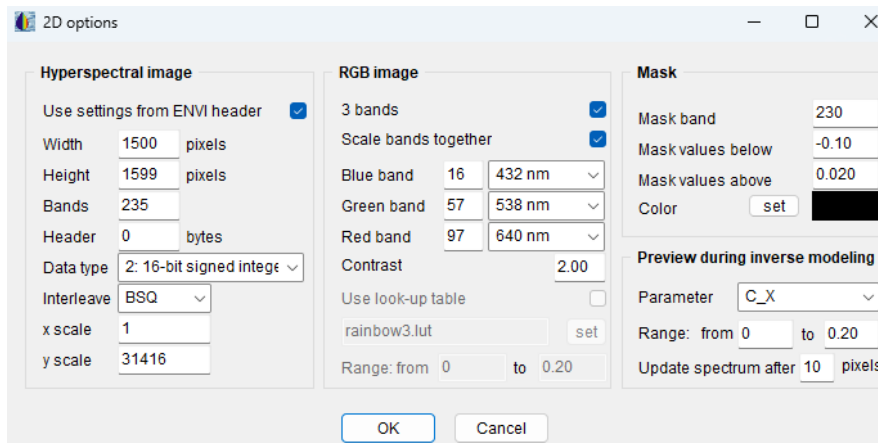


Figure 21: Image file configuration of band representation and land Masking.

The next step is to define the parts of the spectrum that are going to be analyzed and how many iterations you want the model to do for fitting the wavelength curve of the spectrum. In options=>inverse calculation => fit tuning you select the wavelength range; **Error! No se encuentra el origen de la referencia..** In the processing for DESIS images is selected from 430-900 in EnMAP you can use from 400 – 900 part of the spectrum you want to analyse.

The **baseline parameters** that are selected are C(5) green algae set up at 1, C_X TSS set up at 1, C_Y CDOM set up at 1, and the g_dd Sunlint + Path radiance -0.002. These parameters have been defined after trial and error. It is necessary to adapt the g_dsa parameter on some of the DESIS images because of the atmosphere. The exact parameters for training the model of the most representative **pixel of the image spectrum are summarized** in the Table 6: Values for the calibration of the model of the most representative pixel for calibration. The date with a slash on top is an image that has a distortion; in the end, it has not been used in the processing. The inversion that is selected is above the waters, and it is the model of deep waters; even though the lagoon is a shallow water body. The bottom of the lagoon is complex, and most parts of the lagoon have a pretty dark algal surface and dark benthonic life. To know the process of arriving to choose this model of deep waters, go to the Data processing challenges.

Table 6: Values for the calibration of the model of the most representative pixel for calibration. The date with a slash on top is an image that has a distortion; in the end, it has not been used in the processing.

Sensor image	date	Fit.Param C(5)	Fit.Param C_X	Fit.Param C_Y	Fit.Param g_dd
DESIS_002	20210703	11.37	6.706	0.4171	0.05490
DESIS_003	20210703	4.467	6.734	0.3418	0.05487
DESIS_004	20210703	0.9506	3.238	0.2296	0.1251
DESIS_002	20220601	0	6.062	0.3822	1.641
DESIS_001	20220605	2.505	4.362	0.3539	0.08780
DESIS_002	20220605	12.49	9.158	0.6116	0.07946
DESIS_002	20230322	0	8.948	0.4360	-0.00241
DESIS_002	20230503	4.349	4.856	0.2791	0.5062
DESIS_003	20230503	0	5.539	0.1744	0.3037
DESIS_004	20230503	0	3.785	0.1921	0.3150
EnMAP	20230504	11.94	5.255	0.6793	-0.01839
DESIS_002	20230507	7.208	7.463	0.7079	0.2711
DESIS_003	20230507	1.447	5.854	0.2447	0.2438
DESIS_004	20230507	2.952	3.614	0.1952	0.6075
DESIS_002	20230506	11.97	6.128	0.6467	2.550
EnMAP	20230531	10.37	7.301	0.7102	-0.02215
EnMAP	20230623	0	4.518	0.4426	0.005695
EnMAP	20230701	0	4.276	0.5623	0.01892
DESIS_003	20230706	0.07359	5.834	0.5493	0.07568
DESIS_003	20230706	0.1761	6.842	0.2562	0.01041
DESIS_005	20230706	0	2.804	0.003314	0.02009
EnMAP	20230817	25.56	10.26	2.199	-0.05060
DESIS_003	20231029	0	4.922	0.3999	0.3223
EnMAP	20231109	0.7801	6.984	0.7589	-0.01668

Once the parameters are set, it is time to fit them to the most common spectra from the lagoon that you can find. For that, it is necessary that you click a pixel in the image, and the spectrum will display into the main WASI panel. It is imperative that the pixel that is picked has a representative spectrum and tries to fit the parameters. In order to do that it is pressed the invert spectrum and the start button, to see how the red line Figure 22 fits the blue spectrum of the pixel selected. Normally, with 5 iterations, you find a good fit. In other cases, it is necessary to change the parameter values manually and fix the parameters to have a better inversion to the real spectrum.

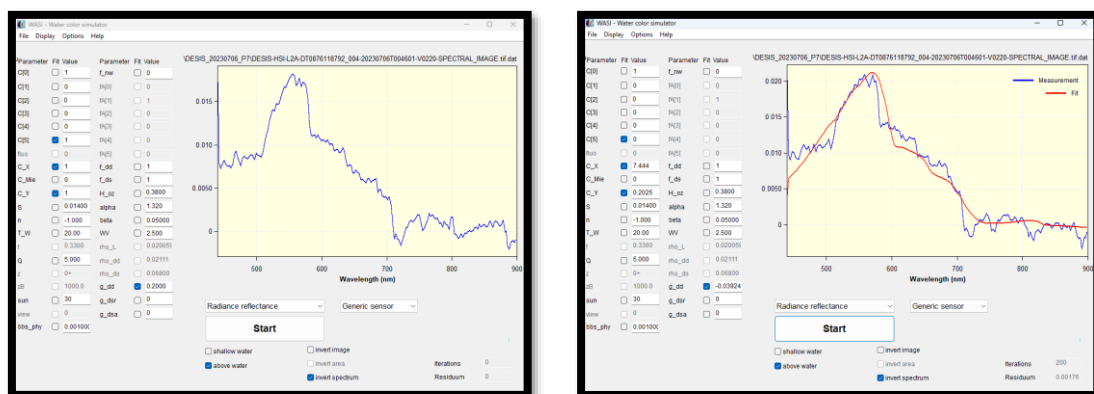


Figure 22: Fit parameters and inversion of the spectrum using the invert spectrum selection and the start button.

Once the spectrum and the fit red spectrum based on the parameters have a proper fit it is selected the inversion of the entire image and the entire image is inverted based on similar iterations.

The result of the inversion are a series of data Figure 23 that have the parameters used for the inversion, the final raster image with the water quality parameters and the visualization of the results:

DESIS_CLIP_20230706_004_AI_4p.AI	5/3/2024 6:48 PM	Adobe Illustrator ...	74,954 KB
DESIS_CLIP_20230706_004_AI_4p.hdr	5/3/2024 6:48 PM	HDR File	1 KB
DESIS_CLIP_20230706_004_AI_maps_Inver...	5/3/2024 6:48 PM	PNG File	144 KB
DESIS_CLIP_20230706_004_AI_samples_4p...	5/3/2024 6:47 PM	PNG File	143 KB
DESIS_CLIP_20230706_004_AI_validation_...	5/3/2024 6:48 PM	PNG File	98 KB
DESIS_CLIP_20230706_004_AI_validation_J...	5/3/2024 6:48 PM	PNG File	112 KB
Fit_DESIS_CLIP_20230706_004.txt	5/3/2024 6:46 PM	Text Document	671 KB
Fit_DESIS_CLIP_20230706_004.WAS16.par	5/3/2024 6:46 PM	PAR File	31 KB

Figure 23: Final data Outputs from the inversion in WASI.

The visualization of the results are found in .png images and Matlap graphics, visualizing the training points/validation points where the model has been trained, the band mask and the band image composition Figure 24. The accuracy of the model is presented in the parameters accuracy graphical representation Figure 25 the blue line represents the training and the red line represents the results, if the two lines are really proximal the better the parameter estimation. The last result is the distribution of the inversion result for every parameter with the scale Figure 26. From these last results, the statistics have been extracted in ArcGIS Pro passing the raster to a point layer and extracting the statistics for every raster.

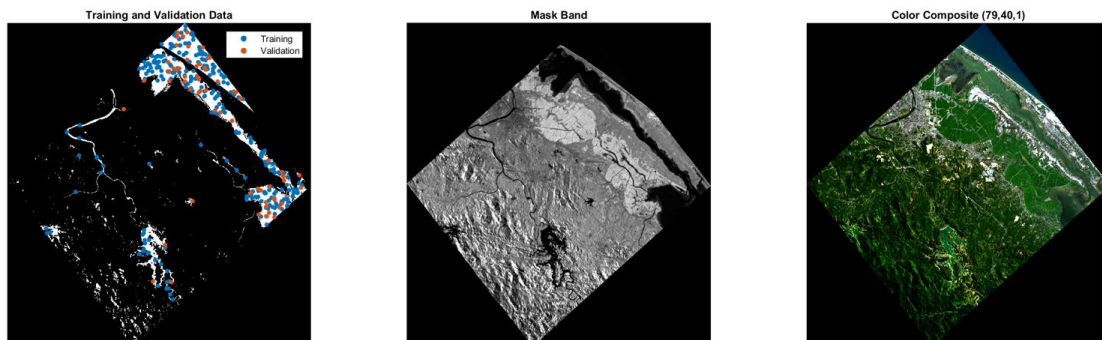


Figure 24: Result visualizing the training points/validation points the band mask the band image composition.

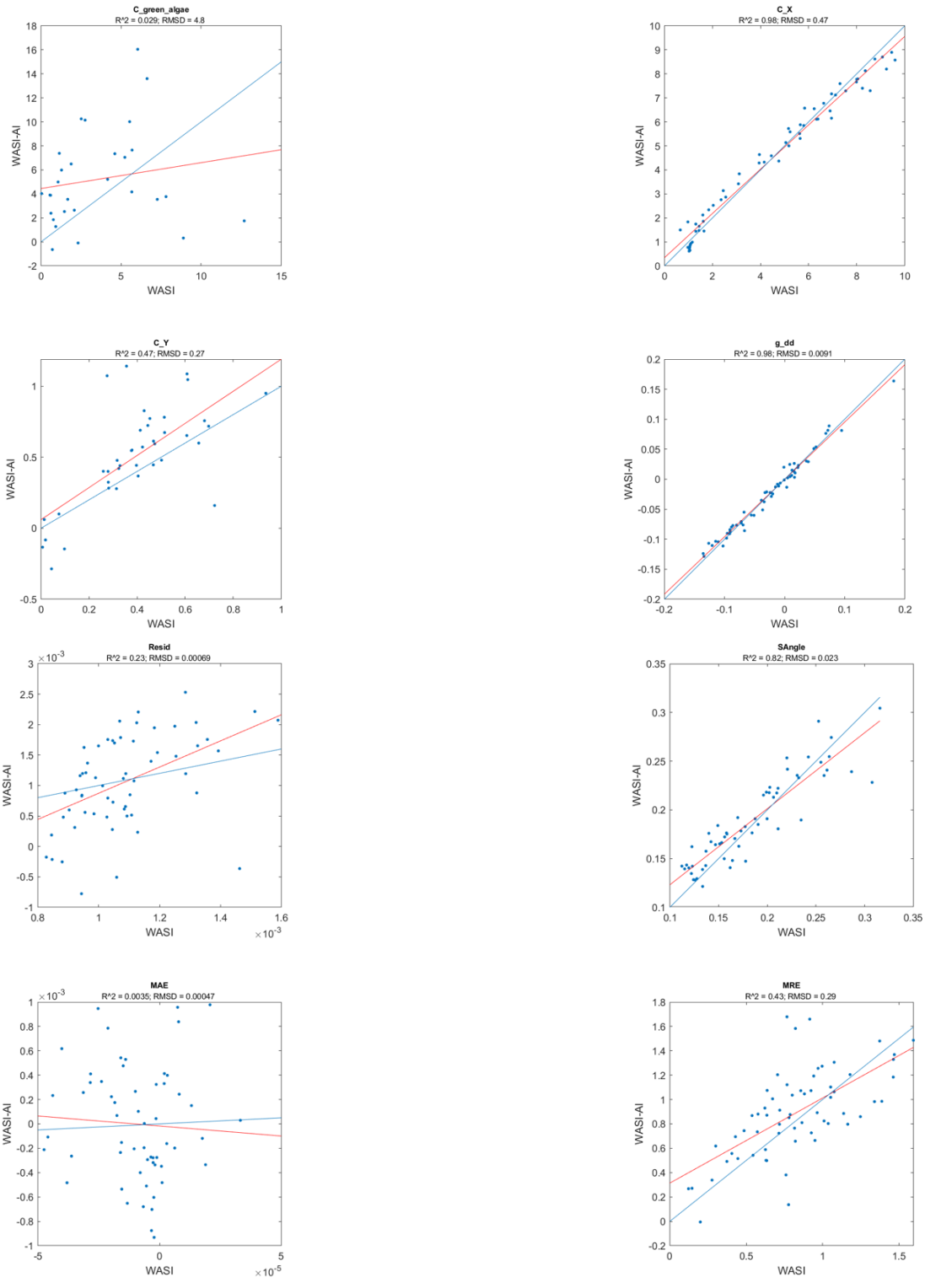


Figure 25: Result visualizing the parameter's accuracy and distribution.

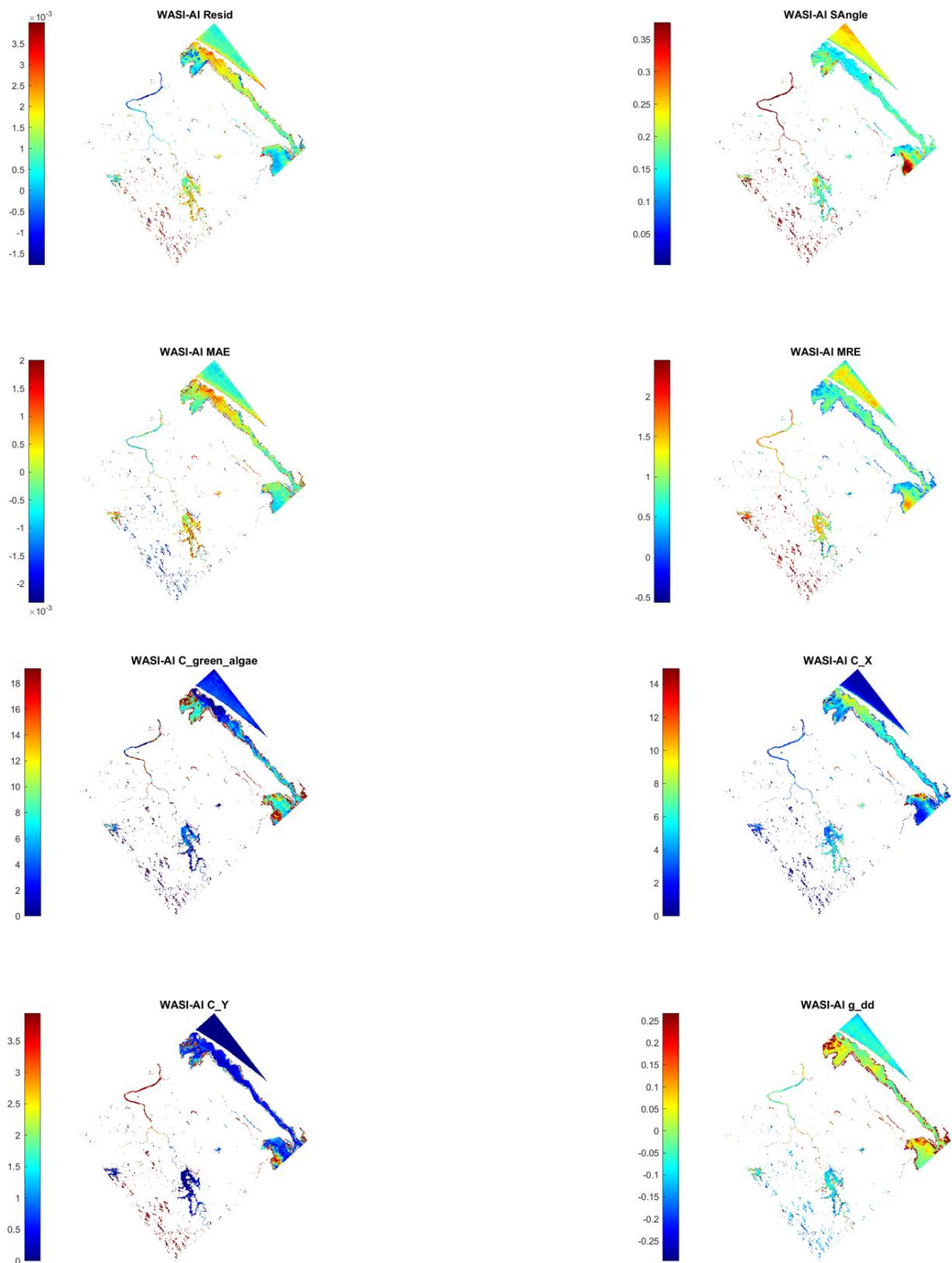


Figure 26: Results visualizing the graphical representation of the inversion for every parameter with the scale.

4.3 DATA PREPROCESSING CHALLENGES

The first challenge was to get familiar with the Hyperspectral data and the input data requirements for the WASI software. WASI software is a powerful software that has

a big learning curve to learn how to use it properly, it has a manual of 125 pages. Dr. Peter Gege Head of Group "Sensor Characterisation and Concepts" (in the following text mentioned always as "Peter") the person that designed WASI6 mentioned in a meeting that the Area Of Interest (AOI) was a lagoon with really shallow water and with this type of shallow waters it is difficult to estimate the water quality parameters. I) because the bottom of the lagoon influences too much the spectral reflectance and II) because if it influences the spectral reflectance and you have different benthonic life in the base of the Lagoon the software has a difficult time annullating the bottom signal of the lagoon. Peter definitely said that this processing would be challenging. III) Also, for water quality parameters is really important to have proper atmospheric corrections because the reflectance of water is really low, and if you add the aerosols and the water vapor interfering with the signal, it is paramount to have a good correction. Peter recommended the atmospheric correction tool called ACOLITE for processing the Atmosphere for water bodies.

The second challenge faced was the format of the satellite images. The original data gathered was Level 1, level 2 of data was needed for the processing step. The next step was to get the atmospheric correction with ACOLITE installed and running. In addition, it was necessary to install Anaconda and the dependencies needed for ACOLITE. There was a handicap on the user name containing spaces "Emma Garcia Boadas". The spaces of the folder user name were inhibiting the ability of anaconda to read the path and create an environment for launching and installing the dependencies of ACOLITE. So it was needed to change the folder username in my personal computer. This resulted in a problem with the SID register number and a restore, the computer was not able to open any software, and the files were unable to copy (All the process is described in the attachments-0).

After solving this problem, ACOLITE was installed and intended to preprocess PRISMA images. Prisma was properly recognized by ACOLITE Figure 28 but it was not able to read the L2 PRISMA image. In the ACOLITE manual it is specified that to process PRISMA level L1 the same images in the L2 level are needed in the same folder to perform the atmospheric correction for water bodies Figure 27. This resulted in the inability to preprocess the data for lack of L2 of PRISMA at that time. The L2 was ordered. At the same time the Italian aerospace service was contacted to ask for alternative atmospheric correction tools available for PRISMA, it was unsuccessful as there was never an answer.

- **PRISMA** Provide the path to the .he5 file (PRS_L1_STD). The official L2C file (PRS_L2C_STD) is required to be present in the same directory as the L1. The L2C file does not have to be specified in your settings file, it will be automatically detected.

Figure 27: Manual screen shot of the requirements to process PRISMA.

Processing Prisma needs to be done with the L2 file in the same directory as the L1. But in any case, the software did not recognize the data. The PRISMA data was extracted again with 7-Zip File Manager and relocated in a shorter path. After the second extraction the ACOLITE software was able to recognize the files Figure 28.

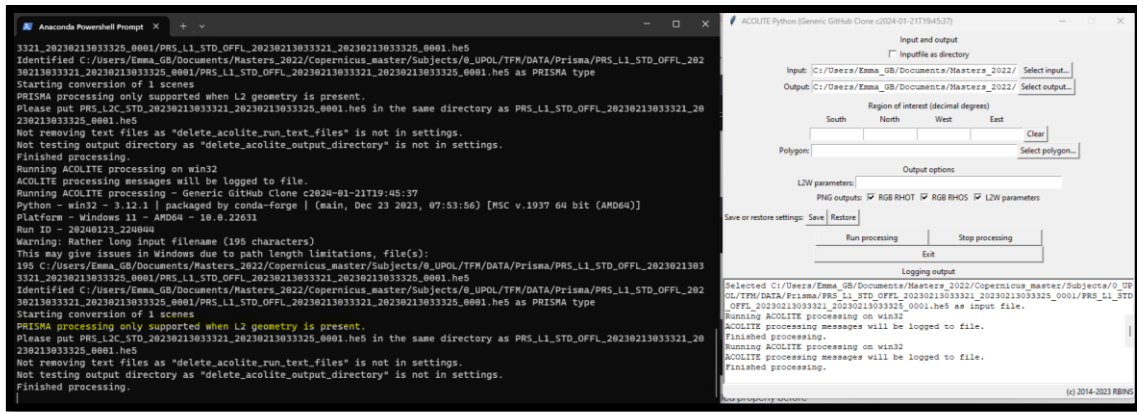


Figure 28: ACOLITE recognize PRISMA image with a shorter path.

Once the PRISMA images level 2 arrived the spectrums of the images were verified. For that it was needed to convert “.he5” format file to a compatible format for WASI software. Transformation with (*Martinrapilly/PRISMA2GeoTIFF: Python Script to Convert He5 PRISMA File to a GeoTIFF*, 2024) script and execution in Google Colab for dependencies and libraries Figure 29. After that the images were transformed to ENVI .hdr format explained previously for WASI loading. Once the Images were loaded in WASI to verify the spectrums, the PRISMA image spectrums of the water were not as expected. The water spectrums for several images can be visualized in the attachments-0. The spectrums are not similar in any case of water spectrums, and some images have erratic water pixels. It was sent to the author of First Evaluation of PRISMA Level 1 Data for Water Applications (Giardino et al., 2020) at the moment there is no reply from him. The PRISMA image processing needs further research to obtain results. In the literature, there are other research papers that also suggest that some of the results are promising; further analyses are necessary to fully characterize the in-orbit calibration of PRISMA for water applications. To this aim, further efforts on the use of more match-ups between satellite and in situ measurements, as well as an improvement of the radiative transfer simulation are required (Giardino et al., 2020). For the arguments enumerated previously it has been decided to not include the PRISMA images in the processing.



Figure 29: PRISMA preprocessing transformation from “.he” to GeoTIF.

The atmospheric correction for EnMAP L1 also needed to be preprocessed. The dataset was EnMAP L1B to preprocess to EnMAP L2 with the tool EnPT in EnMAP toolbox in Qgis. EnPT is well-documented and easy to use it, it will not be documented in this thesis. I was able to process the EnMAP data with a generic atmospheric correction. But the data provider Felix proportioned the EnMAP data L2 with an atmospheric correction adapted for the water.

In the case of DESIS, Felix also proportioned the level 2 data. For DESIS level 2 images, the atmospheric correction was done with Python-Based Atmospheric Correction (PACO). These images were atmospherically reprocessed due to a realization

during the processing of the data. The problems and the facts of this atmospheric correction will be explained in the Processing challenges.

The third challenge was to convert every image to a proper format for WASI processing. The data needed to be converted in ArcGIS PRO with the tool “**Raster to Other Format**”. The raster format needed for WASI6 is **ENVI DAT file**. Once the images are completely converted it is necessary to modify the “.hdr” file with the Band wavelengths, bandwidths and the specific band number that you want to process (it is specific for every sensor) in the attachments-0 there is an example of the proper format.

4.4 PROCESSING CHALLENGES

The First processing challenge was faced in the installation of WASI-AI. Felix recommended using WASI-AI instead of WASI6. An error message was recurrent during the installation process, (Error in => WASI_AI_No_GUI_01.m at line 9) as shown in Figure 26.

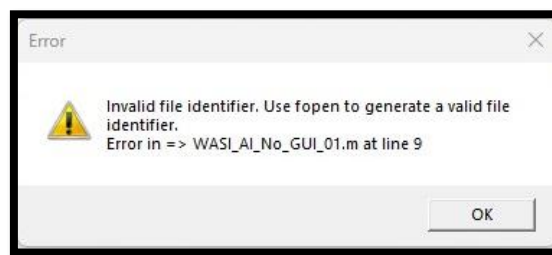


Figure 30: WASI-AI installation error.

Due to the error message, the version of Matlab used was checked, so It was installed the latest version, R2021b, as mentioned in the WASI-AI installation instructions. However, this did not solve the problem. After, it was run the >>mcrinstaller command in Matlab and downloaded the necessary packages from the Matlab website. Despite these efforts, the same error message was encountered upon reinstalling WASI-AI.

An email was sent to the developer of the plugin, to ask for additional installation tips, but no response was received, and there was no additional information elsewhere.

The second challenge was to work with WASI6 2D to process the images and experiment with different parameters. Unfortunately, after a week of working with WASI6, it was not possible to complete any processing tasks. The parameters used for processing were: Sun (Sun angle), T_W (water temperature), S(Exponent of CDOM absorption), C_Y(CDOM), C_Mie (Concentration of non-algal particles of type II), Fa(1) sand, Fa(2)silt different kind of bottom materials, and the depth. There were used papers of reference for the proper regulation of the parameters. Gloria spectrum library (Lehmann et al., 2023) was helpful as a parameter dataset for a water parameters orientation in WASI6 2D.

A processing test was performed on a computer (a powerful gaming computer), and it processed one image in 3 hours. It was the first processing completely finished. The specifications of the computer that performed the test were: 64 RAM processor Ryzen 9 7950X3D with Radeon Graphics. The computer that previously tried the processing had the following specifications: 16 RAM processor Ryzen 7 5800H with Radeon Graphics. Definitely the hardware was a key factor in the unsuccessful processing time.

Once It was possible to have access to a computer with good specifications it was performed several tests with WASI 2D. Initially the GLORIA dataset parameters were used. In the processing usually appeared the following message (Wavelengths of ENVI header are outside valid range, thus wavelengths are taken from file lambda.txt. Check

“Optiond – 2D- x scale”).)Figure 31. The Land pixels were masked with the selection of an appropriate threshold value in the NIR range.

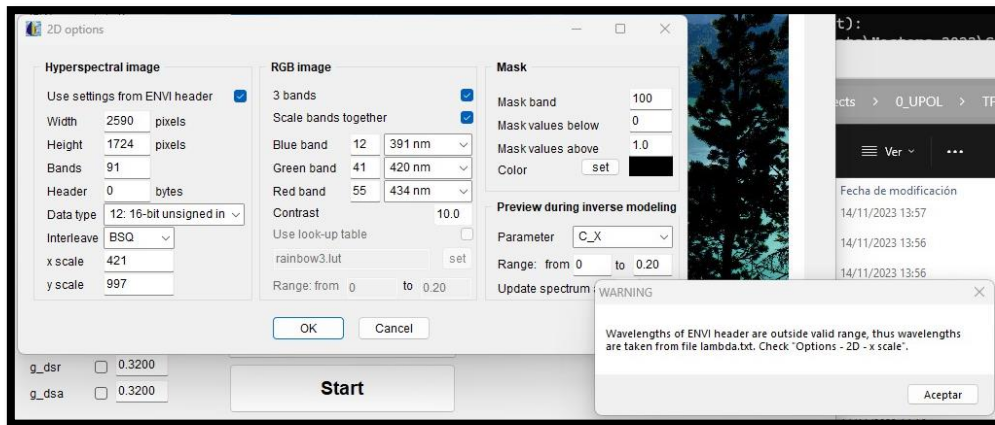


Figure 31: I interpreted that in the 2D options I had to change the x scale and the y scale.

The first results obtained in the processing done in the lab computer were not good. The following images show an example of inconclusive results Figure 32 and Figure 33. Also the parameters used for the test of different processing are founded in the Figure 34.

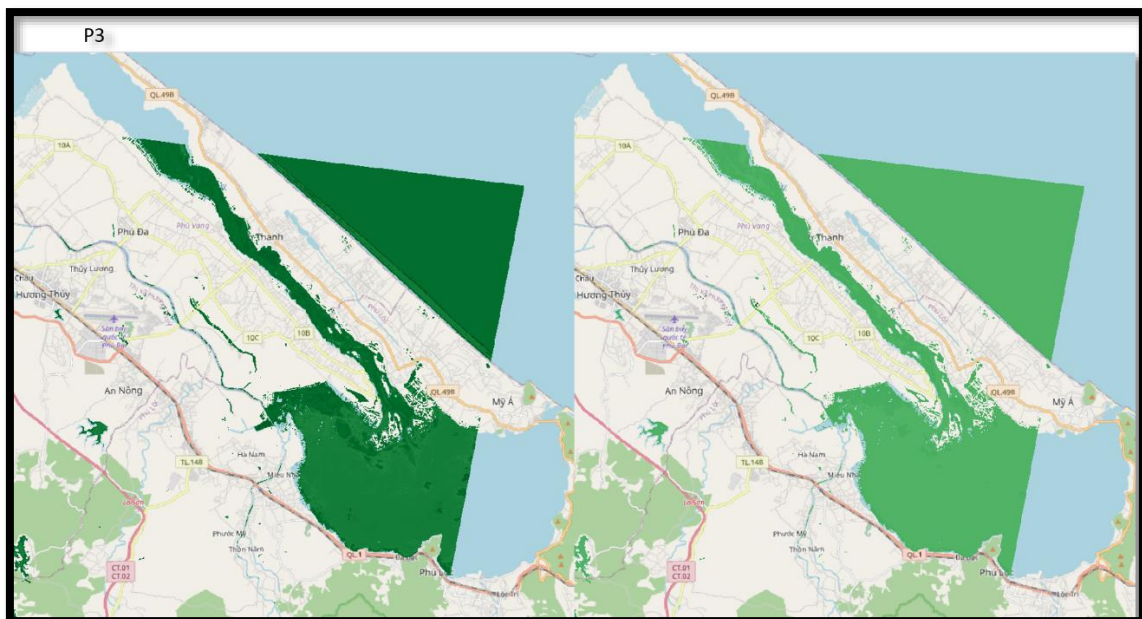


Figure 32: Same image with different parameters different preliminary results.

bodies of the images. The values of ocean water pixels should have had a stable spectrum, and The pixels of the ocean were too noisy. Also, the lagoon's spectrum had a big pick of around 500, 720 and 820 nanometers, and the mean spectrum presented noise. So Peter asked for a processing with a customized atmospheric correction. The actual atmospheric correction **PACO was estimated for land**.

Furthermore, in order to corroborate the difference in atmospheric correction in a meeting, Peter showed me an example of an area where the atmospheric correction was well estimated; in the Hué area, a spectrum of a forest, and the spectrum expected was without spikes of the water windows of the atmosphere. The print of the image has forests and mountains with a really high altitude; that area is well estimated, and the spectrum of the forest is well estimated. The estimation of the atmospheric correction between the high mountains and the sea level made it difficult to estimate the Atmospheric correction and aerosols and water vapor properly. In the following image, there is the spectrum of an arbitrary mean pixel value in the ocean and it looks like the following Figure 35:

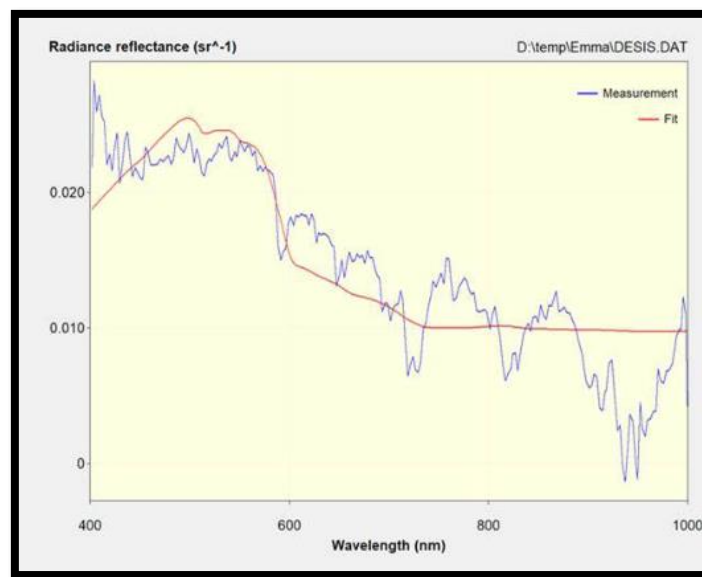


Figure 35: Radiance reflectance mean pixel spectrum from the ocean in blue vs. the estimated ocean fit pixel in red. Image by Peter 2024.

Figure 35 illustrates the problem; Peter overlaid a typical spectrum of water which is created manually (deep water model, WASI parameters: $C4=0.3$, $C_X=2$, $g_{dd}=0.5$, $g_{dsr}=0.32$, $g_{dsa}=0.32$, the other water parameters are zero) and a spectrum of the ocean. Besides the noise, there are three broad dips at the wavelength of water vapor absorption (around 710, 820, and 960 nm), indicating that the correction of water vapor failed. Furthermore, reflectance in the NIR is by far too high, indicating that the path radiance was significantly underestimated.

The necessary data to reprocess the atmosphere were AOT for calibration and a series of spectrum of different dips of the spectrum along the lagoon. The area of interest has high mountains next to the water body, which affects the estimation of water vapor. The atmosphere was reprocessed with AOT of the area and the bands around 720 and 820nm were used to reprocess the images. After an acceptable inversion was performed and results were obtained.

For the **DESIS processing**, we are using the 2D option for the inversion of the entire spectrum with the atmospheric correction already reprocessed. We can find the parameters of the image visualization, the metadata of the image, and the mask that will allow the processing exclusively of water pixels. The mask was properly applied for the processing in WASI is from band 230 using the thresholds -0.01 and 0.02. These thresholds were higher than the other processings.

The last challenge was properly formatting the Reprocessed data with the proper atmospheric correction. The new Reprocessed DESIS images with an optimized PACO atmospheric correction come in a format without georeferencing, so it is precise to substitute the Map info in the HDR with the one that corresponds to the image from the original Level L2 data, like in the code below.

```
ENVI
map info = {UTM, 1, 1, 755040, 1844490, 30, 30, 48, North,WGS-84}
coordinate system string =
{PROJCS["WGS_1984_UTM_Zone_48N",GEOGCS["GCS_WGS_1984",DATUM["D_WGS_1984",SPHEROID["WGS_1984",63781
37.0,298.257223563]],PRIMEM["Greenwich",0.0],UNIT["Degree",0.0174532925199433]],PROJECTION["Transverse_Mercator
"],PARAMETER["False_Easting",500000.0],PARAMETER["False_Northing",0.0],PARAMETER["Central_Meridian",105.0],PARA
METER["Scale_Factor",0.9996],PARAMETER["Latitude_Of_Origin",0.0],UNIT["Meter",1.0]]}
```

The reprocessed images are clipped with a water mask in ArcGIS PRO. First, we load the images and use the tool **“Extract by Mask”**. Then, we proceeded to save the file in the proper format with the tool **“Raster to Other Format.”** Finally, we extracted it in ENVI data format.

As mentioned before in the preprocessing challenges, the image spectrums of Prisma are not as expected. The Prisma level 2 images were checked in WASI, but the results were not as expected, and the values were not coherent. There was no process for these images.

4.5 SUMMARY AND RECOMMENDATIONS

INCURRED PROBLEMS:

- PRISMA atmospheric correction **ACOLITE** need for Level2 images.
- WASI6 processing for images around **10 hours**.
- **Format file** to WASI6 was not properly described in the manual = error in the processing.
- **WASI-AI** much faster **20 min**.
- **DESI** images bad atmospheric correction Level2.
- Not proper parameters due to the bentonitic life at the bottom of the lagoon.
- Processing again with proper parameter deep waters, last results.
- **Bug correction** in the software WASI-AI: it did not take into account the first bands for the modeling. Processing again after the bug correction.

OTHER PROBLEMS

- **Steep learning** curve of WASI6 and WASI-AI.
- Lack of understanding of certain parameters (confusion in the documentation)
- **Processing is time-consuming** (a lot of time dedicated).
- Image data formats and incompatibilities.
- Multiple processing attempts due to lack of references.
- Difficulty of documentation understanding.

RECOMMENDATION FOR OTHER AUTHORS:

- If the **bottom of the water body** is dark/ there is a lot of benthonic life and algal life, and it is diverse; consider the water body as deep water.
- Use **specific atmospheric corrections for water bodies** / customize your own. (Next year, DLR will start to build a new atmospheric correction for tropical areas specifically for water applications, being able to estimate better atmospheric effects and sun glint for DESIS and EnMAP).
- For WASI processing, use the **specific format of .hdr (see in the attachments-0)**
- Do not use WASI6 (time-consuming, no reference of accuracy of your training).
- Install WASI6 executable file and PASTE in the same folder **WASI-AI.exe** file.
- DESIS level 2 images for water quality in **tropical areas** with PACO atmospheric correction need a customized atmospheric correction due to the aerosols and water vapor.
-

It is documented that all these issues occurred. The attachments-0 provide a clearer timeline of issues during the thesis.

4.6 STATISTICAL ANALYSIS OF SATELLITE AND IN-SITU DATA FOR VALIDATION AND PARAMETER SHARED TRENDS ON TSS

This chapter presents the methodology and detailed steps for the statistical analysis. The outcomes of the satellite images are compared with those of the in-situ measurements for data validation. From the in-situ measurements, the TSS value is compared with other water quality parameters to have an idea if the TSS can be an indicator of other parameters. It is needed to take into consideration that the in-situ data and the satellite data are not from the same day, but it is from the same month, also the in-situ data is measured in the laboratory.

4.6.1 Extraction satellite data for comparison with (in-situ data)

First of all, it is needed to clean and put in order the in-situ data. It is needed to select the data from the points that correspond to the AOI and merge all the .csv from different years. This process of cleaning and arranging the .csv is done with Excel. Once we have the in-situ data points it is time to extract the raster values from the in-situ points. It is used the tool “**Extract Multi Values to Points**”. The total number of images (is 23) and they are grouped per date (total dates 15). Selecting the bands corresponding to Algae content, TSS, and CDOM, is Generated for every date a feature file. Once all the points of in-situ data have the data values from the EnMAP and DESIS data it is time to merge the files by the geoprocessing tool “**Merge**”. The Raster values extracted from the raster have different values <Null> and -9999 or others. Everything is set up uniformly. This process ends up with a .csv file containing the satellite data with the temporal-spatial and TSS information in the correct position to be compared with the .csv file (points of the in-situ data with the temporal-spatial and TSS information).

4.6.2 Data plot and data selection

The selection of the data is done from the distribution of data available for the comparison of all the in-situ data points and all the satellite data values for the same stations obtained from the previous step. This data is selected and grouped on proximal dates to be able to do a comparative statistical analysis. For the statistical proposals, it has been decided not to take into account the satellite out-layer point, which has a value of around 300 TSS (mg/L) Figure 36. The dates of the data comparison are selected in Table 7. The next step is to perform the statistical analysis.

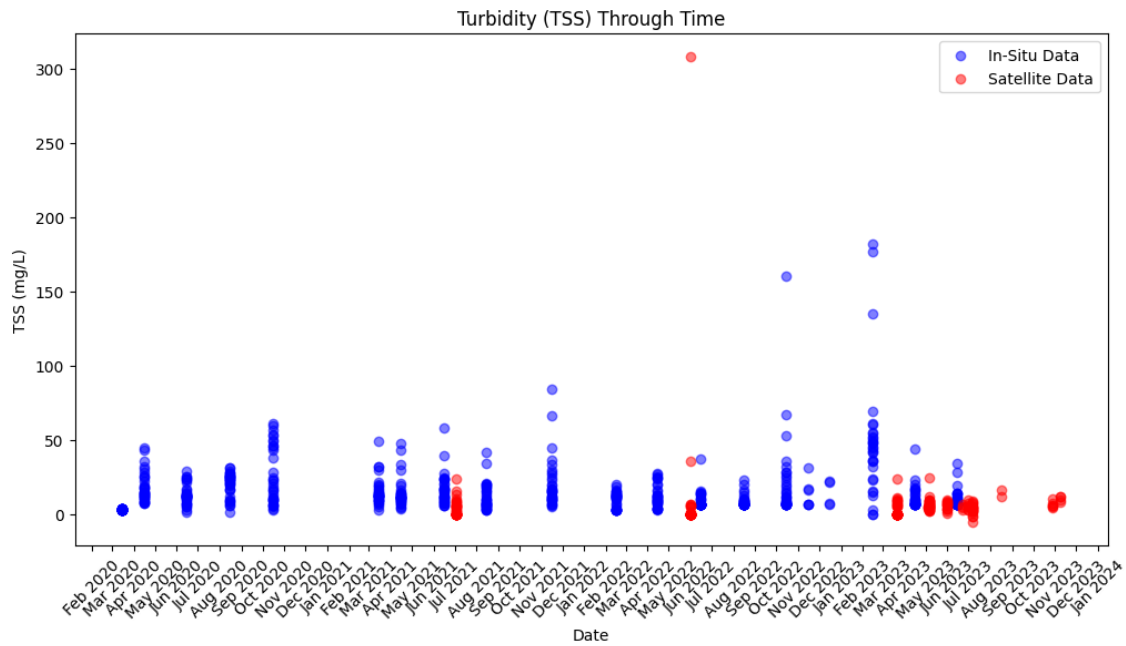


Figure 36: All the TSS information of in-situ data and satellite data extracted from the sample points of the in-situ data.

Table 7: Dates selected for the comparison statistical analysis

Satellite dates	Equivalent In-situ dates	Used dates
2021-07-03	2021-06-15	selected
2022-06-01	2022-06-15	selected
2023-03-22	2023-04-07	selected
2023-06-23	2023-06-17	selected

4.6.3 Statistical analysis of TSS, in-situ data vs satellite data TSS validation

The next step is to compare the TSS value from the in-situ data and the satellite data. It is done with the objective of validating the satellite data and the relationship with the in-situ data. Due to the data characteristics mentioned before it is decided to do several statistical tests and plots. The statistics are done in Python code utilizing the following libraries: pandas, numpy, matplotlib.pyplot, seaborn, scipy.stats, sklearn.linear_model, sklearn.metrics, in the platform Google Colab.

```

pip install pandas numpy matplotlib seaborn scipy
# Import necessary libraries
import pandas as pd
import numpy as np
import matplotlib.pyplot as plt
import seaborn as sns
from scipy.stats import pearsonr, ttest_rel, wilcoxon
from sklearn.linear_model import LinearRegression
from sklearn.metrics import mean_squared_error
from google.colab import files

# Connections of directory in google drive

```

```

from google.colab import drive
drive.mount('/content/drive')

# List the contents of a directory
!ls -lah '/content/drive/MyDrive/TFM/'

# Load in-situ data from CSV
in_situ_data =
pd.read_csv('/content/drive/MyDrive/TFM/in_situ_data_month.csv')

# Load satellite data from CSV
satellite_data =
pd.read_csv('/content/drive/MyDrive/TFM/satellite_data_month.csv')

```

The following step consists of preparing the data for the statistics. First of all, we load the in-situ and satellite data from their respective CSV files. We merge the datasets based on their latitude (Y) and longitude (X) columns. It extracts the necessary and relevant columns for Total Suspended Matter (TSS) from both datasets. And the data is sorted.

```

# Merge datasets on latitude (Y), longitude (X), and date (MMYYYY)
merged_data = pd.merge(in_situ_data, satellite_data, on=['X', 'Y',
'MMYYYY'], suffixes=('_in_situ', '_satellite'))

# Extract total suspended matter values
in_situ_tsm = merged_data['TSS']
satellite_tsm = merged_data['B6_CX_TSS'] # Assuming TSS in satellite
data is in this column

# Drop rows with NaN values in either in-situ or satellite TSS
clean_data = merged_data[['TSS', 'B6_CX_TSS']].dropna()

# Extract the cleaned data
in_situ_tsm = clean_data['TSS']
satellite_tsm = clean_data['B6_CX_TSS']

```

Secondly, it computes statistics for both datasets.

Descriptive Statistics: mean, standard deviation, range and interquartile range (IQR)

```

# Compute descriptive statistics for in-situ and satellite data
in_situ_stats = in_situ_tsm.describe()
satellite_stats = satellite_tsm.describe()

print("Descriptive Statistics for In-situ Data:")
print(in_situ_stats)
print("\nDescriptive Statistics for Satellite Data:")
print(satellite_stats)

# Create a scatter plot

```

```
plt.figure(figsize=(8, 6))
plt.scatter(in_situ_tsm, satellite_tsm)
plt.xlabel('In-situ Total Suspended Matter (TSS)')
plt.ylabel('Satellite Total Suspended Matter (TSS)')
plt.title('Scatter Plot of In-situ vs Satellite Data')
plt.grid(True)
plt.show()
print(in_situ_tsm)
print(satellite_tsm)
```

Pearson Correlation Coefficient: describes the linear relationship between the two datasets.

```
# Calculate Pearson correlation coefficient
corr_coefficient, p_value = pearsonr(in_situ_tsm, satellite_tsm)
print("Pearson Correlation Coefficient:", corr_coefficient)
print("p-value:", p_value)

# Add a line of best fit to the scatter plot
sns.regplot(x=in_situ_tsm, y=satellite_tsm, ci=None, scatter_kws={"s":
50})
plt.xlabel('In-situ Total Suspended Matter (TSS)')
plt.ylabel('Satellite Total Suspended Matter (TSS)')
plt.title(f'Scatter Plot of In-situ vs Satellite Data\n(Pearson
Correlation Coefficient: {corr_coefficient:.2f})')
plt.grid(True)
plt.show()
```

Regression Analysis: describes the statistical correlation giving the slope of the regression, the intercept, and the R-squared value.

```
# Regression analysis
regression_model = LinearRegression().fit(in_situ_tsm.values.reshape(-
1, 1), satellite_tsm.values)
slope = regression_model.coef_[0]
intercept = regression_model.intercept_
r_squared = regression_model.score(in_situ_tsm.values.reshape(-1, 1),
satellite_tsm.values)
print("Regression Coefficients:")
print("Slope:", slope)
print("Intercept:", intercept)
print("R-squared:", r_squared)
```

Paired T-test indicates the difference with a statistical value.

```
# Statistical test (t-test)
t_statistic, t_p_value = ttest_rel(in_situ_tsm, satellite_tsm)
print("T-statistic (paired t-test):", t_statistic)
print("p-value (paired t-test):", t_p_value)
```


Wilcoxon Signed-Rank Test Statistic: non-parametric test used to compare paired samples and is robust against non-normality.

```
# Non-parametric test (Wilcoxon signed-rank test)
wilcoxon_statistic, wilcoxon_p_value = wilcoxon(in_situ_tsm,
satellite_tsm)
print("\nWilcoxon signed-rank test statistic:", wilcoxon_statistic)
print("p-value (Wilcoxon signed-rank test):", wilcoxon_p_value)
```

Root Mean Square Error (RMSE): indicates the average magnitude of error.

```
# Calculate Root Mean Square Error (RMSE)
rmse = np.sqrt(mean_squared_error(in_situ_tsm, satellite_tsm))
print("Root Mean Square Error (RMSE):", rmse)
```

Bland-Altman Plot Analysis: assess the agreement and bias between the two measurement methods. On the x-axis, plot the average of in-situ and satellite measurements, and on the y-axis, it plots the difference between the two measurements. This plot is also known as a difference plot.

```
# Bland-Altman plot
mean_difference = in_situ_tsm - satellite_tsm
mean_diff = np.mean(mean_difference)
std_diff = np.std(mean_difference)
plt.figure(figsize=(8, 6))
plt.scatter((in_situ_tsm + satellite_tsm) / 2, mean_difference)
plt.axhline(mean_diff, color='red', linestyle='--', linewidth=1)
plt.axhline(mean_diff + 1.96 * std_diff, color='blue', linestyle='--',
linewidth=1)
plt.axhline(mean_diff - 1.96 * std_diff, color='blue', linestyle='--',
linewidth=1)
plt.xlabel('Average of In-situ and Satellite TSM')
plt.ylabel('Difference (In-situ TSM - Satellite TSM)')
plt.title('Bland-Altman Plot')
plt.grid(True)
plt.show()
```

The final step for the comparison of the in-situ data and the satellite data has been the plot of the TSS distribution for every sample point. And also another plot with all the values that were exceeding the 50mg/l of TSS.

```
## Plot all the sample points in separated graphs
# Convert the MMYYYY column to datetime format
insitu_data['MMYYYY'] = pd.to_datetime(insitu_data['MMYYYY'],
format='%m/%d/%Y')
satellite_data['MMYYYY'] = pd.to_datetime(satellite_data['MMYYYY'],
format='%m/%d/%Y')

# Extract necessary columns
```

```

insitu_tss = insitu_data[['MMYYYY', 'X', 'Y', 'TSS']]
satellite_tss = satellite_data[['MMYYYY', 'X', 'Y', 'B6_CX_TSS']]

# Rename columns for consistency
satellite_tss.rename(columns={'B6_CX_TSS': 'TSS'}, inplace=True)

# Get unique coordinate pairs
unique_coords = insitu_tss[['X',
'Y']].drop_duplicates().values.tolist()

# Determine global x and y axis limits
all_dates = pd.concat([insitu_tss['MMYYYY'], satellite_tss['MMYYYY']])
all_tss_values = pd.concat([insitu_tss['TSS'], satellite_tss['TSS']])

# Set limits
x_min = all_dates.min() - pd.DateOffset(months=2) # Subtract 2 months
from the min date
x_max = all_dates.max() + pd.DateOffset(months=2) # Add 2 months to
the max date
y_min = all_tss_values.min()
y_max = all_tss_values.max()

# Iterate over each unique coordinate pair and plot
for coord in unique_coords:
    x, y = coord
    insitu_group = insitu_tss[(insitu_tss['X'] == x) &
(insitu_tss['Y'] == y)]
    satellite_group = satellite_tss[(satellite_tss['X'] == x) &
(satellite_tss['Y'] == y)]

    plt.figure(figsize=(12, 6))

    # Plot in-situ data
    plt.scatter(insitu_group['MMYYYY'], insitu_group['TSS'], c='blue',
label='In-Situ Data', alpha=0.5)

    # Plot satellite data
    plt.scatter(satellite_group['MMYYYY'], satellite_group['TSS'],
c='red', label='Satellite Data', alpha=0.5)

    # Format the x-axis to show dates better
    plt.gca().xaxis.set_major_locator(mdates.MonthLocator())
    plt.gca().xaxis.set_major_formatter(mdates.DateFormatter('%b %Y'))

    # Set fixed x and y axis limits
    plt.xlim(x_min, x_max)
    plt.ylim(y_min, y_max)

    # Labels and title

```

```

plt.xlabel('Date')
plt.ylabel('TSS (mg/L)')
plt.title(f'Turbidity (TSS) Through Time at Coordinates ({x},
{y})')
plt.legend()

# Rotate date labels for better readability
plt.xticks(rotation=45)

# Show the plot
plt.show()

```

The second graph values higher than 50mg/l:

```

##Points that have exceeded the 50mg/L threshold
# Filter for TSS values greater than 50
insitu_tss_filtered = insitu_tss[insitu_tss['TSS'] > 50]
satellite_tss_filtered = satellite_tss[satellite_tss['TSS'] > 50]

# Plot the data
plt.figure(figsize=(12, 6))

# Plot in-situ data
plt.scatter(insitu_tss_filtered['MMYYYY'], insitu_tss_filtered['TSS'],
c='blue', label='In-Situ Data', alpha=0.5)

# Plot satellite data
plt.scatter(satellite_tss_filtered['MMYYYY'],
satellite_tss_filtered['TSS'], c='red', label='Satellite Data',
alpha=0.5)

# Format the x-axis to show dates better
plt.gca().xaxis.set_major_locator(mdates.MonthLocator())
plt.gca().xaxis.set_major_formatter(mdates.DateFormatter('%b %Y'))

# Labels and title
plt.xlabel('Date')
plt.ylabel('TSS (mg/L)')
plt.title('Turbidity (TSS) Through Time (TSS > 50)')
plt.legend()

# Rotate date labels for better readability
plt.xticks(rotation=45)

# Show the plot
plt.show()

```

4.6.4 Comparison of the in-situ parameter vs TSS

For the comparisons and relationships of in-situ parameters, the .csv with the previously cleaned data is used, and it is analyzed using several statistical tests. The primary goal is to establish a relationship between TSS and other in-situ parameters, as TSS is the only parameter that can be compared with satellite measurements. The two statistical tests are the **T-test** and the **Spearman Correlation Coefficient**.

For the preparation of the statistical analysis the proper libraries are installed and connected to Google Colab with the files on Google Drive. The data is cleaned from the values that are not numeric (are the values in the dataset that are out of range of the sensitivity of the measured data):

```
pip install pandas numpy matplotlib seaborn scipy
# Import necessary libraries
import pandas as pd
import numpy as np
import matplotlib.pyplot as plt
from scipy.stats import ttest_ind, spearmanr, shapiro

### Connections of directory in google drive
from google.colab import drive
drive.mount('/content/drive')

### List the contents of a directory
!ls -lah '/content/drive/MyDrive/TFM/'

# Load in-situ data from CSV
in_situ_data =
pd.read_csv('/content/drive/MyDrive/TFM/Alldata_2020_2021_modification
_FINAL.csv')

# Load the data
file_path =
'/content/drive/MyDrive/TFM/Alldata_2020_2021_modification_FINAL.csv'
# Display the first few rows of the data
print(data.head())

# Identify and print non-numeric values
non_numeric_columns = ['id', 'MMYYYY', 'date', 'X', 'Y']
for column in data.columns:
    if column not in non_numeric_columns:
        non_numeric_values = data[pd.to_numeric(data[column],
errors='coerce').isna()][column].unique()
        if len(non_numeric_values) > 0:
            print(f"Non-numeric values in {column}:
{non_numeric_values}")

# Convert relevant columns to numeric, converting non-numeric values
to NaN
for column in data.columns:
    if column not in non_numeric_columns:
```

```

        data[column] = pd.to_numeric(data[column], errors='coerce')

# Check for missing values
print(data.isnull().sum())

```

The first statistical test was the T-test comparing the TSS to the rest of the parameters. As it was showing, a very small p-value (less than 0.05) indicated strong evidence against the null hypothesis, suggesting that there **is a statistically significant difference between the compared groups**.

```

target = 'TSS'
p_values = {}

for column in data.columns:
    if column not in non_numeric_columns + [target]:
        t_stat, p_val = ttest_ind(data[target].dropna(),
data[column].dropna(), nan_policy='omit')
        p_values[column] = p_val

print(p_values)

# Pearson Correlation Bar Chart
# Exclude non-numeric columns and rows with NaN in the target column
numeric_data =
data.drop(columns=non_numeric_columns).dropna(subset=[target])
pearson_correlations =
numeric_data.corr(method='pearson')[target].drop(target)

plt.figure(figsize=(12, 8))
pearson_correlations.plot(kind='bar', color='skyblue')
plt.title('Pearson Correlations with TSS')
plt.xlabel('Parameters')
plt.ylabel('Pearson Correlation Coefficient')
plt.show()

```

Due to the previous results another statistical test was done, the Shapiro-Wilk test used to determine the use of the **Spearman Correlation Coefficient**. Once the statistics were determined, the visualization of the results started.

```

# Spearman Correlation Coefficient
stat, p = shapiro(numeric_data[target])
print(f'Shapiro-Wilk Test for TSS: p-value={p}')

if p < 0.05:
    spearman_correlations =
numeric_data.corr(method='spearman')[target].drop(target)

    plt.figure(figsize=(12, 8))
    spearman_correlations.plot(kind='bar', color='lightcoral')

```

```
plt.title('Spearman Correlations with TSS')
plt.xlabel('Parameters')
plt.ylabel('Spearman Correlation Coefficient')
plt.show()
else:
    print('TSS is normally distributed, using Pearson correlations.')
```

5 RESEARCH 2

GEOVISUALIZATION OF THE WATER QUALITY IN THE TAM LAGOON

The following chapter is centered on the geovisualization process. It describes in detail the methodology and the techniques implemented for the execution of the visualization part.

5.1 DATA FOR GEOVISUALIZATION

For the geovisualization part, there are two different data used: (1) the water quality parameters derived from the hyperspectral images and (2) the in-situ parameters. Available hyperspectral images are listed in Table 8 below. In-situ data are listed in

Table 9.

Table 8: Data of water quality.

Sensor	Date	Resolution	Spatial Extent	Water quality
DEGIS	20210703	30m	100%	C_Y (CDOM) C_X (TSS) Algae
DEGIS	20220601	30m	25%	C_Y (CDOM) C_X (TSS) Algae
DEGIS	20220605	30m	35%	C_Y (CDOM) C_X (TSS) Algae
DEGIS	20230322	30m	50%	C_Y (CDOM) C_X (TSS) Algae
DEGIS	20230503	30m	100%	C_Y (CDOM) C_X (TSS) Algae
EnMAP	20230504	30m	20%	C_Y (CDOM) C_X (TSS) Algae
DEGIS	20230506	30m	25%	C_Y (CDOM) C_X (TSS) Algae
DEGIS	20230507	30m	100%	C_Y (CDOM) C_X (TSS) Algae
EnMAP	20230531	30m	30%	C_Y (CDOM) C_X (TSS) Algae
EnMAP	20230623	30m	20%	C_Y (CDOM) C_X (TSS) Algae
EnMAP	20230701	30m	45%	C_Y (CDOM) C_X (TSS) Algae
DEGIS	20230706	30m	75%	C_Y (CDOM) C_X (TSS) Algae
EnMAP	20230817	30m	10%	C_Y (CDOM) C_X (TSS) Algae
DEGIS	20231029	30m	25%	C_Y (CDOM) C_X (TSS) Algae
EnMAP	20231109	30m	45%	C_Y (CDOM) C_X (TSS) Algae

Table 9: In situ data of non algae particles suspended sediments or TSS

Parameters	Unit	Month
TSS	mg/l	Mar-20
		Apr-20
		Jun-20
		Aug-20
		Oct-20
		Mar-21
		Apr-21
		Jun-21
		Aug-21

Parameters	Unit	Month
TSS	mg/l	Oct-21
		Feb-22
		Apr-22
		Jun-22
		Aug-22
		Oct-22
		Nov-22
		Dec-22
		Feb-23
		Apr-23
Jun-23		

The used flood layers are from the Global Flood Monitoring (Global Flood Monitoring, 2024). Topographical basemaps are from the available ArcGIS Online layers storage.

5.2 THESIS DATA VISUALIZATION POSSIBILITIES

Analysis of visualization possibilities

There are different approaches to visualization with the type of data we have. The most used now for the distribution of scientific data is to adopt an Open Data style and do a web map or interactive map, leaving open the download or use of data through web services. These digital possibilities are brilliant for easy diffusion, but they need to be maintained through time, and at the same time, they make sense if you want to do continuous monitoring and upload the data recurrently.

Possibilities:

- Analogic/static maps
- web and digital maps
 - Storytelling map
 - ArcGIS Online map
 - animations
 - other technological solutions

In our case, the in-situ data is provided by the FloodAdaptVN Project and is collected from the Vietnamese authorities. The Data that has been managed is sensitive and not publicly available so it has been opted for a static paper map and an animation. The possibilities that have been contemplated are the following:

- basic methods of single images visualization (rasters) on the basemap (see methods of cartographic visualization above)
- multivariate mapping
 - bivariate mapping (two colors for representation of water quality on every date)
 - multivariate mapping (to summarize the water quality parameters)

Geovisualization aim and Target group:

The main aim of the map and animation is to depict changes in water quality over time, specifically focusing on satellite results for TSS, CDOM, and algae content (less precise). In addition to satellite data, in-situ data will also be included to reinforce the results. It's important to note that the only parameter present in both the in-situ and satellite data is TSS.

The main target groups for these maps would be experts and general public.

Map for experts:

The main objective is the diffusion of the data to the authorities that are collaborators on the FloodAdaptVN Project these authorities are:

- Department of Natural Resources and Environment (DONRE), Thua Thien Hue Province, is a specialized agency of the Provincial People's Committee, performing the function of advising and assisting the Provincial People's Committee in state management of natural resources and environment, including: Land; Water Resources; Mineral resources and Geology; Environment; Meteorology and Hydrology; Climate Change; Measurement and map; integrated and unified management of sea, islands and lagoons; manage and organize the implementation of public services in the fields of the Department's functions(FloodAdaptVN | FloodAdaptVN, 2024).
- Thua Thien Hue Provincial Commanding Committee of Natural Disaster Prevention and Control, Search and Rescue (CCNDPC/SR) is responsible for the development and implementation of plans for natural disaster prevention, control and response as well as for the integration of related contents into local socio-economic development and construction plans. The committee bundles

competences of all relevant departments and other stakeholders and enables the mainstreaming of the results of FloodAdaptVN into the provincial planning framework and administrative action (FloodAdaptVN | FloodAdaptVN, 2024).

They want to know everything in the greatest detail. It is recommended to map individual indicators as they know how to work with it and to complement with statistics and indications of the technical procedure used.

Map for General public Animation:

- The main objective is to deliver easy to read and understandable map animation to the authorities that are collaborators on the FloodAdaptVN Project. They will be responsible for the diffusion of the information to the provincial planning framework, this might imply administrative action for the further use of satellite data.
- The main characteristics of this are that it is easy to understand, and there is no need to spend a large amount of time looking at it.

5.3 STATIC DATA VISUALIZATION METHODOLOGY

The most common cartographic method of the geovisualization of the type of data from the analyses is the area method with classified or non-classified color scales. And also point methods for the in-situ data with a simple color scale. The basic method how to visualize the raster images is just to put a colored layer on the topographic basemap. The more advanced method, which also involves some statistical measurements and analysis, is the transfer of the raster image into the regular grid. This is the approach selected within this thesis visualization part.

Generalization map, hexagons

Firstly, a hexagonal tessellation of 500,000 square meters per hexagon is generated using **“Generate Tessellation”**. Then, a point centroid is created using **“Raster to Point”** for every pixel using the data of the raster with **“Extract Multi Values to Points”**. Finally, we do the mean of the points for every Hexagon and aggregate the data with **“Aggregate Points”**. With this tool, we aggregate the points, and it is possible to do the mean of all the points fitting in every hexagon Figure 37. With this data we generate the bivariate map of hexagons for the TSS and the CDOM.

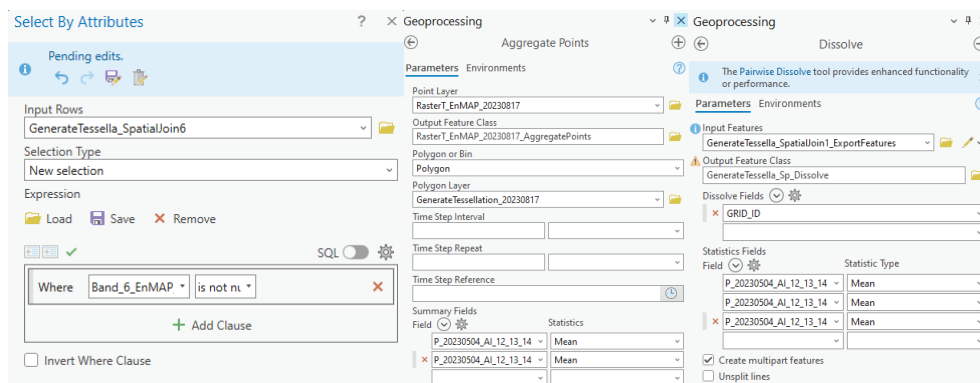


Figure 37: Tools to generate a summary of water quality in a regenerated grid.

Statistics of the hexagon-grided satellite data are generated to visualize a time summary of the data in one map:

First, we need to join all the layers that form the same dates and homogenize the overlapping parts. We create fields for every band parameter and another field for the date of the image, with the fields calculator in ArcGIS Pro. After it is used, the tool **“Merge”** incorporates the layers together that have the same levels. Finally, the

“**Summarize Attributes**” is done to the mean join to merge the attributes that are repeated. This tool generates a table join to the grid. This process is repeated until we have a layer with all the satellite data summarized.

Once all the layers are generated, the statistics of all the layers are calculated by doing a “**Summarize Attributes**”, which includes the mean, minimum, maximum, standard deviation, and variance. The last step is to create the map of maximum and minimum summarizing all of the period.

Colored scale

For the color scale and the map generation, two different types of users were consulted; the first group was cartographic experts, and the other group was the general public. The conclusion of the test was that the people understood better the scales where the color was related to the thematic layer in the case of TSS brown color and CDOM kind of pink. The preferred color scheme for the map from the audience was obtained from Kristen Thyng in a talk on perceptual color maps in metaplot lip for oceanography SciPy2015 (Enthought, 2015). In Figure 38, Kristen proposes a standardized color scale for the TSS, CDOM, and Chlorophyll green algae.

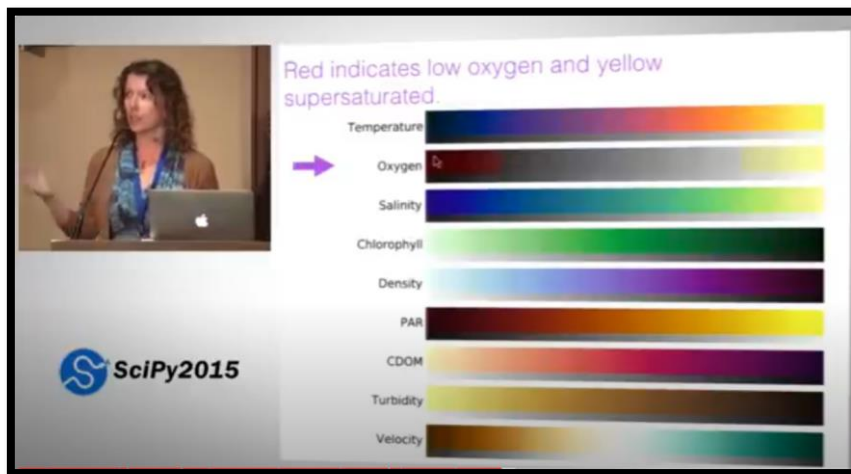


Figure 38: Standardized color scale for the TSS, CDOM and Algae (Enthought, 2015).

The scale determination Figure 40 of every value was related to the biological needs for water consumption and the lagoon's safety:

For the TSS, it was taken into consideration the Vietnamese regulation for surface water quality Circular No. 01/2023/TT-BTNMT (phủ, 2023). The regulation has four levels of limitations in the water quality that are explained in Figure 39. The TSS ideal limit for the aquatic life and the lagoon is 50 mg/l and was the maximum value in the scale for the maps of TSS.

The CDOM values calculated in WASI were done with wavelength $\lambda_0 = 440 \text{ nm}$ and $S = 0.014 \text{ nm}^{-1}$, which can be considered representative of a great variety of water types. For delimitating the color scale of the CDOM it has been taken into consideration several studies: The first one calculated the CDOM on six different geographical regions the mean CDOM absorption coefficients at 440 nm were found to vary in the ranges $0.063\text{--}0.35 \text{ m}^{-1}$ (Nima et al., 2019). There are two studies done in highly polluted rivers in China $a_{CDOM}(440)$ water mean values within the range $0.6\text{--}2.4 \text{ m}^{-1}$ (Li et al., 2016; Shao et al., 2017; Zheng et al., 2023). There is another study where it studies the different factors that affect the measurements of CDOM in rivers and lakes of the United States calculates the CDOM in a $e_{a440} \text{ m}^{-1}$ and the values obtained from the lakes have a maximum of 25.10 m^{-1} similar to some of the values of our lagoon (Brezonik et al., 2015). Due to the diversity of values and no agreement on a value regulation or

standardization it has been opted for a scale that represents the best visual representation for the range of values in the lagoon.

For the green algae concentration it needs to take into consideration that the values obtained have low accuracy and high ambiguity levels. In order to visualize the algae concentration and generate the scale it has been taken into consideration that high concentrations of Chl-a (typically at concentrations greater than 0.45 µg/L) can indicate increased nutrient availability supporting the growth of macroalgae (De'ath & Fabricius, 2010; Devlin & Brodie, 2023). So the maximum value in the scale is 50 µg/L.

TT	Parameter	Unit	Limited value			
			A		B	
			A1	A2	B1	B2
3	COD	mg/l	10	15	30	50
4	Dissolved Oxygen (DO)	mg/l	̄ 6	̄ 5	̄ 4	̄ 2
5	Total Suspended Solids (TSS)	mg/l	20	30	50	100

Figure 39: QCVN 08-MT:2015/BTNMT Circular of Surface water quality. A1 (Used for domestic water supply purposes (after applying normal treatment), A2 (Used for domestic water supply purposes but must be applied suitable treatment technology), B1 (Used for irrigation, irrigation or other uses with similar water quality requirements or uses as type B2), B2 (Water transportation and other purposes with low quality water requirements) (phủ, 2023).

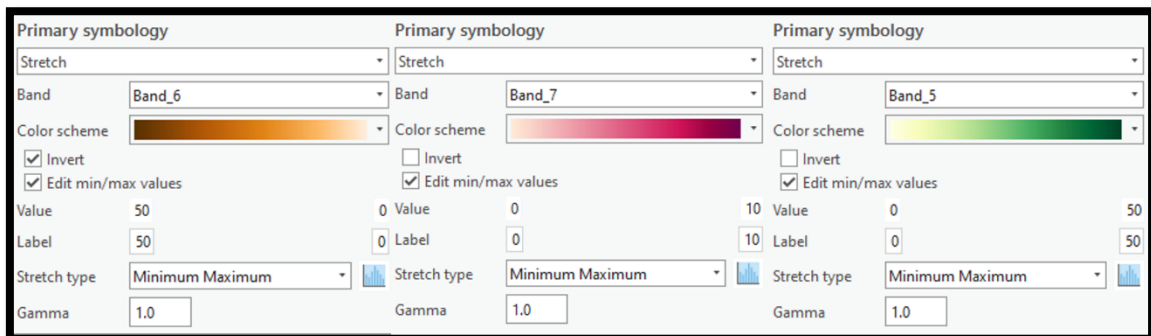


Figure 40: Legend.

POSTERS CREATIONS

Finally, the static maps have been arranged with Adobe Illustrator. All the outputs have been arranged for an easy understanding of the lagoon's state through time of the water quality parameters Figure 41. The cartographic methods used for these outcomes are unclassified colors for the raster image visualization and classified color for the visualization in the summary period in hexagons.

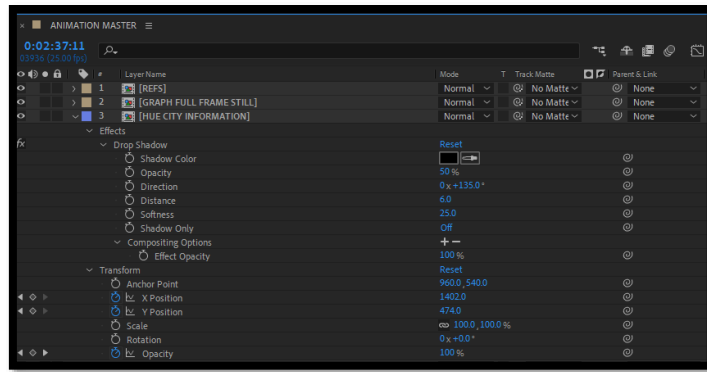


Figure 43: Main functionalities used in the animation.

The animation is built in four sections, the introduction, the map graphic of Vietnam and the area of interest, the timeline of data showing the change of TSS Figure 44 and finally the final summary of the data with references to close the animation.

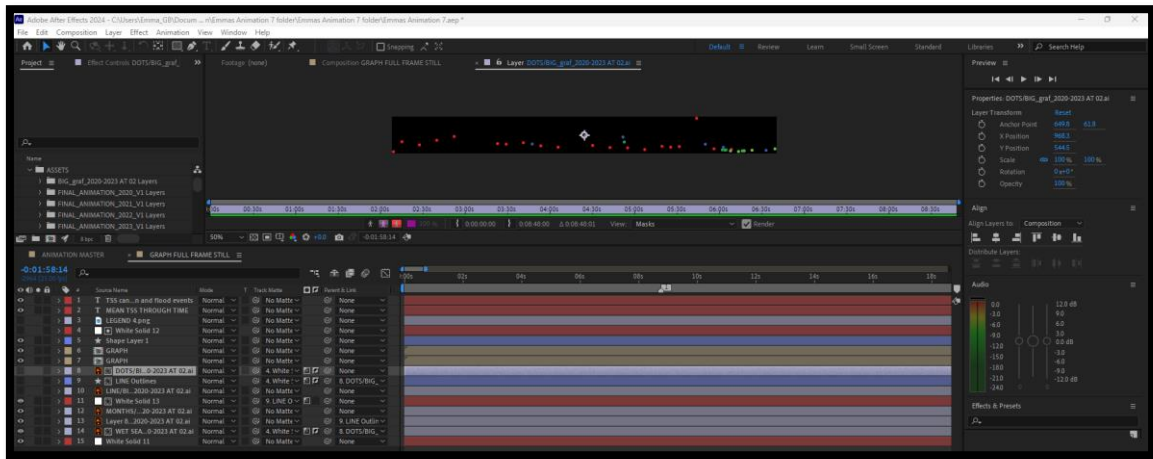


Figure 44: Structure of the layers in Adobe After Effects in the animation.

For the exporting, it was rendered, and the voice of the animation was recorded in an external AI solution Naturalreaders and incorporated in Adobe After Effects (AI Voices - NaturalReader Home, 2024).

6 RESULTS

The Following chapter gathers all the final outputs of the thesis. In the first part, there are the results of the analysis part with the outputs of the water quality parameters from the model and the statistics for the satellite validation. In the second part, visualization results are presented, along with static visualization and animation.

6.1 RESULTS OF THE WATER QUALITY ANALYSIS

The following water quality parameter results are performed with the inversion modeling of WASI6 2D and the AI plugin. The model used for the processing is the deep-water model. Even though the lagoon had a mean depth of 2 meters, the deep-water model was giving more robust results due to the ununiformed of the lagoon base and the reflectance that this was providing.

The following images show a sample of the processing results (for the entire results, go to attachments-0). There are three types of data. 1) The resulting image with the water quality parameter and two different graphs indicates 2) the estimation of the model's calibration before training and 3) the accuracy of the model's results once it is trained with water quality parameters. These three types of results are obtained for all the images processed.

Figure 45, Figure 48, Figure 50 show the fitting parameters for the calibration of the spectrum trend of the pixel selected in color blue and the model spectrum with the parameters in red. The verification of the accuracy of the training and the modeling of the parameters is in red and the regression expected to fit is in blue Figure 46, Figure 49, Figure 51. If the two trends are close to each other, it means that the parameter can be expected as a good result, as the figures mentioned above show, the parameter of algae is the less accurate.

As you can see in the fit parameters, these inversions are done using a model for deep waters. This model performed better for the parameter characterization Table 10; the only parameter that underperformed was the algae content. The model used does not take into account the bottom reflectance of the lagoon. As you can see in Table 11 below, the R square errors that are lower than 0.40 have not been taken into account as good results and are highlighted in red. The table represents the accuracy of the results for every image and parameter. The visualization of every result can be seen in the attachments-0.

Parameters obtained in the results from WASI manual:

Table 10: WASI parameters from the results.

WASI parameter	Symbol	Default	Units	Description
C [5]	Ci	2, 0	µg/l	Concentration of phytoplankton class number I, I = 0.5 in this case is green algae
C_X	CL	0.5	mg/l	Concentration of non-algal particles of type I TSS
g_dd	gdd	0.02	sr ⁻¹	Fraction of sky radiance due to direct solar radiation
C_Y	Y	0.3	m ⁻¹	CDOM absorption coefficient at wavelength a440

Table 11: Accuracy results of the second attempt with the WASI- AI plugging, deep water model.

Sensor image	date	Fit.Param C(5)	Fit.Param C_X	Fit.Param C_Y	Fit.Param g_dd	R^2 C(5)	RMSD C(5)	R^2 C_X	RMSD C_X	R^2 C_Y	RMSD C_Y	R^2 g_dd	RMSD g_dd
DESES_002	20210703	11.37	6.706	0.4171	0.05490	0.69	3.1	0.97	0.41	0.92	0.12	0.99	0.0047
DESES_003	20210703	4.467	6.734	0.3418	0.05487	0.5	2.7	0.95	0.3	0.89	0.094	0.96	0.0072
DESES_004	20210703	0.9506	3.238	0.2296	0.1251	0.039	1.5	0.99	0.091	0.76	0.035	0.99	0.0028
DESES_002	20220601	0	6.062	0.3822	1.641	0.27	14	0.89	0.63	0.61	0.27	0.99	0.022
DESES_001	20220605	2.505	4.362	0.3539	0.08780	0.42	7.1	0.83	0.97	0.81	0.1	0.95	0.012
DESES_002	20220605	12.49	9.158	0.6116	0.07946	0.66	2.7	0.88	0.74	0.92	0.064	0.95	0.0097
DESES_002	20230322	0	8.948	0.4360	-0.00241	0.27	7.1	0.77	0.96	0.84	0.17	0.98	0.025
DESES_002	20230503	4.349	4.856	0.2791	0.5062	0.036	3	0.9	0.52	0.74	0.1	0.95	0.022
DESES_003	20230503	0	5.539	0.1744	0.3037	0.18	0.87	0.99	0.15	0.6	0.062	0.99	0.0092
DESES_004	20230503	0	3.785	0.1921	0.3150	0.18	1.5	0.99	0.12	0.88	0.047	1	0.0031
EnMAP	20230504	11.94	5.255	0.6793	-0.01839	0.082	2.6	0.98	0.22	0.95	0.051	0.77	0.0028
DESES_002	20230507	7.208	7.463	0.7079	0.2711	0.092	10	0.64	1.5	0.58	0.25	0.96	0.02
DESES_003	20230507	1.447	5.854	0.2447	0.2438	0.00051	5.9	0.74	0.93	0.46	0.27	0.97	0.037
DESES_004	20230507	2.952	3.614	0.1952	0.6075	0.15	1.4	0.95	0.3	0.58	0.048	0.99	0.0087
DESES_002	20230506	11.97	6.128	0.6467	2.550	0.059	7.1	0.75	1	0.87	0.2	1	0.014
EnMAP	20230531	10.37	7.301	0.7102	-0.02215	0.24	2.7	0.95	0.37	0.88	0.2	0.7	0.0038
EnMAP	20230623	0	4.518	0.4426	0.005695	0.044	2.1	0.98	0.19	0.97	0.031	0.94	0.003
EnMAP	20230701	0	4.276	0.5623	0.01892	0.039	15	0.95	0.59	0.94	0.1	0.93	0.0069
DESES_003	20230706	0.07359	5.834	0.5493	0.07568	0.003	10	0.92	0.41	0.47	0.26	0.77	0.021
DESES_003	20230706	0.1761	6.842	0.2562	0.01041	0.5	4.3	0.95	0.63	0.2	0.29	0.98	0.01
DESES_005	20230706	0	2.804	0.003214	0.02009								
EnMAP	20230817	25.56	10.26	2.199	-0.05060	0.036	6.6	0.96	0.89	0.88	0.14	0.8	0.0076
DESES_003	20231029	0	4.922	0.3999	0.3223	0.0031	2.6	0.85	0.6	0.7	0.15	0.99	0.0069
EnMAP	20231109	0.7801	6.984	0.7589	-0.01668	0.31	3.5	0.94	0.92	0.66	0.38	0.54	0.012

6.1.1 Water quality parameter results for EnMAP

The processing of EnMAP data was performed with two different models. The first model tried was the shallow water inversion with WASI software and the second model tried was the deep-water model with WASI-AI. The method that had better results was the deep-water model that is explained in the 4.4 chapter in the justification of methods. The results obtained and analyzed were from the deep-water model. In the **attachments-0** you can find the results.

The first attempt of image processing was processed using the shallow waters model due to the shallow depth of the lagoon which has an average of 2m depth. Also, during the first inversion the fitting parameters of water depth temperature and diatom, the zB (depth), the temperature parameter did not fit the FA(2) and the FA(2). The results were not as accurate as expected and the second attempt proceeded. Peter suggested to process the data with the deep-water inversion because the color of the water and the benthonic organisms that are in the bottom of the lagoon were difficult to quantify.

On the following lines you can find an example of the two attempts, for all the results consult the attachments-0.

6.1.2 Results of first testing EnMAP model of shallow waters

The results of the first testing EnMAP model of shallow waters are presented in Figure 45, Figure 46, and Figure 47.

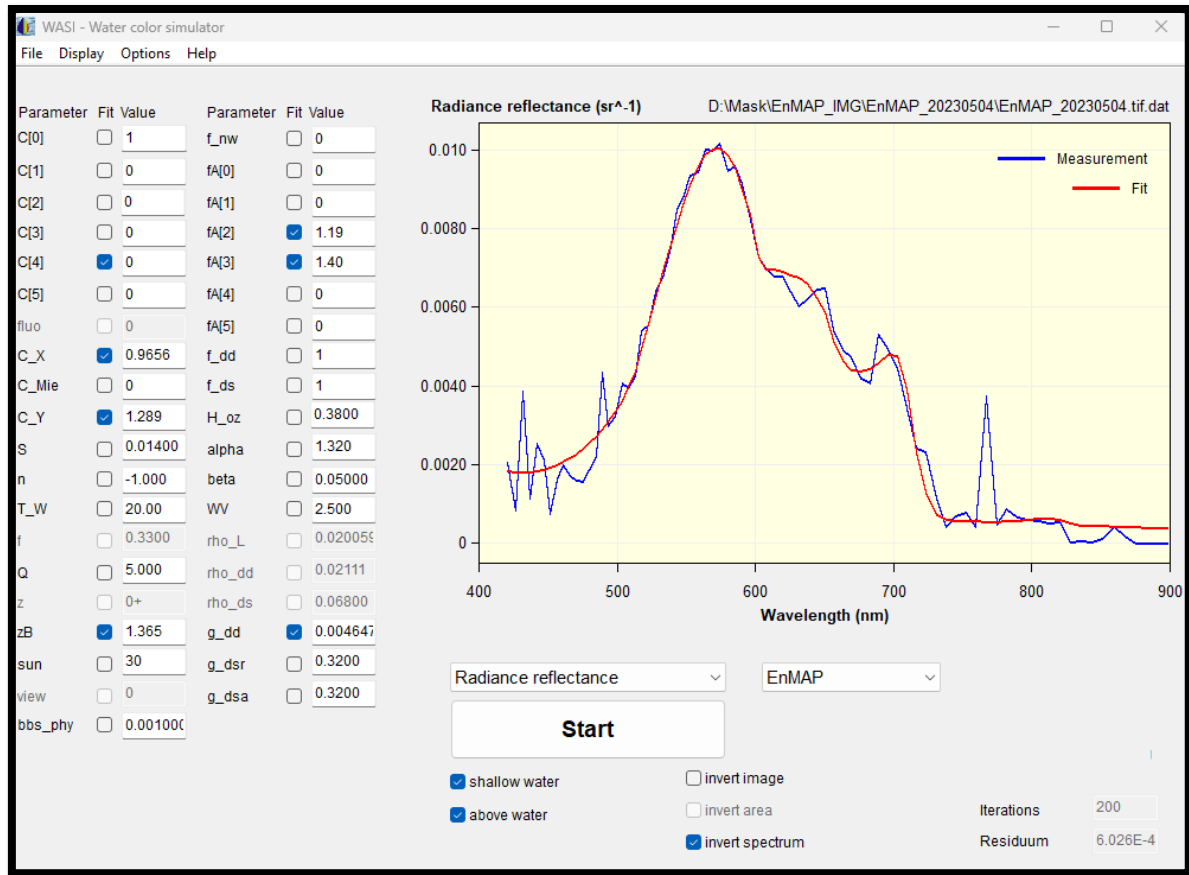
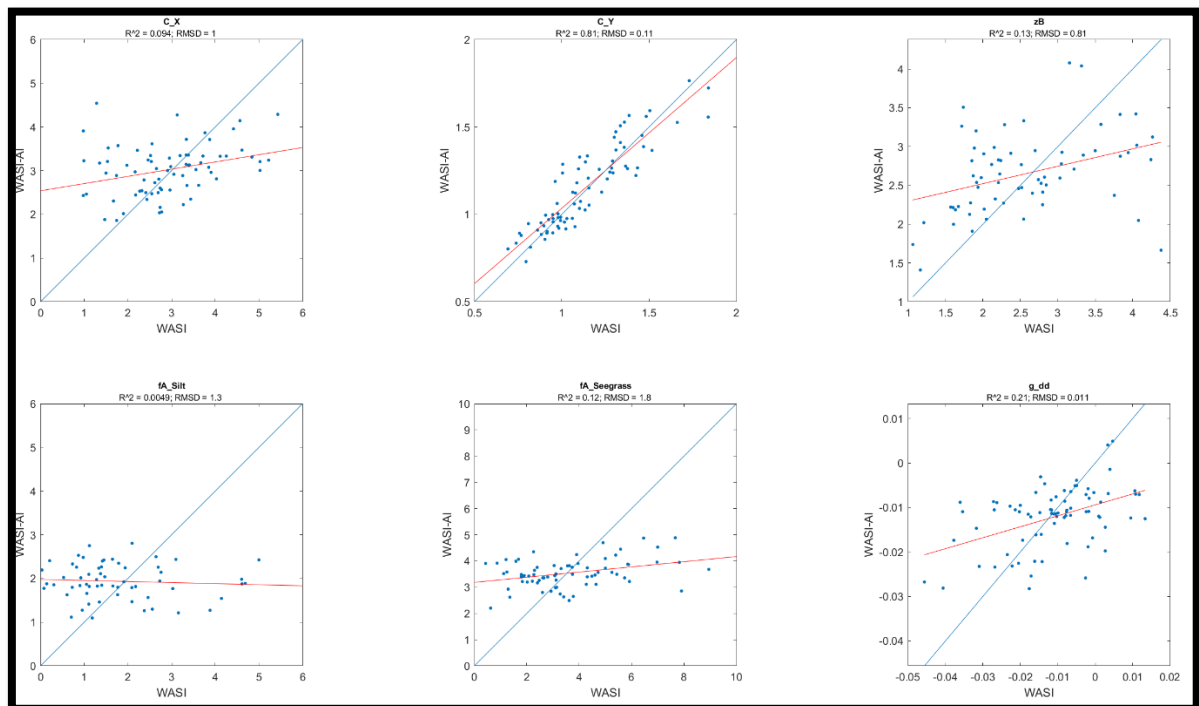
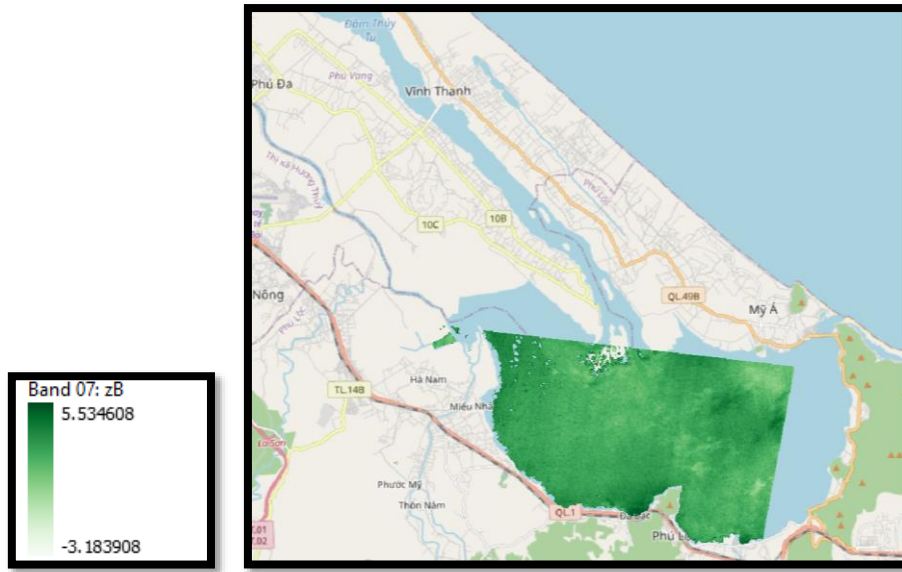


Figure 45: Fit parameters EnMAP_20230504.tif_AI_validation_Fit_parameters_6p.



**Figure 46: Water quality estimation parameter R^2 Error
EnMAP_20230504.tif_AI_validation_Fit_parameters_6p.**



**Figure 47: C_Y CDOM normalized to the minimum and maximum
EnMAP_20230504.tif_AI_validation_Fit_parameters_6p.**

6.1.3 Results of analysis EnMAP Model of deep water:

The results of the first testing EnMAP model of deep waters are presented in Figure 48, and Figure 49.

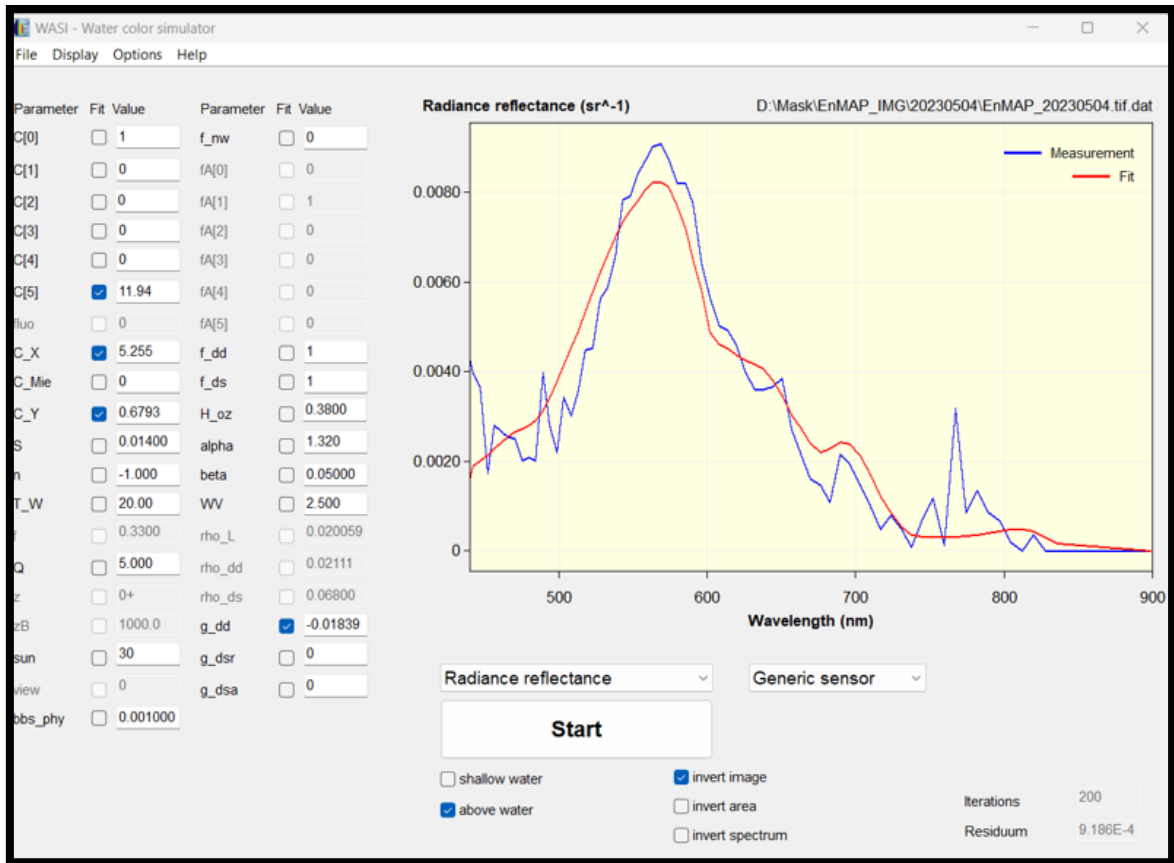


Figure 48: EnMAP image date 2023-05-04 parameter data setup.

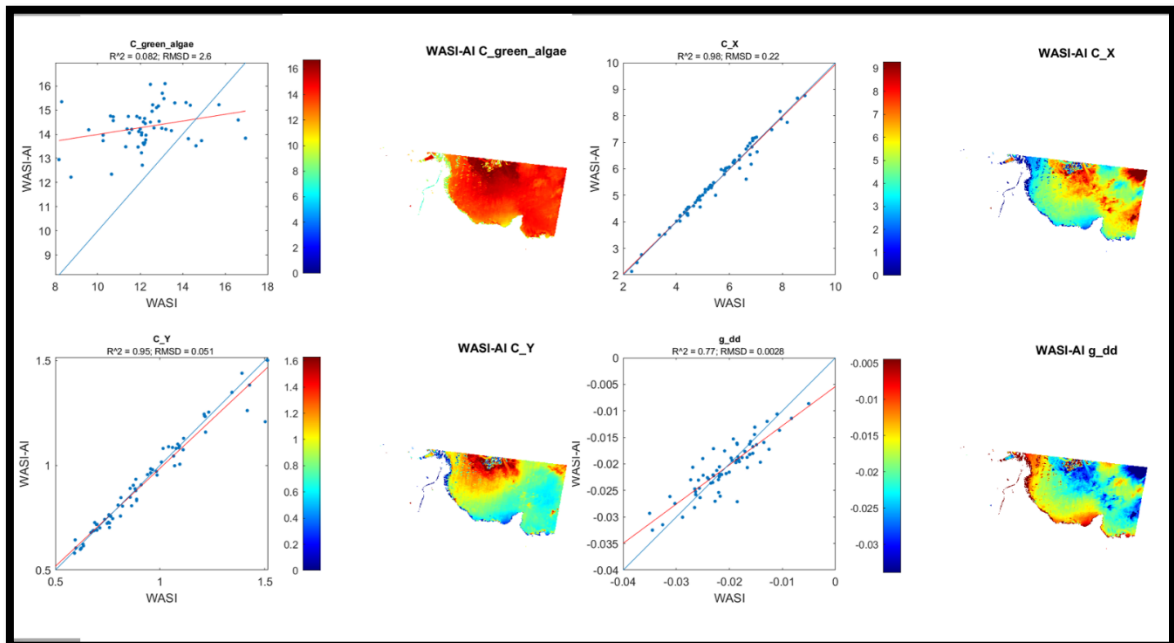


Figure 49: EnMAP image date 2023-05-31 process results.

6.1.4 Results of analysis DESIS Model of deep water:

The DESIS data has been processed using the deep-water model. Below, you can find an example of 3 of May 2023 the same date as the example of EnMAP data above. For the rest of the results, check the attachments-0.

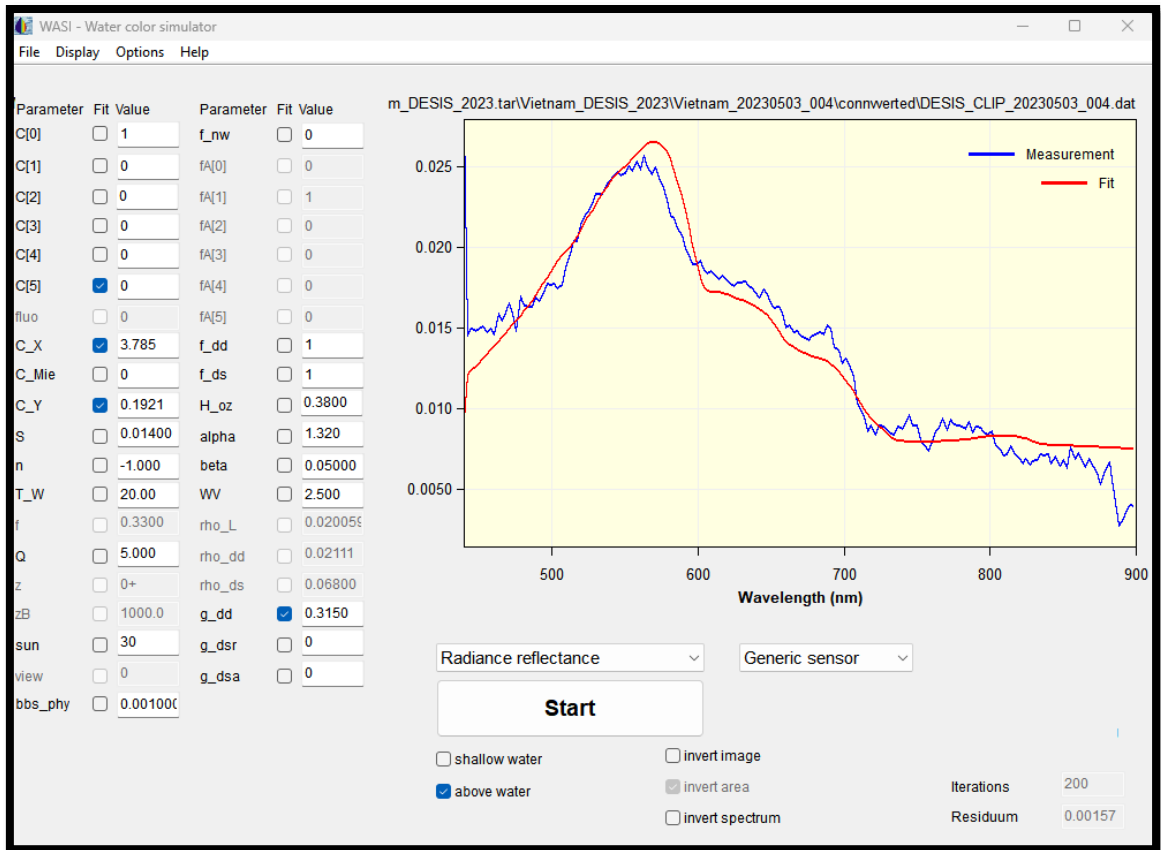


Figure 50: DESIS image date 2023-05-03 parameter data setup.

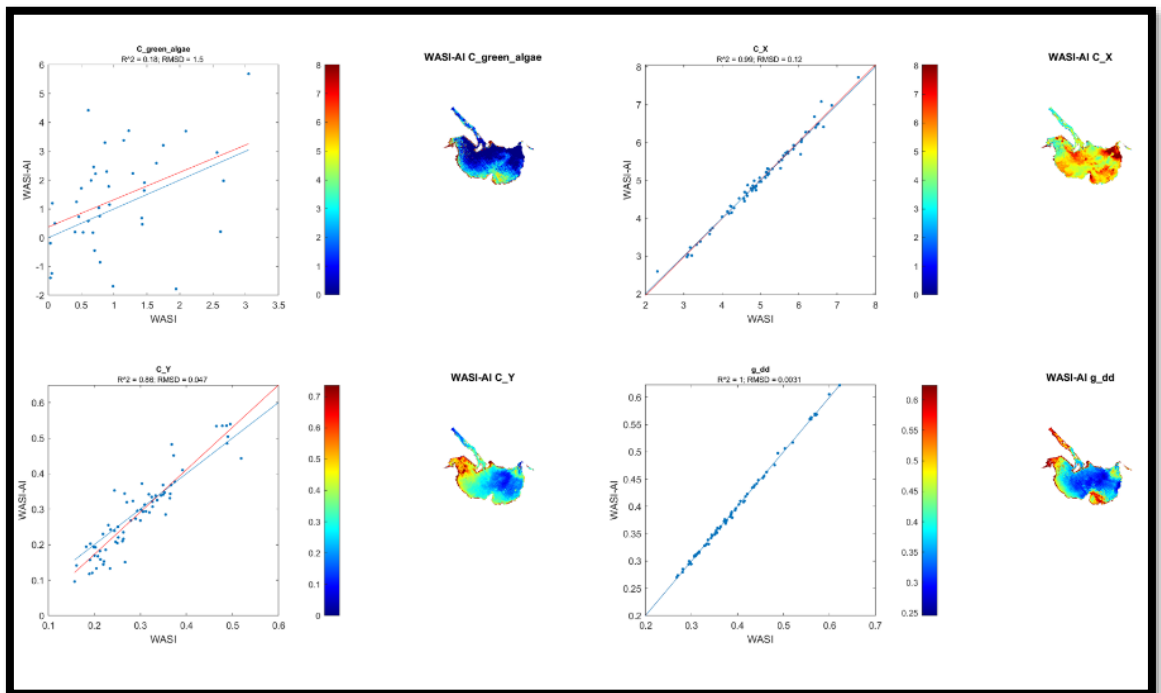


Figure 51: DESIS image date 2023-05-03 process results.

6.1.5 Results of analysis pixel statistics of every image

The tables below show the results of all the satellite images, giving the basic statistics of the green algae(b5) Table 12, TSS(b6) Table 13, and CDOM(b7)

. Statistics: maximum, minimum, mode, mean, standard deviation, count of pixels, supposed number of outliers, sum, range of data, and coefficient of variation. All of the pixel graphs can be found in the attachments-0.

Table 12: For Green algae (b5):

Satellite id	date	Min	MAX	Mean	Std. DEV	Median	count	Outliers	Range	Coefficient of variation
b5_002	20210703	-14.814961	502.0867	28.8778	48.767887	10.342206	51,518	8,657	516.901662	1.688767
b5_003	20210703	-21.42453	453.542999	16.963669	31.132282	7.374285	69,398	10,463	474.967529	1.835233
b5_004	20210703	-45.528076	94.588516	2.672837	10.811388	0.702438	111,130	10,730	140.116592	4.044911
b5_002	20220601	-1,939.92	394.663635	14.847768	86.830146	16.617296	56,119	4,818	2,334.58	5.848027
b5_001	20220605	-28.893463	1,332.05	25.980694	75.72397	7.643422	100,929	14,634	1,360.94	2.914625
b5_002	20220605	-0.709541	248.941772	5.369219	12.554395	2.462795	32,413	3,866	249.651314	2.338216
b5_002	20230322	-655.247498	14,669.37	42.042336	388.080231	10.080113	95,609	11,634	15,324.62	9.230701
b5_002	20230503	-5.313478	4,293.59	31.52671	144.41884	5.138801	39,121	5,916	4,298.90	4.580841
b5_003	20230503	-52.542664	2,660.88	26.751785	160.971815	1.37073	69,883	6,964	2,713.43	6.017237
b5_004	20230503	-8.145119	692.998169	4.796058	24.031155	1.313506	117,596	8,730	701.143288	5.010606
EnMAP_b5	20230504	6.168607	18.195557	13.992068	1.507163	14.089135	78,904	7,144	12.02695	0.107716
b5_002	20230507	-58.673782	6,786.77	154.228214	459.515449	16.679588	47,955	7,344	6,845.44	2.979451
b5_003	20230507	-32.828194	146,549.50	113.407176	838.491946	2.360433	73,824	10,464	146,582.33	7.393641
b5_004	20230507	-3.789515	141.988937	3.089872	2.844827	2.595866	130,644	7,943	145.778452	0.920694
EnMap_b5	20230531	-14.46604	59.221298	14.802967	5.338437	13.75651	74,713	5,113	73.687338	0.360633
EnMAP_b5	20230623	-1.664466	136.086731	3.419501	3.584975	2.602804	52,920	6,147	137.751197	1.048391
EnMAP_b5	20230701	-440.238892	263.891449	12.078706	27.206412	8.107659	100,401	9,658	704.130341	2.252428
b5_003	20230706	-1.194243	7,217.84	90.893844	313.345574	9.669502	55,551	6,884	7,219.03	3.447379
b5_004	20230706	-44.038677	4,666.45	53.542015	201.358768	4.409311	87,708	13,990	4,710.49	3.760762
EnMAP_b5	20230817	15.892406	836.688538	49.776561	82.529253	24.667809	14,263	2,458	820.796131	1.657994
b5_003	20231029	-52.634563	615.707214	4.008636	10.499907	3.028264	107,377	2,758	668.341778	2.619322
EnMAP_b5	20231109	0	22.263939	8.906693	3.876792	7.985634	75,669	2,378	22.263939	0.435267
b5_002	20230506	-25.22957	45,462.55	720.71955	3,342.24	15.717632	54,154	9,755	45,487.78	4.63737

Table 13: for TSS (b6)

Satellite id	date	Min	MAX	Mean	Std. DEV	Median	count	Outliers	Range	Coefficient of variation
b6_002	20210703	1.841748	31.95854	9.347807	4.086722	8.354604	51,468	3,981	30.116792	0.437185
b6_003	20210703	0.100488	76.314583	8.789259	4.647607	7.523797	69,236	8,222	76.214095	0.528783
b6_004	20210703	0.013688	16.388601	4.001149	1.960473	3.661849	110,896	4,622	16.374913	0.489978
b6_002	20220601	0.000145	543.495789	15.227128	41.032573	6.375768	56,118	4,911	543.495644	2.694702
b6_001	20220605	0.00169	83.203308	5.921524	3.297805	5.024756	100,730	8,121	83.201618	0.556918
b6_002	20220605	0.039157	22.571362	5.993665	2.413511	5.693965	32,418	869	22.532205	0.402677
b6_002	20230322	0.001621	98.86911	10.504324	6.507022	9.047771	95,313	7,818	98.86749	0.619461
b6_002	20230503	0.003114	50.373158	6.702286	3.736381	5.872778	39,169	2,342	50.370043	0.557479
b6_003	20230503	0.002325	44.472103	5.573988	2.139078	5.394371	69,696	3,212	44.469778	0.383761
b6_004	20230503	0.657296	42.927696	5.302634	1.736946	5.123161	116,797	7,031	42.2704	0.327563
EnMAP_b6	20230504	-1.627455	17.369652	5.181932	1.888172	5.189063	79,434	5,860	18.997106	0.364376
b6_002	20230506	0.014293	95.972984	9.162628	6.196502	7.255368	54,128	5,164	95.958692	0.67628
b6_002	20230507	0.00276	132.08078	10.908117	6.346638	9.336432	47,904	4,118	132.07802	0.581827
b6_003	20230507	0.006044	554.766724	8.19768	4.787185	7.606857	73,655	4,565	554.76068	0.583968
b6_004	20230507	0.00263	34.421196	3.988356	1.836511	3.874566	130,572	3,201	34.418566	0.460468
EnMAP_b6	20230531	-5.518095	52.233105	7.327144	3.705104	7.586504	74,746	7,886	57.7512	0.505668
EnMAP_b6	20230623	-0.694345	56.107769	4.88045	1.600683	4.540905	52,823	3,346	56.802114	0.327979
EnMAP_b6	20230701	-7.2793	41.17429	5.531371	3.787497	4.517515	100,245	4,161	48.45359	0.68473
b6_003	20230706	0.000333	54.070488	7.708011	7.130466	5.393634	55,514	7,719	54.070155	0.925072
b6_004	20230706	0.000584	22.739246	5.092872	2.718295	4.963282	87,623	1,336	22.738663	0.533745
EnMAP_b6	20230817	-2.028209	57.146366	13.457529	7.699852	11.221877	14,278	1,046	59.174575	0.572159
b6_003	20231029	0.000002	17.779194	6.189105	2.217444	6.118179	107,174	6,128	17.779191	0.358282
EnMAP_b6	20231109	-4.623858	43.343288	8.417314	4.98855	8.479774	75,658	7,979	47.967147	0.592653

Table 14: for the CDOM (b7)

Satellite id	date	Min	MAX	Mean	Std. DEV	Median	count	Outliers	Range	Coefficient of variation
b7_002	20210703	-0.505985	51.346275	2.527515	4.680564	1.012594	51,484	6,528	51.85226	1.851844
b7_003	20210703	-2.711896	17.993557	1.28629	1.708169	0.677709	69,359	9,560	20.705453	1.327982
b7_002	20220601	-10.283276	756.590271	13.784162	57.193352	0.445374	56,153	6,538	766.873547	4.149208
b7_001	20220605	0.066793	145.053879	4.356615	13.384926	0.627775	100,749	16,292	144.987085	3.072322
b7_002	20220605	-0.126971	5.189118	0.561517	0.418214	0.432174	32,388	3,388	5.316089	0.744793
b7_002	20230322	-4.600204	425.460846	3.807429	20.790203	0.584002	95,568	12,393	430.061049	5.460431
b7_002	20230503	-0.111826	22.885811	0.779489	1.287606	0.496736	39,157	2,867	22.997637	1.65186
b7_003	20230503	-0.128326	47.533958	0.611396	2.521799	0.232015	69,851	3,849	47.662284	4.124658
b7_004	20230503	-3.913582	8.882	0.365048	0.401157	0.300321	117,327	5,905	12.795582	1.098913
EnMAP_b7	20230504	-0.637419	3.394783	0.891064	0.309413	0.852428	79,450	2,559	4.032202	0.34724
b7_002	20230506	-2.087211	2,087.43	36.705078	165.360513	1.527407	54,143	8,941	2,089.52	4.505113
b7_002	20230507	-9.550667	61.762245	4.425699	8.028493	1.534501	47,948	7,547	71.312912	1.814062
b7_003	20230507	-1.505186	2,525.88	5.616863	26.354162	0.457889	73,794	8,883	2,527.38	4.691972
b7_004	20230507	-0.623244	2.735208	0.174228	0.161727	0.194435	130,687	16,504	3.358451	0.928252
EnMAP_b7	20230531	-0.396894	10.438498	1.435639	1.302755	1.047302	74,792	4,186	10.835391	0.907439
EnMAP_b7	20230623	0.100115	12.541666	0.727806	0.436394	0.65072	52,867	2,703	12.441551	0.599602
EnMAP_b7	20230701	-4.811146	4.758733	0.886099	0.589417	0.790593	100,281	3,967	9.569879	0.665182
b7_003	20230706	-42.78746	225.456146	1.885739	4.798414	0.897349	55,544	8,110	268.243607	2.54458
b7_004	20230706	-2.642303	92.246605	1.670536	4.311819	0.541443	87,712	10,698	94.888908	2.5811
EnMAP_b7	20230817	-9.30038	12.569364	2.583473	1.675506	2.062628	14,265	2,090	21.869743	0.648548
b7_003	20231029	-5.328195	404.866272	0.743242	9.411623	0.360109	107,447	4,683	410.194467	12.662928
EnMAP_b7	20231109	-467.024628	131.534943	1.487172	11.873088	1.213896	75,743	7,480	598.55957	7.98367
b7_004	20210703	-0.6487	63.642746	0.606765	2.172736	0.303088	110,772	11,080	64.291446	3.580852

6.2 RESULTS OF THE STATISTICAL ANALYSIS TSS VALIDATION

The First results are from the comparative analysis of the in-situ data to the satellite data and the trends of this data. The second results are the ones showing the relationship between the TSS and the rest of the parameters of the in-situ data.

6.2.1 Results of the comparative in-situ vs satellite TSS concentration

Descriptive Statistics V2:

- **In-situ Data:**
 - The mean TSS is 12.20 mg/l, with a standard deviation of 5.59 mg/l.
 - The TSS values range from 5.6 mg/l to 27.20 mg/l.
 - The interquartile range (IQR) shows that 50% of the TSS values fall between 7.10 mg/l and 14.80 mg/l.
- **Satellite Data:**
 - The mean TSS is 7.15 mg/l, with a much higher standard deviation of 6.64mg/l.
 - The TSS values range from 0.83 mg/l to 35.98 mg/l.

- The IQR shows that 50% of the TSS values fall between 4.45 mg/l and 7.25 mg/l, indicating a wide range of variability.
- **Pearson Correlation Coefficient:** 0.844
 - There is a low negative correlation between the in-situ and satellite TSS measurements.
 - The p-value is 0.854, indicating that the correlation is not statistically significant.

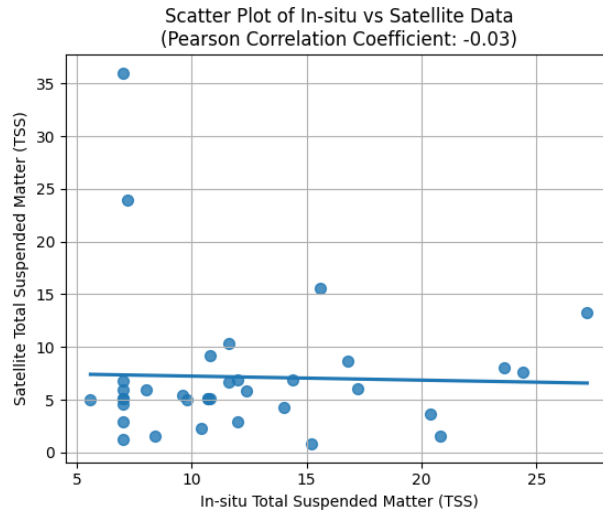


Figure 52: Scatter plot of the in-situ vs satellite data showing the Pearson correlation coefficient.

- **Regression Analysis:**
 - The slope of the regression line is -0.038, and the intercept is 7.62.
 - The R-squared value is 0.001, meaning that approximately 0.10% of the variability in satellite TSS can be explained by the in-situ TSS measurements.
 - This suggests a **very weak relationship** between the two measurements, with most of the variability unaccounted for by the regression model.

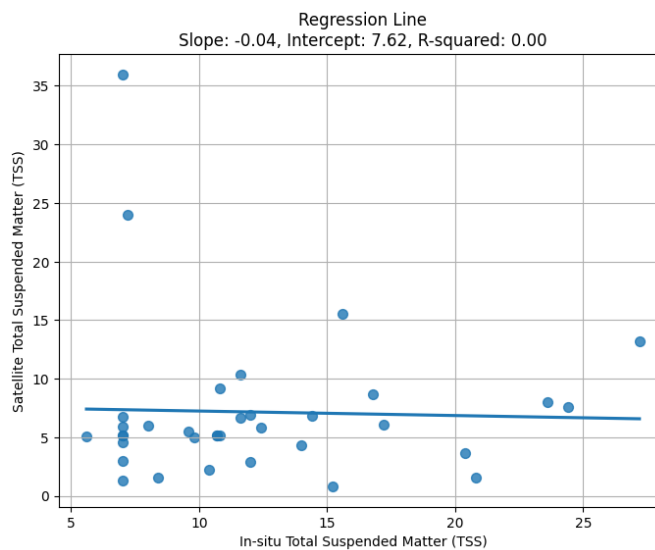


Figure 53: Scatter plot of the in-situ vs satellite data showing the linear regression line with the values of slope interception and R-squared.

Paired T-test:

- **T-statistic: 3.39**
 - The t-test yields a t-statistic indicating a **significant difference** between the mean TSS values from in-situ and satellite measurements.
 - The p-value is 0.0018, indicating that this difference is statistically significant.

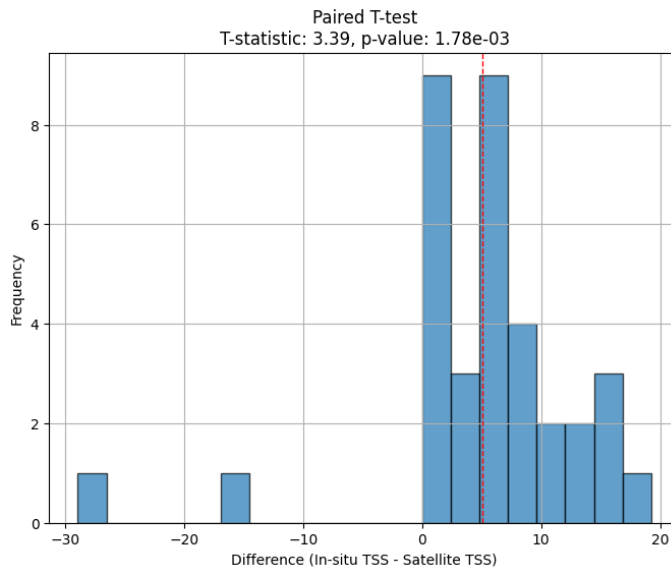


Figure 54: The paired T-test.

Wilcoxon Signed-Rank Test:

- **Wilcoxon Signed-Rank Test Statistic: 67.0**
 - The Wilcoxon signed-rank test yields a very low p-value (1.19e-05), indicating a statistically significant difference between the paired samples.
 - This non-parametric test is used to compare paired samples and is robust against non-normality. The significant result suggests that there are **differences in the paired data** that the t-test might not detect due to its assumptions.



Figure 55: Wilcoxon Signed-Rank Test.

Root Mean Square Error (RMSE):

- **RMSE:** 10.05
 - The RMSE of 10.05 indicates the average magnitude of error between the satellite and in-situ TSS measurements.
 - This suggests substantial differences between the measurements.

Bland-Altman Plot Analysis:

The Bland-Altman plot analysis can be visualized in Figure 56 and it shows the following data:

- **Mean Difference:** 5.05
 - This result indicates that, on average, the **in-situ TSS measurements are higher** than the satellite TSS measurements.
 - The small mean difference points out that there is no substantial systematic bias between the two measurement methods. The mean difference points out a potential systematic bias where satellite measurements tend to underestimate TSS.
- **Standard Deviation of Differences:** 8.69
 - The high standard deviation of the difference and the wide limits of agreement (mean difference $\pm 1.96 * \text{std_diff}$) indicate a **considerable variability** between the individual in-situ and satellite TSS measurements, with potential outliers.
 - This reinforces the finding from the RMSE, showing substantial discrepancies between the two methods on a point-by-point basis.

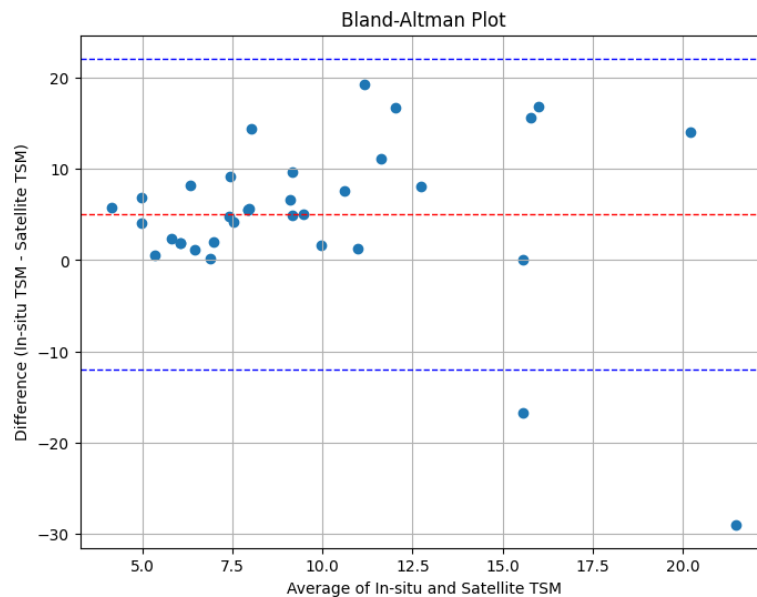


Figure 56: Bland-Altman plot.

Plots of all the sample points from the in-situ data, containing the in-situ data of the point and also the satellite data of the point though time. Find in the following lines there are three examples of the plots Figure 57, Figure 58, and Figure 59, for seeing the rest look in the **attachments-0**.

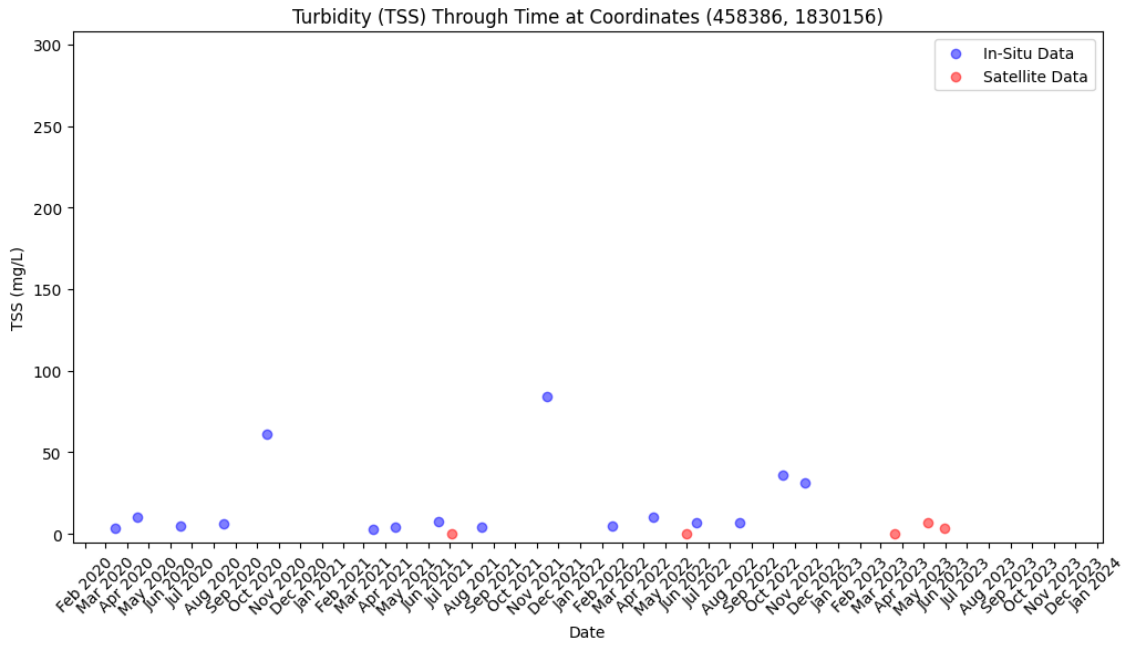


Figure 57: Point sample data of In-situ and satellite point id NSH7 coordinates 458386 1830156.

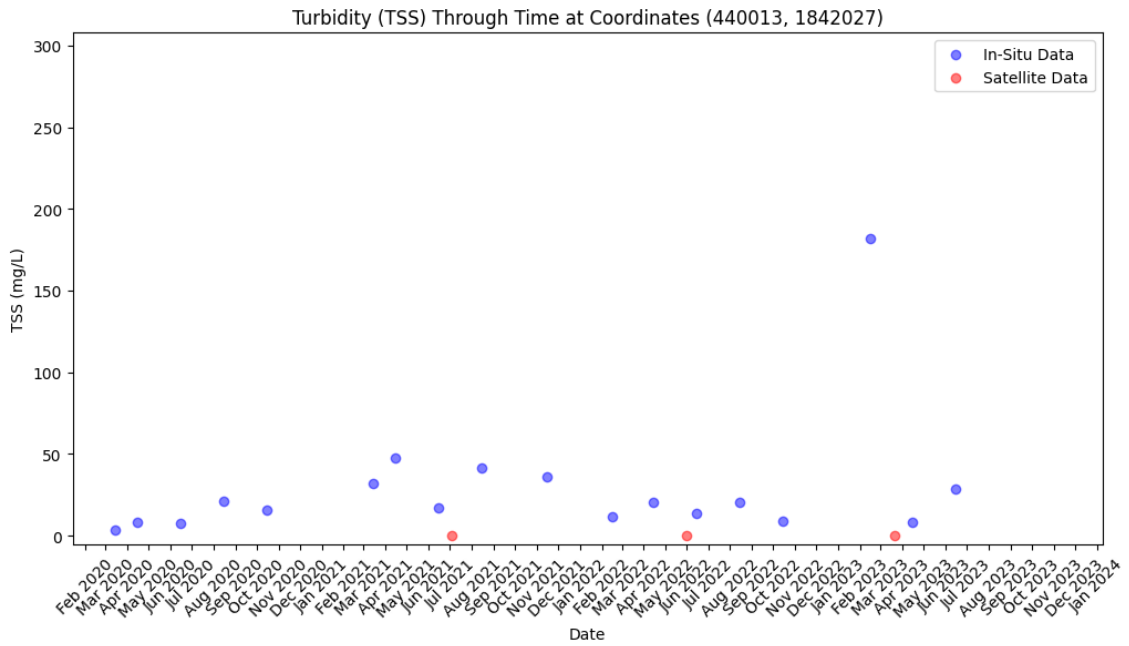


Figure 58: Point sample data of In-situ and satellite point id NPTG4 coordinates 440013 1842027.

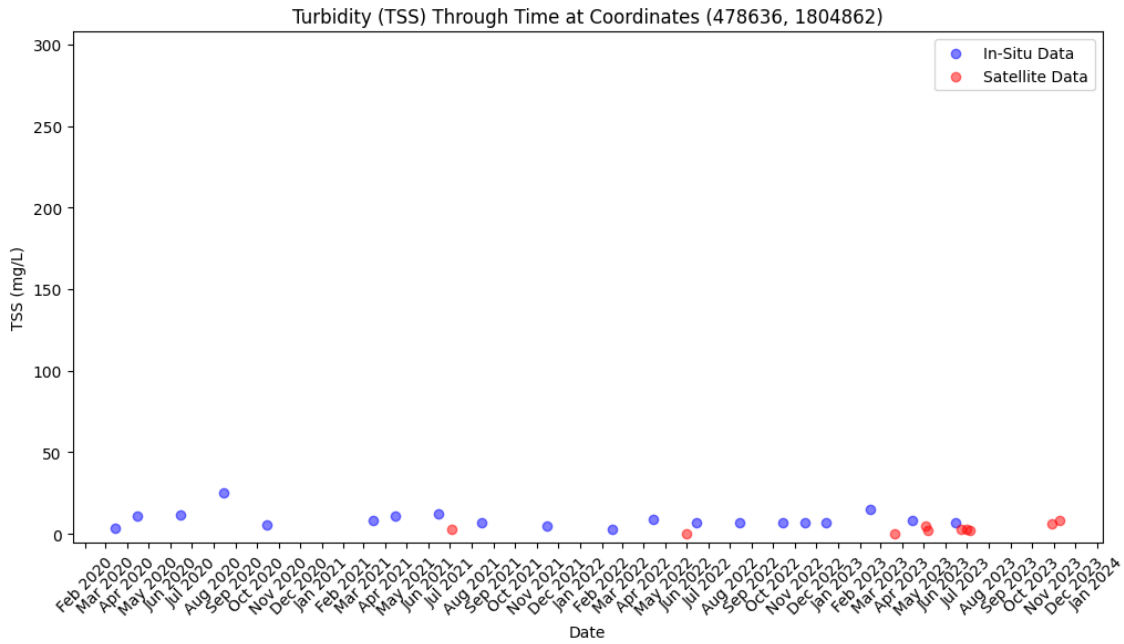


Figure 59: Point sample data of In-situ and satellite point id NDCH1 coordinates 478636 1804862.

Results of how many times the values have exceeded the 50mg/l from the in-situ data and satellite data Figure 60.

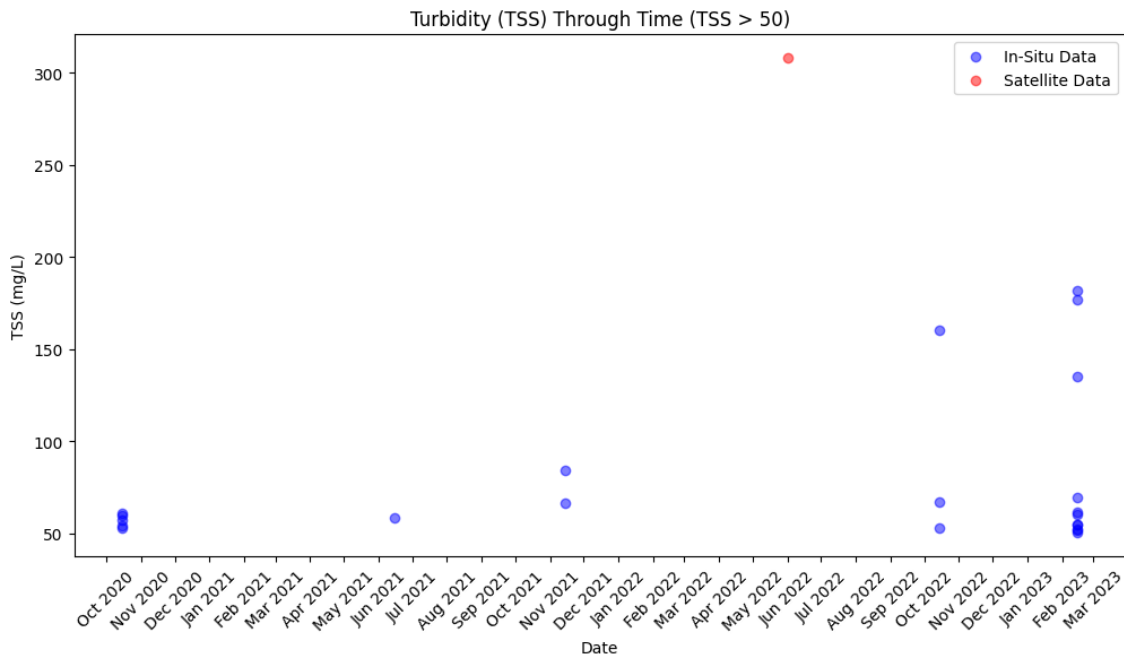


Figure 60: Point sample data of In-situ and satellite points that have exceeded the 50mg/l.

In-Situ Data Points with TSS > 50:

	MMYYYY	X	Y	TSS
144	2020-10-15	458386	1830156	61.0
154	2020-10-15	459618	1832583	54.0
157	2020-10-15	459032	1832119	57.0
158	2020-10-15	459040	1831609	53.0
160	2020-10-15	462652	1827551	59.5

263	2021-06-15	450795	1837274	58.4
324	2021-11-15	458386	1830156	84.4
351	2021-11-15	491059	1808879	66.6
506	2022-10-15	438814	1842194	52.8
511	2022-10-15	461233	1830750	66.8
514	2022-10-15	459618	1832583	160.5
604	2023-02-15	439114	1841538	177.0
605	2023-02-15	440013	1842027	182.0
607	2023-02-15	455944	1834220	52.4
608	2023-02-15	461233	1830750	54.8
612	2023-02-15	450795	1837274	51.6
614	2023-02-15	459032	1832119	54.4
616	2023-02-15	462078	1827273	60.5
622	2023-02-15	475684	1817004	50.1
623	2023-02-15	481813	1810780	135.0
627	2023-02-15	489856	1802640	61.5
628	2023-02-15	491059	1808879	69.2

Satellite Data Points with TSS > 50:

id	MMYYYY	X	Y	TSS
408	NPTG12	2022-06-01	448037	1836262 307.7997

6.2.2 Results comparison of all the parameter vs TSS in in-situ data

T-test has been realized by comparing the TSS to the rest of the parameters.

T-test in pairs for the TSS value:

```
{'TEMP_oC': 5.787671222245099e-47,
'pH': 4.566805876460814e-28,
'DO': 2.049159803669277e-40,
'BOD5': 1.3473821537517115e-65,
'COD': 8.879676825453233e-12,
'NH4+-N': 2.411196295639746e-35,
'NO2-': 2.967898456685398e-88,
'NO3-': 7.383395304681256e-88,
'PO43-': 4.8004039673761317e-88,
'As': 1.8319765975954256e-88,
'Cd': 1.4838069037775312e-88,
'Pb': 1.5352346219439283e-88,
'Cu': 3.7859178840607327e-88,
'Zn': 6.036277321232673e-88,
'Mn': 6.601417934557531e-88,
'Hg': 1.4751972931502617e-88,
'Fe': 6.955805750686107e-85,
'Coliform': 3.067859766261029e-34}
```

Interpreting Small P-values: A very small p-value (typically less than 0.05) indicates strong evidence against the null hypothesis, suggesting that there is a statistically significant difference between the compared groups.

The Shapiro–Wilk test has been used to choose the correlation method to use. In that case, the p-value indicates that the data is not normally distributed; the value is very small.

Shapiro-Wilk Test for TSS: p-value=2.9130588875693885e-36

The proper correlation coefficient to use is the Spearman Correlation Coefficient. The relationship between the total values of the TSS and the particular water parameters has been calculated and shown.

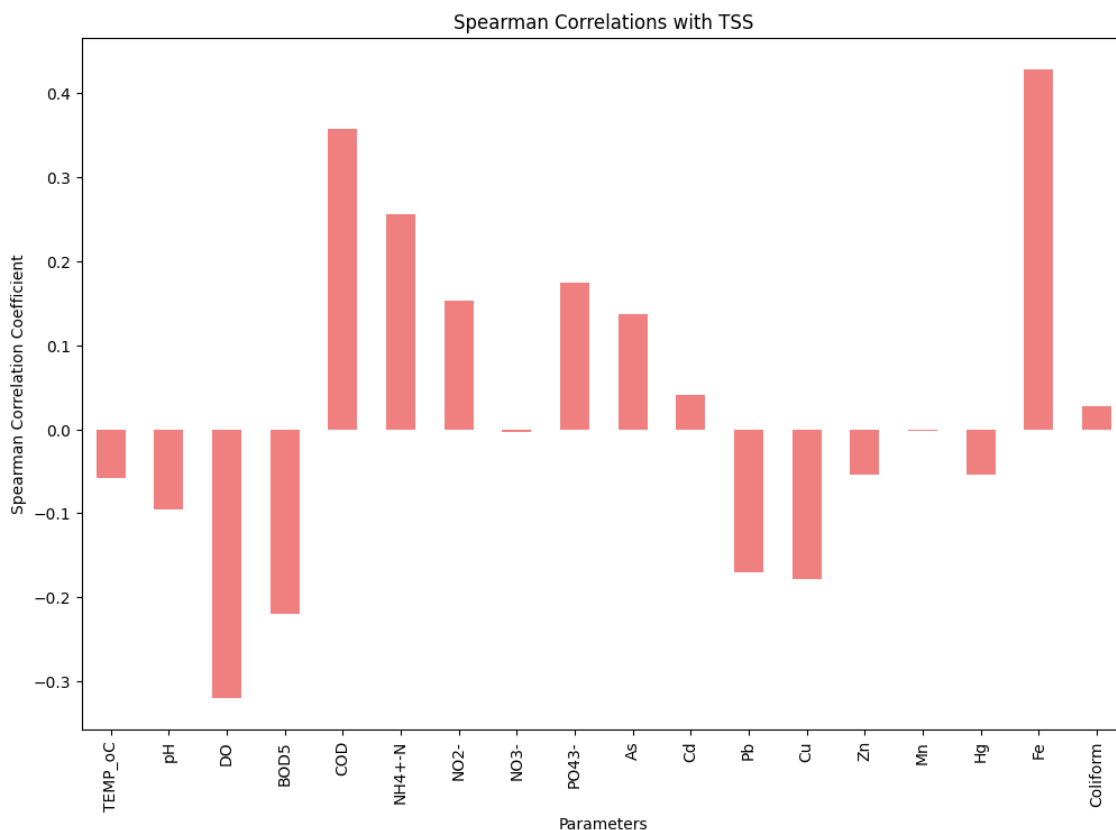


Figure 61: Plot of the Spearman correlations with TSS and the other in-situ parameters.

Values between -0.3 and 0.4 indicate that the correlations between TSS and the other parameters are weak to moderate. This means that the relationship is either weakly linear or potentially non-linear.

- -0.3 to -0.1: Weak negative correlation. As one parameter increases, TSS slightly decreases.
- -0.1 to 0.1: Very weak or no correlation. There is little to no linear relationship between TSS and the parameter.
- 0.1 to 0.3: Weak positive correlation. As one parameter increases, TSS slightly increases.
- 0.3 to 0.4: Moderate positive correlation. As one parameter increases, TSS moderately increases.

The Spearman correlation shows a moderate positive correlation for CDO and Fe and a moderate negative correlation for DO.

20
/
21

WATER QUALITY

20
/
23

Total Suspended Solids (TSS) and Colored Dissolved Organic Mater (CDOM), Tam Giang Lagoon, Vietnam 2021–2023.

Tam Giang Coastal Lagoon is the largest lagoon in Southeast Asia covering an area of 216 km². It has a mean depth of 2 m and a maximum depth of 5–15 m in the inlets region.

TSS refers to organic and mineral solids suspended in the water column. These can come from surface runoff, catchment areas, rivers, or the coast or be resuspended from the bottom of the water body.

The TSS parameter is closely linked with water transparency/turbidity and Secchi disk depth. Turbidity events can contain several substances important for water bodies' management. For example, a high turbidity of 20 TSS mg/l in drinking water can harbor microbial pathogens and reduce the efficacy of disinfection. In Vietnam, the water quality Circular No. 43/2011/TT-BTNNT regulates the concentration.

CDOM is the portion of dissolved organic matter in natural waters that absorbs visible light. The sources of CDOM in aquatic ecosystems include two parts: autochthonal (microbial and phytoplankton) and allochthonous sources (terrestrial and anthropogenic inputs).

CDOM affects pH and alkalinity, forms chemical complexes with metals (with implications for their bioavailability and toxicity), and acts as a transport agent for metals and nonpolar organic contaminants.

The following map represents the TSS and CDOM content gathered with hyperspectral satellite images from 2021 to 2023. The small maps offer a detailed view of the two contents simultaneously, while the bar charts indicate the distribution of values of the satellite images in hexagons. The TSS and CDOM measurements gathered with the WASI model present a high accuracy.

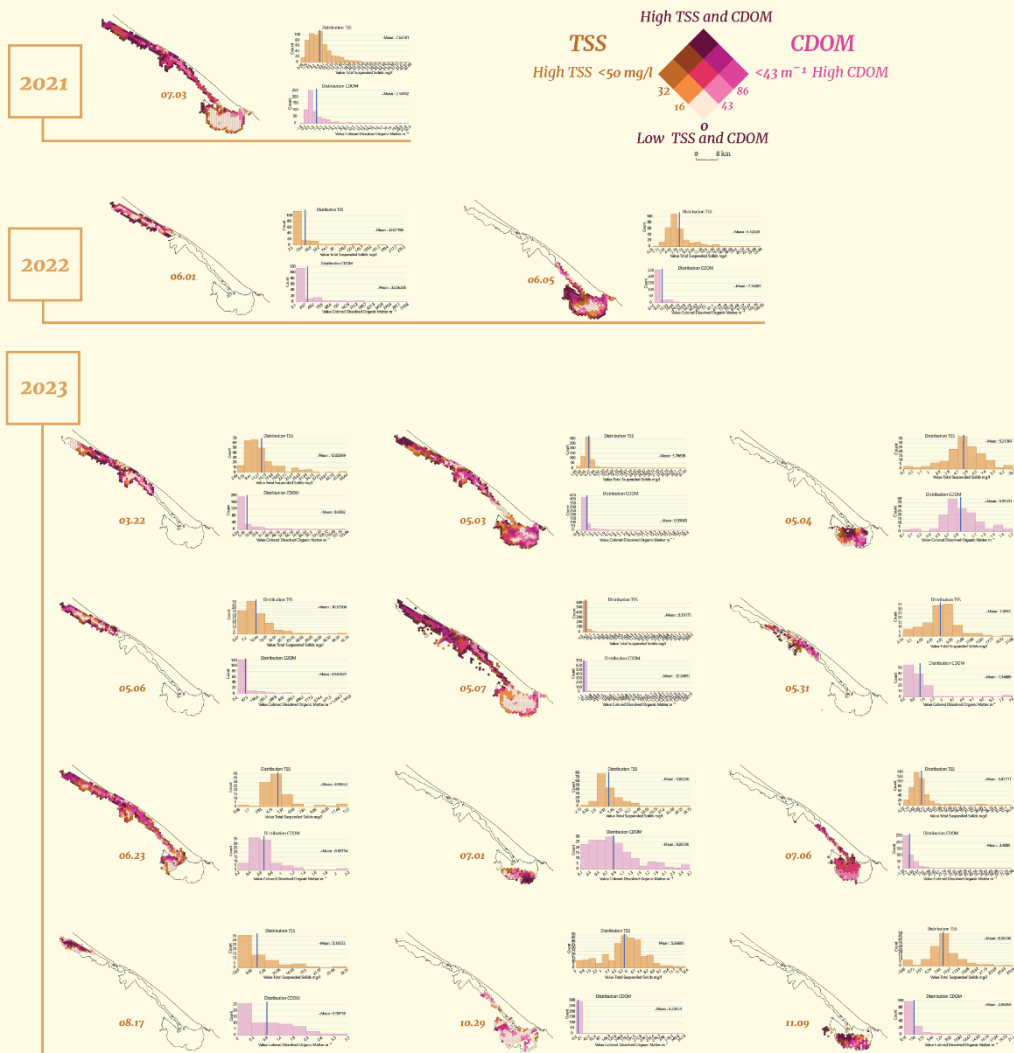


Figure 65: Map poster TSS & CDOM.

6.3.2 Map animation:

For the animation, it is selected to visualize the TSS parameter through time Figure 66, Figure 67 because it is the only parameter that it has registered for the satellite data, and it also contains credible in-situ results. Also, as summary is visualized Figure 68, the synthetic map is also done for the map posters, showing the differences between the minimum and the maximum values of the period. In the animation it is also incorporated the data of the flooding mentioned in the visualization data chapter. This layer has been visualized in a simple color scale for the TSS of in-situ and satellite data, and the flooding represents a uniform color for the delimitation of the event. The animation is on the attachment-2(digital format).



Figure 66: Map animation timeline graph.

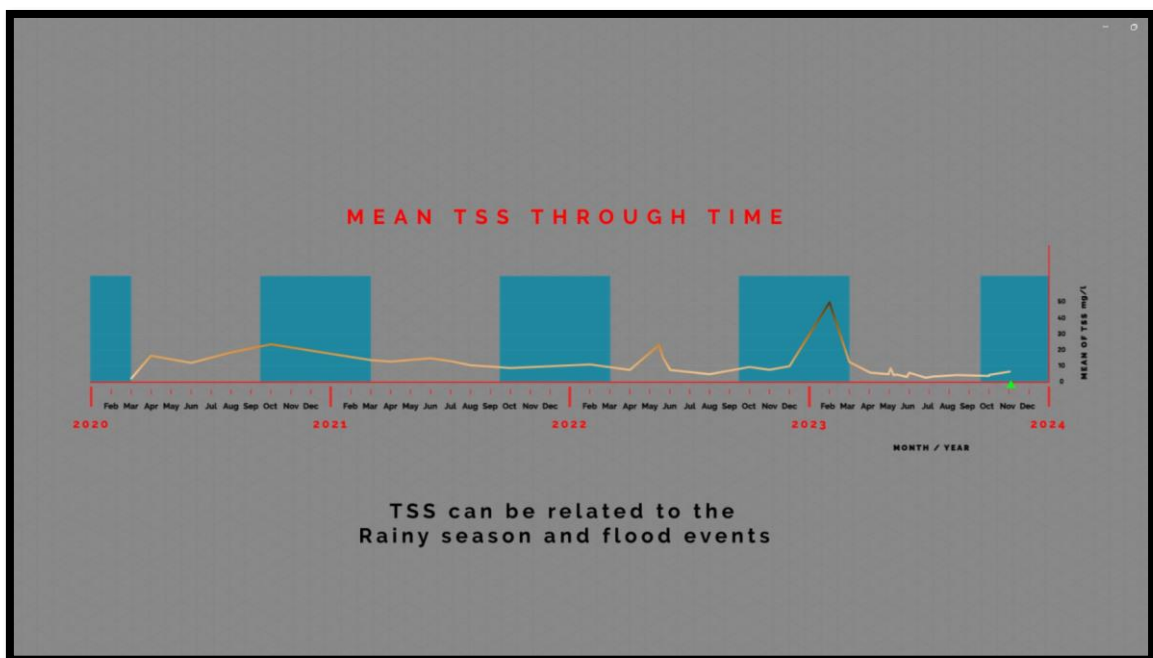


Figure 67: Map animation graph.

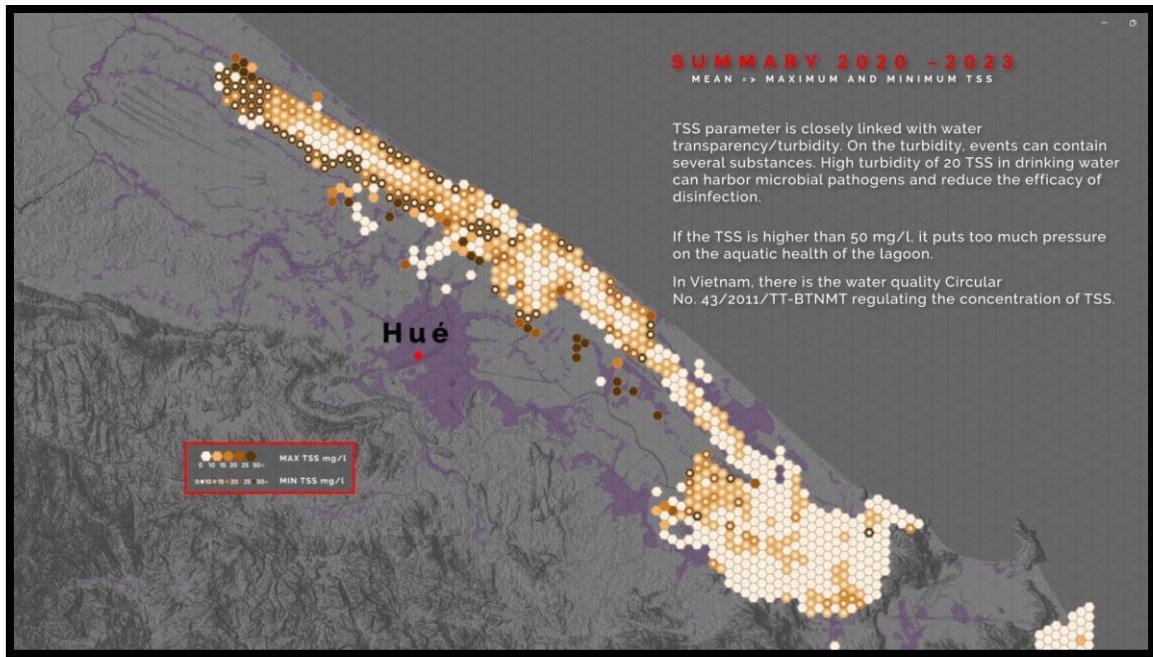


Figure 68: Map animation summary.

7 DISCUSSION

In the following chapter, it will be discussed the results and some of the challenges faced during the thesis. First, will be discussed the analytical part, after, the statistics discussion is done to compare in-situ versus satellite data, and finally, the geovisualization outcomes are discussed.

7.1 WATER QUALITY RETRIVAL ANALISIS

Water quality retrieval for inland water is a field that is still under study and has many variables to consider. One of the key factors in the analysis for shallow waters is the bottom of the water body, which is diverse, this type of water has a large benthonic and algal population, and the substrate is diverse. In our case, we opted to process the data as a deep-water body due to the low accuracy of the shallow-water model as it is explained in chapter 4.4 processing challenges.

A paramount aspect in the model application for water modeling is to have specific atmospheric corrections for water bodies or, customize your own. In our case, for the processing of DESIS data, level 2 is needed for the customization of the atmospheric correction. Moreover, the EnMAP images had to go through a selection and face dismissal of several images due to the sun glint. All these issues affected the inaccuracy of results during the processing (Next year, DLR will start to build a new atmospheric correction for tropical areas specifically for water applications, being able to estimate better atmospheric effects and sun glint for DESIS and EnMAP).

The water quality parameters were calculated using WASI-AI with the module WASI-2D. There is high accuracy in the TSS and CDOM results observable in Table 11, and Table 15: Summary Accuracy of Water Quality Parameters.. Those tables depict the results for the accuracy and ambiguity of each parameter. Out of the four **parameters extracted** from the model, **three** of them (TSS, CDOM, and the Atmospheric parameter) show high accuracy and low ambiguity. This high accuracy for TSS and CDOM corroborates the findings of Gege et. al (2014), who emphasized the effectiveness of physics-based models for water quality assessment. The parameter that exhibits low accuracy and significant ambiguity in the calculation is the green algae content. The **cells highlighted in red** in Table 11 mainly represent the estimation of the green algae and show low accuracy, with R-squared errors lower than 0.40. On the other hand, we observe high accuracy in the TSS and CDOM in Table 11, Figure 49, and Figure 51. Due to the low accuracy and ambiguity of the green algae extracted parameters, it has not been trusted as an accurate representation of the green algae content and distribution of the lagoon. The results are not going to be discussed in depth for the lack of accuracy.

Table 15: Summary Accuracy of Water Quality Parameters.

Parameter	R-squared	RMSD	Accuracy	Ambiguity
TSS	0.95	0.37	High	Low
CDOM	0.92	0.12	High	Low
Green Algae	0.039	1.5	Low	High

The following lines discuss the parameters that are accurate with other trusted fonts to highlight the concentration of the results. The Table 16 statistical summary of the results of the three parameters is the following:

Table 16: Summary of results extracted from every parameter.

Parameter	Min all images	Max all images	Mean all images	Standard deviation	Median all images	Coefficient of variation
Green algae	-1939.92	146549.50	60.47	3342.24	7.37	9.230
TSS	-7.28	543.50	7.539	41.032573	6.38	2.694
CDOM	-467.02	2525.88	3.822	165.360513	0.65	12.662

For the **green algae** concentration, the literature suggests that high concentrations of Chl-a (typically $>0.45 \mu\text{g/l}$) can indicate increased nutrient availability. The green algae mean values often exceed the $0.45 \mu\text{g/l}$ threshold, indicating periods of high nutrient availability and potential for macroalgae growth. The very high values (e.g., $146549.50 \mu\text{g/l}$ on 2023/05/07) could suggest extreme eutrophication events or data anomalies/outliers.

The mean values of **TSS** are within the acceptable range for TSS, but occasionally, high values suggest temporary water quality issues (TSS maximum values exceed 50 mg/l (e.g., 543.495789 mg/l on 2022/06/01)). The spatial distribution of TSS revealed higher values in the northern and central parts of the lagoon, correlating with areas of greater water movement and deposition. This pattern aligns with the lagoon's expected hydrodynamic behavior and emphasizes the need for targeted monitoring in these regions. We have taken into account the surface water quality Circular No. 01/2023/TT-BTNMT (phủ, 2023) to contrast the results.

The data shows high variability and some very high **CDOM** levels, which could be due to organic pollution or specific events leading to increased organic matter in the water, or outliers. The mean CDOM values vary, with some very high means like 36.705078 m^{-1} on 2023/05/06. The maximum values for CDOM also show substantial variation, with some dates showing very high CDOM levels (e.g., 2525.88 m^{-1} on 2023/05/07). CDOM concentrations were notably higher along the lagoon's borders. Similar findings have been reported in other studies, suggesting that CDOM is more concentrated near shorelines (Qiang et al., 2023). The Tam Giang Lagoon, a mixed water body, displayed CDOM values at 440 nm within expected mid-range levels for such environments. However, the mode of CDOM values across the images exceeded usual concentrations for non-salty waters, indicating a potential overestimation by the model.

Challenges in Using Inversion Models

While inversion models offer valuable insights, several challenges remain:

Accurate **atmospheric correction** is crucial for reliable model outputs, but persistent challenges remain in addressing atmospheric effects over water bodies like the sun's glint and the water vapor of the atmosphere (Kiselev et al., 2015). Specifically, due to the sun glint, a large number of images in this project have been discarded.

The high dimensionality of hyperspectral data poses challenges in data processing and analysis, requiring advanced techniques and computational resources.

Accurate calibration of inversion models requires **ground-truth data**, especially for shallow water models, which is often lacking in current studies and also in the one conducted (Maier et al., 2021). Moreover, it is essential to know how the model works and to have a learning period to understand the ambiguities that the model can face due to the physical properties being calculated.

Past water quality research in Tam Gian Lagoon

Chapter 2.8 contains past research on lagoon water quality. These studies highlight significant pollution sources and the lagoon's environmental carrying capacity (Frignani et al., 2007; Hạng et al., 2017; Thi Thu Trang et al., 2020; Trang et al., 2013). Here

highlights the key differences between the literature and the in-situ parameter concentration values used for the results in the thesis:

Turbidity: Indicated as TSS and NTU are in a similar range of values.

- **Nitrite (NO₂-):** The in-situ mean and max values are significantly lower than the literature review, indicating possibly better water quality in terms of nitrate levels in the actual data of this study's in-situ parameters.
- **Ammonium (NH₄⁺-N):** The in-situ max value is much higher than the literature review, suggesting occasional spikes in ammonium levels.
- **Biochemical Oxygen Demand (BOD₅) and Chemical Oxygen Demand (COD):** Both parameters show a wider range in in-situ measurements, with higher maximum values compared to the literature, indicating variability in organic pollution levels.
- **Coliform:** In-situ measurements show a much wider range and higher maximum value, indicating more significant contamination events compared to the literature.

However, this study relied on traditional in-situ measurements, which lacked spatial and temporal coverage. A solution to consider is hyperspectral remote sensing for water quality retrieval.

Further improvements

On the EO with hyperspectral images, there is a lack of temporal and spatial coverage. It is especially reduced due to the cloud coverage, sun glint effect, and atmosphere artifacts; this is observed in the different articles of EO. A further improvement could be the temporal sampling and the implementation of better water atmospheric corrections. Also, it would be crucial to get lagoon-based spectrums to estimate better the bottom reflectance of the lagoon in the case of implementing a water model for shallow waters.

Comprehensive models with wide and extended explanations of limitations and clear, complete, and easy-to-understand user manuals are needed. Moreover, it is crucial that the models integrate various data sources and accurately assess water quality.

One thing to point out is that next year, an improvement of the PACO atmospheric correction for tropical areas will be implemented, specifically for water applications, due to the actual lack of aerosols and water vapor correction perceived in DESIS and EnMAP images of tropical areas.

7.2 STATISTICAL ANALYSIS AND TSS VALIDATION

The statistical analysis has been realized, taking into consideration that the dates of the satellite images do not correspond to the in-situ data, so an exact comparison has not been estimated. However, the statistical comparison is done by comparing the satellite data with the most similar day available of the in-situ data. The satellite images that had in-situ data from the same month were 2022-06-01 and 2023-06-23. However, executing a Pearson correlation of the monthly dates was not conclusive due to an outlier, and there was not enough information to conclude with a statistical analysis, as can be seen in the image below Figure 69.

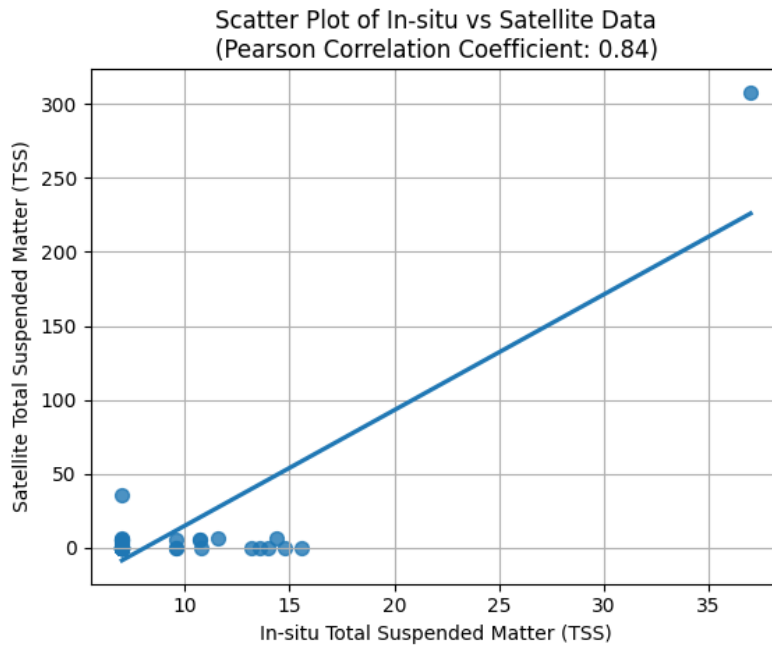


Figure 69: Scatterplot with the strict data selected and the outlier.

It was decided to exclude the outlier and include more data, as indicated in the 5.2 data point selection. The data selection resulted in the following correlation:

Comparison of satellite vs in-situ TSS data

The analysis indicates a very weak Pearson correlation coefficient (-0.032) and a low R-squared value (0.001) between in-situ and satellite TSS measurements, implying a negligible relationship between the two. The majority of the variability in satellite TSS remains unexplained by the in-situ measurements. Moreover, the high standard deviation and RMSE for satellite data signify **significant variability and error** in satellite measurements when compared to in-situ measurements. The Bland-Altman analysis also confirms substantial discrepancies between the two methods.

Results from **statistical tests**, including the paired t-test and Wilcoxon signed-rank test, show noteworthy differences between the in-situ and satellite measurements, suggesting that the two methods do not produce equivalent TSS values.

After examining the test results and comparing the satellite data with the in-situ data, it is apparent that **there is a weak correlation between the two**. As a result, it is important to consider the practical implications of these differences. While satellite data can be used to estimate in-situ TSS measurements, it is crucial to exercise caution due to the significant variability and potential errors. In particular, satellite measurements may not always accurately reflect actual in-situ conditions, especially in cases with high variability or outliers.

To address this issue, it is recommended to combine satellite data with periodic in-situ measurements for more accurate water quality assessment. This integrated approach can help validate and calibrate satellite observations, ultimately improving the reliability of remote sensing for TSS estimation.

Comparison of all the parameters vs TSS in the in-situ data

T-test suggests that there is no correlation between the different parameters and the TSS.

Spearman correlation for nonnormal distributed datasets indicates that the correlations between TSS and the other parameters are weak to moderate. This means

that the relationship is either weakly linear or potentially non-linear. Spearman correlation shows a moderate positive correlation for CDO and Fe and a moderate negative correlation for DO. It can be said that the most relatable correlation is the positive correlation between TSS and Fe due to it being superior to 0.4.

The results from the comparison of the rest of the parameters with the TSS results have a weak correlation except for Fe, which is a characteristic element for oxidized sediment that can be transported in the river. This is reflected in the positive relationship of TSS and the increase of Fe at the same time.

7.3 GEOVISUALIZATION

In the course of the thesis, the data preparation and data analysis processing took much more time than expected. For this reason, the visualization part does not implement a larger number of advanced visualization methods, but after the analysis of visualization options, the best possible one was selected (in the opinion of the author and according to expert consultations with the thesis supervisors), and this was subsequently implemented in the creation of map posters and the resulting animation. However, there are several works that focus on multivariate mapping that can provide further inspiration (not only) for visualizing hyperspectral data.

The series of maps generated for the Tam Giang Lagoon utilized the **hexagonal tessellation method** to generalize and visualize the spatial distribution of water quality parameters, including TSS and CDOM. This approach was chosen for its ability to effectively represent complex data over extensive geographic areas without overwhelming the viewer with excessive detail. The expert maps incorporated a detailed and explicit representation of the data, including bivariate mapping, hexagonal tessellation, and advanced statistical summaries, to ensure that data interpretation was precise and actionable. Specifically, a hexagonal grid of 500,000 square meters per hexagon was applied, with the mean values of TSS and CDOM calculated for each cell. This visualization technique facilitated the identification of spatial patterns and anomalies in water quality data. This allowed for a comprehensive visual analysis of water quality changes over the entire period, **incorporating statistical measures such as minimum and maximum.**

The visualization employed color scales chosen in consultation with both cartographic experts and the public. The aim was to develop a perceptual color map that accurately represents thematic layers. The brown color scale was chosen for TSS to represent turbidity, while a pink color was used for CDOM to denote organic content, and the green scale was used for green algae content. **Kristen Thyng's standardized color scale was employed for this purpose** (Enthougt, 2015). The values of the determination of the scale's values were consulted with the Vietnamese regulation and literature for a proper adjustment on the minimum and maximum. The parameter that was a little bit doubtful and that there were too many divergences in concentration values was the CDOM, so it was represented with the scale that best suited the visual representation.

Aim and target groups for geovisualization

The visualization outputs were designed to meet the specific needs of different target groups, ensuring that both technical and non-technical audiences could effectively engage with the data.

Maps for Experts

The primary objective for experts was to provide detailed insights into water quality changes that could inform policy decisions and environmental management strategies. This included individual mapping of water quality indicators like TSS, CDOM, and algae concentrations. The expert maps were designed for authorities collaborating on the FloodAdaptVN Project, such as:

- Department of Natural Resources and Environment (DONRE), Thua Thien Hue Province: Tasked with managing natural resources and environmental concerns, including land, water, and meteorological parameters (FloodAdaptVN, 2024).
- Thua Thien Hue Provincial Commanding Committee of Natural Disaster Prevention and Control, Search and Rescue (CCNDPC/SR): This committee is responsible for disaster management and integrating research findings into local planning frameworks (FloodAdaptVN, 2024).

Maps for the General Public (Animation)

The primary objective for the general public was to convey complex water quality data in a manner that was easy to understand, engaging, and accurate. The animated maps were designed to simplify complex phenomena, focusing on the essentials, limiting the information, and showing just one of the parameters. The animation targeted a broader audience, including local residents and non-expert stakeholders, who would benefit from visual, easy-to-understand representations of water quality trends in the region for their awareness of the lagoon's dynamic. This is done in Adobe After Effects to create smooth transitions and emphasize key trends over time.

Challenges in static visualization:

The research in this field was small due to the large part of the time that it took to analyze the datasets. First of all, the inconvenience of a lack of data between months and also spatially, not all the dates had full coverage in the lagoon. The lack of data is also difficult to communicate to the user.

For the multivariate mapping, the raster size and the lagoon's shape made it challenging to define a proper static map visualization. Several geovisualization methods were tested, like in Figure 66. However, after a discussion with the supervisor, it was decided to generate the outputs presented in the thesis.

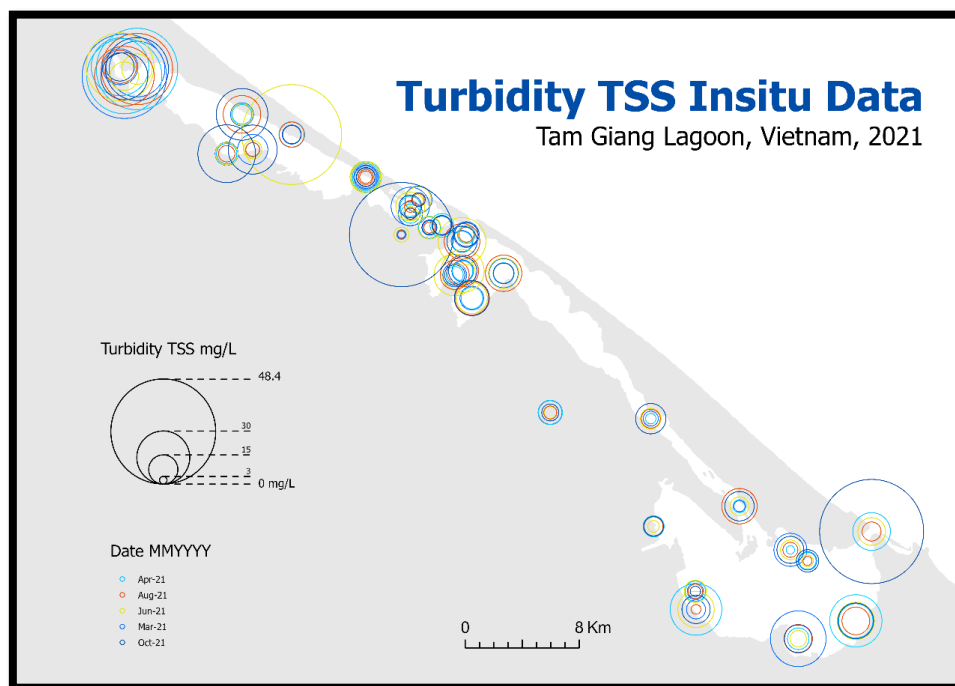


Figure 70: Sample test of a proportional map symbol to visualize the different quantities through time.

Challenges in the animation:

The animation incorporated multiple layers, including raster images, point data, polygon data, and web services that were converted to a raster format. All the layers with additional fake (to facilitate the generation of the timeline) layers were exported in

an .AIX file and transferred to Adobe After Effects. This was a big challenge as the layout and the resolution of the raster needed to be resized for a proper fit. Moreover, some of the flooding data was from a web service, and I was unable to change the color or export the data to be modified.

The overall size of the animation and the rendering time of the preview were another challenge to manage in Adobe After Effects. Another challenge was to get the fake layers between dates that were empty to have some kind of element for the exportation. All the fake layers contain a point situated in Hue City (under the actual red square Figure 71). That is the reason that against the cartographic principle, the hue city has a point for defining the center of the city even though the urban area is a big extension on the map. This solution does not follow the cartographic rules but was the best fit found to solve the fake layers needed for a correct visualization in the timeline. The transfer of such an amount of data to Adobe After Effects and the generation of a layer that was visually appealing and followed some of the cartographic rules took a lot of time and was complicated.



Figure 71: Hue City point occulting the fake layers.

The animation was a trade-off between cartographic rules, design, and a visually pleasing output. Overall, the animation tried to accomplish all the cartographic rules and be as accurate and precise as possible with the graphics and the timeline of events.

The plugin ArcGIS Maps for Adobe Creative Cloud contained so many bugs, it was temperamental and not consistent.

Future directions on geovisualization in water quality

While the static maps and animations were chosen for this project, continuous collaboration between the project and the community can explore web-based and interactive mapping solutions, provided that data sensitivity is addressed. Web maps can offer dynamic updates and enhanced user interactivity, beneficial for continuous monitoring efforts and getting in line with the digital twin direction. Also, future projects could explore integrating real-time data feeds, such as Internet of Things based water quality sensors, to provide up-to-the-minute insights into water quality dynamics (O. Ighalo et al., 2020).

Another topic to be further explored is advanced multivariate mapping techniques. Those could offer even more comprehensive visualizations, capturing the interactions between multiple water quality parameters, even though further exploration of raster data would be needed (John Nelson Maps, 2021). Another factor for further studies could be the engagement of color scales for a better understanding of water quality parameters and an agreement on standardized regulations for remote sensing parameters for the ecological health of the lagoon.

NOTE: Length of the text part of the thesis

The length of the text part exceeds the scope of the assignment. The reason for this is the large number of tables and figures, which would not be appropriate for the sake of clarity and comprehensibility to be moved to the appendices of the thesis. The increased length has been consulted with the thesis supervisor and has been assessed as adequate for the stated purpose.

8 CONCLUSION

Water quality in inland bodies is a critical environmental indicator and resource that provides essential ecosystem services, including sustaining biodiversity, supporting agriculture, and enabling recreational activities. The increasing levels of pollutants and the impact of human activities on water bodies have prompted significant research into water quality dynamics. Despite advancements in environmental monitoring, Tam Giang Lagoon remains under-monitored for its size, accessibility challenges, and limited technological infrastructure. The Tam Giang Lagoon is a vital ecosystem, representing the largest coastal lagoon in Southeast Asia, yet it faces threats from pollution and sedimentation that require continuous monitoring and management. In this context, Earth Observation (EO) technologies, combined with hyperspectral data analysis, offer a promising approach to enhance our understanding and management of such complex aquatic ecosystems.

Motivated by this need, this thesis focused on developing a comprehensive methodology for assessing water quality parameters in the Tam Giang Lagoon using hyperspectral remote sensing images of EnMAP, and DESIS from 2021 to 2023 and inversion models. The objective was to retrieve and analyze key water quality indicators, including TSS, CDOM, and green algae concentrations, by experimenting with the capabilities of WASI-AI software based on neural network training and the WASI-2D module. The thesis also aimed to explore the geovisualization techniques to effectively communicate these complex datasets to both expert and non-expert audiences.

The water quality analysis revealed significant spatial patterns and temporal trends in TSS and CDOM, indicating areas on the central-north of the lagoon and the borders of the lagoon, respectively, of concern and potential management focus within the lagoon for higher concentrations. Despite the challenge faced in retrieving accurate data for green algae concentrations due to the model, the study successfully highlighted the importance of atmospheric corrections and model calibration for enhancing the accuracy of remote sensing data in aquatic environments. The statistical analysis underscored the complexity of correlating satellite data with in-situ measurements, emphasizing the need for data validation of the same data for a robust water quality assessment.

In terms of geovisualization, the development of static maps and animations provided a multifaceted approach to disseminating water quality information. The hexagonal tessellation method facilitated a clear representation of water quality parameters, while animations offered an engaged way to visualize changes over time. The visualization outputs were tailored for specific target groups, applying techniques of user-centric design with detailed maps for experts to aid in decision-making and simplified and guided animations for the general public to raise awareness of the lagoon's dynamics.

In conclusion, this thesis represents a significant step in utilizing Hyperspectral EO and geovisualization to enhance water quality monitoring in the Tam Giang Lagoon. It demonstrates the potential of combining EO technologies with in-situ data analysis and visualization techniques to provide actionable insights for aquatic ecosystems. As the methodologies and tools developed in this study are open and adaptable, they can be extended and refined for future research and applied in other regions. It is a fact that this work will contribute to increased awareness and understanding of water quality issues, prompting more informed management and conservation efforts in the Vietnamese entities that it will be shared with. The next steps involve refining the inversion models, validating the accuracy of retrieved data, and expanding the visualization capabilities to incorporate more multivariate maps, real-time data feeds, and interactive web-based platforms if it is agreed with the data providers.

REFERENCES AND INFORMATION SOURCES

- Advanced Cartography* | University of Kentucky College of Arts & Sciences. (n.d.). Retrieved 2 August 2024, from <https://www.as.uky.edu/advanced-cartography-1>
- AI Voices—NaturalReader Home*. (n.d.). Retrieved 8 August 2024, from <https://www.naturalreaders.com/>
- Albert, A., & Mobley, C. D. (2003). An analytical model for subsurface irradiance and remote sensing reflectance in deep and shallow case-2 waters. *Optics Express*, *11*(22), 2873–2890. <https://doi.org/10.1364/OE.11.002873>
- Aquaculture of the Tam Giang-Cau Hai lagoon* | FloodAdaptVN. (n.d.-a). Retrieved 11 March 2024, from https://floodadapt.eoc.dlr.de/results/05_Aquaculture/index.html
- Aquaculture of the Tam Giang-Cau Hai lagoon* | FloodAdaptVN. (n.d.-b). Retrieved 8 March 2024, from https://floodadapt.eoc.dlr.de/results/05_Aquaculture/index.html
- Balla, D., Zichar, M., Kiss, E., Szabó, G., & Mester, T. (2022). Possibilities for Assessment and Geovisualization of Spatial and Temporal Water Quality Data Using a WebGIS Application. *ISPRS International Journal of Geo-Information*, *11*(2), Article 2. <https://doi.org/10.3390/ijgi11020108>
- Balla, D., Zichar, M., Tóth, R., Kiss, E., Karancsi, G., & Mester, T. (2020). Geovisualization Techniques of Spatial Environmental Data Using Different Visualization Tools. *Applied Sciences*, *10*(19), Article 19. <https://doi.org/10.3390/app10196701>
- Barnsley, M., Settle, J., Cutter, M., Lobb, D., & Teston, F. (2004). The PROBA/CHRIS mission: A low-cost smallsat for hyperspectral multiangle observations of the Earth surface and atmosphere. *IEEE T. Geoscience and Remote Sensing*, *42*, 1512–1520.
- Battersby, S. E., & Goldsberry, K. P. (2010). Considerations in Design of Transition Behaviors for Dynamic Thematic Maps. *Cartographic Perspectives*, *65*, Article 65. <https://doi.org/10.14714/CP65.127>
- Braga, F., Fabbretto, A., Vanhellefont, Q., Bresciani, M., Giardino, C., Scarpa, G. M., Manfè, G., Concha, J. A., & Brando, V. E. (2022). Assessment of PRISMA water reflectance using autonomous hyperspectral radiometry. *ISPRS Journal of Photogrammetry and Remote Sensing*, *192*, 99–114. <https://doi.org/10.1016/j.isprsjprs.2022.08.009>
- Brando, V., & Dekker, A. (2003). Satellite hyperspectral remote sensing for estimating estuarine and coastal water quality. *Geoscience and Remote Sensing, IEEE Transactions On*, *41*, 1378–1387. <https://doi.org/10.1109/TGRS.2003.812907>
- Brezonik, P. L., Olmanson, L. G., Finlay, J. C., & Bauer, M. E. (2015). Factors affecting the measurement of CDOM by remote sensing of optically complex inland waters. *Remote Sensing of Environment*, *157*, 199–215. <https://doi.org/10.1016/j.rse.2014.04.033>
- Brocca, L., Barbetta, S., Camici, S., Ciabatta, L., Dari, J., Filippucci, P., Massari, C., Modanesi, S., Tarpanelli, A., Vreugdenhil, M., Alfieri, L., Avanzi, F., Rains, D., Miralles, D. G., Domeneghetti, A., Castelli, M., & Camps-Valls, G. (2024). A Digital Twin of the terrestrial water cycle: A glimpse into the future through high-resolution Earth observations. *Frontiers in Science*, *1*. <https://doi.org/10.3389/fsci.2023.1190191>
- Bulgarelli, B., Kisselev, V. B., & Roberti, L. (1999). Radiative transfer in the atmosphere-ocean system: The finite-element method. *Applied Optics*, *38*(9), 1530–1542. <https://doi.org/10.1364/ao.38.001530>

Capolupo, A., Monterisi, C., Spasiano, D., Ferraro, A., Mali, M., Fratino, U., & Tarantino, E. (2022). A WebGIS Prototype for Visualizing and Monitoring the Spatio-temporal Changes in Seawater Quality. In O. Gervasi, B. Murgante, S. Misra, A. M. A. C. Rocha, & C. Garau (Eds.), *Computational Science and Its Applications – ICCSA 2022 Workshops* (pp. 340–353). Springer International Publishing. https://doi.org/10.1007/978-3-031-10545-6_24

Chidiac, S., El Najjar, P., Ouaini, N., El Rayess, Y., & El Azzi, D. (2023). A comprehensive review of water quality indices (WQIs): History, models, attempts and perspectives. *Re/Views in Environmental Science and Bio/Technology*, 22(2), 349–395. <https://doi.org/10.1007/s11157-023-09650-7>

Chowdary, V. M., Ramakrishnan, D., Srivastava, Y. K., Chandran, V., & Jeyaram, A. (2009). Integrated Water Resource Development Plan for Sustainable Management of Mayurakshi Watershed, India using Remote Sensing and GIS. *Water Resources Management*, 23(8), 1581–1602. <https://doi.org/10.1007/s11269-008-9342-9>

Colab.google. (n.d.). Colab.Google. Retrieved 28 July 2024, from <http://0.0.0.0:8080/>

de los Reyes, R., Langheinrich, M., Schwind, P., Richter, R., Pflug, B., Bachmann, M., Müller, R., Carmona, E., Zekoll, V., & Reinartz, P. (2020). PACO: Python-Based Atmospheric Correction. *Sensors*, 20(5), Article 5. <https://doi.org/10.3390/s20051428>

De'ath, G., & Fabricius, K. (2010). Water quality as a regional driver of coral biodiversity and macroalgae on the Great Barrier Reef. *Ecological Applications*, 20(3), 840–850. <https://doi.org/10.1890/08-2023.1>

Dekker, A. G., Phinn, S. R., Anstee, J., Bissett, P., Brando, V. E., Casey, B., Fearn, P., Hedley, J., Klonowski, W., Lee, Z. P., Lynch, M., Lyons, M., Mobley, C., & Roelfsema, C. (2011). Intercomparison of shallow water bathymetry, hydro-optics, and benthos mapping techniques in Australian and Caribbean coastal environments. *Limnology and Oceanography: Methods*, 9(9), 396–425. <https://doi.org/10.4319/lom.2011.9.396>

Desktop GIS Software | Mapping Analytics | ArcGIS Pro. (n.d.). Retrieved 28 July 2024, from <https://www.esri.com/en-us/arcgis/products/arcgis-pro/overview>

Devlin, M., & Brodie, J. (2023). Nutrients and Eutrophication. In A. Reichelt-Brushett (Ed.), *Marine Pollution – Monitoring, Management and Mitigation* (pp. 75–100). Springer Nature Switzerland. https://doi.org/10.1007/978-3-031-10127-4_4

DiBiase, D., MacEachren, A. M., Krygier, J. B., & Reeves, C. (1992). Animation and the Role of Map Design in Scientific Visualization. *Cartography and Geographic Information Systems*, 19(4), 201–214. <https://doi.org/10.1559/152304092783721295>

Dierssen, H. M., Gierach, M., Guild, L. S., Mannino, A., Salisbury, J., Schollaert Uz, S., Scott, J., Townsend, P. A., Turpie, K., Tzortziou, M., Urquhart, E., Vandermeulen, R., & Werdell, P. J. (2023). Synergies Between NASA's Hyperspectral Aquatic Missions PACE, GLIMR, and SBG: Opportunities for New Science and Applications. *Journal of Geophysical Research: Biogeosciences*, 128(10), e2023JG007574. <https://doi.org/10.1029/2023JG007574>

Disperati, L., & Viridis, S. G. P. (2015). Assessment of land-use and land-cover changes from 1965 to 2014 in Tam Giang-Cau Hai Lagoon, central Vietnam. *Applied Geography*, 58, 48–64. <https://doi.org/10.1016/j.apgeog.2014.12.012>

Downloads | Notepad++. (n.d.). Retrieved 25 July 2024, from <https://notepad-plus-plus.org/downloads/>

Earth Observation Graphic Bureau | ReMedia. (n.d.). Retrieved 18 April 2024, from <https://www.remediagroup.it/eogb/>

Earth Resources Observation And Science (EROS) Center. (2000). *Earth Observing One (EO-1)—Hyperion* [Tiff]. [object Object]. <https://doi.org/10.5066/P9JXHMO2>

Enthought (Director). (2015, July 10). *Perceptual Color Maps in matplotlib for Oceanography | SciPy 2015 | Kristen Thyng* [Video recording]. <https://www.youtube.com/watch?v=XjHzLUnHeM0>

Esposito, M., & Marchi, A. Z. (2019). In-orbit demonstration of the first hyperspectral imager for nanosatellites. *International Conference on Space Optics — ICSO 2018, 11180*, 760–770. <https://doi.org/10.1117/12.2535991>

FloodAdaptVN | FloodAdaptVN. (n.d.). Retrieved 30 March 2024, from <https://floodadapt.eoc.dlr.de/index.html>

Fortes, A. C. C. (2018). *Índice de qualidade de água para consumo humano: Uma proposta de ferramenta para a vigilância da qualidade da água comunicar os resultados à sociedade*. <https://www.arca.fiocruz.br/handle/icict/61969>

Fortes, A. C. C., Barrocas, P. R. G., & Kligerman, D. C. (2023). Water quality indices: Construction, potential, and limitations. *Ecological Indicators*, *157*, 111187. <https://doi.org/10.1016/j.ecolind.2023.111187>

Free Online Spreadsheet Software: Excel | Microsoft 365. (n.d.). Retrieved 28 July 2024, from <https://www.microsoft.com/en-us/microsoft-365/excel>

Frignani, M., Piazza, R., Bellucci, L. G., Cu, N. H., Zangrando, R., Albertazzi, S., Moret, I., Romano, S., & Gambaro, A. (2007). Polychlorinated biphenyls in sediments of the Tam Giang-Cau Hai Lagoon, Central Vietnam. *Chemosphere*, *67*(9), 1786–1793. <https://doi.org/10.1016/j.chemosphere.2006.05.119>

GCP/VIE/029/ITA - IMOLA Project Integrated Management of Lagoon Activities in Tam Giang Cau Hai Lagoon (Thua Thien Hue Province) (Phase 1). (n.d.).

Gege, P. (2002). *Error propagation at inversion of irradiance reflectance spectra in case-2 waters*.

Gege, P. (2004). The water color simulator WASI: An integrating software tool for analysis and simulation of optical in situ spectra. *Computers & Geosciences*, *30*(5), 523–532. <https://doi.org/10.1016/j.cageo.2004.03.005>

Gege, P. (2014). WASI-2D: A software tool for regionally optimized analysis of imaging spectrometer data from deep and shallow waters. *Computers & Geosciences*, *62*, 208–215. <https://doi.org/10.1016/j.cageo.2013.07.022>

Gholizadeh, M. H., Melesse, A. M., & Reddi, L. (2016a). A Comprehensive Review on Water Quality Parameters Estimation Using Remote Sensing Techniques. *Sensors*, *16*(8), Article 8. <https://doi.org/10.3390/s16081298>

Gholizadeh, M. H., Melesse, A. M., & Reddi, L. (2016b). A Comprehensive Review on Water Quality Parameters Estimation Using Remote Sensing Techniques. *Sensors*, *16*(8), Article 8. <https://doi.org/10.3390/s16081298>

Giardino, C., Brando, V. E., Dekker, A. G., Strömbeck, N., & Candiani, G. (2007). Assessment of water quality in Lake Garda (Italy) using Hyperion. *Remote Sensing of Environment*, *109*(2), 183–195. <https://doi.org/10.1016/j.rse.2006.12.017>

Giardino, C., Brando, V. E., Gege, P., Pinnel, N., Hochberg, E., Knaeps, E., Reusen, I., Doerffer, R., Bresciani, M., Braga, F., Foerster, S., Champollion, N., & Dekker, A. (2019). Imaging Spectrometry of Inland and Coastal Waters: State of the Art, Achievements and Perspectives. *Surveys in Geophysics*, *40*(3), 401–429. <https://doi.org/10.1007/s10712-018-9476-0>

Giardino, C., Bresciani, M., Braga, F., Cazzaniga, I., De Keukelaere, L., Knaeps, E., & Brando, V. E. (2017). Chapter 5—Bio-optical Modeling of Total Suspended Solids. In D. R. Mishra, I. Ogashawara, & A. A. Gitelson (Eds.), *Bio-optical Modeling and Remote Sensing of Inland Waters* (pp. 129–156). Elsevier. <https://doi.org/10.1016/B978-0-12-804644-9.00005-7>

Giardino, C., Bresciani, M., Braga, F., Fabbretto, A., Ghirardi, N., Pepe, M., Gianinetto, M., Colombo, R., Cogliati, S., Ghebrehiwot, S., Laanen, M., Peters, S., Schroeder, T., Concha, J. A., & Brando, V. E. (2020). First Evaluation of PRISMA Level 1 Data for Water Applications. *Sensors*, *20*(16), Article 16. <https://doi.org/10.3390/s20164553>

Giardino, C., Candiani, G., Bresciani, M., Lee, Z., Gagliano, S., & Pepe, M. (2012). BOMBER: A tool for estimating water quality and bottom properties from remote sensing images. *Computers & Geosciences*, *45*, 313–318. <https://doi.org/10.1016/j.cageo.2011.11.022>

Giuliani, S., Romano, S., Turetta, C., Cu, N. H., Bellucci, L. G., Capodaglio, G., Mugnai, C., Nhon, D. H., & Frignani, M. (2011). Soils and sediments of the Thua Thien-Hue Province (central Vietnam): Recognizing trace element sources and the likely influence of natural events. *Journal of Environmental Monitoring*, *13*(5), 1383–1392. <https://doi.org/10.1039/C0EM00706D>

Global Flood Monitoring. (n.d.). Retrieved 17 July 2024, from <https://portal.gfm.eodc.eu/>

Goal 6 | *Department of Economic and Social Affairs*. (n.d.). Retrieved 7 August 2024, from <https://sdgs.un.org/goals/goal6>

Gorman, E. T., Kubalak, D. A., Patel, D., Dress, A., Mott, D. B., Meister, G., & Werdell, P. J. (2019). The NASA Plankton, Aerosol, Cloud, ocean Ecosystem (PACE) mission: An emerging era of global, hyperspectral Earth system remote sensing. *Sensors, Systems, and Next-Generation Satellites XXIII*, *11151*, 78–84. <https://doi.org/10.1117/12.2537146>

Goyens, C., Lavigne, H., Dille, A., & Vervaeren, H. (2022). Using Hyperspectral Remote Sensing to Monitor Water Quality in Drinking Water Reservoirs. *Remote Sensing*, *14*(21), Article 21. <https://doi.org/10.3390/rs14215607>

Guanter, L., Kaufmann, H., Segl, K., Foerster, S., Rogass, C., Chabrillat, S., Kuester, T., Hollstein, A., Rossner, G., Chlebek, C., Straif, C., Fischer, S., Schrader, S., Storch, T., Heiden, U., Mueller, A., Bachmann, M., Mühle, H., Müller, R., ... Sang, B. (2015). The EnMAP Spaceborne Imaging Spectroscopy Mission for Earth Observation. *Remote Sensing*, *7*(7), Article 7. <https://doi.org/10.3390/rs70708830>

Gurlin, D. (n.d.). *NEAR INFRARED-RED MODELS FOR THE REMOTE ESTIMATION OF CHLOROPHYLL-a CONCENTRATION IN OPTICALLY COMPLEX TURBID PRODUCTIVE WATERS: FROM IN SITU MEASUREMENTS TO AERIAL IMAGERY*.

Hằng, P., Chăn, M., Nguyen, S., & Le, A. T. (2017, April 5). *Proposal for solutions for reasonable use of natural resources and environmental protection of Tam Giang—Cau Hai lagoon area in Thua Thien—Hue province*.

Heege, T., Kiselev, V., Wettle, M., & Nguyen Nghia, H. (2014). Operational multi-sensor monitoring of turbidity for the entire Mekong Delta. *International Journal of Remote Sensing*, *35*, 2910–2926. <https://doi.org/10.1080/01431161.2014.890300>

Hestir, E. L., Brando, V. E., Bresciani, M., Giardino, C., Matta, E., Villa, P., & Dekker, A. G. (2015). Measuring freshwater aquatic ecosystems: The need for a hyperspectral global mapping satellite mission. *Remote Sensing of Environment*, *167*, 181–195. <https://doi.org/10.1016/j.rse.2015.05.023>

- Hirai, Y., Nguyen, V. L., Ta, T., ヒライユキヒロ, & 幸弘平井. (2008, March 1). *Assessment of impacts of sea level rise on Tam Giang-Cau Hai lagoon area based on a geomorphological survey map*. <https://www.semanticscholar.org/paper/Assessment-of-impacts-of-sea-level-rise-on-Tam-Hai-Hirai-Nguyen/1b76f6017b0e245de4a38e2ae98b5e69d81f7224>
- Information package & Course catalogue*. (n.d.). Retrieved 2 August 2024, from <https://stag.tul.cz/ects/fakulty/FP/KGD/PKR?lang=en>
- Installation—EnPT 0.20.1 documentation*. (n.d.). Retrieved 1 April 2024, from https://enmap.git-pages.gfz-potsdam.de/GFZ_Tools_EnMAP_BOX/EnPT/doc/installation.html#installing-enpt-along-with-qgis-and-the-enmap-box-backend-gui
- Irina Fabrikant, S., Rebich-Hespanha, S., Andrienko, N., Andrienko, G., & Montello, D. R. (2008). Novel Method to Measure Inference Affordance in Static Small-Multiple Map Displays Representing Dynamic Processes. *The Cartographic Journal*, 45(3), 201–215. <https://doi.org/10.1179/000870408X311396>
- itsupport. (2023, July 24). *GIS For Water Resource & Watershed Management*. SGL. <https://www.sglgis.com/gis-for-water-resource/>
- Jia, J., Chen, J., Zheng, X., Wang, Y., Guo, S., Sun, H., Jiang, C., Karjalainen, M., Karila, K., Duan, Z., Wang, T., Xu, C., Hyyppä, J., & Chen, Y. (2021). Tradeoffs in the Spatial and Spectral Resolution of Airborne Hyperspectral Imaging Systems: A Crop Identification Case Study. *IEEE Transactions on Geoscience and Remote Sensing*, PP, 1–18. <https://doi.org/10.1109/TGRS.2021.3096999>
- JICA 報告書 PDF 版(JICA Report PDF). (n.d.). Retrieved 30 June 2024, from <https://openjicareport.jica.go.jp/>
- John Nelson Maps (Director). (2021). *Million and One Ways to Make a Multivariate Map* [Video recording]. <https://www.youtube.com/watch?v=8WuEHBq4oM>
- Kallio, K. (2007). *Remote Sensing as a Tool For Monitoring Lake Water Quality* (pp. 237–245). <https://doi.org/10.1002/9780470511121.ch20>
- Kenneth Field,. (n.d.). *Cartography. The Definitive Guide to Making Maps* | Esri Press. ESRI Press. Retrieved 29 March 2024, from <https://www.esri.com/en-us/esri-press/browse/cartography-the-definitive-guide-to-making-maps>
- Kirk, J. (2010). Light and Photosynthesis in Aquatic Systems. *Light and Photosynthesis in Aquatic Ecosystems, Third Edition, Vol. VI*, 1–651. <https://doi.org/10.1017/CBO9781139168212>
- Kiselev, V., Bulgarelli, B., & Heege, T. (2015). Sensor independent adjacency correction algorithm for coastal and inland water systems. *Remote Sensing of Environment*, 157, 85–95. <https://doi.org/10.1016/j.rse.2014.07.025>
- Kiss, E., Zichar, M., Fazekas, I., Karancsi, G., & Balla, D. (2020). Categorization and geovisualization of climate change strategies using an open-access WebGIS tool. *Infocommunications Journal*, 12(1), 32–37. <https://doi.org/10.36244/ICJ.2020.1.5>
- Kisselev, V. B., Roberti, L., & Perona, G. (1994). An application of the finite element method to the solution of the radiative transfer equation. *Journal of Quantitative Spectroscopy and Radiative Transfer*, 51(4), 603–614. [https://doi.org/10.1016/0022-4073\(94\)90114-7](https://doi.org/10.1016/0022-4073(94)90114-7)
- Koleva, R., Zaev, E., Babunski, D., Rath, G., & Ninevski, D. (2023). IoT System for Real-Time Water Quality Measurement and Data Visualization. *2023 12th*

Mediterranean Conference on Embedded Computing (MECO), 1–4.
<https://doi.org/10.1109/MECO58584.2023.10155050>

Kou, L., Labrie, D., & Chylek, P. (1993). Refractive indices of water and ice in the 0.65- to 2.5- μm spectral range. *Applied Optics*, 32(19), 3531–3540.
<https://doi.org/10.1364/AO.32.003531>

Kraak, M.-J., & Ormeling, F. J. (2013). *Cartography: Visualization of Spatial Data*. Routledge.

Krassanakis, V., Skopeliti, A., Keskin, M., & Cybulski, P. (2023). Geovisualization: Current Trends, Challenges, and Applications. *Geographies*, 3(4), Article 4.
<https://doi.org/10.3390/geographies3040043>

Krutz, D., Müller, R., Knodt, U., Günther, B., Walter, I., Sebastian, I., Säuberlich, T., Reulke, R., Carmona, E., Eckardt, A., Venus, H., Fischer, C., Zender, B., Arloth, S., Lieder, M., Neidhardt, M., Grote, U., Schrandt, F., Gelmi, S., & Wojtkowiak, A. (2019). The Instrument Design of the DLR Earth Sensing Imaging Spectrometer (DESIS). *Sensors*, 19(7), Article 7. <https://doi.org/10.3390/s19071622>

Kutser, T., Koponen, S., Kallio, K. Y., Fincke, T., & Paavel, B. (2017). Chapter 4—Bio-optical Modeling of Colored Dissolved Organic Matter. In D. R. Mishra, I. Ogashawara, & A. A. Gitelson (Eds.), *Bio-optical Modeling and Remote Sensing of Inland Waters* (pp. 101–128). Elsevier. <https://doi.org/10.1016/B978-0-12-804644-9.00004-5>

Kutser, T., Paavel, B., Verpoorter, C., Ligi, M., Soomets, T., Toming, K., & Casal, G. (2016). Remote Sensing of Black Lakes and Using 810 nm Reflectance Peak for Retrieving Water Quality Parameters of Optically Complex Waters. *Remote Sensing*, 8(6), Article 6. <https://doi.org/10.3390/rs8060497>

Kutser, T., Pierson, D. C., Kallio, K. Y., Reinart, A., & Sobek, S. (2005). Mapping lake CDOM by satellite remote sensing. *Remote Sensing of Environment*, 94(4), 535–540.
<https://doi.org/10.1016/j.rse.2004.11.009>

Lee, Z., Carder, K. L., & Arnone, R. A. (2002). Deriving inherent optical properties from water color: A multiband quasi-analytical algorithm for optically deep waters. *Applied Optics*, 41(27), 5755–5772. <https://doi.org/10.1364/AO.41.005755>

Lehmann, M. K., Gurlin, D., Pahlevan, N., Alikas, K., Conroy, T., Anstee, J., Balasubramanian, S. V., Barbosa, C. C. F., Binding, C., Bracher, A., Bresciani, M., Burtner, A., Cao, Z., Dekker, A. G., Di Vittorio, C., Drayson, N., Errera, R. M., Fernandez, V., Ficek, D., ... Yue, L. (2023). GLORIA - A globally representative hyperspectral in situ dataset for optical sensing of water quality. *Scientific Data*, 10(1), 100. <https://doi.org/10.1038/s41597-023-01973-y>

Lewis, M. D., Gould, R. W., Arnone, R. A., Lyon, P. E., Martinolich, P. M., Vaughan, R., Lawson, A., Scardino, T., Hou, W., Snyder, W., Lucke, R., Corson, M., Montes, M., & Davis, C. (2009). The Hyperspectral Imager for the Coastal Ocean (HICO): Sensor and data processing overview. *OCEANS 2009*, 1–9.
<https://doi.org/10.23919/OCEANS.2009.5422336>

Li, S., Zhang, J., Mu, G., Ju, H., Rui, W., Li, D., & Shabbir, A. (2016). Spatiotemporal Characterization of Chromophoric Dissolved Organic Matter (CDOM) and CDOM-DOC Relationships for Highly Polluted Rivers. *Water*, 8, 399.
<https://doi.org/10.3390/w8090399>

Liu, Y.-N., Sun, D.-X., Hu, X.-N., Ye, X., Li, Y.-D., Liu, S.-F., Cao, K.-Q., Chai, M.-Y., Zhou, W.-Y.-N., Zhang, J., Zhang, Y., Sun, W.-W., & Jiao, L.-L. (2019). The Advanced Hyperspectral Imager: Aboard China's GaoFen-5 Satellite. *IEEE Geoscience and Remote Sensing Magazine*, 7(4), 23–32. *IEEE Geoscience and Remote Sensing Magazine*. <https://doi.org/10.1109/MGRS.2019.2927687>

- Loizzo, R., Guarini, R., Longo, F., Scopa, T., Formaro, R., Facchinetti, C., & Varacalli, G. (2018). Prisma: The Italian Hyperspectral Mission. *IGARSS 2018 - 2018 IEEE International Geoscience and Remote Sensing Symposium*, 175–178. <https://doi.org/10.1109/IGARSS.2018.8518512>
- Luong, C., Tien, D., & Nga, N. (2020). Hydrophyte communities in the Tam Giang—Cau Hai lagoon. *Tạp Chí Khoa Học và Công Nghệ Biển*, 20, 199–208. <https://doi.org/10.15625/1859-3097/20/2/12965>
- Ma, T., Zhang, D., Li, X., Huang, Y., Zhang, L., Zhu, Z., Sun, X., Lan, Z., & Guo, W. (2023). Hyperspectral remote sensing technology for water quality monitoring: Knowledge graph analysis and Frontier trend. *Frontiers in Environmental Science*, 11. <https://doi.org/10.3389/fenvs.2023.1133325>
- MacEachren, A., & Kraak, J. A. (2001). Research challenges in geovisualization. *Cartography Geograph. Inf. Sci*, 28, 3–12.
- Mahmoud, S. H., S. Ahmed, S., Zhu, D. Z., Gan, T. Y., Loewen, M. R., van Duin, B., & Mahmood, K. (2023). Monitoring the spatial distribution of water quality of an urban stormwater pond using satellite images. *Ecological Informatics*, 77, 102205. <https://doi.org/10.1016/j.ecoinf.2023.102205>
- Mai, G., Huang, W., Cai, L., Zhu, R., & Lao, N. (2022). Narrative Cartography with Knowledge Graphs. *Journal of Geovisualization and Spatial Analysis*, 6(1), 4. <https://doi.org/10.1007/s41651-021-00097-4>
- Maier, P. M., Keller, S., & Hinz, S. (2021). Deep Learning with WASI Simulation Data for Estimating Chlorophyll a Concentration of Inland Water Bodies. *Remote Sensing*, 13(4), Article 4. <https://doi.org/10.3390/rs13040718>
- MAP Animations—YouTube. (n.d.). Retrieved 29 July 2024, from <https://www.youtube.com/playlist?list=PLm8wGDhHPmWwRnWwbbEbtZr55yI3c72CT>
- Marek Pieniążek. (2014). *Graficzna prezentacja danych statystycznych Wykresy, mapy, GIS*. <https://stat.gov.pl/statystyka-regionalna/publikacje-regionalne/podreczniki-atlasy/podreczniki/graficzna-prezentacja-danych-statystycznych-wykresy-mapy-gis,2,1.html>
- Martinrapilly/PRISMA2GeoTIFF: Python script to convert he5 PRISMA file to a GeoTIFF. (n.d.). Retrieved 6 April 2024, from <https://github.com/martinrapilly/PRISMA2GeoTIFF/tree/main>
- Matsunaga, T., Iwasaki, A., Tsuchida, S., Iwao, K., Tanii, J., Kashimura, O., Nakamura, R., Yamamoto, H., Kato, S., Obata, K., Mouri, K., & Tachikawa, T. (2019). HISUI Status Toward 2020 Launch. *IGARSS 2019 - 2019 IEEE International Geoscience and Remote Sensing Symposium*, 4495–4498. <https://doi.org/10.1109/IGARSS.2019.8899179>
- Mobley, C. (1994). Light and Water: Radiative Transfer in Natural Waters. In *Academic Press*.
- Monday Maps! (n.d.). YouTube. Retrieved 29 July 2024, from <http://www.youtube.com/playlist?list=PLAKq3CHj8bHhRtWLn5VxrrVB2Iz5QUGJl>
- Morel, A. (1974)—IOCCG. (n.d.). Retrieved 6 July 2024, from <https://ioccg.org/bibliography/morel-a-1974/>
- Morel, A. Y., & Gordon, H. R. (1980). Report of the working group on water color. *Boundary-Layer Meteorology*, 18(3), 343–355. <https://doi.org/10.1007/BF00122030>

Motion Graphics Efficiency and VR Features at the Core of What's New in After Effects CC. (2017, October 18). *Adobe.Com*. <https://blogs.adobe.com/creativecloud/motion-graphics-efficiency-and-vr-features-at-the-core-of-whats-new-in-after-effects-cc/>

Müller, R. (n.d.). *ATBD L1A, L1B, L1C, L2A Processors. 1*.

Nghiem, L., Stive, M., Verhagen, H., & Wang, Z. B. (2007). Morphodynamics of Hue tidal inlets, Vietnam. *Asian and Pacific Coasts Conference, September 21-24, 2007, Nanjing, China*.

Nima, C., Frette, Ø., Hamre, B., Stamnes, J. J., Chen, Y.-C., Sørensen, K., Norli, M., Lu, D., Xing, Q., Muyimbwa, D., Ssenyonga, T., Stamnes, K. H., & Erga, S. R. (2019). CDOM Absorption Properties of Natural Water Bodies along Extreme Environmental Gradients. *Water, 11*(10), Article 10. <https://doi.org/10.3390/w11101988>

Niroumand-Jadidi, M., & Bovolo, F. (2021). WATER QUALITY RETRIEVAL AND ALGAL BLOOM DETECTION USING HIGH-RESOLUTION CUBESAT IMAGERY. *ISPRS Annals of the Photogrammetry, Remote Sensing and Spatial Information Sciences, V-3-2021*, 191–195. XXIV ISPRS Congress <q>Imaging today, foreseeing tomorrow</q>, Commission III - 2021 edition, 5–9 July 2021. <https://doi.org/10.5194/isprs-annals-V-3-2021-191-2021>

Niroumand-Jadidi, M., Bovolo, F., & Bruzzone, L. (2019). Novel Spectra-Derived Features for Empirical Retrieval of Water Quality Parameters: Demonstrations for OLI, MSI, and OLCI Sensors. *IEEE Transactions on Geoscience and Remote Sensing, 57*(12), 10285–10300. *IEEE Transactions on Geoscience and Remote Sensing*. <https://doi.org/10.1109/TGRS.2019.2933251>

Niroumand-Jadidi, M., Bovolo, F., Bruzzone, L., & Gege, P. (2020). Physics-based Bathymetry and Water Quality Retrieval Using PlanetScope Imagery: Impacts of 2020 COVID-19 Lockdown and 2019 Extreme Flood in the Venice Lagoon. *Remote Sensing, 12*(15), Article 15. <https://doi.org/10.3390/rs12152381>

O. Ighalo, J., Adeniyi, A., & Marques, G. (2020). Internet of Things for Water Quality Monitoring and Assessment: A Comprehensive Review. In *Studies in Computational Intelligence* (pp. 245–259). https://doi.org/10.1007/978-3-030-51920-9_13

Object, object. (n.d.). *Preliminary assessment of organochlorine pesticide residues in the sediment from several estuaries and Tam Giang—Cau Hai lagoon, Thua Thien Hue, 2005*. Retrieved 25 March 2024, from <https://core.ac.uk/reader/229043660>

Ogashawara, I., Mishra, D. R., & Gitelson, A. A. (2017). Chapter 1 - Remote Sensing of Inland Waters: Background and Current State-of-the-Art. In D. R. Mishra, I. Ogashawara, & A. A. Gitelson (Eds.), *Bio-optical Modeling and Remote Sensing of Inland Waters* (pp. 1–24). Elsevier. <https://doi.org/10.1016/B978-0-12-804644-9.00001-X>

Ogryzek, M., & Ciski, M. (2018). Cartographic Methods of Presentation the Average Transaction Prices of the Undeveloped Land. *Civil and Environmental Engineering Reports, 28*(2), 85–100. <https://doi.org/10.2478/ceer-2018-0021>

O'Shea, R. E., Pahlevan, N., Smith, B., Boss, E., Gurlin, D., Alikas, K., Kangro, K., Kudela, R. M., & Vaičiūtė, D. (2023). A hyperspectral inversion framework for estimating absorbing inherent optical properties and biogeochemical parameters in inland and coastal waters. *Remote Sensing of Environment, 295*, 113706. <https://doi.org/10.1016/j.rse.2023.113706>

Overview: Ocean Optics Web Book. (n.d.). Retrieved 25 June 2024, from <https://www.oceanopticsbook.info/view/introduction/overview>

Peters, T., Jongerius, Y. R., Franken, J. T., Ponsioen, L. A., & Tieleman, O. C. (2015). Project Hue: Report and field study on the water related problems and solutions in

and around the Cau Hai lagoon and the Tu Hien inlet, Vietnam. *Master Project Report*. <https://repository.tudelft.nl/islandora/object/uuid%3A78bd29c1-1c13-4d2e-a5c6-44ed107c19b3>

phủ C. T. tin điện tử C. (n.d.). *Thông tư số 01/2023/TT-BTNMT của Bộ Tài nguyên và Môi trường: Ban hành quy chuẩn kỹ thuật quốc gia về chất lượng môi trường xung quanh*. Retrieved 7 July 2024, from <http://vanban.chinhphu.vn/?pageid=27160&docid=207647>

Pope, R., & Fry, E. (1997). Absorption spectrum (380–700 nm) of pure water. II. Integrating cavity measurements. *Applied Optics*, 36, 8710–8723. <https://doi.org/10.1364/AO.36.008710>

Quantification of shallow water quality parameters by means of remote sensing. (n.d.). <https://doi.org/10.1191/0309133303pp357ra>

Rast, M., & Painter, T. H. (2019). Earth Observation Imaging Spectroscopy for Terrestrial Systems: An Overview of Its History, Techniques, and Applications of Its Missions. *Surveys in Geophysics*, 40(3), 303–331. <https://doi.org/10.1007/s10712-019-09517-z>

Richter, R., Heege, T., Kiselev, V., & Schläpfer, D. (2014). Correction of ozone influence on TOA radiance. *International Journal of Remote Sensing*, 35(23), 8044–8056. <https://doi.org/10.1080/01431161.2014.978041>

Ritchie, J., Zimba, P., & Everitt, J. (2003). Remote Sensing Techniques to Assess Water Quality. *Photogrammetric Engineering & Remote Sensing*, 69. <https://doi.org/10.14358/PERS.69.6.695>

Robinson, A. C., Kettunen, P., Delazari, L., & Çöltekin, A. (2023). New directions for the state of the art and science in Cartography. *International Journal of Cartography*, 9(2), 143–149. <https://doi.org/10.1080/23729333.2023.2216334>

Robinson, A. H., Morrison, J. L., Muehrcke, P. C., Kimerling, A. J., & Guptill, S. C. (1994). *Elements of Cartography*. John Wiley & Sons Australia, Limited.

Santini, F., Alberotanza, L., Cavalli, R. M., & Pignatti, S. (2010). A two-step optimization procedure for assessing water constituent concentrations by hyperspectral remote sensing techniques: An application to the highly turbid Venice lagoon waters. *Remote Sensing of Environment*, 114(4), 887–898. <https://doi.org/10.1016/j.rse.2009.12.001>

Shao, T., Zheng, H., Song, K., Zhao, Y., & Zhang, B. (2017). Influence of environmental factors on absorption characteristics of suspended particulate matter and CDOM in Liaohe River watershed, northeast China. *Environmental Science and Pollution Research*, 24(23), 19322–19337. <https://doi.org/10.1007/s11356-017-9480-9>

Software—IOCCG. (n.d.). Retrieved 23 March 2024, from <https://ioccg.org/resources/software/>

Thanh, T. D., Thaïnh, T. Ñ., Ñieãn, T. V., & Chieãn, Ñ. Ñ. (2002). *INLET CHANGE IN TAM GIANG - CAU HAI LAGOON AND COASTAL FLOOD*.

Thi Thu Trang, C., Thanh, T., Thaïnh, T., Duy Vinh, V., & Anh Tu, T. (2020). Assessment of the environmental carrying capacity of pollutants in Tam Giang-Cau Hai Lagoon (Viet Nam) and solutions for the environment protection of the lagoon. *Science of The Total Environment*, 762. <https://doi.org/10.1016/j.scitotenv.2020.143130>

- Toming, K., Kutser, T., Laas, A., Sepp, M., Paavel, B., & Nõges, T. (2016). First Experiences in Mapping Lake Water Quality Parameters with Sentinel-2 MSI Imagery. *Remote Sensing*, 8(8), Article 8. <https://doi.org/10.3390/rs8080640>
- Tran, D., Thanh, T., Van, H., Tran Dinh, L., & Thao, N. (2001). Detecting the inlet change in Tam Giang – Cau Hai lagoon, Vietnam Centre, and a contribution from remote sensing data. *Spatial Information Technology: Remote Sensing and Geographical Information Systems*, 1, 647–651.
- Tran, D., Tran Dinh, L., & Do, H. (2006). *Application of remote Sensing for coastal hazard monitoring in Tam Giang—Cau Hai Lagoon, Vietnam*.
- Tran Thanh, T. (2011). *Morphodynamics of seasonally closed coastal inlets at the central coast of Vietnam*.
- Trang, C. T. T., Thanh, T. D., & Sinh, L. X. (2013). ASSESSMENT OF POLLUTION LOAD INTO TAM GIANG - CAU HAI LAGOON AND A PREDICTION TO 2020. *Vietnam Journal of Marine Science and Technology*, 13(3), Article 3. <https://doi.org/10.15625/1859-3097/13/3/3534>
- Tversky, B., Morrison, J. B., & Betrancourt, M. (2002). Animation: Can it facilitate? *International Journal of Human-Computer Studies*, 57(4), 247–262. <https://doi.org/10.1006/ijhc.2002.1017>
- UCGIS Bok Visualizer and Search. (n.d.). UCGIS Bok Visualizer and Search. Retrieved 29 July 2024, from <https://gistbok-topics.ucgis.org/>
- Uddin, Md. G., Nash, S., & Olbert, A. I. (2021). A review of water quality index models and their use for assessing surface water quality. *Ecological Indicators*, 122, 107218. <https://doi.org/10.1016/j.ecolind.2020.107218>
- UN, & Association, I. C. (2020). *Mapping for a sustainable world /: Menno-Jan Kraak, Robert E. Roth, Britta Ricker, Ayako Kagawa and Guillaume Le Sourd*. UN,. <https://digitallibrary.un.org/record/3898826>
- Uudeberg, K., Aavaste, A., Kõks, K.-L., Ansper, A., Uusõue, M., Kangro, K., Ansko, I., Ligi, M., Toming, K., & Reinart, A. (2020). Optical Water Type Guided Approach to Estimate Optical Water Quality Parameters. *Remote Sensing*, 12(6), Article 6. <https://doi.org/10.3390/rs12060931>
- Vanhellemont, Q. (2024). *Acolite/acolite* [Python]. <https://github.com/acolite/acolite> (Original work published 2021)
- Vector Graphics Software – Adobe Illustrator*. (n.d.). Retrieved 28 July 2024, from <https://www.adobe.com/products/illustrator.html>
- Virdis, S. G. P. (2014). An object-based image analysis approach for aquaculture ponds precise mapping and monitoring: A case study of Tam Giang-Cau Hai Lagoon, Vietnam. *Environmental Monitoring and Assessment*, 186(1), 117–133. <https://doi.org/10.1007/s10661-013-3360-7>
- World health organization. (2024). *Guidelines for drinking-water quality: Small water supplies*.
- Yang, H., Kong, J., Hu, H., Du, Y., Gao, M., & Chen, F. (2022). A Review of Remote Sensing for Water Quality Retrieval: Progress and Challenges. *Remote Sensing*, 14(8), Article 8. <https://doi.org/10.3390/rs14081770>
- Zdravcheva, N. D. (2019). Hyperspectral environmental monitoring. *IOP Conference Series: Materials Science and Engineering*, 614(1), 012014. <https://doi.org/10.1088/1757-899X/614/1/012014>

Zhang, Q., Kang, Y., & Roth, R. (2023). The Ethics of AI-Generated Maps: DALL·E 2 and AI's Implications for Cartography (Short Paper). *DROPS-IDN/v2/Document/10.4230/LIPics.GIScience.2023.93*. 12th International Conference on Geographic Information Science (GIScience 2023).
<https://doi.org/10.4230/LIPics.GIScience.2023.93>

Zheng, K., Shao, T., Ning, J., Zhuang, D., Liang, X., & Ding, X. (2023). Water quality, basin characteristics, and discharge greatly affect CDOM in highly turbid rivers in the Yellow River Basin, China. *Journal of Cleaner Production*, *404*, 136995.
<https://doi.org/10.1016/j.jclepro.2023.136995>

LIST OF ATTACHMENTS

ATTACHMENTS-0

1 LIST OF PHOTOSYNTHETIC LIVE IN THE LAGOON	1
2 .HRD FILE FORMAT	2
3 CHALLENGES ANACONDA FOR ACOLITE	144
4 ERRATIC DATA OF PRISMA IMAGERY	155
5 ATMOSPHERIC CORRECTION FOR EnMAP	15
6 SOFTWARE INSTALLATION	222
7 TIMELINE OF EVENTS	255
8 DESIS RESULTS	30
9 ENMAP RESULTS OF THE FIRST AND SECOND ATTEMPT	499
10 IMAGE RESULTS FROM WASI PITXEL DISTRIBUTION OF THE PROCESS IMAGES DESI AND ENMAP (BAR CHART)	611
11 SUMMARY FROM HEXAGON IMAGE RESULTS DISTRIBUTION OF THE IMAGE SUMMARY (BAR CHART)	80
12 GRAPH FOR COMPARING IN-SITU AND SATELLITE DATA	888

ATTACHMENTS-1

Map Posters (digital)

ATTACHMENTS-2

Animation (digital)

ATTACHMENTS-3

Poster (digital)

ATTACHMENTS-4

Web (digital)

DIGITAL STRUCTURE

Document Text

Input_Data:

 Satellite data

 In-situ data

Output_Data:

 Attachment-1 Map Poster

 Attachment-2 Animation

WEB

 Poster

1 LIST OF PHOTOSYNTHETIC LIVE IN THE LAGOON

- Phytoplankton: In Tam Giang - Cau Hai lagoon, there are a total of 283 species belonging to 6 different layers of algae, Of which 188 species of **diatom**, 40 species of **blue green algae**, 27 species of **Dinophyta**, 13 species of **glaucophytes**, 11 species of **Euglenophyta** and 4 species of yellow algae(Hằng et al., 2017).
- Seaweed: 48 species of seaweed have been discovered in four sectors (Blue-Green seaweed, Red seaweed, Brown seaweed, and Green seaweed) (Hằng et al., 2017).
- Seagrass: determined 6 species of seagrasses in the lagoon belong to 3 families and 3 genera, most of them distributed in Thuy Tu Lagoon and Tam Giang Lagoon (Hằng et al., 2017).
- Zooplankton: There are 57 species belonging to 28 genera, 25 families, 9 orders and 3 sectors. Sam Lagoon area has the highest number of species, and Cau Hai area has the least number of species. The number of dry-season species is more than the number of rainy-season ones (Ton, T. P. V& ink, 2009).
- Benthic fauna: 203 benthic species have been identified, in which, 92 species of mollusk account for 45.32% of total benthic species, 51 species of crustacean, 49 species of silkworms, 3 species of echinoderm and 8 others (Nguyen, H. Y, Tran, Đ. T., Lang, V. K. & Nguyen, T. T,2010).
- Seagrass ecosystem: Seagrasses are widely distributed with a total area of 4246.44 hectares, of which Sam lagoon and Cau Hai lagoon are the largest seagrass areas (Hằng et al., 2017) (Peters et al., 2015).
- Mangrove ecosystem: In the Tam Giang - Cau Hai lagoon system, mangrove forests occupy about 80.36 ha and are distributed in some places, in typically, Rucha mangroves on the Tam Giang Lagoon (Huong Phong Commune, Huong Tra Town), Bu Lu River mouthwater estuary, O Lau estuary, Huong estuary (Tan My tourist site) (Hằng et al., 2017).

2 .HRD FILE FORMAT

```
ENVI
description = {
DESIS-HSI-L2A-DT0377734488_003-20191023T073716-V0220-SPECTRAL_IMAGE.tif}
samples = 1429
lines = 1591
bands = 235
header offset = 0
file type = TIFF
data type = 2
interleave = tif
byte order = 0
map info = {UTM, 1, 1, 769740, 1830690, 30, 30, 48, North,WGS-84}
coordinate system string =
{PROJCS["WGS_1984_UTM_Zone_48N",GEOGCS["GCS_WGS_1984",DATUM["D_WGS_1984
",SPHEROID["WGS_1984",6378137,298.257223563]],PRIMEM["Greenwich",0],UNIT["Degre
e",0.017453292519943295]],PROJECTION["Transverse_Mercator"],PARAMETER["latitude_o
f_origin",0],PARAMETER["central_meridian",105],PARAMETER["scale_factor",0.9996],PARA
METER["false_easting",500000],PARAMETER["false_northing",0],UNIT["Meter",1]]}
band names = {
Band 1,
Band 2,
Band 3,
Band 4,
Band 5,
Band 6,
Band 7,
Band 8,
Band 9,
Band 10,
Band 11,
Band 12,
Band 13,
Band 14,
Band 15,
Band 16,
Band 17,
Band 18,
Band 19,
Band 20,
Band 21,
Band 22,
Band 23,
Band 24,
Band 25,
Band 26,
Band 27,
Band 28,
Band 29,
Band 30,
Band 31,
Band 32,
Band 33,
Band 34,
Band 35,
Band 36,
Band 37,
Band 38,
Band 39,
Band 40,
Band 41,
Band 42,
Band 43,
Band 44,
```

Band 45,
Band 46,
Band 47,
Band 48,
Band 49,
Band 50,
Band 51,
Band 52,
Band 53,
Band 54,
Band 55,
Band 56,
Band 57,
Band 58,
Band 59,
Band 60,
Band 61,
Band 62,
Band 63,
Band 64,
Band 65,
Band 66,
Band 67,
Band 68,
Band 69,
Band 70,
Band 71,
Band 72,
Band 73,
Band 74,
Band 75,
Band 76,
Band 77,
Band 78,
Band 79,
Band 80,
Band 81,
Band 82,
Band 83,
Band 84,
Band 85,
Band 86,
Band 87,
Band 88,
Band 89,
Band 90,
Band 91,
Band 92,
Band 93,
Band 94,
Band 95,
Band 96,
Band 97,
Band 98,
Band 99,
Band 100,
Band 101,
Band 102,
Band 103,
Band 104,
Band 105,
Band 106,
Band 107,
Band 108,
Band 109,

Band 110,
Band 111,
Band 112,
Band 113,
Band 114,
Band 115,
Band 116,
Band 117,
Band 118,
Band 119,
Band 120,
Band 121,
Band 122,
Band 123,
Band 124,
Band 125,
Band 126,
Band 127,
Band 128,
Band 129,
Band 130,
Band 131,
Band 132,
Band 133,
Band 134,
Band 135,
Band 136,
Band 137,
Band 138,
Band 139,
Band 140,
Band 141,
Band 142,
Band 143,
Band 144,
Band 145,
Band 146,
Band 147,
Band 148,
Band 149,
Band 150,
Band 151,
Band 152,
Band 153,
Band 154,
Band 155,
Band 156,
Band 157,
Band 158,
Band 159,
Band 160,
Band 161,
Band 162,
Band 163,
Band 164,
Band 165,
Band 166,
Band 167,
Band 168,
Band 169,
Band 170,
Band 171,
Band 172,
Band 173,
Band 174,

Band 175,
Band 176,
Band 177,
Band 178,
Band 179,
Band 180,
Band 181,
Band 182,
Band 183,
Band 184,
Band 185,
Band 186,
Band 187,
Band 188,
Band 189,
Band 190,
Band 191,
Band 192,
Band 193,
Band 194,
Band 195,
Band 196,
Band 197,
Band 198,
Band 199,
Band 200,
Band 201,
Band 202,
Band 203,
Band 204,
Band 205,
Band 206,
Band 207,
Band 208,
Band 209,
Band 210,
Band 211,
Band 212,
Band 213,
Band 214,
Band 215,
Band 216,
Band 217,
Band 218,
Band 219,
Band 220,
Band 221,
Band 222,
Band 223,
Band 224,
Band 225,
Band 226,
Band 227,
Band 228,
Band 229,
Band 230,
Band 231,
Band 232,
Band 233,
Band 234,
Band 235}
wavelength units = Nanometer
data ignore value = -32768
wavelength = {
401.43,

404.1,
406.72,
409.23,
411.71,
414.24,
416.81,
419.34,
421.91,
424.54,
427.19,
429.76,
432.35,
434.88,
437.39,
439.85,
442.39,
444.92,
447.66,
450.24,
452.79,
455.47,
458.08,
460.65,
463.18,
465.72,
468.2,
470.67,
473.26,
475.77,
478.47,
481.14,
483.7,
486.29,
488.89,
491.45,
493.87,
496.4,
499.14,
501.65,
504.22,
506.82,
509.44,
512.05,
514.59,
517.07,
519.56,
522.09,
524.59,
527.12,
529.66,
532.23,
534.83,
537.46,
540.05,
542.59,
545.11,
547.66,
550.28,
552.81,
555.46,
557.98,
560.52,
563.08,
565.69,
568.31,

570.9,
573.48,
576.0,
578.5,
581.03,
583.56,
586.13,
588.68,
591.24,
593.86,
596.48,
598.94,
601.51,
604.09,
606.65,
609.16,
611.7,
614.24,
616.8,
619.42,
622.01,
624.61,
627.08,
629.56,
632.12,
634.62,
637.14,
639.66,
642.22,
644.85,
647.47,
649.92,
652.49,
655.14,
657.62,
660.12,
662.66,
665.2,
667.75,
670.38,
673.06,
675.7,
678.26,
680.81,
683.37,
685.77,
688.32,
690.78,
693.37,
696.01,
698.72,
701.31,
703.82,
706.64,
709.27,
711.68,
713.92,
716.27,
718.79,
721.45,
724.11,
726.75,
729.35,
731.93,
734.27,

736.8,
739.4,
741.89,
744.42,
747.03,
749.64,
752.17,
755.07,
757.64,
760.23,
762.86,
764.81,
767.47,
770.23,
772.61,
775.24,
777.9,
780.49,
782.98,
785.48,
788.16,
790.47,
793.07,
795.8,
798.27,
801.06,
803.98,
806.57,
809.05,
811.6,
814.16,
816.78,
819.66,
822.71,
824.16,
827.07,
829.08,
832.1,
834.78,
836.59,
839.97,
841.87,
844.56,
847.63,
849.83,
852.36,
855.27,
857.78,
860.2,
862.77,
865.34,
867.87,
870.49,
873.08,
875.67,
878.66,
881.42,
882.98,
885.21,
887.98,
890.82,
893.95,
895.87,
898.26,
901.1,

903.66,
905.88,
908.53,
911.52,
914.67,
916.46,
918.28,
920.83,
923.74,
926.97,
929.56,
931.75,
934.39,
937.19,
939.3,
941.82,
944.64,
947.18,
949.48,
951.8,
954.12,
957.21,
959.47,
962.2,
965.32,
968.0,
970.33,
972.8,
975.93,
978.52,
979.9,
981.89,
984.74,
988.77,
991.56,
993.05,
995.54,
997.82,
999.98}
fwhm = {
4.2,
3.8,
3.8,
3.6,
3.8,
3.6,
3.2,
3.4,
3.4,
3.6,
3.6,
3.4,
3.2,
3.2,
3.2,
3.2,
3.2,
3.2,
3.4,
3.4,
3.2,
3.2,
3.4,
3.4,
3.2,
3.2,
3.4,
3.4,
3.2,
3.2,

3.4,
3.4,
3.4,
3.4,
3.6,
3.6,
3.6,
3.4,
3.4,
3.4,
3.2,
3.4,
3.4,
3.6,
3.4,
3.6,
3.6,
3.4,
3.4,
3.2,
3.2,
3.4,
3.4,
3.4,
3.4,
3.6,
3.4,
3.4,
3.6,
3.6,
3.8,
3.8,
3.8,
3.8,
3.6,
3.4,
3.4,
3.4,
3.4,
3.4,
3.2,
3.2,
3.2,
3.4,
3.4,
3.6,
3.4,
3.4,
3.4,
3.2,
3.2,
3.6,
3.0,
3.4,
3.4,
3.6,
3.6,
3.4,
3.4,
3.2,
3.4,
3.4,
3.2,
3.4,
3.4,
3.6,
3.6,

3.4,
3.2,
3.2,
3.2,
3.0,
3.2,
3.2,
3.2,
3.6,
3.2,
3.0,
3.6,
3.0,
3.8,
2.6,
3.2,
3.4,
2.8,
3.4,
3.2,
3.0,
3.2,
3.2,
3.2,
3.2,
3.2,
3.2,
3.4,
3.4,
3.4,
3.4,
4.0,
3.2,
3.2,
3.6,
3.6,
3.6,
3.6,
3.0,
3.2,
3.8,
3.6,
3.0,
3.8,
4.0,
3.8,
3.0,
3.8,
4.0,
3.6,
3.6,
3.4,
3.4,
3.6,
3.6,
3.6,
3.6,
3.6,
3.6,
3.6,
2.8,
3.4,
3.6,
3.4,
3.6,

3.8,
3.6,
3.4,
3.6,
5.0,
3.4,
3.0,
3.8,
6.6,
4.4,
3.4,
3.0,
3.4,
3.2,
3.2}

3 CHALLENGES ANACONDA FOR ACOLITE

In the following lines, you will see the steps I followed:

I wanted to run ACOLITE (software package to perform atmospheric correction for water bodies), and the GitHub documentation says to run it inside an environment like Anaconda.

Installing the first Anaconda was not able to create a new environment in the Anaconda command PowerShell prompt. Googling the error, they suggested that the error was due to the username folder containing spaces between the words "Emma Garcia Boadas".

I proceeded to change the Username folder following a YouTube tutorial: https://www.youtube.com/watch?v=Y5_Q2BmTx3Y

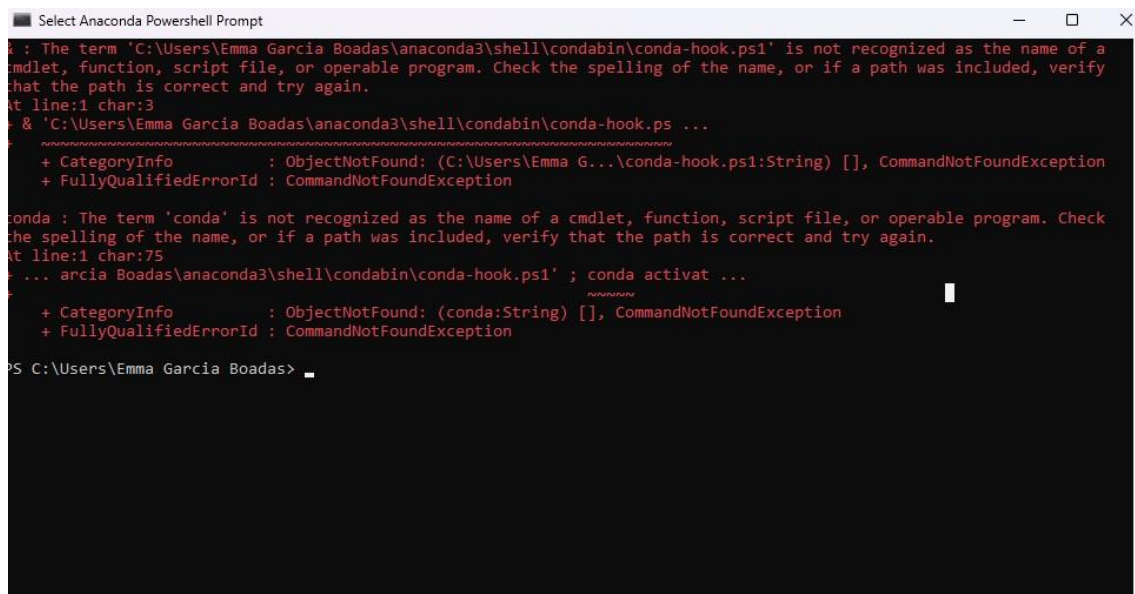
The video suggested performing a user recovery (System Properties > System Protection> Creating a restore point manually) if the name change was going wrong, which I did.

In the middle of the name change the SID register number of the old user was not matching.

I cancelled the operation and ran the recovery.

After the recovery was done, I had my original user's name with just the folder structure, and the new user folder with the structure folder and the data inside.

At the time, Anaconda was making a different error than before.



```
Select Anaconda Powershell Prompt
PS C:\Users\Emma Garcia Boadas\anaconda3\shell\condabin> conda-hook.ps1
PS C:\Users\Emma Garcia Boadas\anaconda3\shell\condabin> conda-hook.ps1
PS C:\Users\Emma Garcia Boadas\anaconda3\shell\condabin> conda
PS C:\Users\Emma Garcia Boadas\anaconda3\shell\condabin> conda activate
PS C:\Users\Emma Garcia Boadas>
```

Figure 72: Anaconda power shell error.

After this unsuccessful change of user name folder my computer was not running properly, I was not able to open any software and I was not able to copy the information of the disk.

I recurred to the it department of the university of Salzburg for help they copied as much information they could from my disc during safe mode and they restored my computer from factory settings. I had been two weeks already with no computer and the University of Salzburg was not able to proportion myself with a computer that I could use with administrative right to install and pre-process the data. At this point I had my computer back and I started again to start the preprocessing.

4 ERRATIC DATA OF PRISMA IMAGERY

PRISMA images the spectrums are not similar to EnMAP or DESIS:

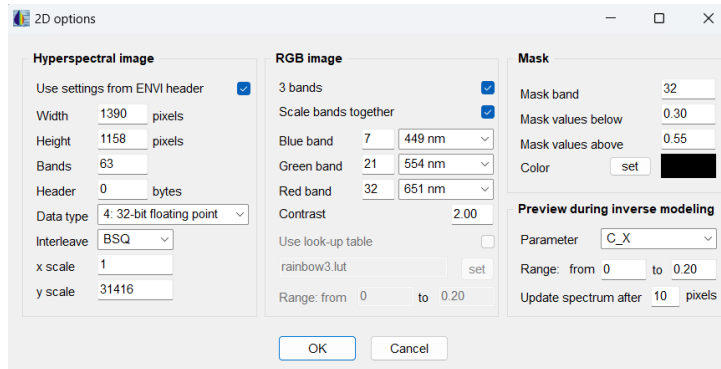


Figure 73: Parameters of visualization of the PRISMA images.

Image 20230708

The water has two types of spectrums. As shown in the image below, there are light grey areas on the north limit of the lagoon and dark gray, almost black areas in the center of the lagoon.

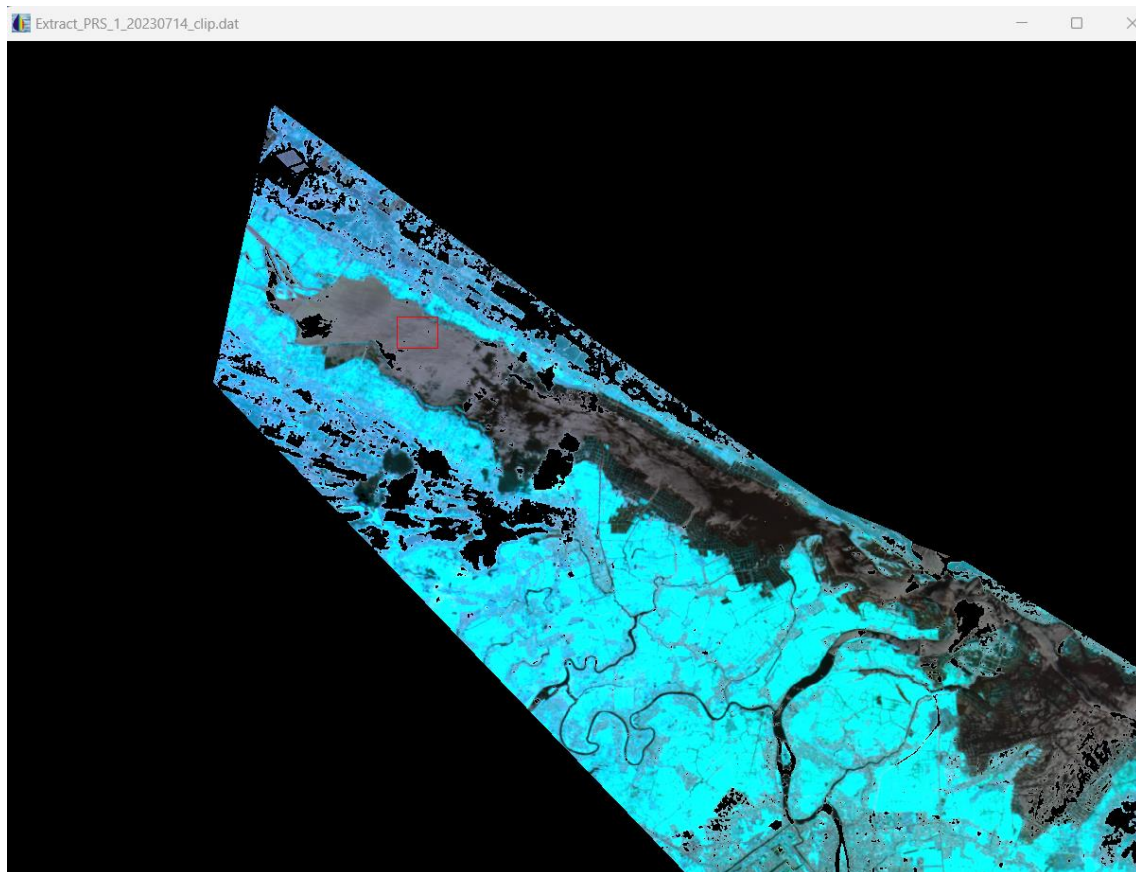


Figure 74: Visualization of PRISMA image 20230708.

The images' lighter areas of water bodies are like the following spectrum.

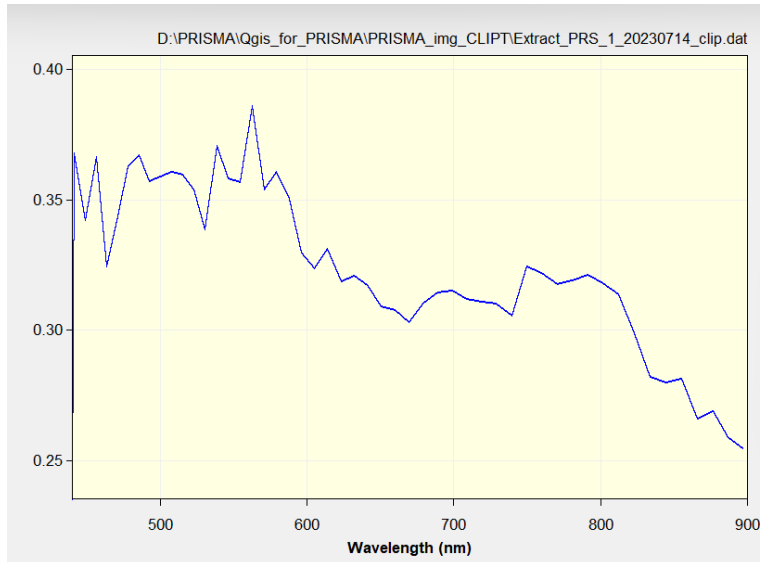


Figure 75: Spectrum of light areas in the water body.

The dark areas of the water are not better, but they are more similar to the other PRISMA images.

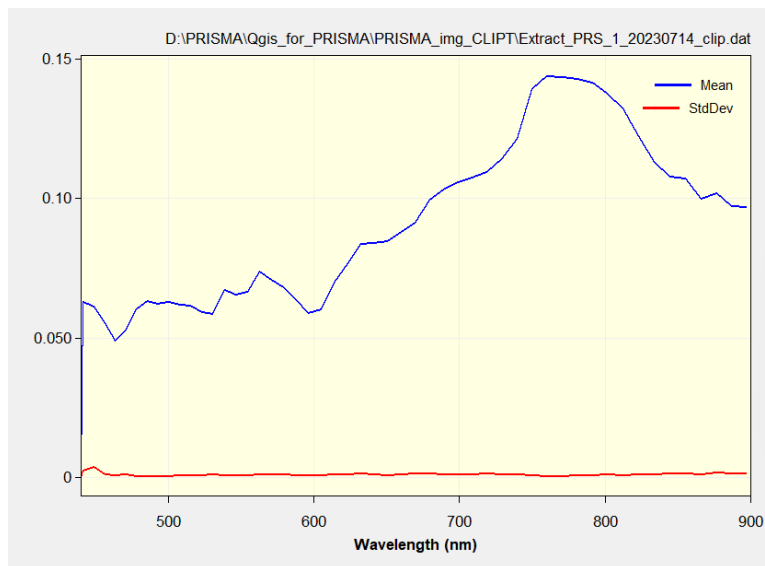


Figure 76: Spectrum of dark areas in the water body.

Image 20230603

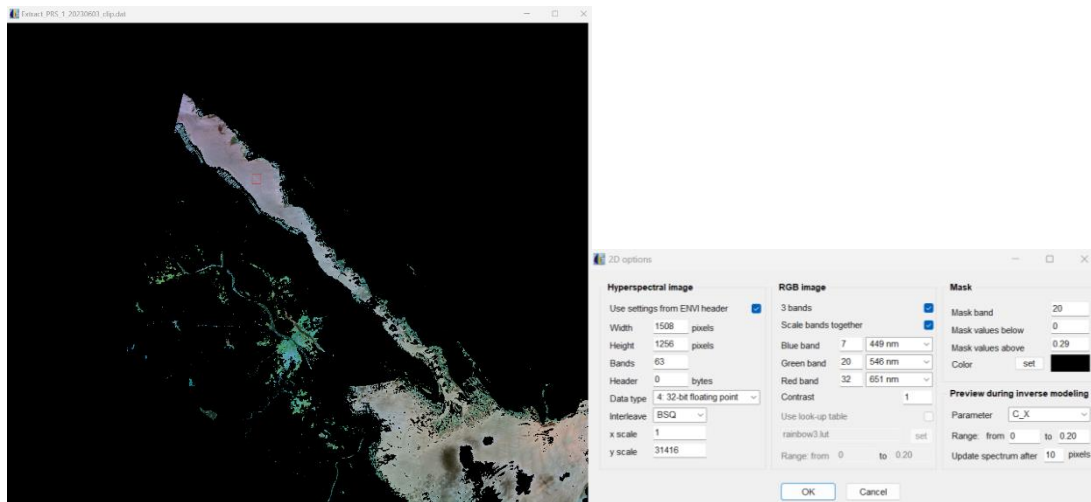


Figure 77: Visualization of PRISMA image 20230603.

Has a similar spectrum of the dark area of the image of **20230708** but is much noisier.

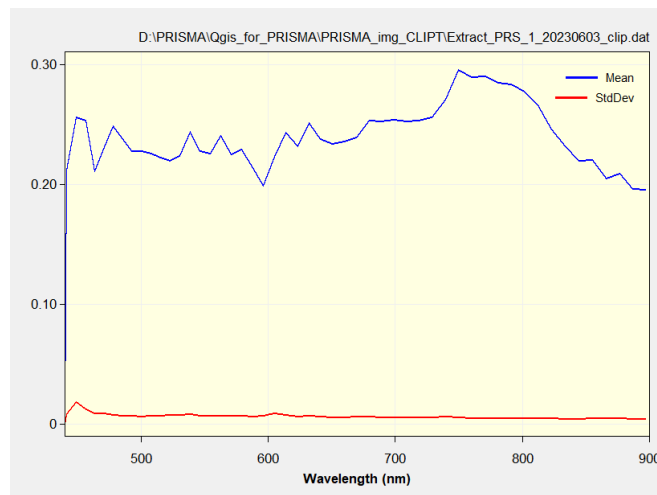


Figure 78: Spectrum means from the red square in the PRISMA image 20230603, the similar spectrum of dark water areas from the previous image.

Image 20230418

image has doubtful pixel values in the northern part of the lagoon half of the lagoon is with erratic values or dry? For the information found by the author, the lagoon was not dry at the date of acquisition.

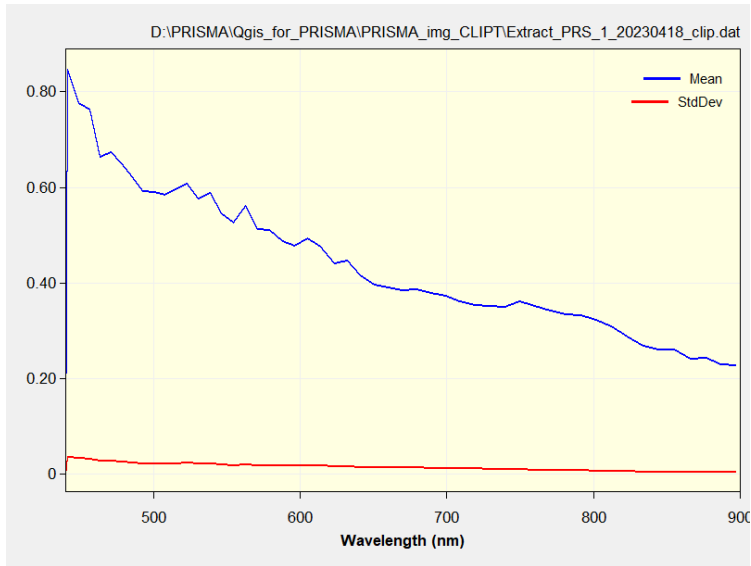


Figure 81: Spectrum from a northern part of the lagoon next to the pixels that appear erratic.

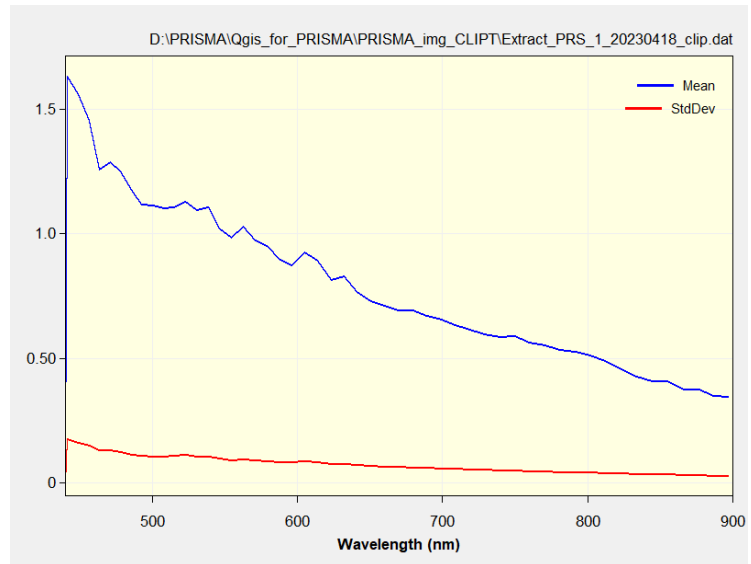


Figure 82: Spectrum from a central part of the lagoon next to the pixels that appear erratic.

5 ATMOSPHERIC CORRECTION FOR ENMAP

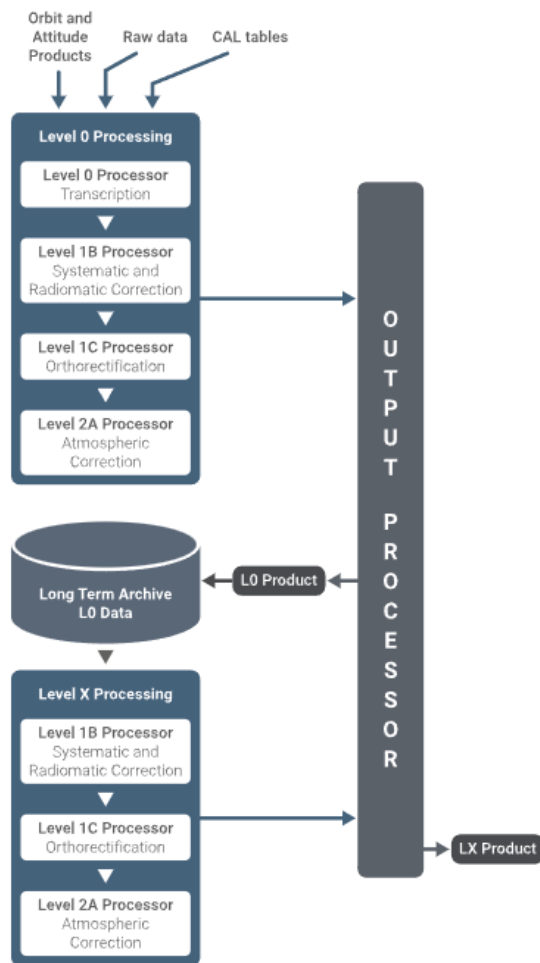


Figure 83: Process for Atmospheric correction EnMAP
https://www.enmap.org/data_access/

atmospheric and water surface correction (Heege et al., 2014; Kiselev et al., 2015; Richter et al., 2014). This algorithms all the pixels with clouds and sun glint (Müller, n.d.).

Most applications are envisioned to use the Level 2A product for further analysis.
https://www.enmap.org/data_access/

Level 1C Processor

The geometric correction processor orthorectifies images using different methods and performs the resampling of the image (with and without automatically

extracted GCPs)
https://www.enmap.org/data_access/

Level 2A Processor will convert the Level 1C products to surface reflectance separately for land and water applications. This split procedure is quite unique in data processing and should give the user the possibility to select the best result according to the area of interest (land or water or combined). The atmospheric correction involves generation of sun glint maps for water surfaces by identification of specular reflections, detection (and correction) of haze and cirrus, estimation of aerosol optical thickness and columnar water vapor and retrieval of surface reflectance after adjacency correction. Auxiliary data for further processing are attached, but not applied.

The Atmospheric correction over water algorithm applied is described in the Level 2A Processor (Atmospheric Correction Water) ATBD: Modular Inversion Processor, EOMAP GmbH (MIP). This consists of i) Monochromatic LUTs (Bulgarelli et al., 1999; Kiselev et al., 1994), ii) Pixel-wide adjacency,

Atmospheric correction DESIS

Atmospheric Correction Processor L2A This ATBD describes an algorithm for the atmospheric correction of DESIS data over land surfaces using the PACO code (python version of ATCOR code). The method for land is applied over flat or mountainous terrain and converts top-of-atmosphere radiance imagery (L1C) into surface reflectance data (L2A). The flat terrain case is processed with L1C data. In case of a mountainous terrain, a Digital Elevation Model (DEM) is needed to include a correction of topographic effects and the orthorectified (L1C) product is input to the L2A processor.

A DEM processing in L2A is only performed if a corresponding DEM (the DEM has to correspond exactly to the L1C scene and the L1C scene has to be orthorectified using this DEM) is available for the scene and if at least 1% of the scene pixels have slope values greater than a certain threshold (6 degrees). The paragraph is extracted from the Processing chain technical guide (Müller, n.d.). The images used for this processing had been process with a variation of PACO adapting and customizing the atmospheric correction on water bodies with atmospheric measurements.

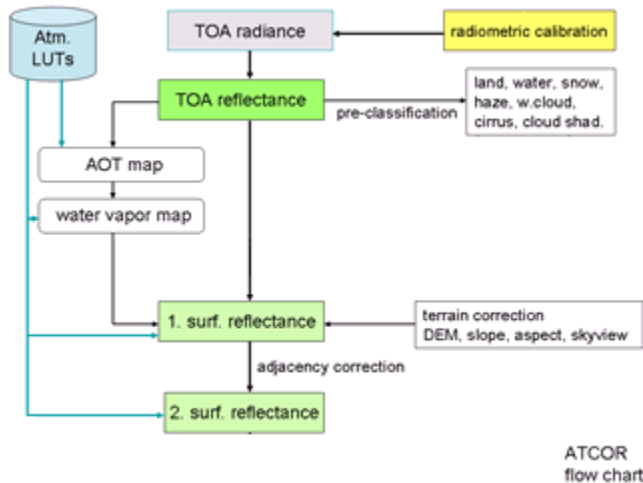


Figure 84: Process for Atmospheric correction DESIS (Müller, n.d.).

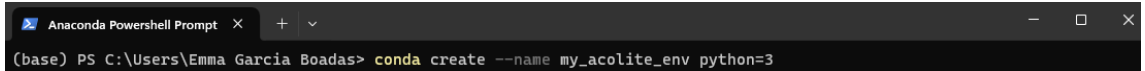
6 SOFTWARE INSTALLATION

ACOLITE

ACOLITE is a processing tool that combines Atmospheric correction algorithms for aquatic applications of various satellite missions (Vanhellemont, 2021/2024).

1. Open a Terminal or Command Prompt:
First of all it is necessary to create a Conda Environment. Open a terminal or a command prompt of your Anaconda.
2. Create a Conda Environment:

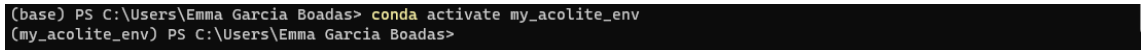
Use the command `conda create --name my_acolite_env python=3` to create a new environment. In this case the environment name is “my_acolite_env”.



```
Anaconda Powershell Prompt x + v - □ x
(base) PS C:\Users\Emma Garcia Boadas> conda create --name my_acolite_env python=3
```

Figure 85: Creation of the environment.

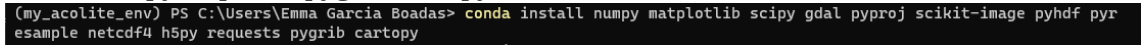
3. Activate the Conda environment:
It is necessary to activate the conda environment to be able to work inside it. You can do it writing the command in `conda activate my_acolite_env`.



```
(base) PS C:\Users\Emma Garcia Boadas> conda activate my_acolite_env
(my_acolite_env) PS C:\Users\Emma Garcia Boadas>
```

Figure 86: Activate the Conda environment.

4. Install required Packages for running Acolite:
ACOLITE is coded in Python 3, and requires the following Python packages to run: numpy matplotlib scipy gdal pyproj scikit-image pyhdf pyresample netcdf4 h5py requests pygrib cartopy

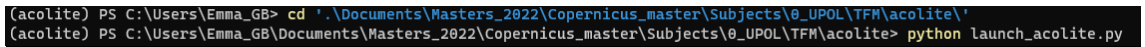


```
(my_acolite_env) PS C:\Users\Emma Garcia Boadas> conda install numpy matplotlib scipy gdal pyproj scikit-image pyhdf pyresample netcdf4 h5py requests pygrib cartopy
```

Figure 87: Install the required packages.

5. Run acolite:

To launch ACOLITE Gui run the following.



```
(acolite) PS C:\Users\Emma_GB> cd '..\Documents\Masters_2022\Copernicus_master\Subjects\0_UPOL\TFM\acolite\'
(acolite) PS C:\Users\Emma_GB\Documents\Masters_2022\Copernicus_master\Subjects\0_UPOL\TFM\acolite> python launch_acolite.py
```

Figure 88: Launch ACOLITE Gui.

There is a second way to launch ACOLITE with command line:

The ACOLITE CLI can also be used to retrieve the LUTs required for a list of sensors before running any processing. E.g. for setting up a Docker container. In the following examples "python launch_acolite.py" can also be replaced by "dist\acolite\acolite" or "dist\acolite\acolite.exe" for the binary version.

```
All supported multispectral sensors:
python launch_acolite.py --retrieve_luts

Get the LUT for named sensors (here S2A/MSI and S2B/MSI):
python launch_acolite.py --retrieve_luts --sensor S2A_MSI,S2B_MSI

Get the generic LUT for processing hyperspectral sensors:
python launch_acolite.py --retrieve_luts --sensor hyper
```

Figure 89: How to luncth ACOLITE with command line(Vanhellemont, 2021/2024).

ENPT – ENMAP PROCESSING TOOL INSTALLATION

EnPT (the EnMAP processing tool) is an automated pre-processing EnMAP hyperspectral satellite data. It provides free and open-source features to transform EnMAP Level-1B data to Level-2A. The code has been developed at the German Research Centre for Geosciences Potsdam (GFZ) as an alternative to the processing chain of the EnMAP Ground Segment. I have followed the installation of the EnPT documentation is really well documented (Installation — EnPT 0.20.1 Documentation, n.d.)

WASI6 (WATER COLOUR SIMULATOR) INSTALLATION

WASI6 is a tool for the simulation of water optical properties and light field parameters of deep and shallow waters. Also it is able to complet data analysis of instruments disposed above the water surface and submerged in the water(Gege, 2014).

The installation of WASI6 instructions were provided by Felix cosupervisor.

1. Download **Setup_WASI6.exe** from (*Software - IOCCG*, n.d.) **¡Error! No se encuentra el origen de la referencia..**
2. Install WASI-6
3. Replace the installed exe with the separately provided **WASI6.exe**
4. Then download **Install_WASI-AI.exe**
5. Unpack it and follow the installation instructions (1. Matlab runtime then 2. WASI)
6. To Run WASI AI, WASI-6 must have been started and an image loaded

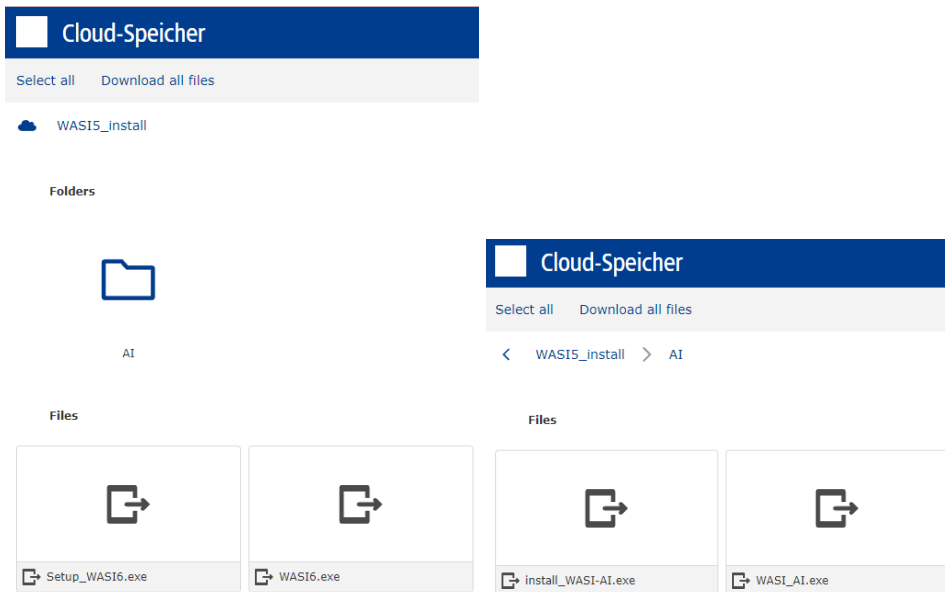


Figure 90: Download files.

WASI-AI MODULE INSTALLATION

Once you have installed WASI6 with **Setup_Wasi6.exe**:

1. Download **WASI6.exe** and **WASI_AI.exe** ¡Error! No se encuentra el origen de la referencia..
2. Paste the two files downloaded on the C/ software folder and replace the file **WASI6.exe** ¡Error! No se encuentra el origen de la referencia..
3. Once it is done, you will be able to visualize the AI module in Options ¡Error! No se encuentra el origen de la referencia..

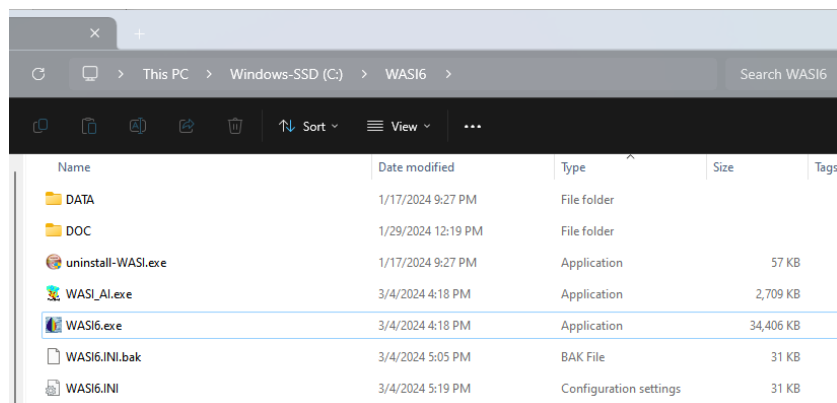


Figure 91: Software folder.

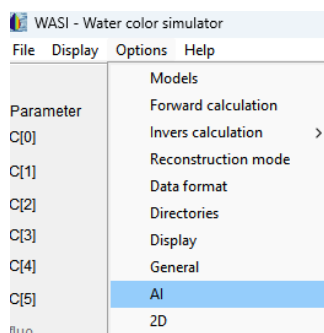


Figure 92: AI toolbox.

7 TIMELINE OF EVENTS

October

2023 10 09

The thesis topic got accepted.

November

2023 11 05

WASI6 installation instructions were provided by Felix.

1. Install WASI-6
2. Replace the installed exe with the separately provided WASI6.exe
3. Then download WASI-AI
4. Unpack it and follow the installation instructions (1. Matlab runtime then 2. WASI)
5. To Run WASI AI, WASI-6 must have been started and an image loaded

2023 11 07

Meeting with the supervisors kickoff the project. In the meeting was Zara told us that she would ask for a virtual machine in Salzburg to be able to process the data.

2023 11 07

Installation of WASI6 succeeded installation of WASI-AI not succeeded.

First, I installed the WASI6 without a problem copying the exe file and executing the self intallator . In the case of the installation WASDY-AI I had a message error at the end of the installation (Error in => WASI_AI_No_GUI_01.m at line 9 as the image below).

I thought the error was related to the Matlab version, so I installed the version R2021b (I read the Readme). After I installed this version, it was not still working. So I opened Matlab, ran the >>mcrinstaller, and downloaded from the web site of Matlab the packages needed.

After this installation, I uninstalled WASI-AI and installed it again. The same error appeared.

2023 11 07

Felix, helped me with the opening of WASI6 I had open as an administrator every time.

2023 11 23

Masters day

2023 11 27

Zahara suggests working with the planetary computer. This computer is like and API for data in to the cloud it do not meet the characteristic of a Virtual Machine. Microsoft offers another service that offers Azure Virtual Machines and the cloud with your Azure free account just for free 200 dollars when you pass the limit you have to pay so you pay for the time that the virtual machine is opened and depending the resources you are using in the machine. to open tis account it ask mee my credit cart.

2023 11 28

Identification of the necessary Preprocessing Enmap needs pre processing from L1 to L2, PRISMA needs preprocessing from L1 to L2 and DESIS already is pre processed to L2 no need to pre processing

For the EnMap Preprocessing, it can be used the processing tool **EnPT - EnMAP Processing Tool (v0.8.4)**.

The **ACOLITE** atmospheric correction can be used for the PRISMA data. I have sent an email to the support team, and they never answered whether there was another option or tool specifically to process prisma data from L1 to L2.

Generation of a **document** for preprocessing and bands that could be potentially used for water quality stimation.

December

2023 12 05

Meeting with the WASI creator to be able to open images and process them. It is an introduction to the software image format to introduce there and how to process images.

2023 12 06

Meeting with Zahara She told me that we can process the images in January with her.

I told her that on the 8-9 of January I will be on Salzburg to process the images she agrees on meeting and process it together.

The next 2 weeks I was centered in the exams in UPOL.

2023 12 21

Felix reorder the EnMap images for L2, and DESIS images that were reprocessed.

2023 12 22

The administration of the DLR communicates that I can not have a contract so I can not have access to the computers of the DLR to process the data. Not having access to a powerful computer.

Supposedly I had to start the contract on the 2nd of January.

January

2024 01 02

In my personal computer, trying to run an environment in anaconda my folder user name contained spaces and anaconda was not able to read the folder.

I tried to create a new user and user folder in my computer and did not work. To recover my previous computer state, I performed a user recovery and the files that I had in my original user had been moved in my new user file during the recovery. All the software was not working in my computer. I was not able to do a copy of my hard drive.

The problem was that in one user there was two user folders. And if I deleted one user folder can affect the SID register number because it is associated with the two of them.

2024 01 08

At the university of Salzburg I ask support for having access to a computer with administrative writhes to install the software's.

2024 01 10

Zara Asks the masters coordinator Barbara she says that is not possible to let me access to any computer to install the software's because since they had a civer attach they do not allow it.

2024 01 12

I get the proper documentation that the DLR administration was asking for. The proper documentation and a contract is equal to have access to a DLR computer.

2024 01 15

The IT department help me recovering the data from my hard drive, and Resetting my computer it takes a week.

2024 01 19

Meeting with Zara in Salzburg for EnMap image preprocessing and ".hdr" file format.

2024 01 21

I was able to restore **my personal PC to FACTORY SETINGS** and install all the software's that I needed to it.

2024 01 22

Converting the EnMap images to the **correct format** with ArcGis PRO and modifying the ".hdr" file to introduce them in WASI6

2024 01 23

Installation of ACOLITE completed and testing how to process with it.

I ask Felix if we can other the PRISMA L2.

2024 01 26

We received all the DESIS L2 data.

2024 01 29

Find out that I cannot preprocess the images of PRISMA in ACOLITE because it needs the L1 and the L2 in the same folder.

February

2024 02 05

I had been working with WASI6 for a week WASI6 has not been able to finish any process.

The parameters using for a processing was: Sun (Sun angle), T_W (water temperature), S(Exponent of CDOM absorption), C_Y(CDOM), C_Mie (Concentration of non-algal particles of type II), Fa(1) sand, Fa(2) a different kind of material, and the depth.

Felix provided papers of reference for the proper regulation of the parameters. Gloria spectrum and parameter dataset for the water parameters in Wasi as an orientation.

2024 02 06

Felix proportion me instructions to install the AI plugging of WASI but it did not work. He tried again and it is not working.

2024 02 07

Emailing the programmer of the plugging Milad Niroumand Jadidi (not DLR) he never answers my email.

2024 02 09

I ask a friend for processing and image in his computer with a powerfull gaming computer it processed one image in 3 hours. It was my first processing. Specifications 64 RAM processor Ryzen 9 7950X3D with Radeon Graphics.

2024 02 12

Felix suggest me to contact Peter if I have questions of WASI set up. At this point I have just been able to do one processing and I do not have any setup that I am sure that it works.

2024 0215

I ask in Olomouts if I can have access to a powerful computer to process the images

2024 02 21

Jan Bruce let me have access to a powerful computer in Olomouts I start to do tests with the parameters.

March

2024 03 01

I trabell to Munich and, I had access to the powerful computers of the DLR, acces to the L2 of the hyperspectral images. Also able to come in person and ask help from Peter the author of the WASI6 software.

2024 03 04

I am able to recive help From Peter because I have had my first results from Olomouts and si needed support with that.

Petter has the proper version of WASI6 and WASI AI to bee able to process images more quickly.

2024 03 13

I notice that I have and error in the processing due to the software version I ask if peter can proportion me the proper version of the software (WASI-AI is still in improvement) Also he points out that my “.hdr” file was not properly setup.

2024 03 21

Peter told me that I was not having good results with DESIS for the bad atmospheric correction. He contacted Raquel for an improvement of the atmospheric correction.

2024 03 29

I have a meeting with Peter to have and improvement of the EnMap processing he sugested to process the lagoon as a deep water inversion.

April

2024 04 06

All the EnMAP images are processed properly.

2024 04 08

The DESIS processing is failing and the results are not looking accurate enough.

2024 04 09

The images are going to be reprocessed. Peter has told me that Raquel now has two weeks of holiday. So maybe the images could be processed in two weeks.

2024 04 24

Raquel reprocessed some of the DESIS images.

May

2024 05 10

The images DESIS were reprocessed.

2024 05 20

It was asked by the Vietnamese authorities if they could guide the information on the collection of the insitu data for comparison with the satellite data.

June

2024 06 17

The statistical analysis was performed to compare in-situ and satellite data.

July and August

Finalizing the geovisualization, website, and written report.

8 DESIS RESULTS

Automatic name folder after processing WASI-AI:
 DESI_CLIP_sea_20210703__002_AI_maps_Fit_parameters_4p

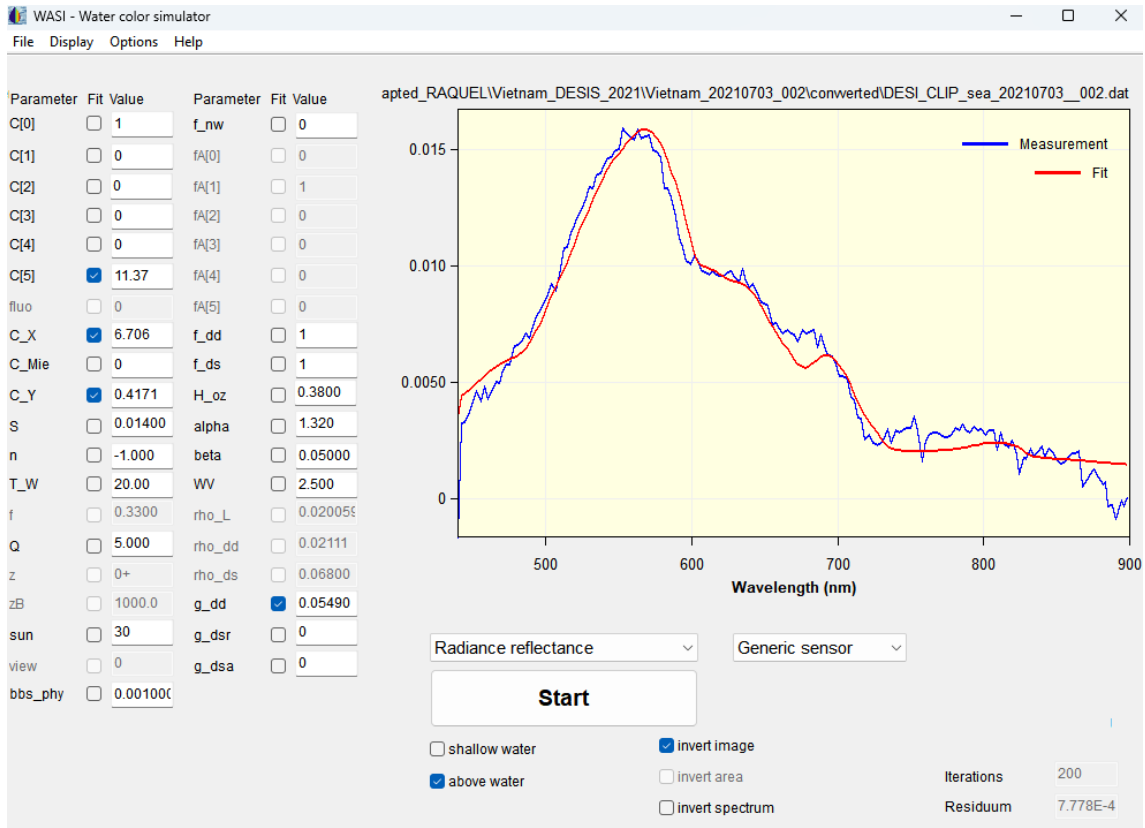


Figure 93: DESIS image date 2021-07-03 parameter data setup.

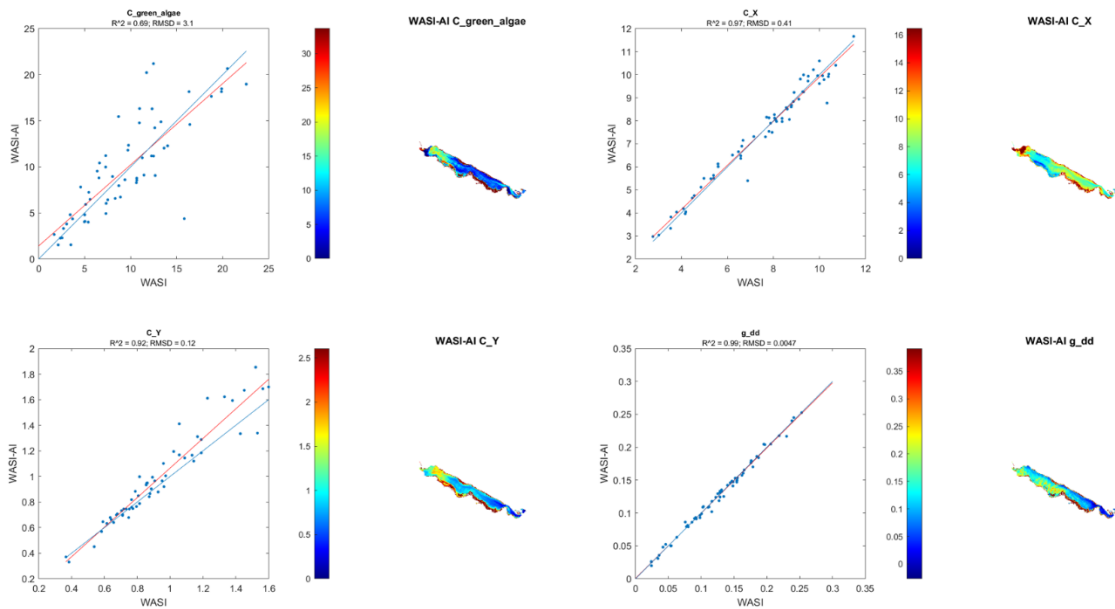


Figure 94: DESIS image date 2021-07-03 process results.

Automatic name folder after processing WASI-AI:
 DESI_CLIP_sea_20210703__003_AI_maps_Fit_parameters_4p

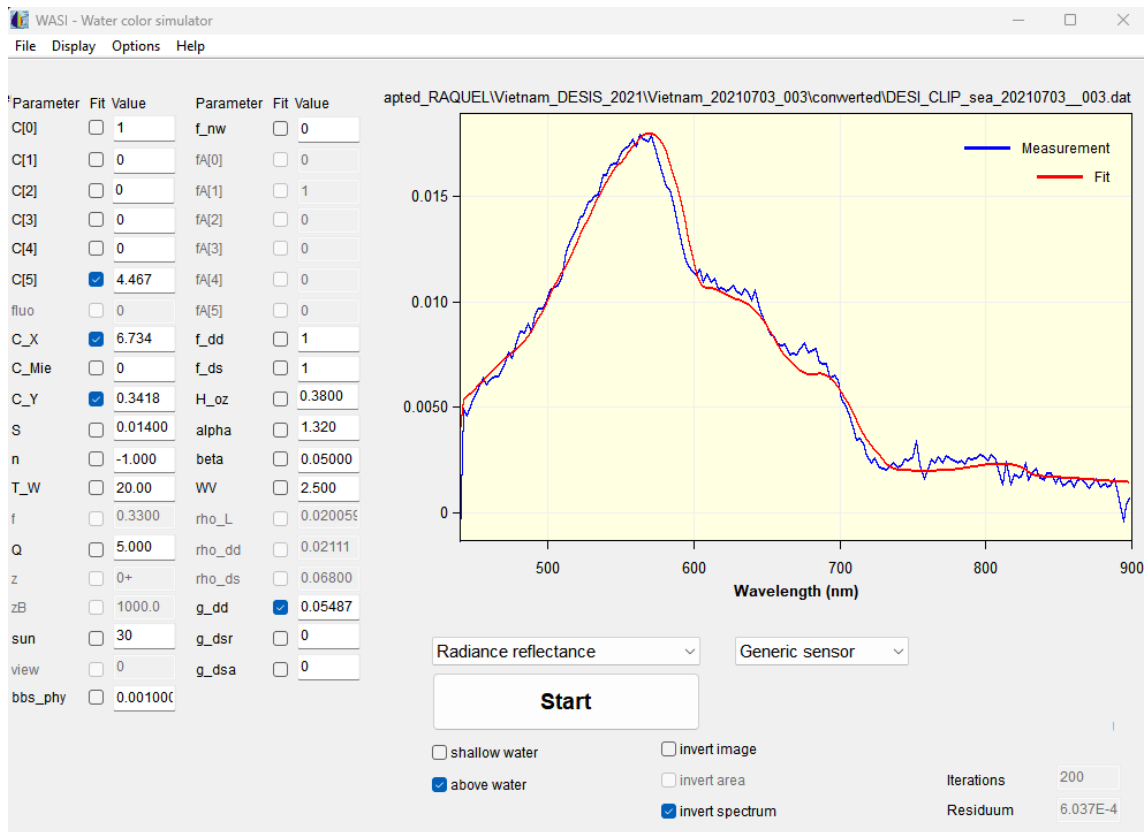


Figure 95: DESIS image date 2021-07-03 parameter data setup.

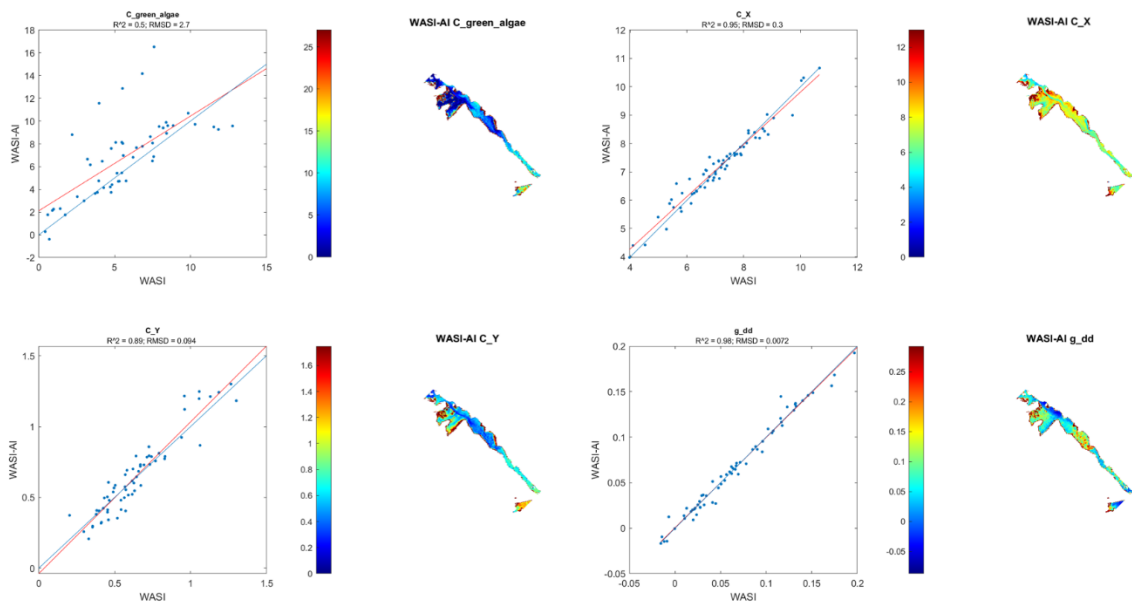


Figure 96: DESIS image date 2021-07-03 process results.

Automatic name folder after processing WASI-AI:
 DESI_CLIP_sea_20210703_004_AI_maps_Fit_parameters_4p

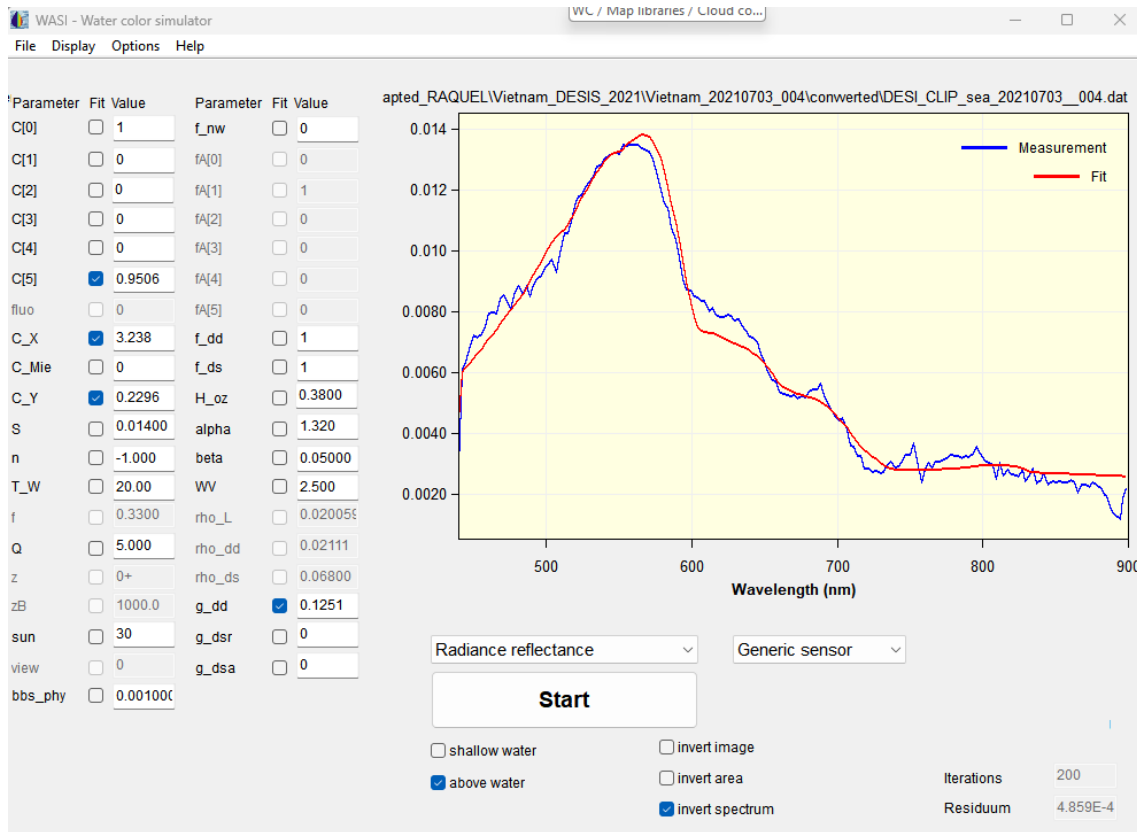


Figure 97: DESIS image date 2021-07-03 parameter data setup.

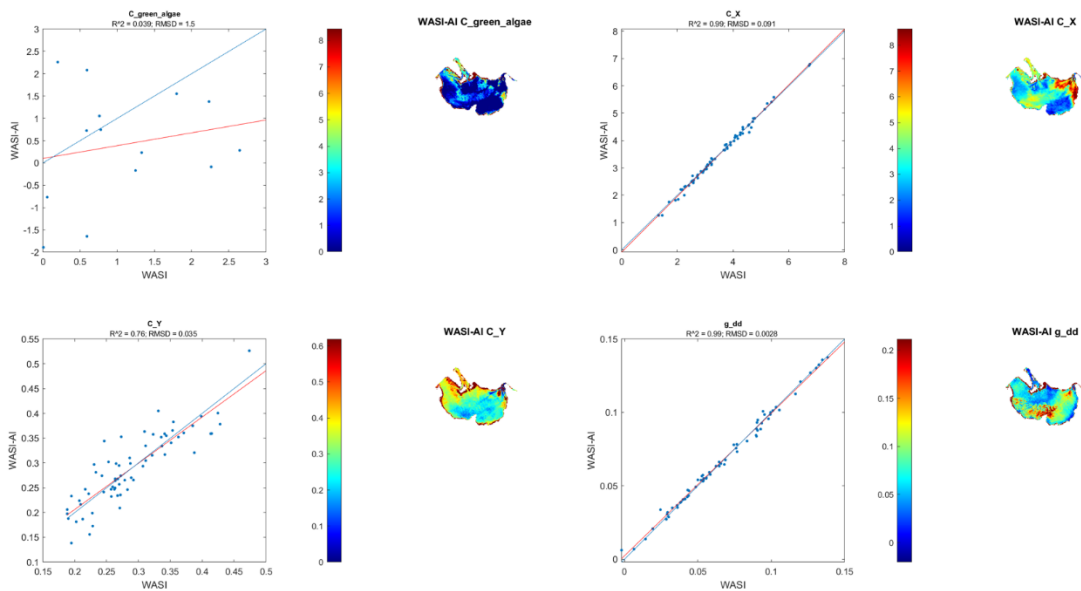


Figure 98: DESIS image date 2021-07-03 process results.

Automatic name folder after processing WASI-AI:
 DESIS_CIP_sea_20220601_AI_maps_Fit_parameters_4p

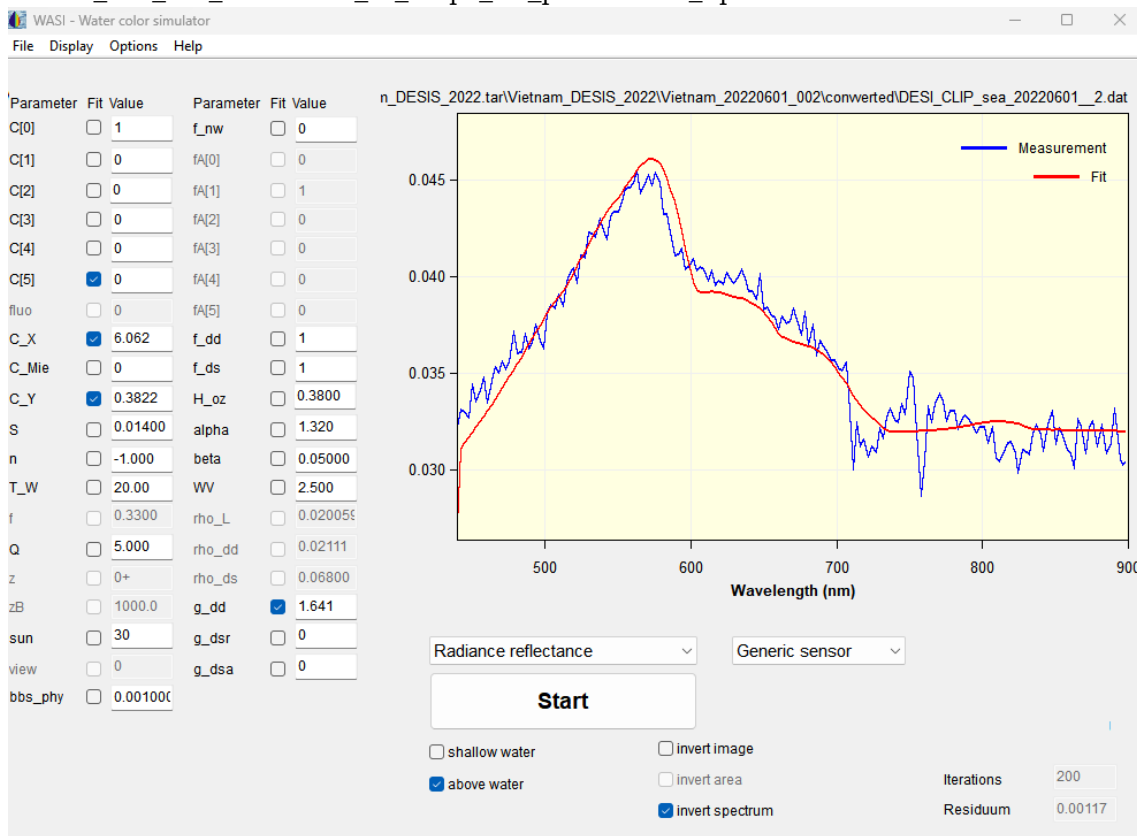


Figure 99: DESIS image date 2022-06-01 parameter data setup.

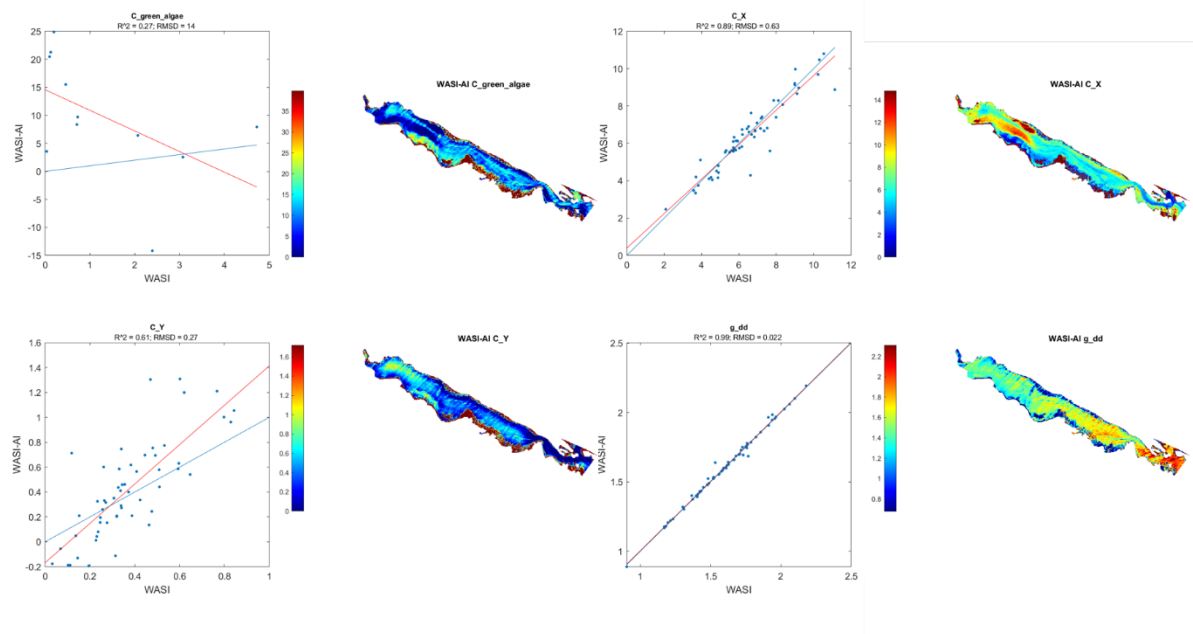


Figure 100: DESIS image date 2022-06-01 process results.

Automatic name folder after processing WASI-AI:
 DESIS_CIP_20220605_001_AI_maps_Fit_parameters_4p

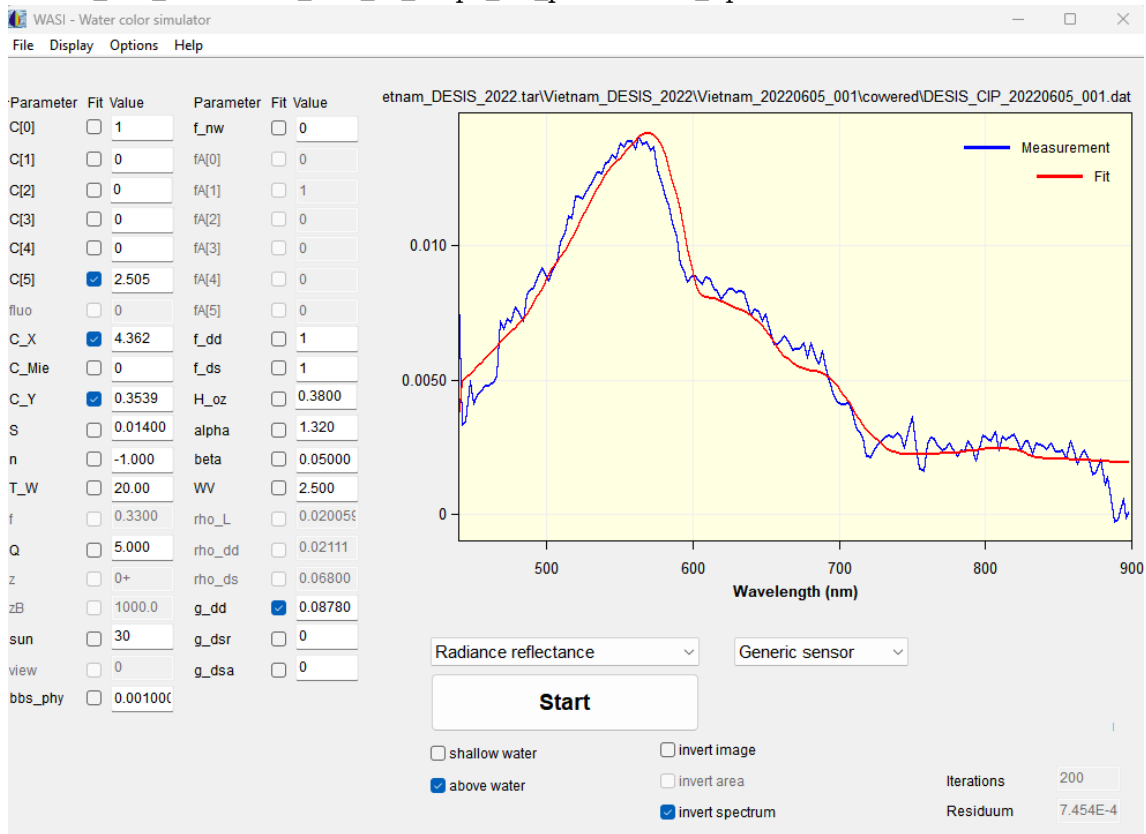


Figure 101: DESIS image date 2022-06-05 parameter data setup.

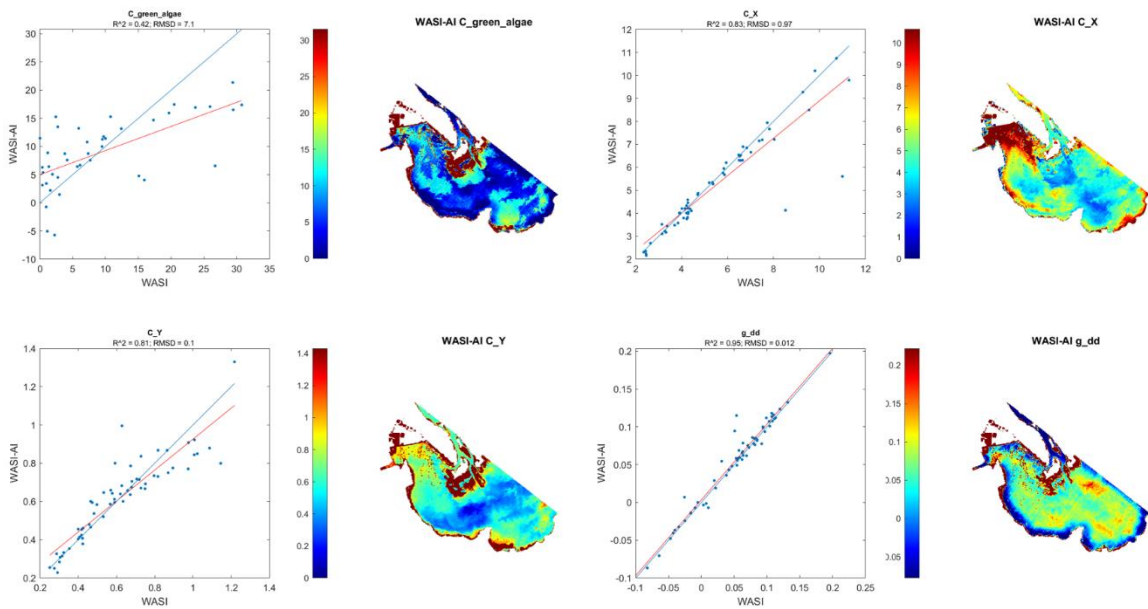


Figure 102: DESIS image date 2022-06-05 process results.

Automatic name folder after processing WASI-AI:
 DESIS_CIP_20220605_002_AI_maps_Fit_parameters_4p.png

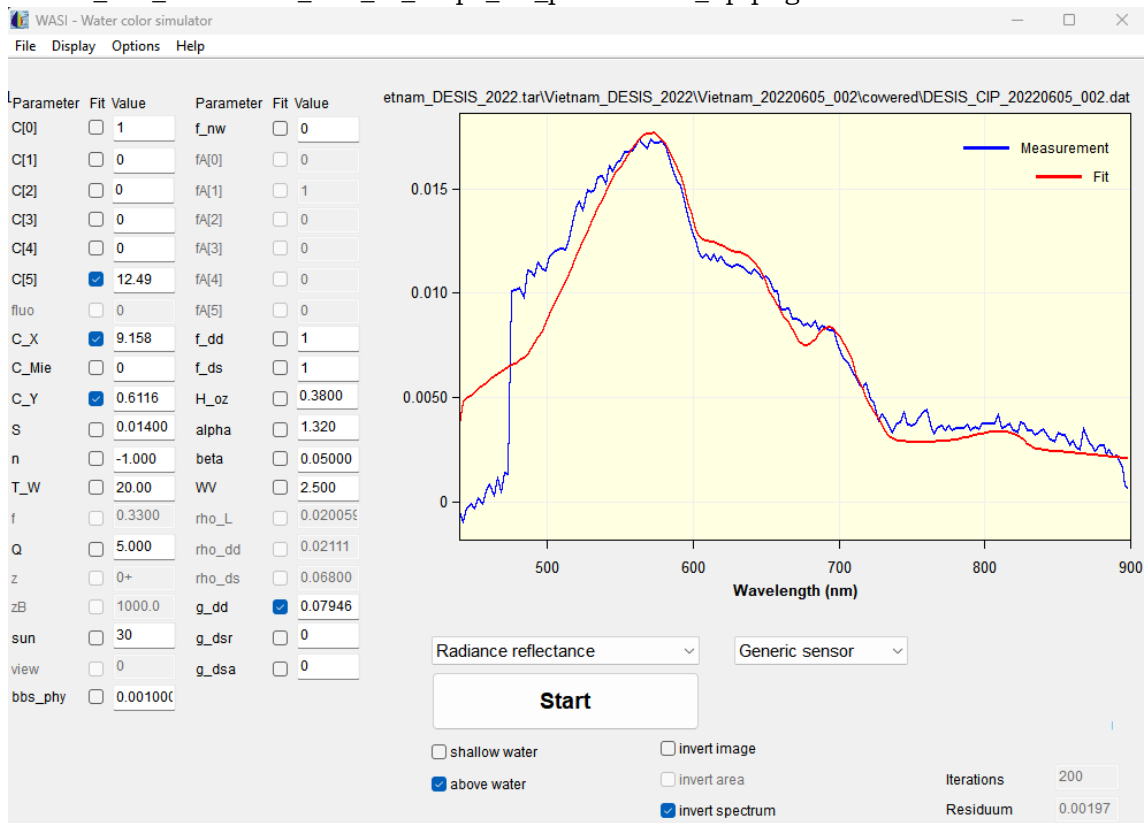


Figure 103: DESIS image date 2022-06-05 parameter data setup.

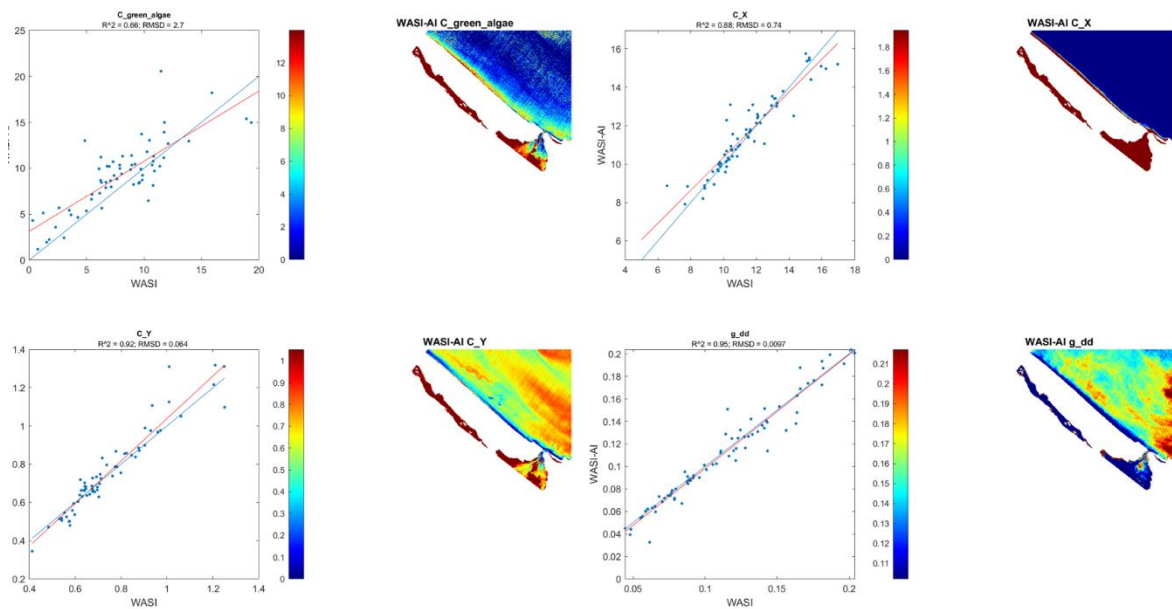


Figure 104: DESIS image date 2022-06-05 process results.

Automatic name folder after processing WASI-AI:
 DESIS_CLIP_20230322_002_AI_maps_Fit_parameters_4p

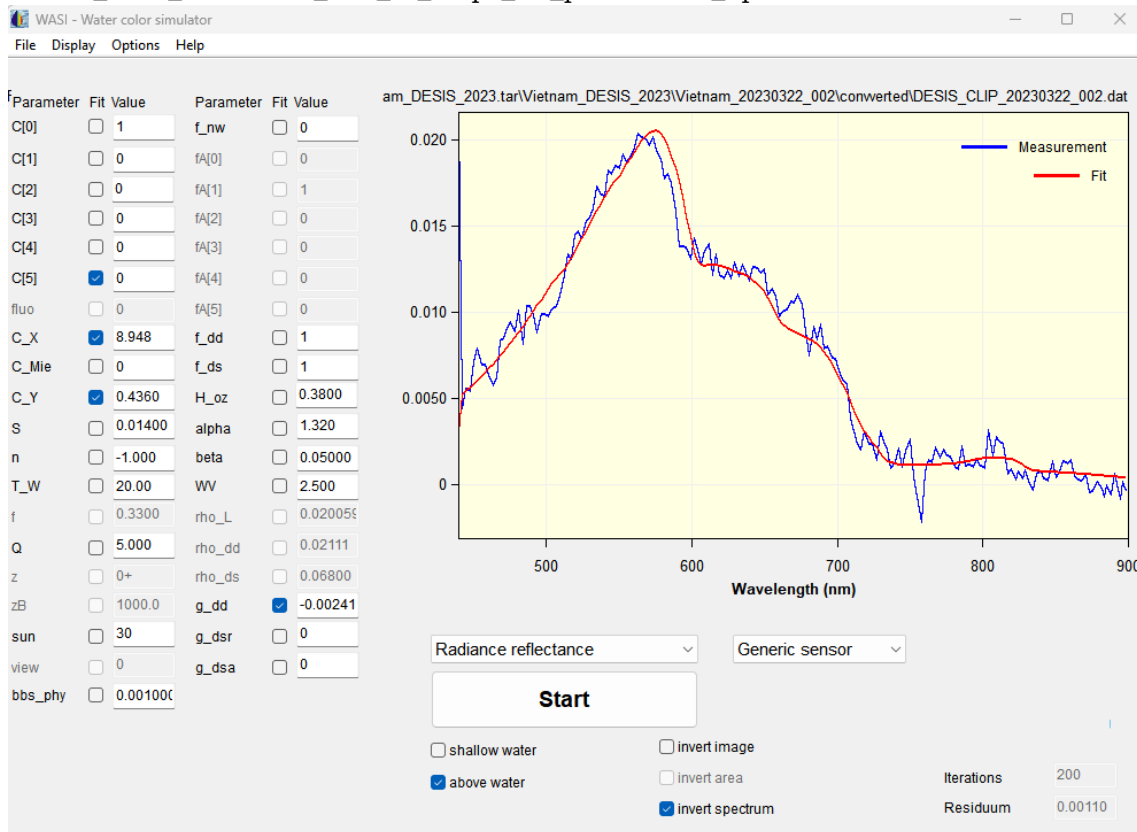


Figure 105: DESIS image date 2023-03-22 parameter data setup.

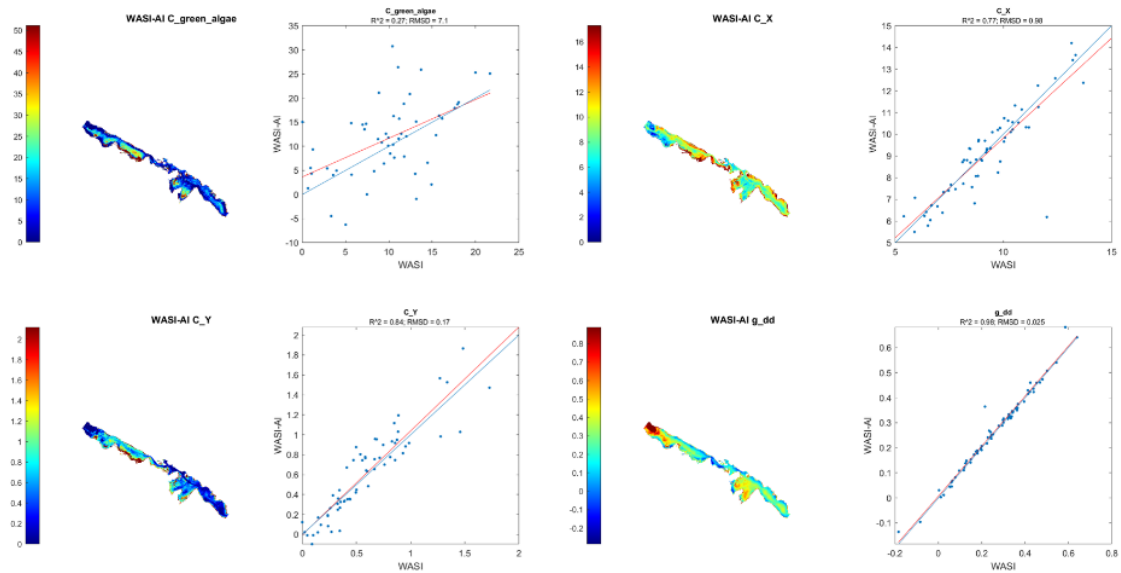


Figure 106: DESIS image date 2023-03-22 process results.

Automatic name folder after processing WASI-AI:
 DESIS_CLIP_20230503_002_AI_maps_Fit_parameters_4p

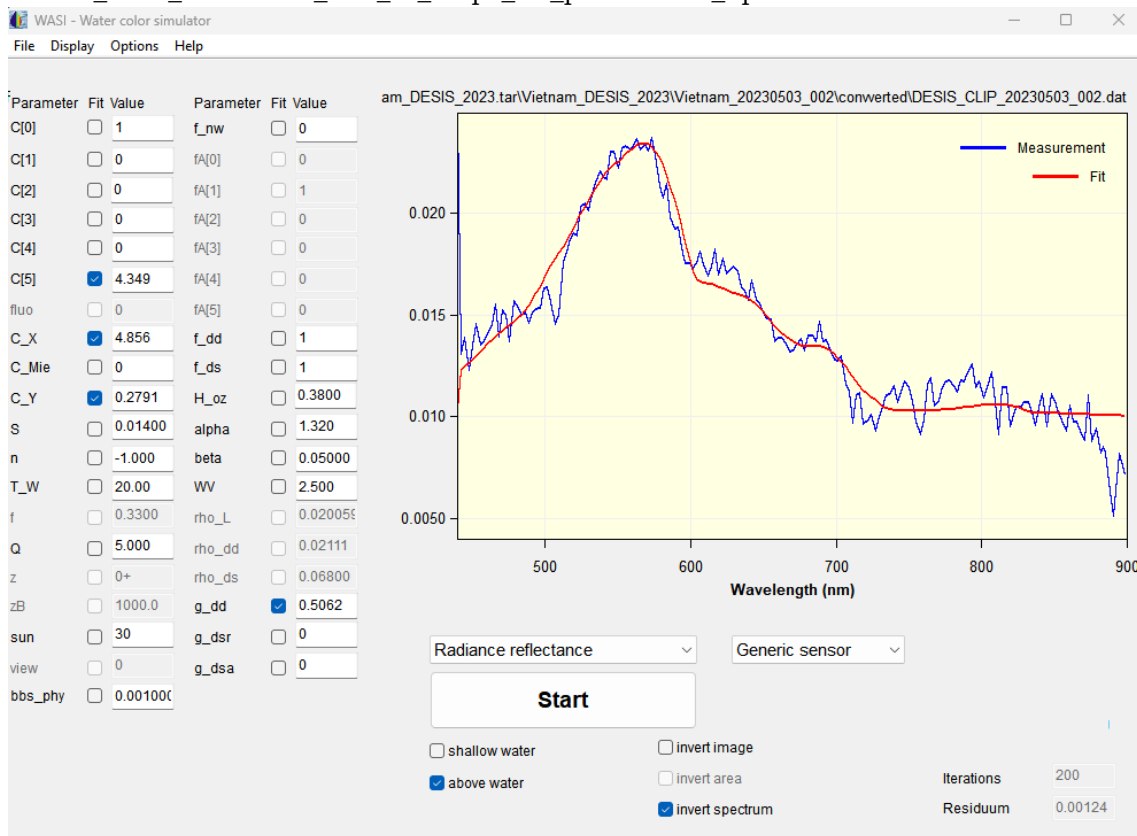


Figure 107: DESIS image date 2023-05-03 parameter data setup.

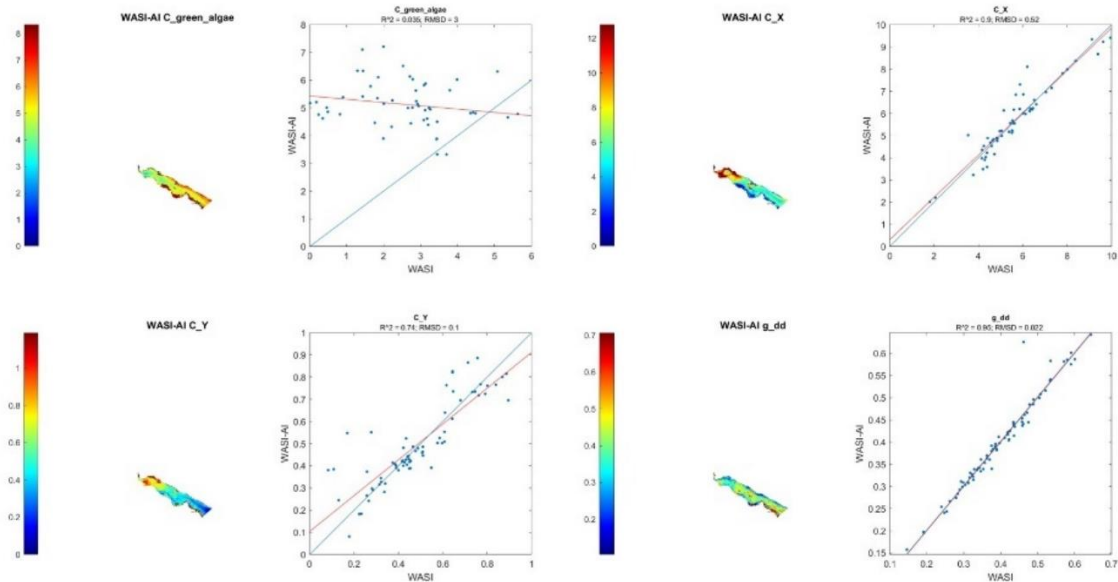


Figure 108: DESIS image date 2023-05-03 process results.

Automatic name folder after processing WASI-AI:
 DESIS_CLIP_20230503_003_AI_maps_Fit_parameters_4p

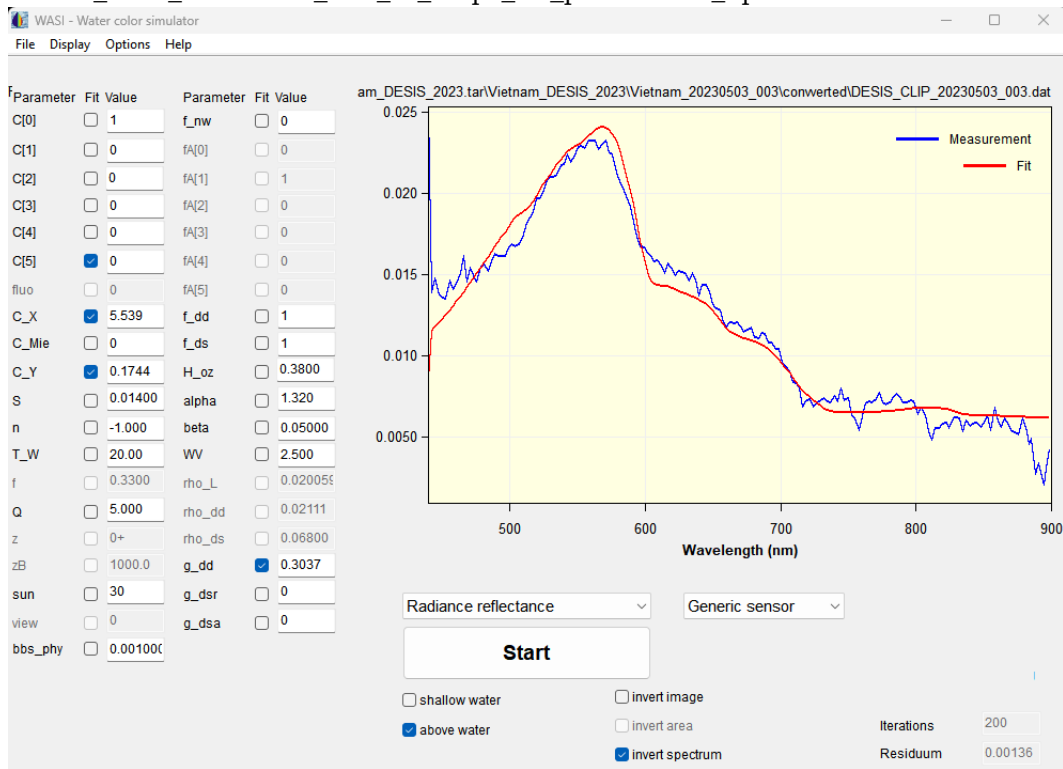


Figure 109: DESIS image date 2023-05-03 parameter data setup.

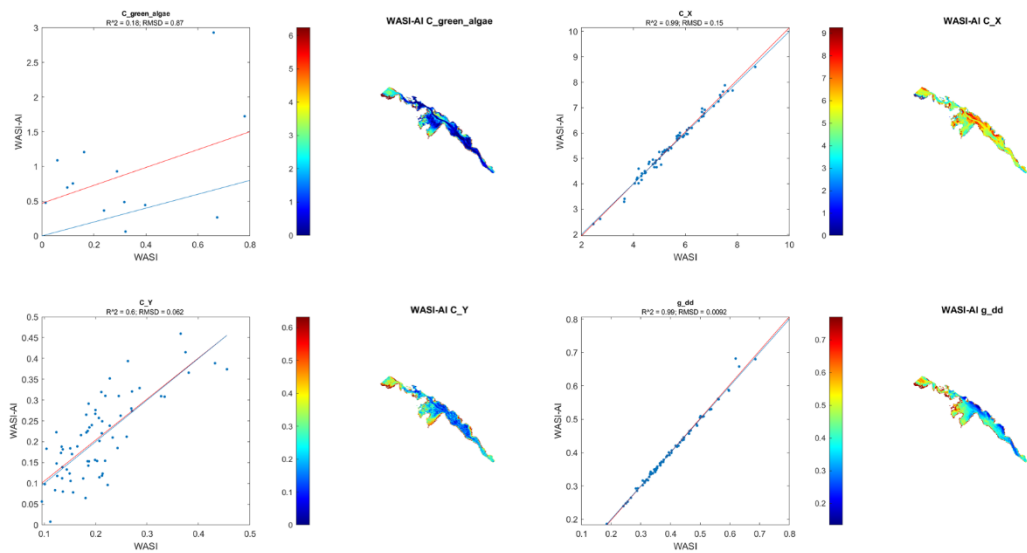


Figure 110: DESIS image date 2023-05-03 process results.

Automatic name folder after processing WASI-AI:
 DESIS_CLIP_20230503_004_AI_maps_Fit_parameters_4p

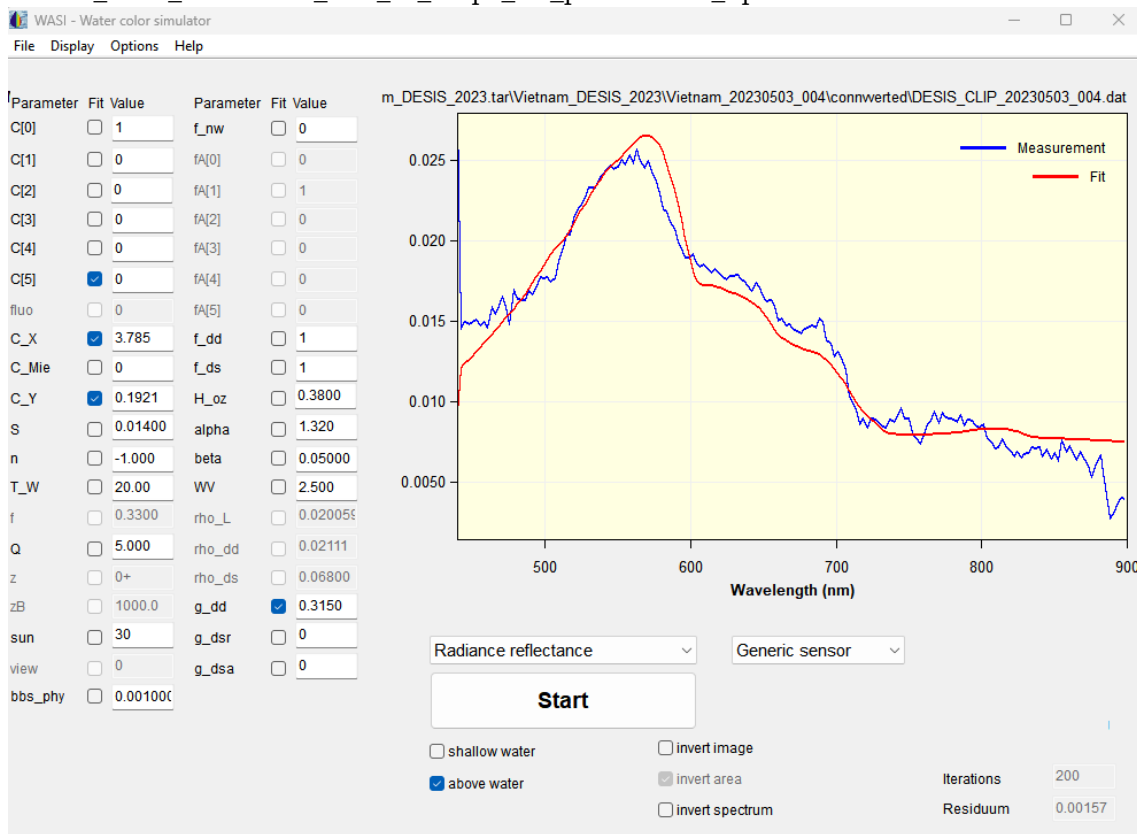


Figure 111: DESIS image date 2023-05-03 parameter data setup.

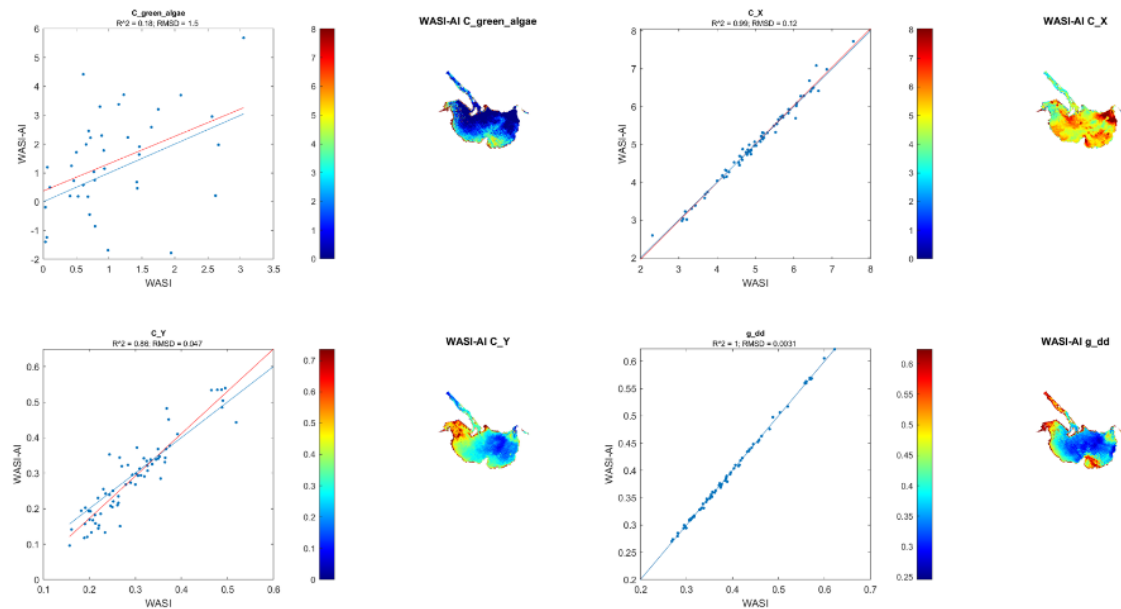


Figure 112: DESIS image date 2023-05-03 process results.

Automatic name folder after processing WASI-AI:
 DESIS_CLIP_20230507_002_AI_maps_Fit_parameters_4p

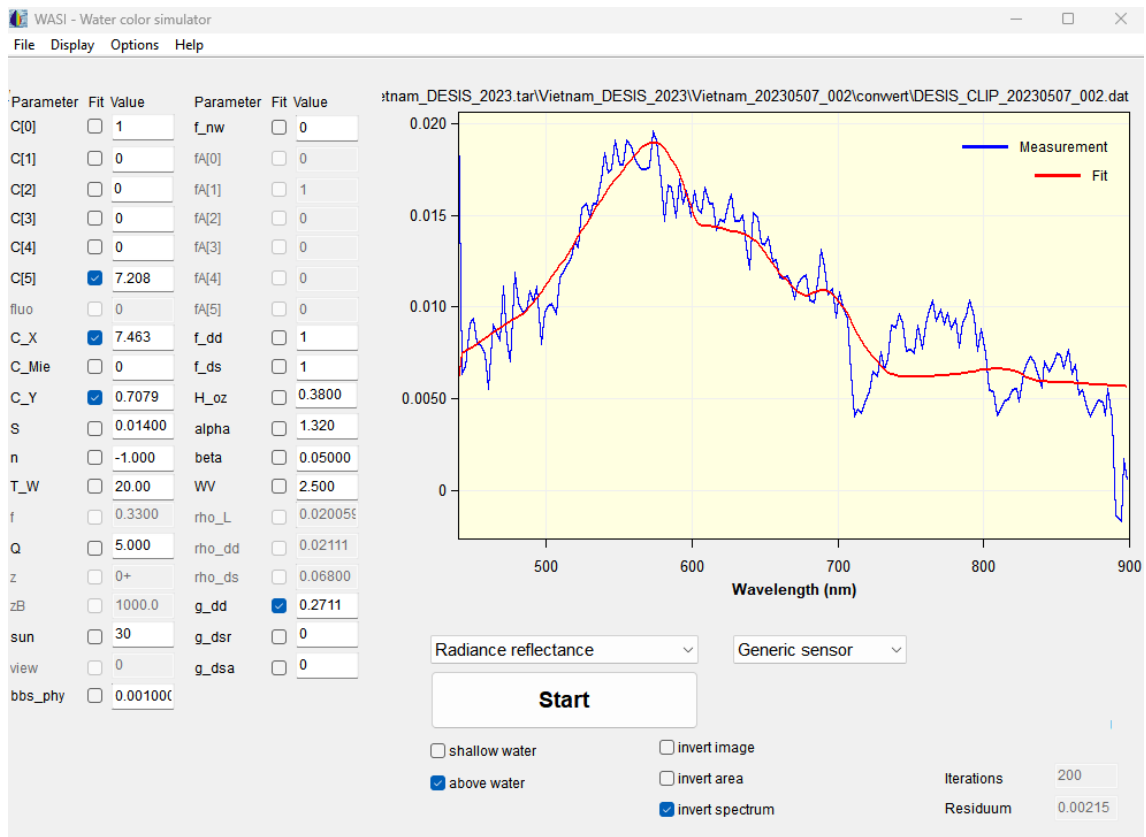


Figure 113: DESIS image date 2023-05-07 parameter data setup version 1.

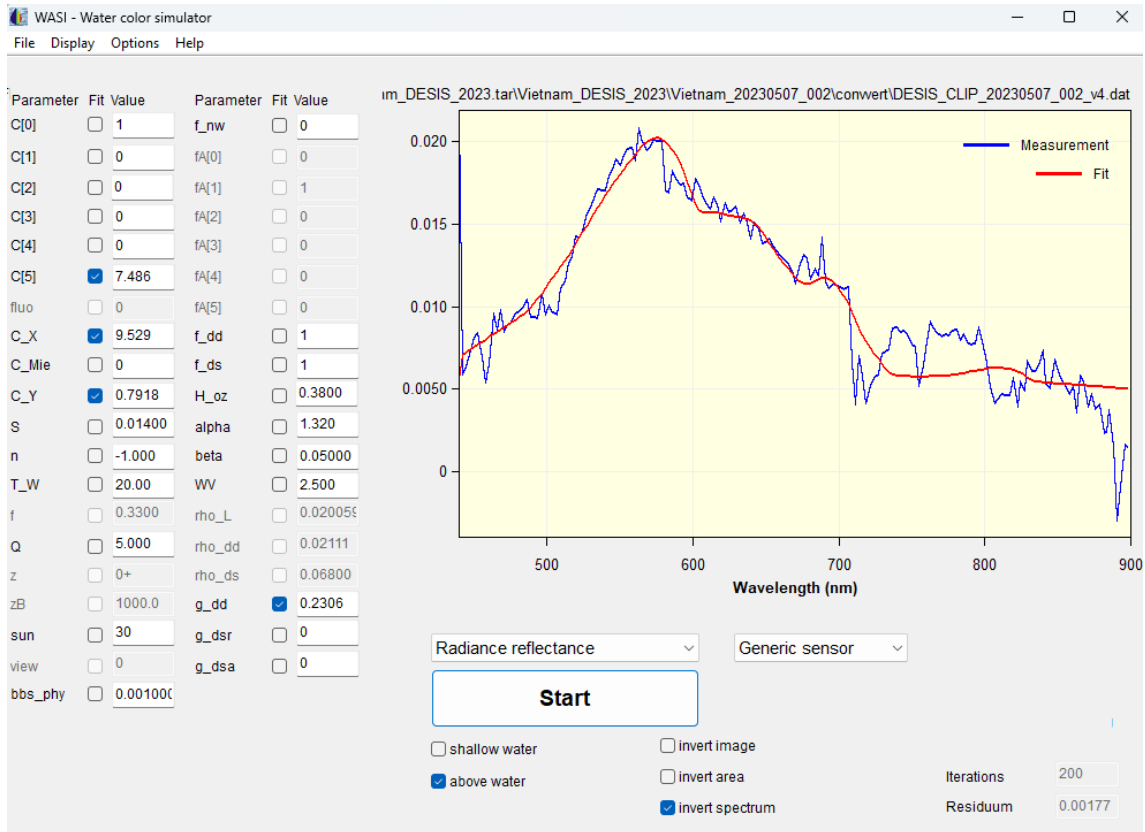


Figure 114: DESIS image date 2023-05-07 parameter data setup version 2.

This image is noisy in general, but it has brought good results. also, in the image, there are stripes of the satellite.

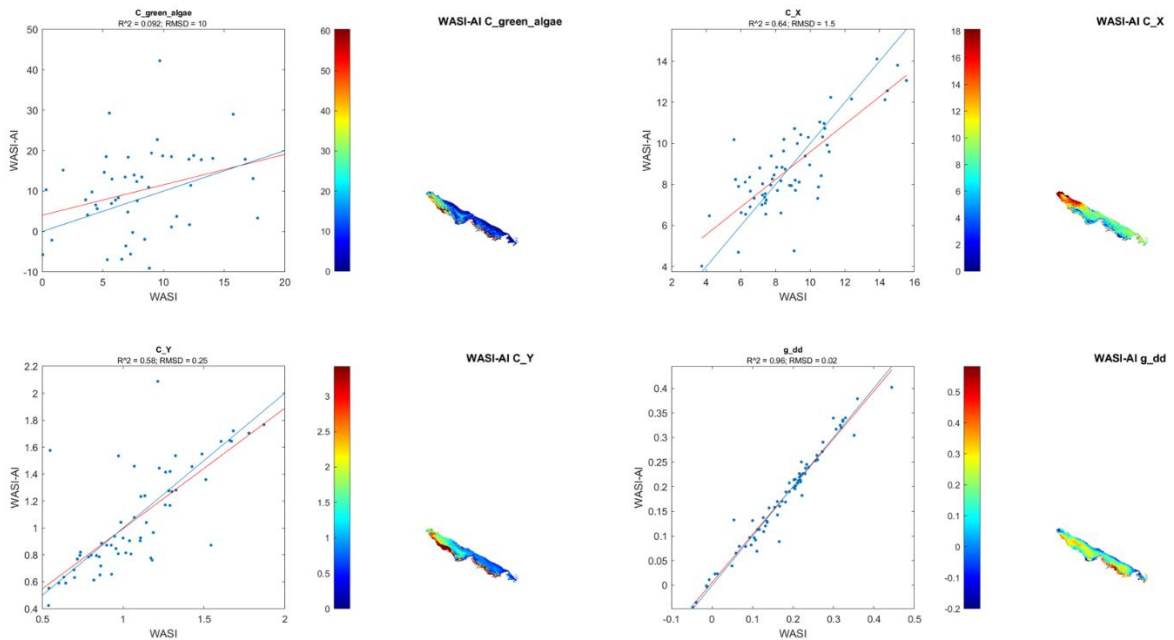


Figure 115: DESIS image date 2023-05-07 process results.

Automatic name folder after processing WASI-AI:
 DESIS_CLIP_20230507_003_AI_maps_Fit_parameters_4p

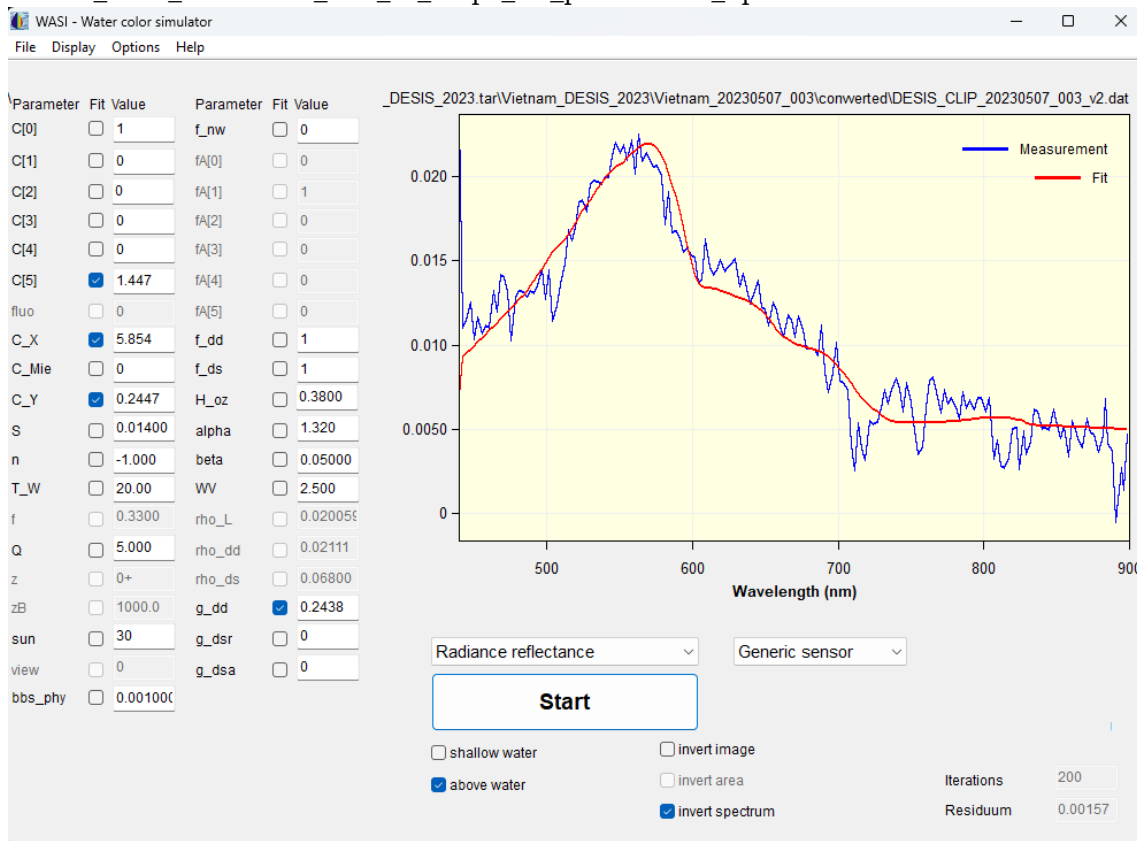


Figure 116: DESIS image date 2023-05-07 parameter data setup.

The second processing

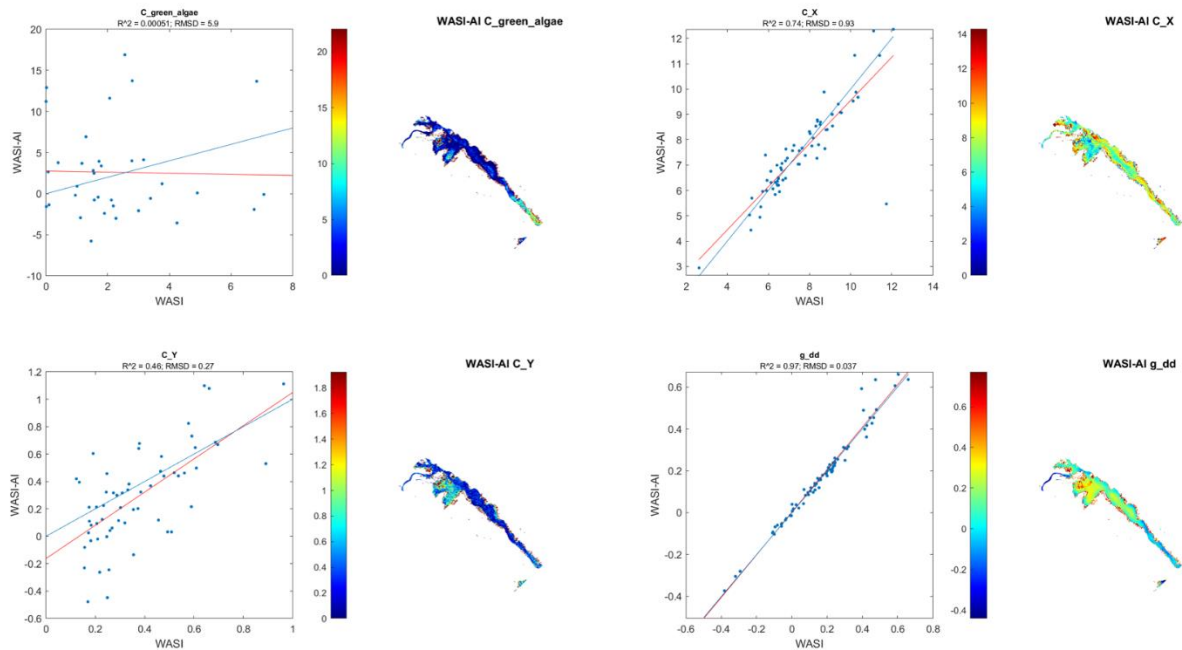


Figure 117: DESIS image date 2023-05-07 process results.

Automatic name folder after processing WASI-AI:
 DESIS_CLIP_20230507_004_AI_maps_Fit_parameters

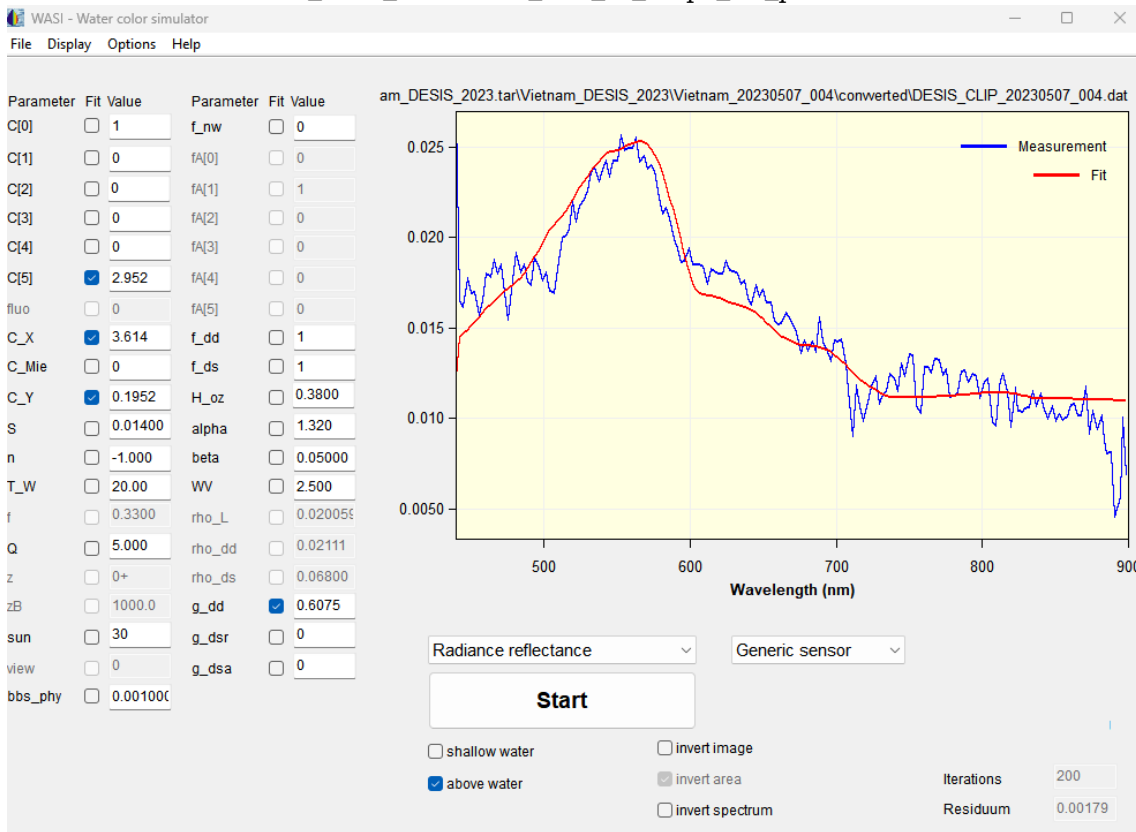


Figure 118: DESIS image date 2023-05-07 parameter data setup.

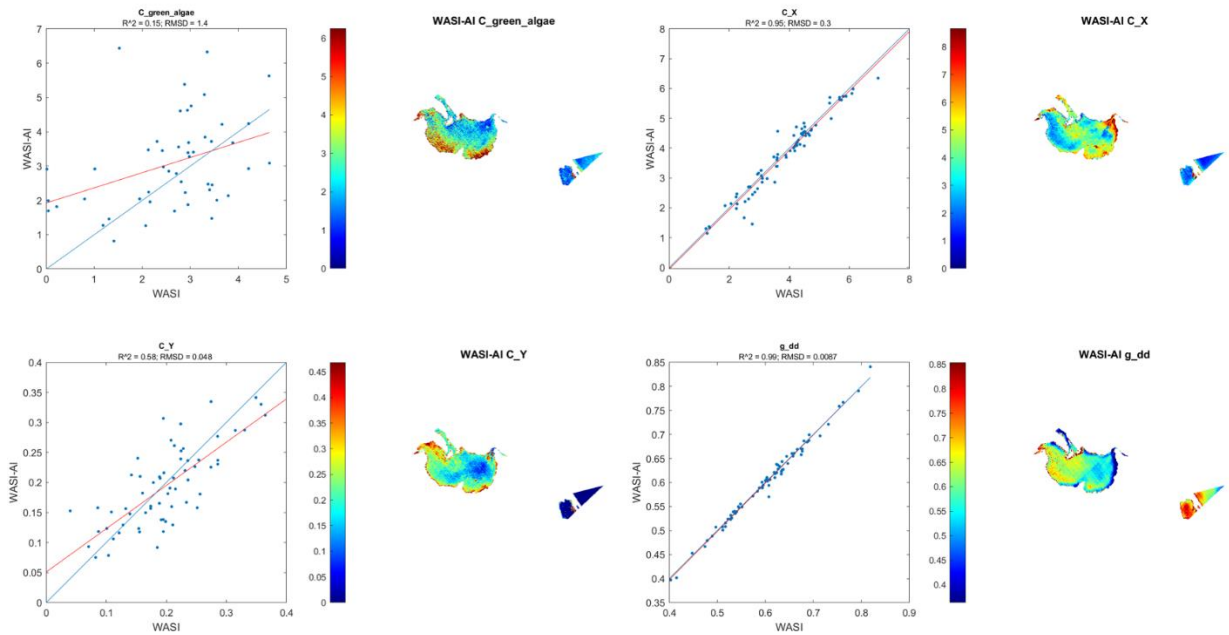


Figure 119: DESIS image date 2023-05-07 process results.

Automatic name folder after processing WASI-AI:
 DESIS_CLIP_20230506_002_AI_maps_Fit_parameters_4p

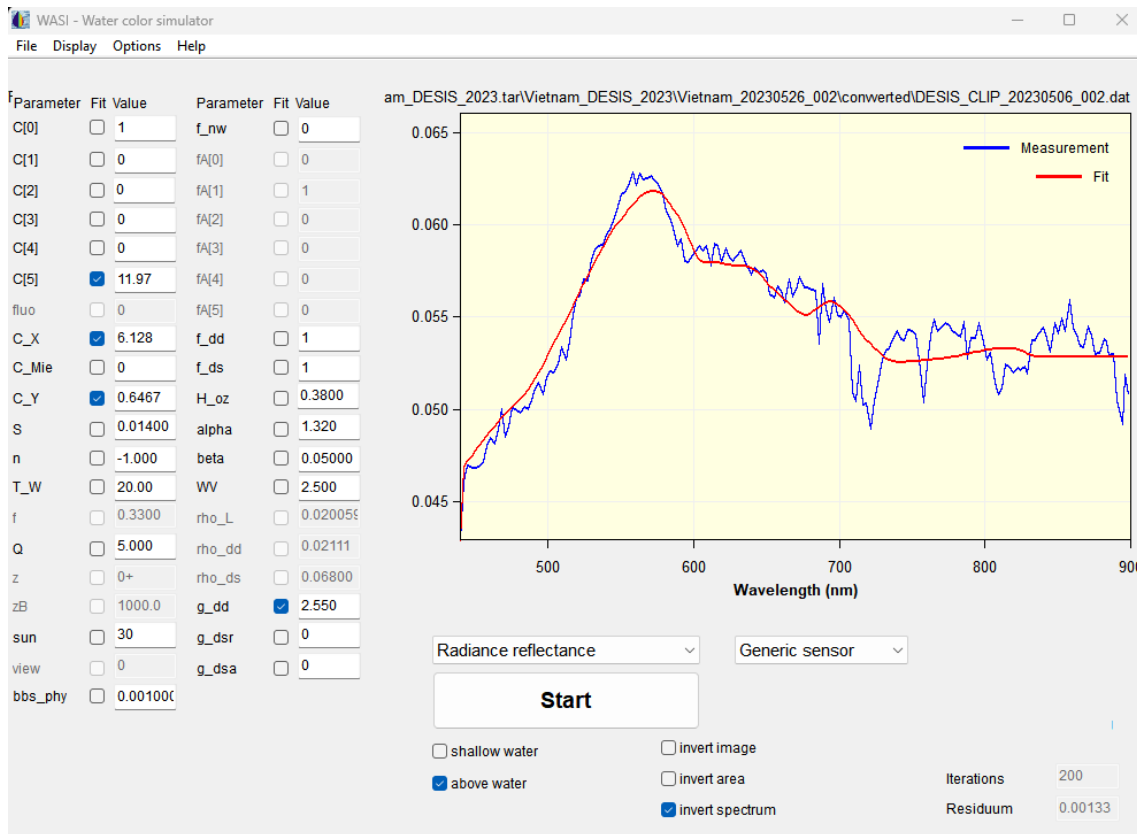


Figure 120: DESIS image date 2023-05-06 parameter data setup.

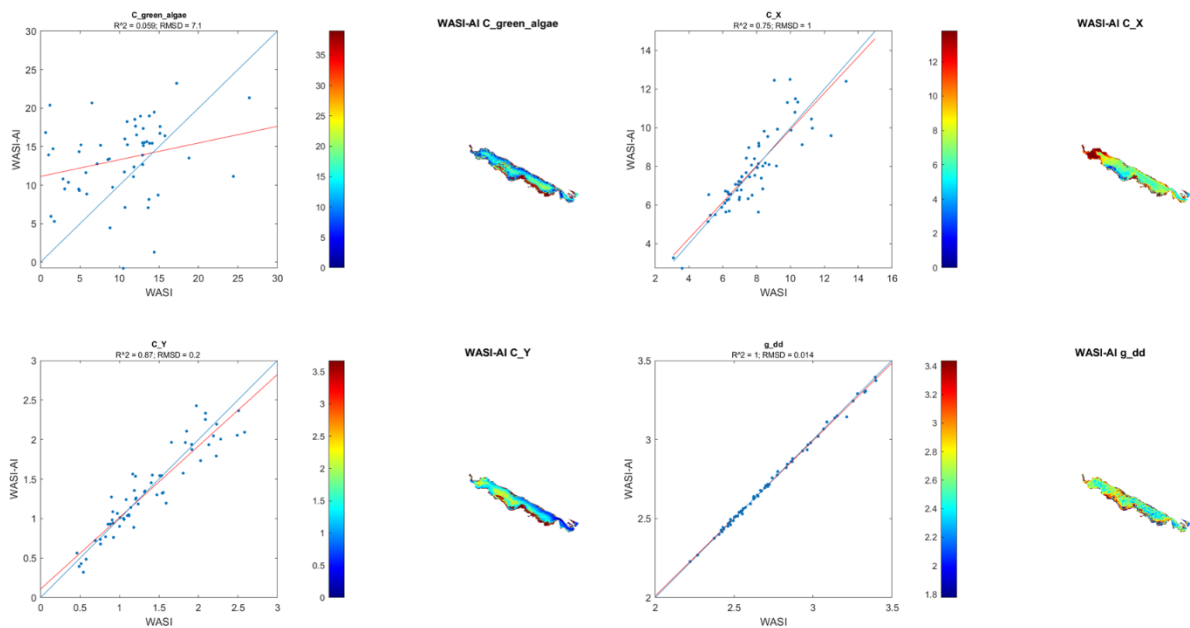


Figure 121: DESIS image date 2023-05-06 process results.

Automatic name folder after processing WASI-AI:
 DESIS_CLIP_20230706_003_AI_maps_Fit_parameters_4p

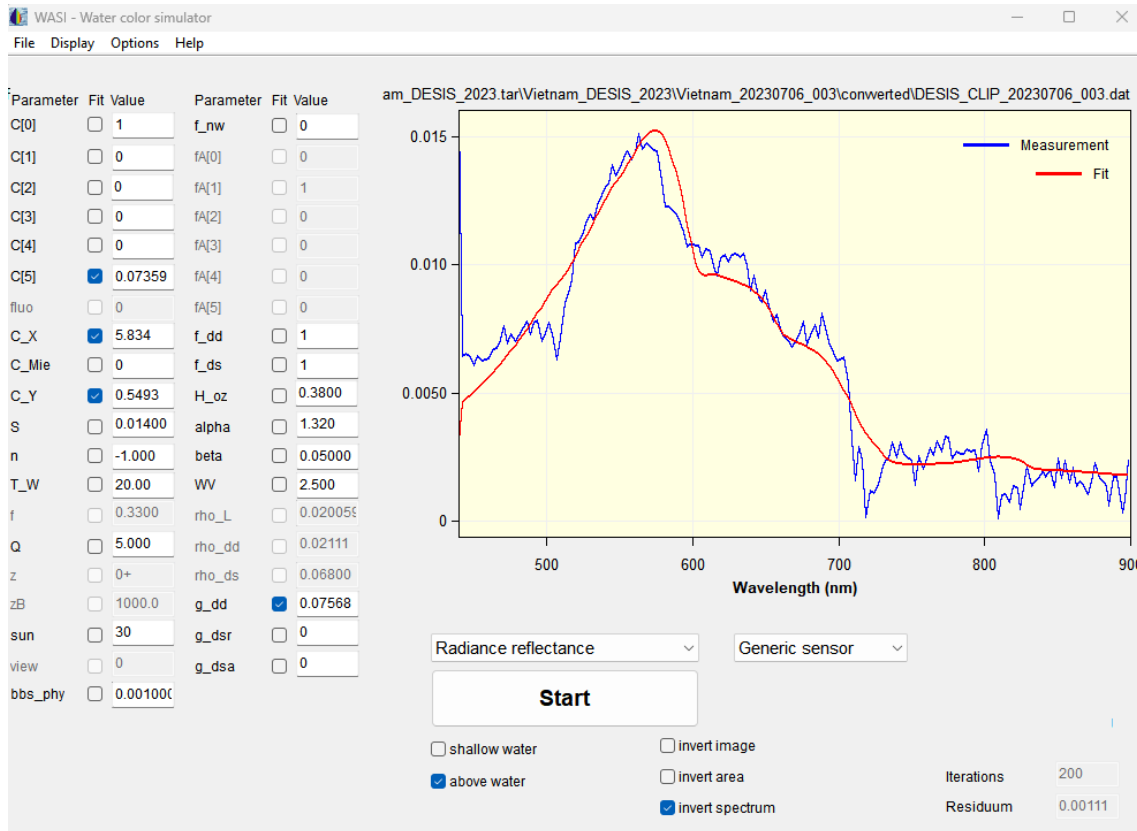


Figure 122: DESIS image date 2023-07-06 parameter data setup.

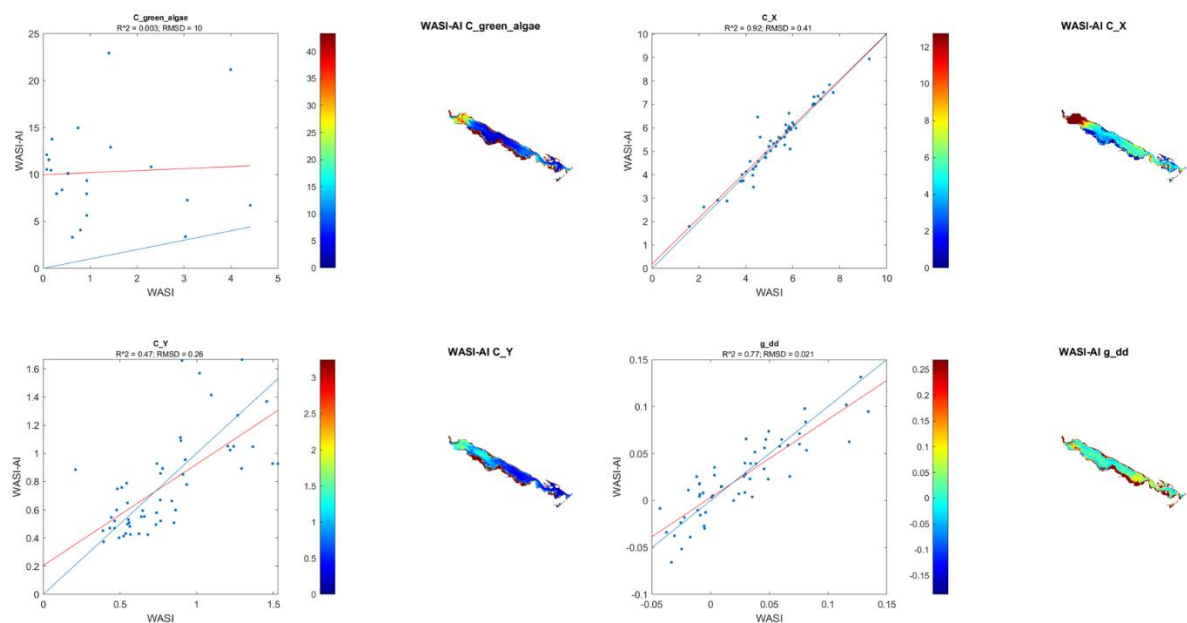


Figure 123: DESIS image date 2023-07-06 process results.

Automatic name folder after processing WASI-AI:
 DESIS_20230706_004_AI_maps_Fit_parameters_4p

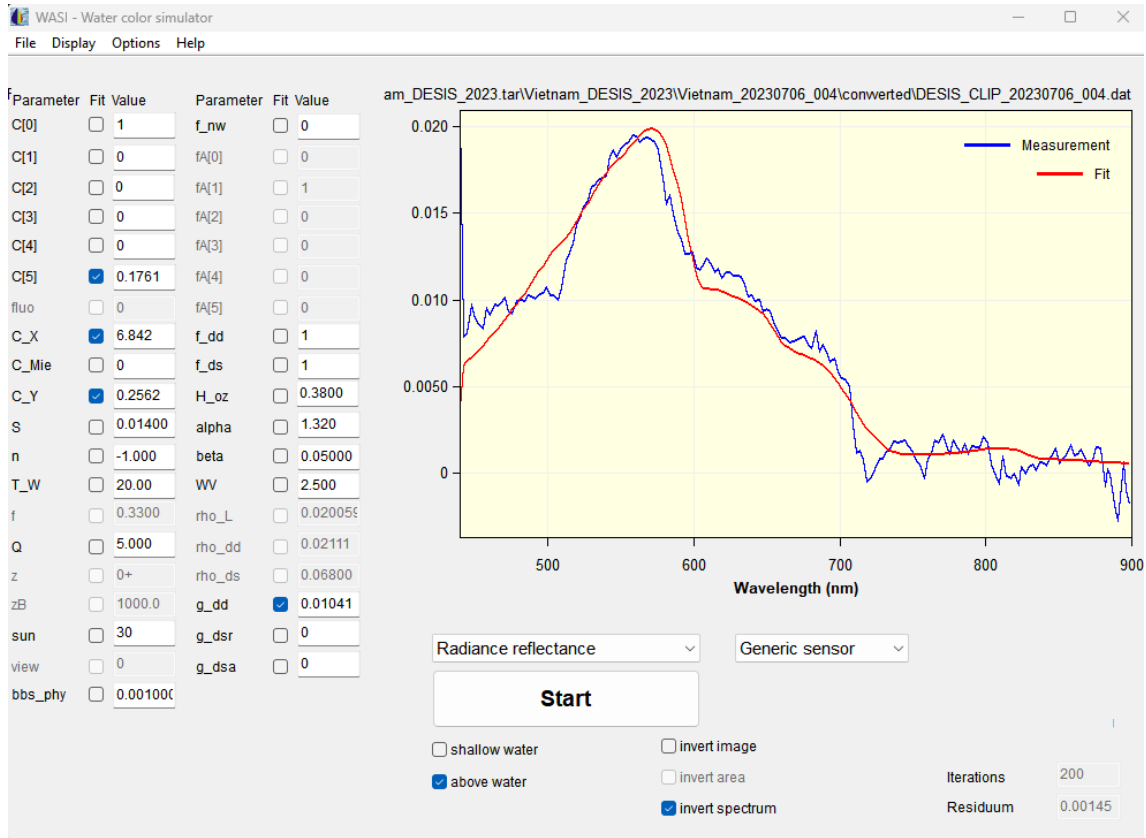


Figure 124: DESIS image date 2023-07-06 parameter data setup.

The best result was with a none clip image.

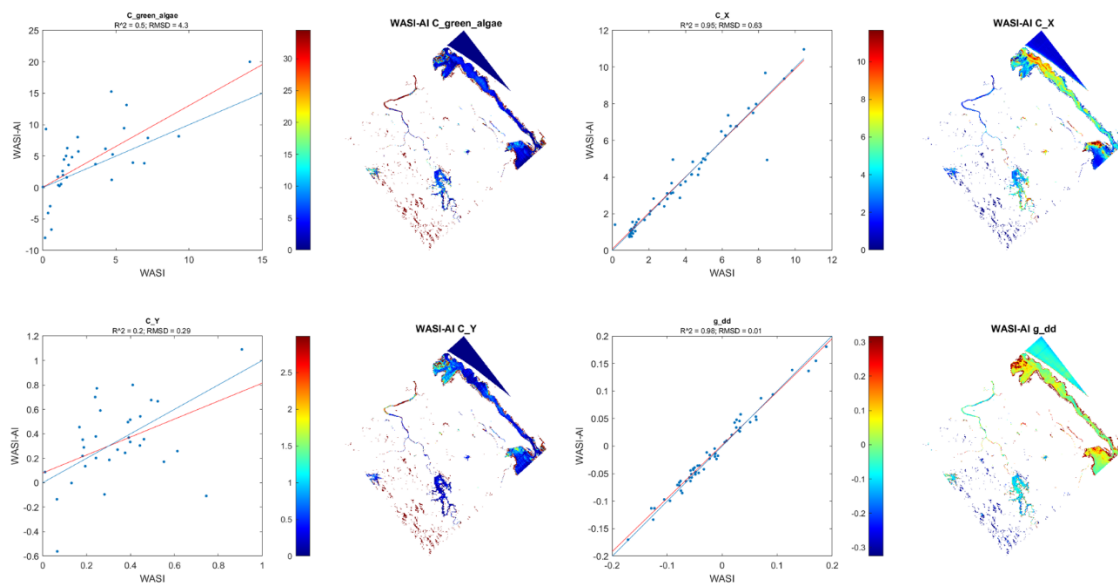


Figure 125: DESIS image date 2023-07-06 process results.

Automatic name folder after processing WASI-AI:
 DESIS_CLIP_20230706_005_AI_samples_4p

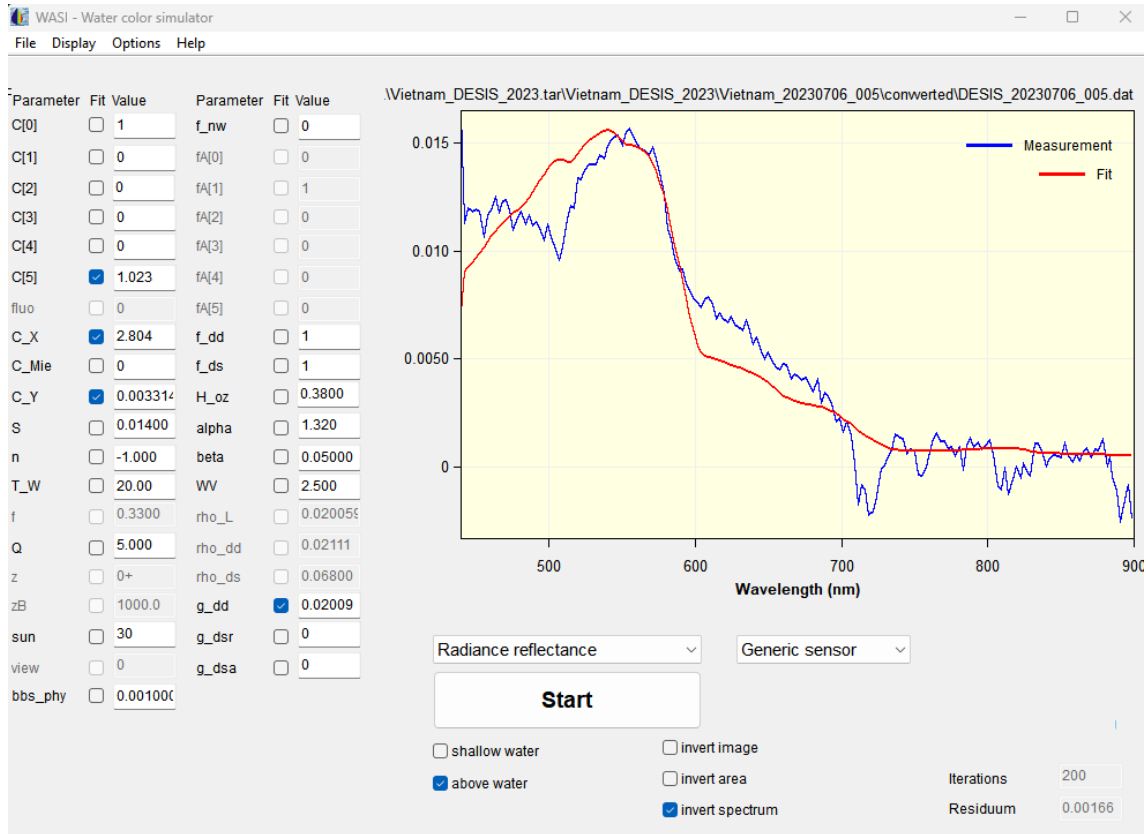


Figure 126: DESIS image date 2023-10-29 parameter data setup. Distortion data in this result is not included due to deformation on the lagoon.

Automatic name folder after processing WASI-AI:
 DESIS_CLIP_20231029_003_AI_maps_Fit_parameters_4p

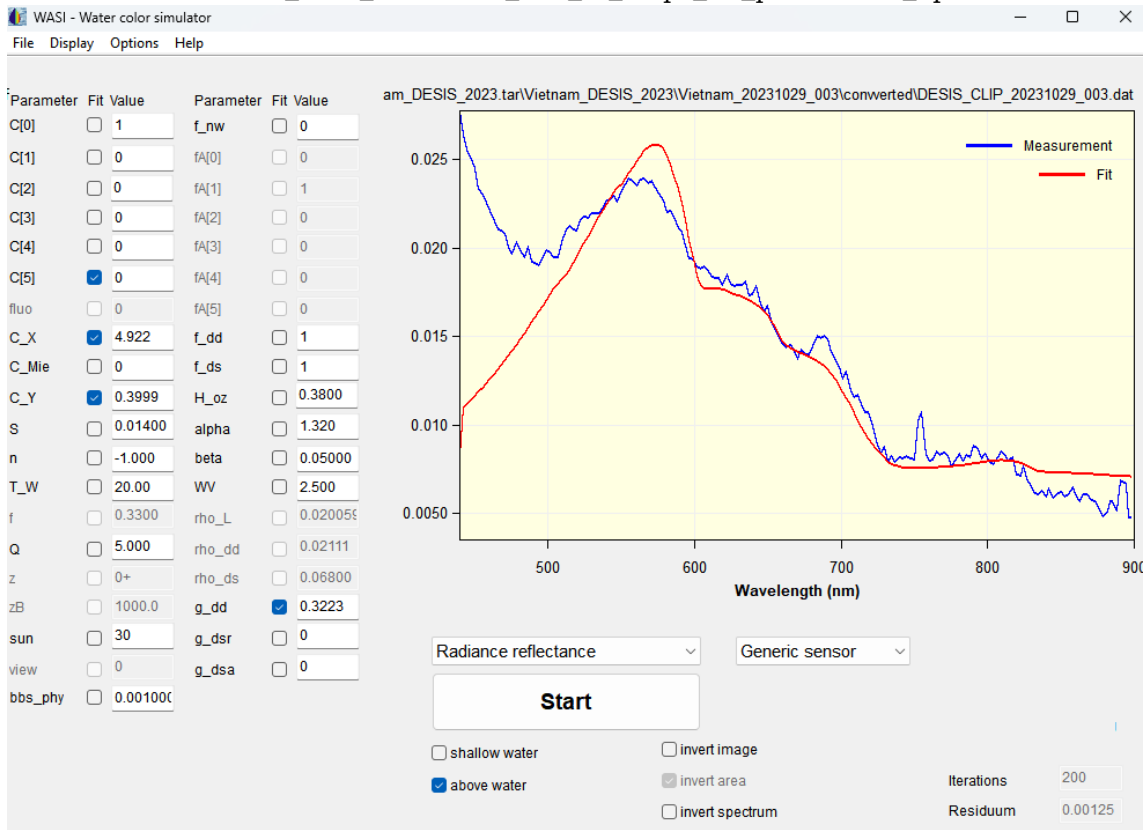


Figure 127: DESIS image date 2023-10-29 parameter data setup.

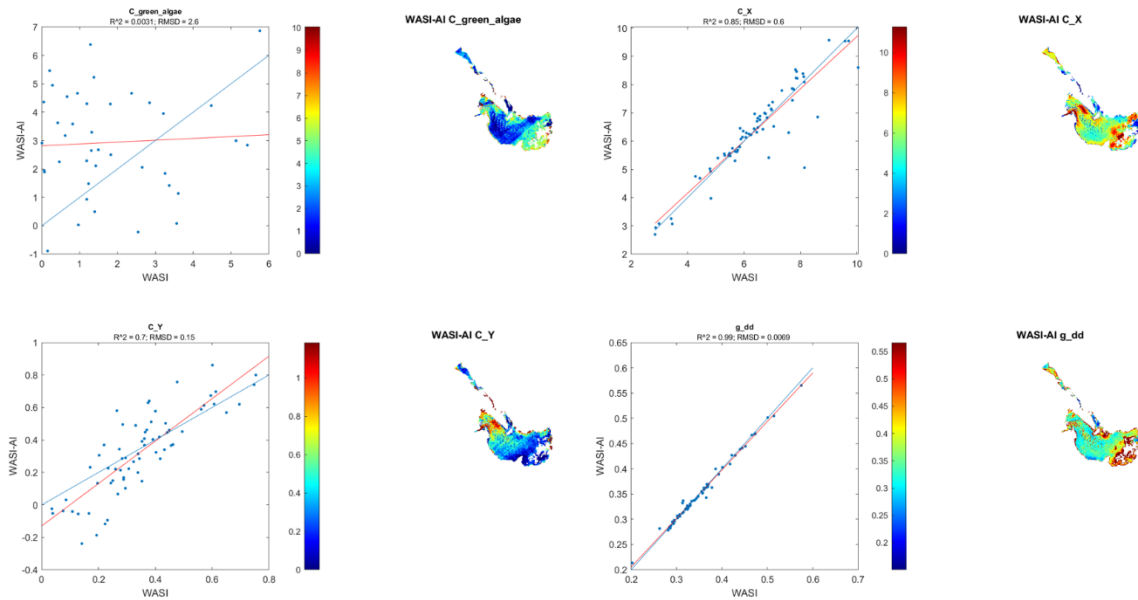


Figure 128: DESIS image date 2023-10-29 process results.

9 ENMAP RESULTS OF THE FIRST AND SECOND ATTEMPT

First Attempt WASI software Model of shallow waters:

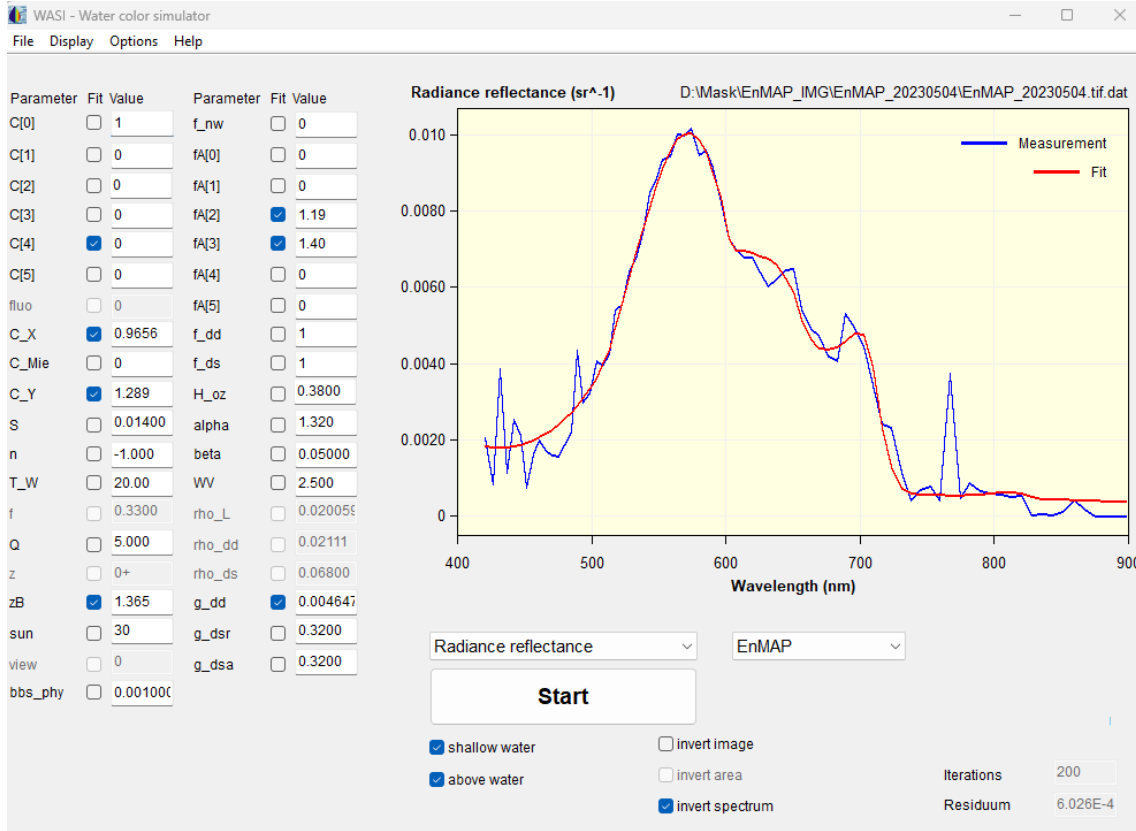


Figure 129: Fit parameters EnMAP_20230504.tif_AI_validation_Fit_parameters_6p.

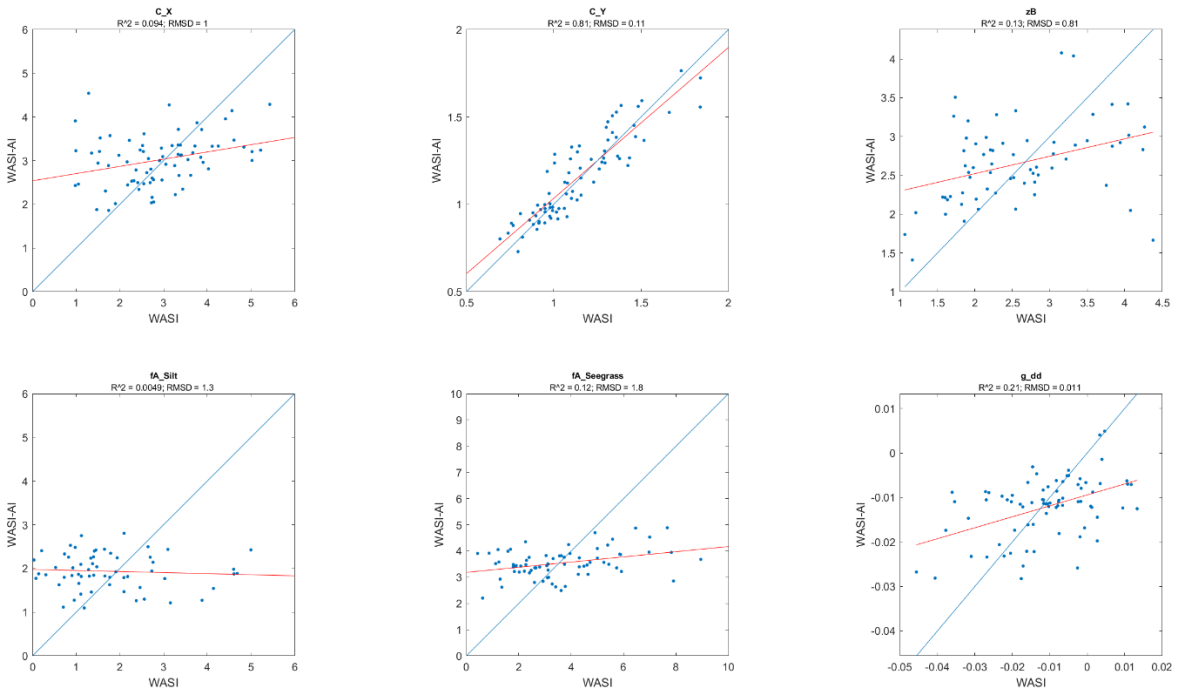


Figure 130: Water quality estimation parameter R² Error EnMAP_20230504.tif_AI_validation_Fit_parameters_6p.

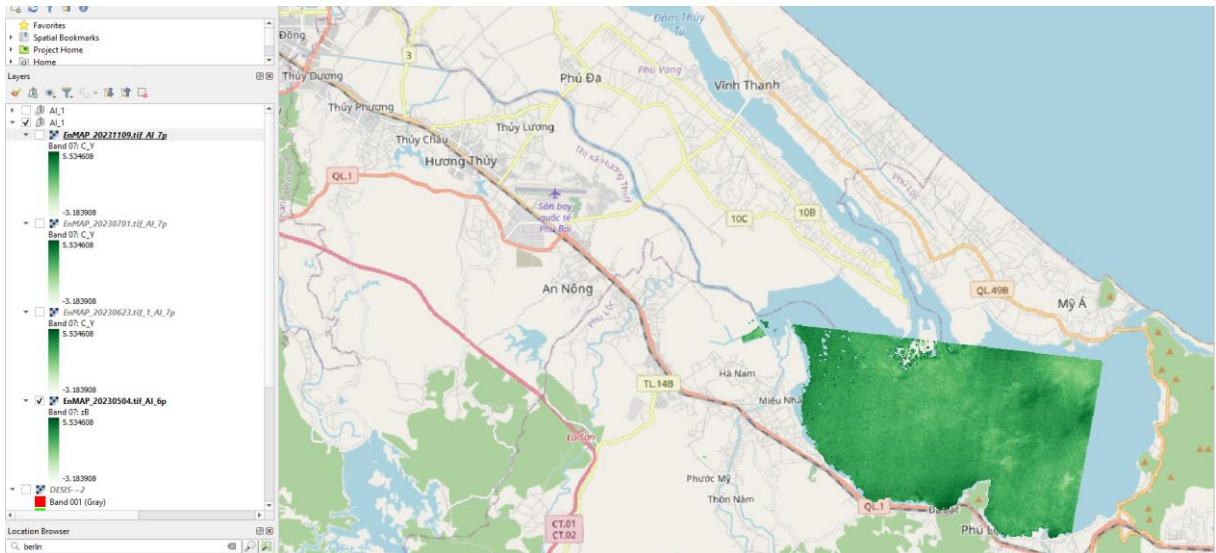


Figure 131: C_Y CDOM normalized to the minimum and maximum EnMAP_20230504.tif AI validation Fit parameters_6p.

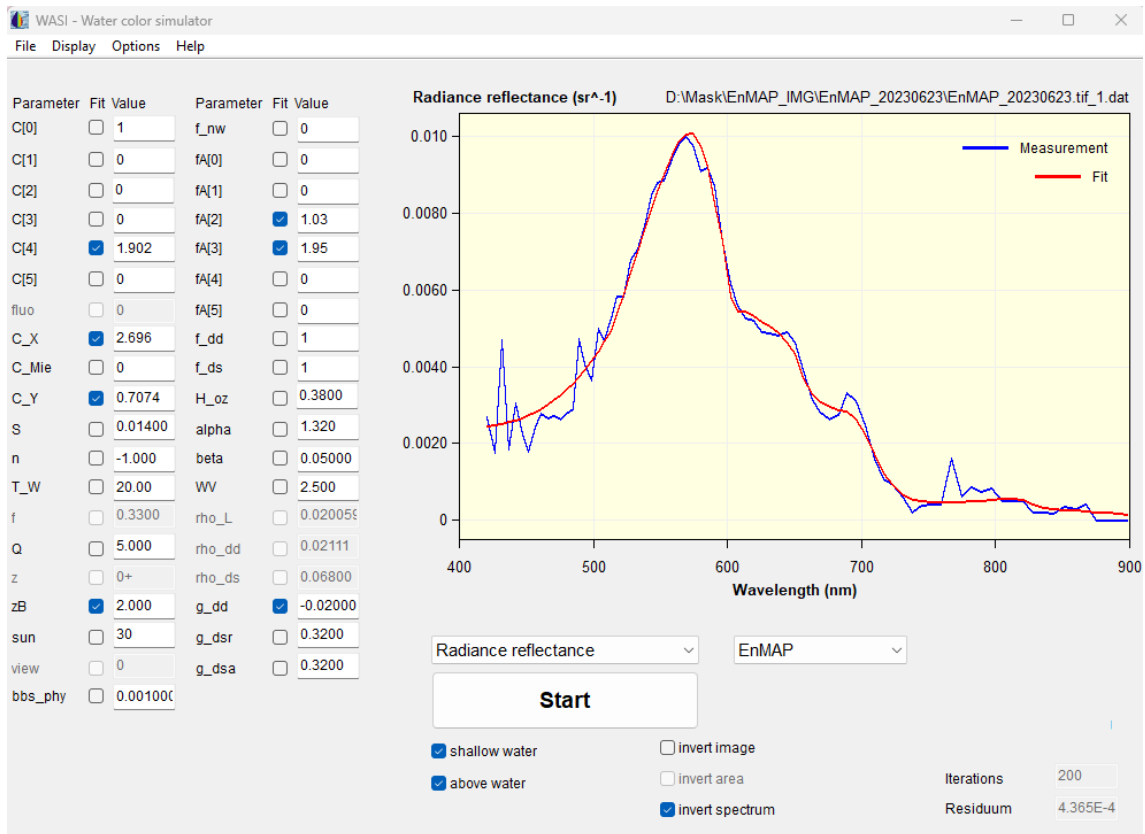
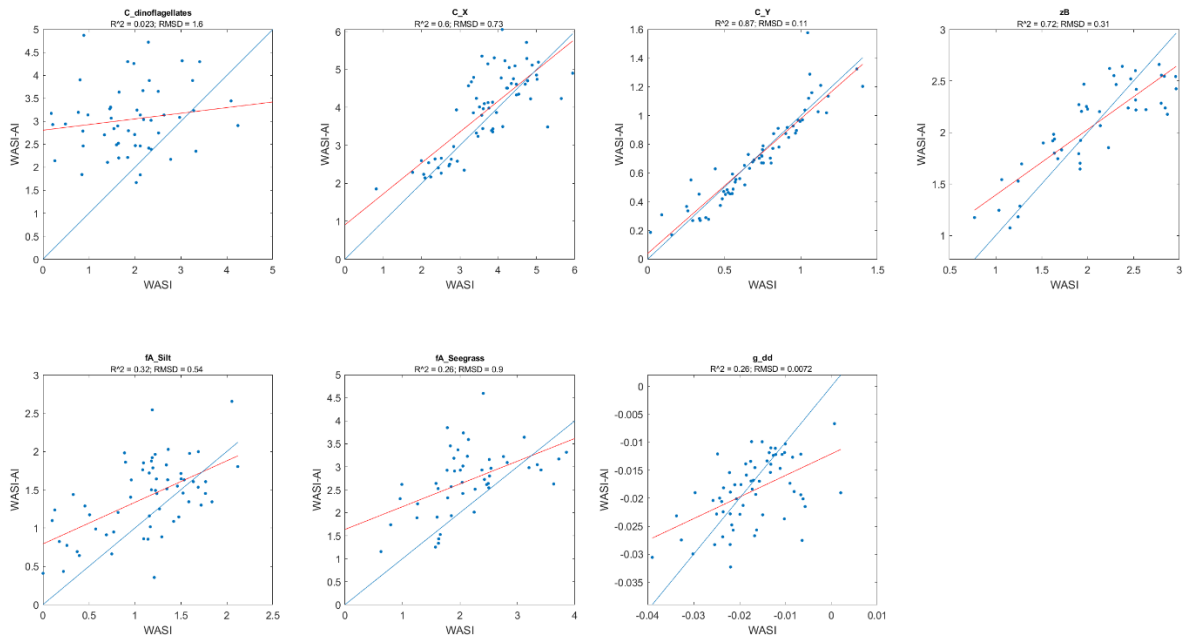
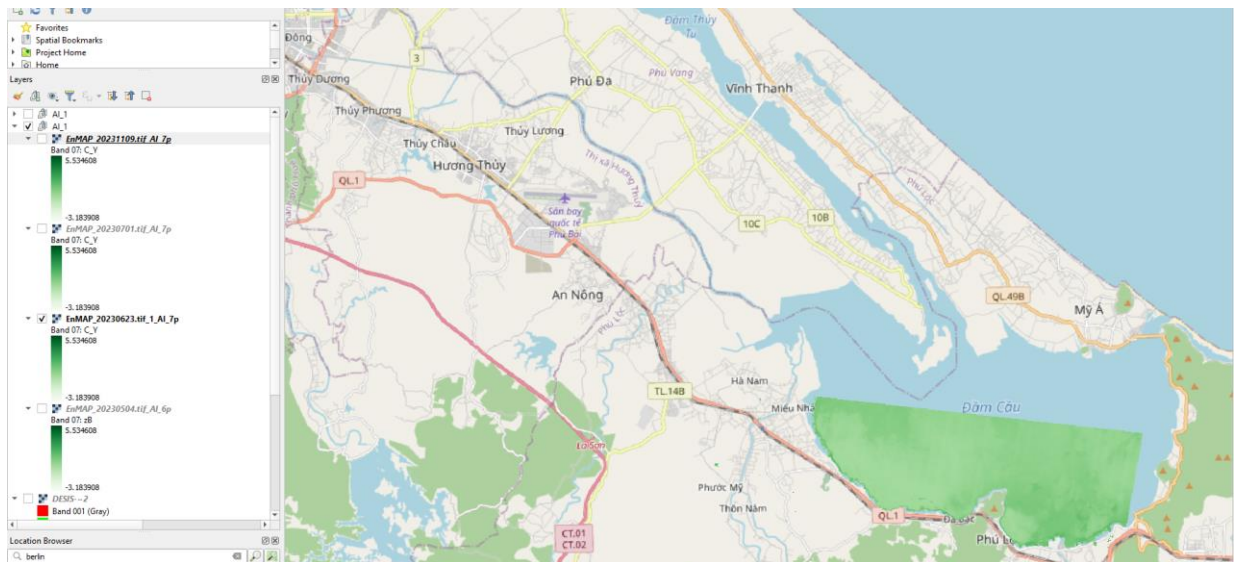


Figure 132: Fit parameters EnMAP_20230623.tif_1 AI validation Fit parameters_7p.



**Figure 133: Water quality estimation parameter R² Error
EnMAP_20230623.tif_1_AI_validation_Fit_parameters_7p.**



**Figure 14: C_Y CDOM normalized to the minimum and maximum
EnMAP_20230623.tif_1_AI_validation_Fit_parameters_7p.**

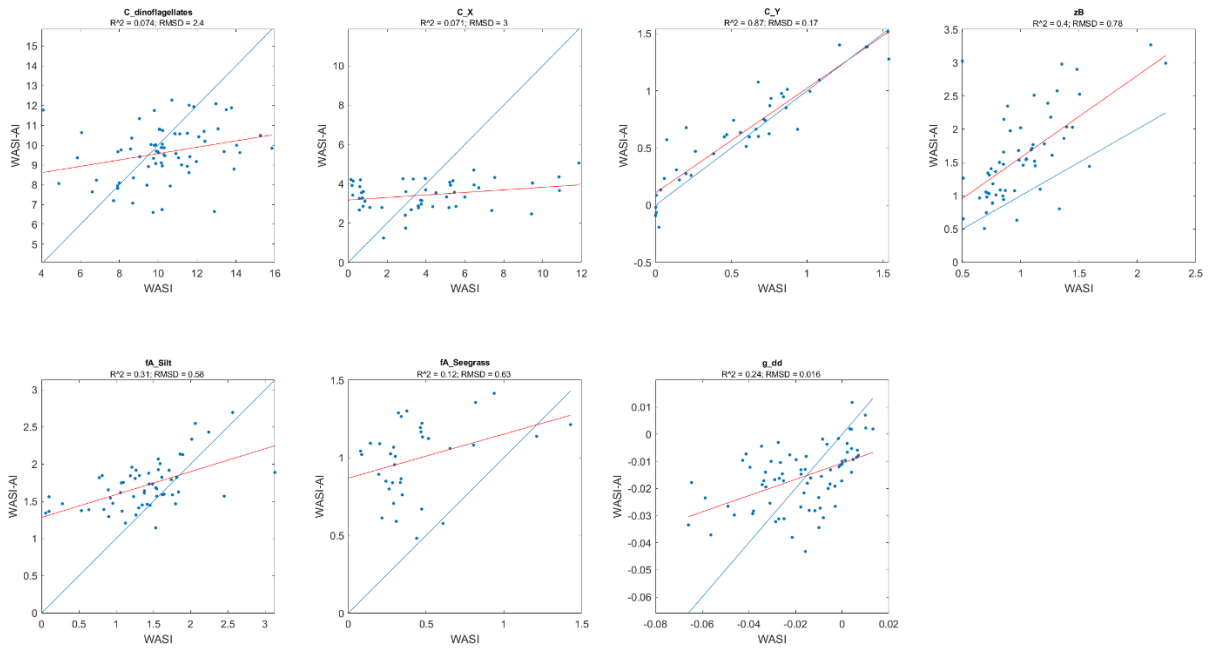


**Figure 135: Water quality estimation parameter R² Error
EnMAP_20230701.tif_AI_validation_Fit_parameters_7p.**

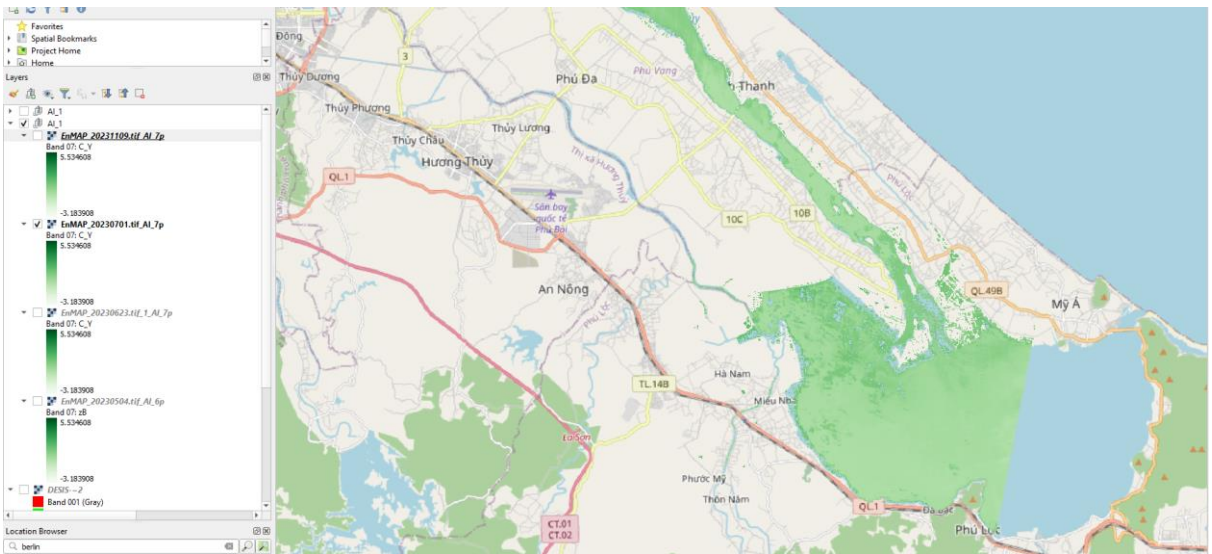


**Figure 136: C_Y CDOM normalized to the minimum and maximum
EnMAP_20230701.tif_AI_validation_Fit_parameters_7p.**

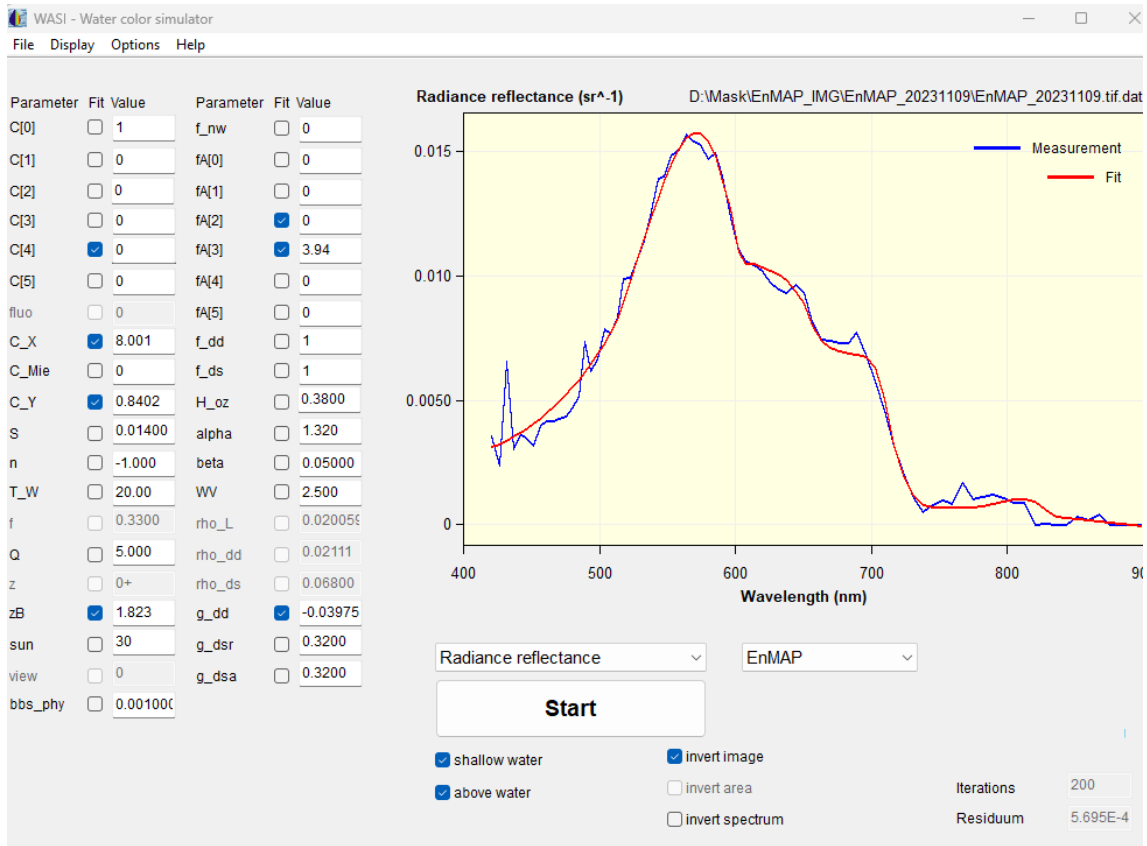


Figure 137: Fit parameter EnMAP_20231109.tif AI_validation_Fit_parameters_7p.

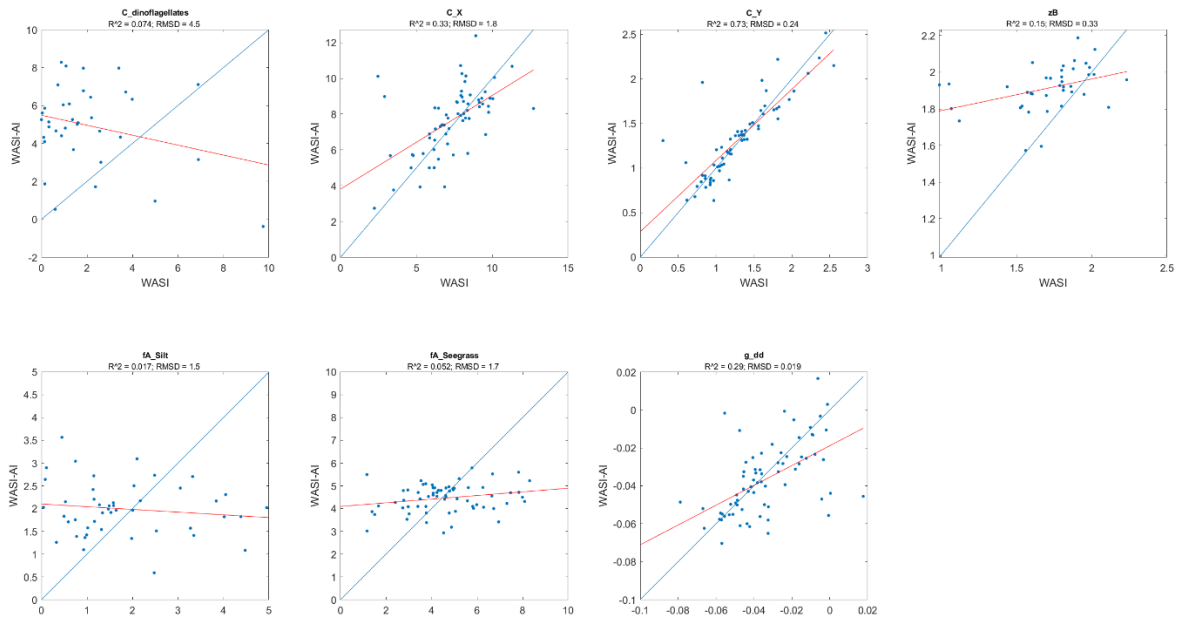


Figure 138: Water quality estimation parameter R^2 Error EnMAP_20231109.tif AI_validation_Fit_parameters_7p.

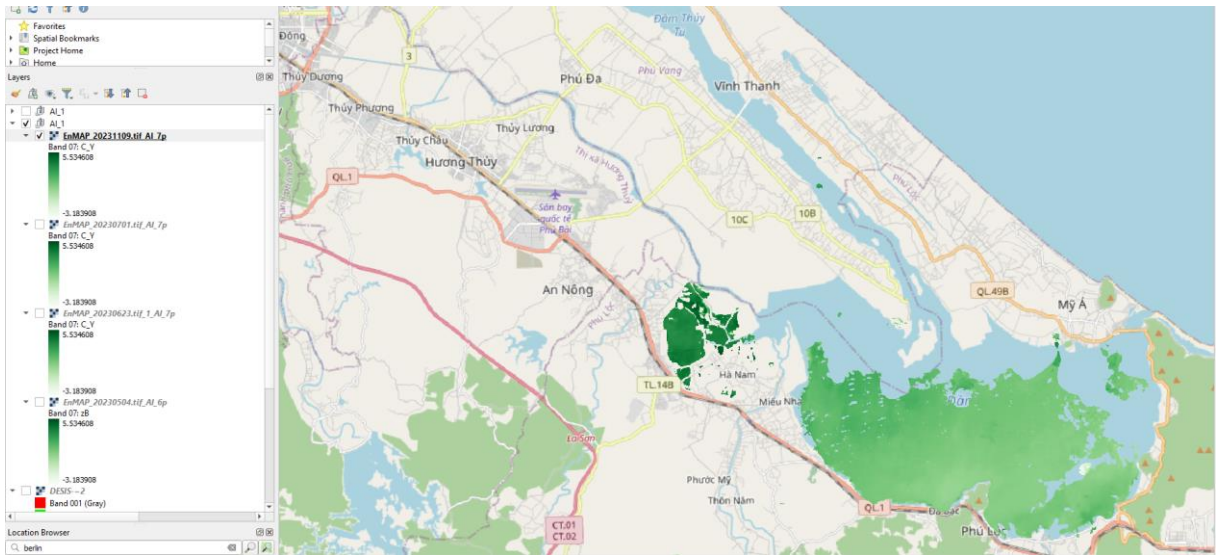


Figure 139: C_Y CDOM normalized to the minimum and maximum EnMAP_20231109.tif_AI_validation_Fit_parameters_7p.

Second Attempt EnMAP Model of deep water:

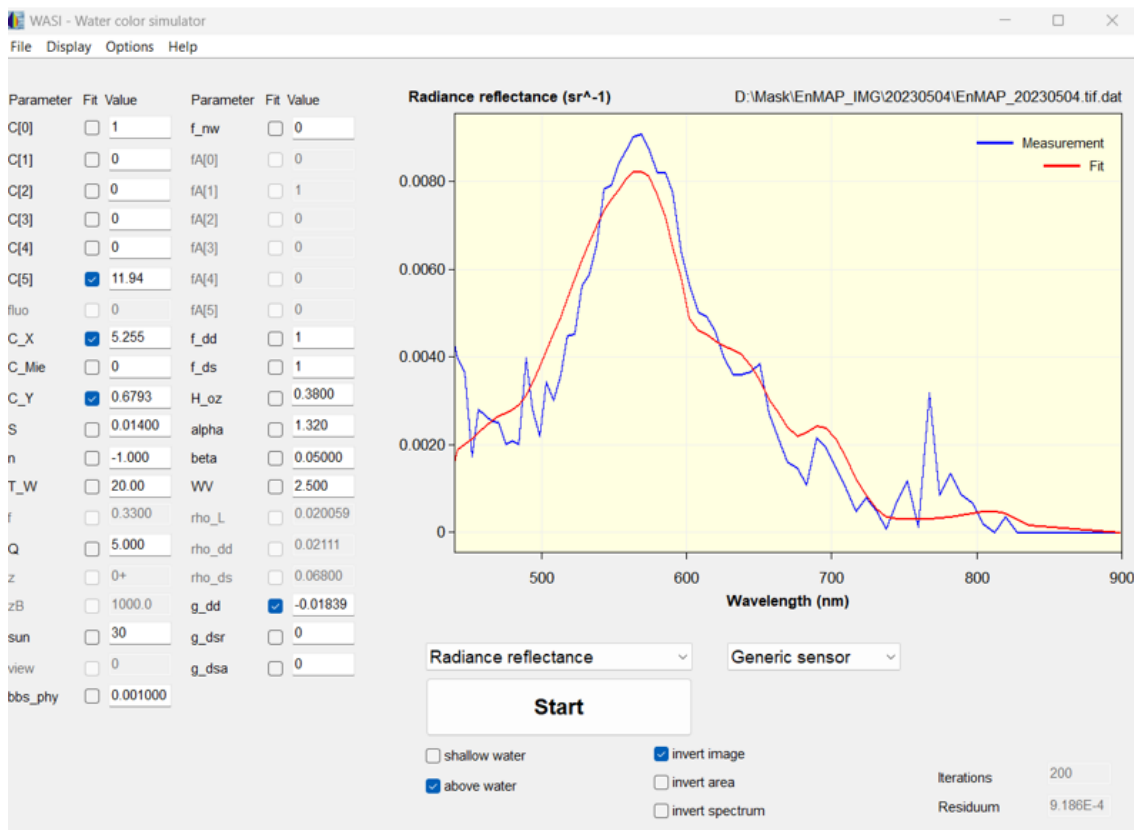


Figure 140: EnMAP image date 2023-05-04 parameter data setup.

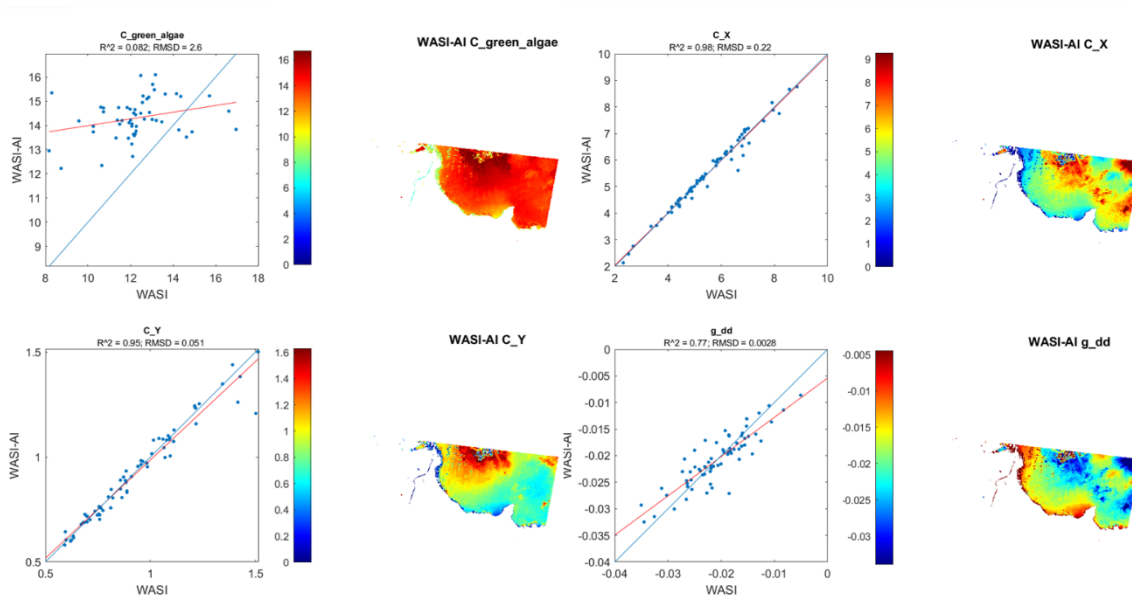


Figure 141: EnMAP image date 2023-05-31 process results.

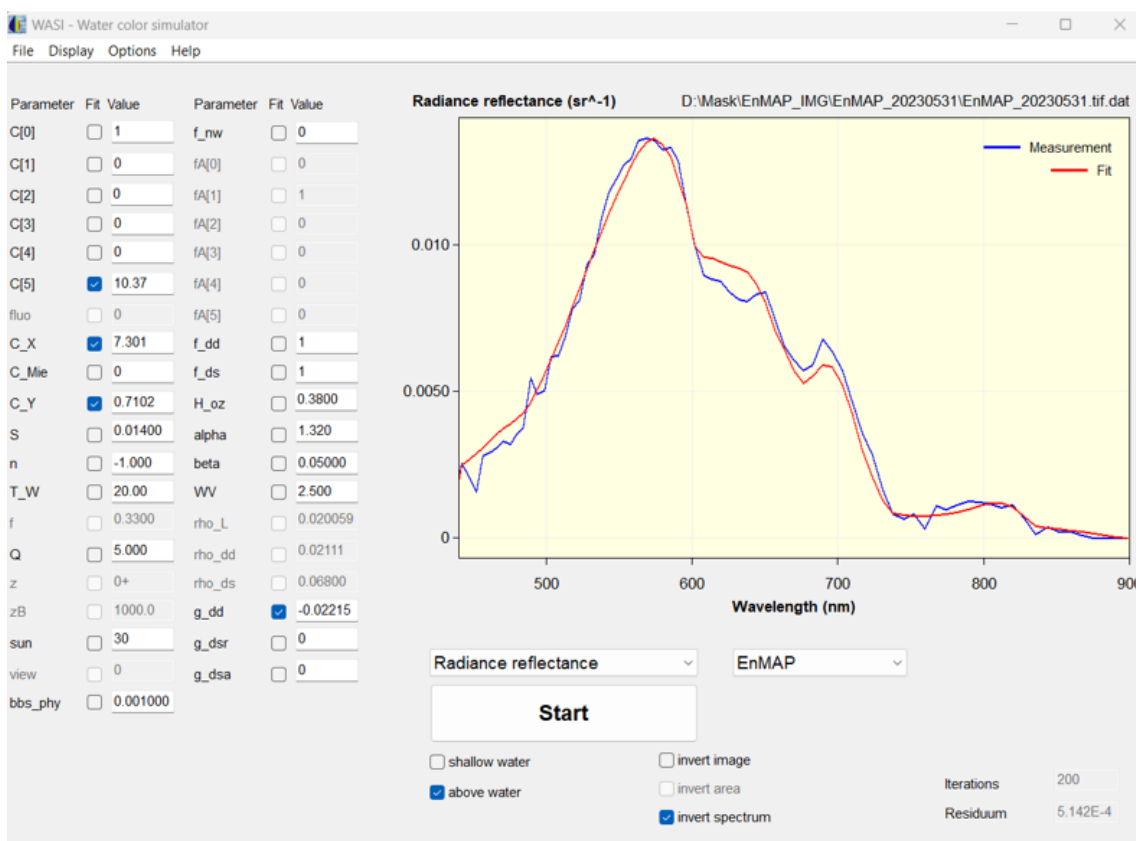


Figure 142: EnMAP image date 2023-05-31 parameter data setup.

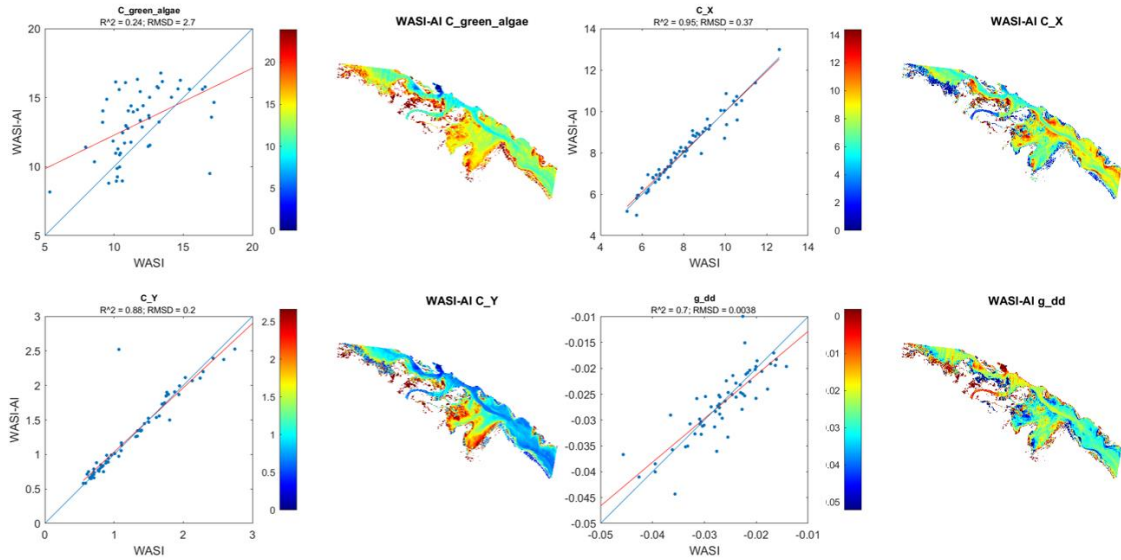


Figure 143: EnMAP image date 2023-05-31 process results.

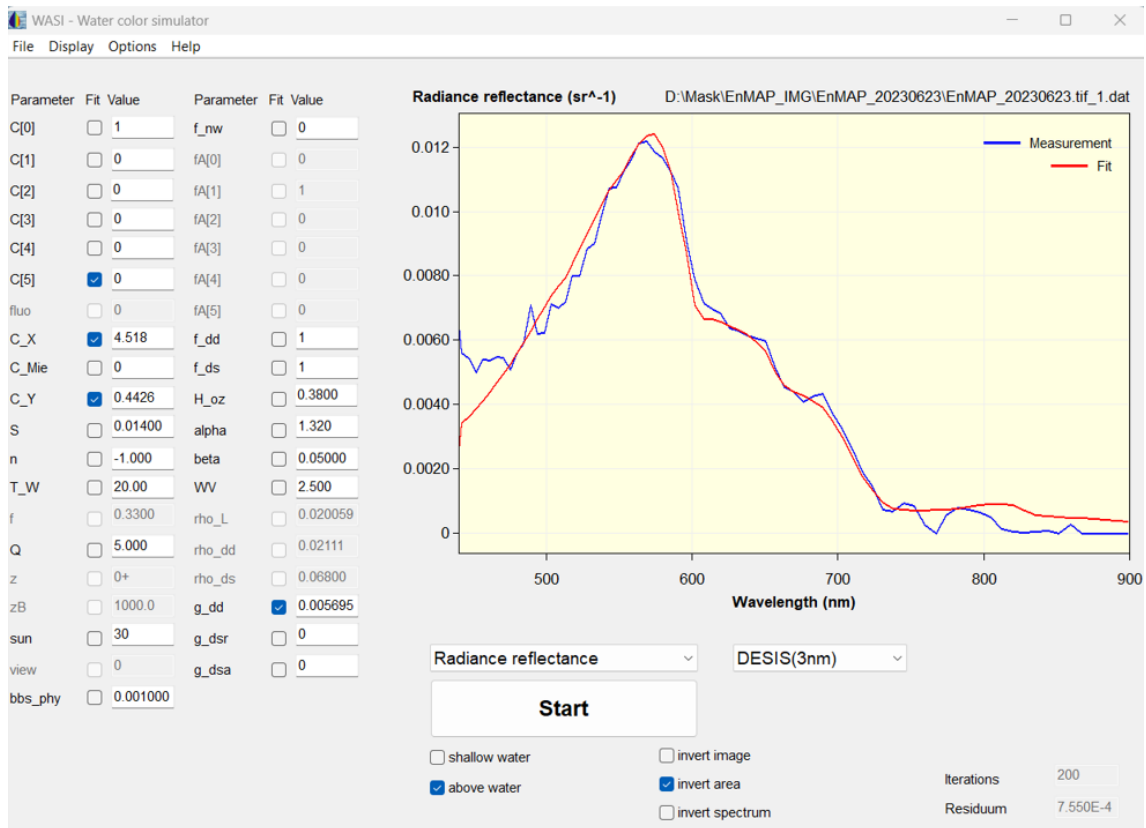


Figure 144: EnMAP image date 2023-06-23 parameter data setup.

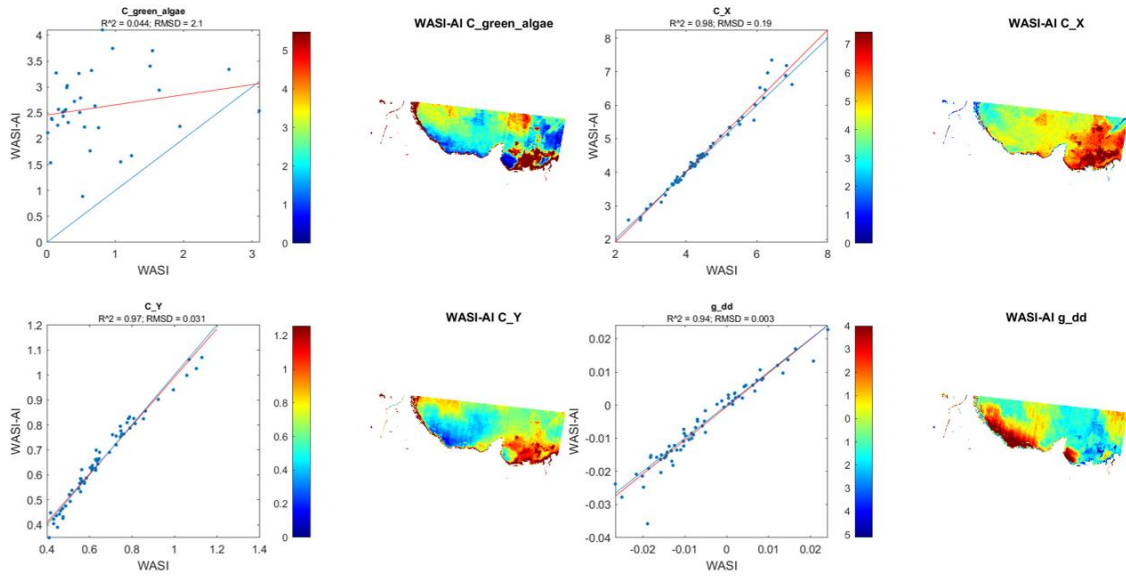


Figure 145: EnMAP image date 2023-06-23 process results.

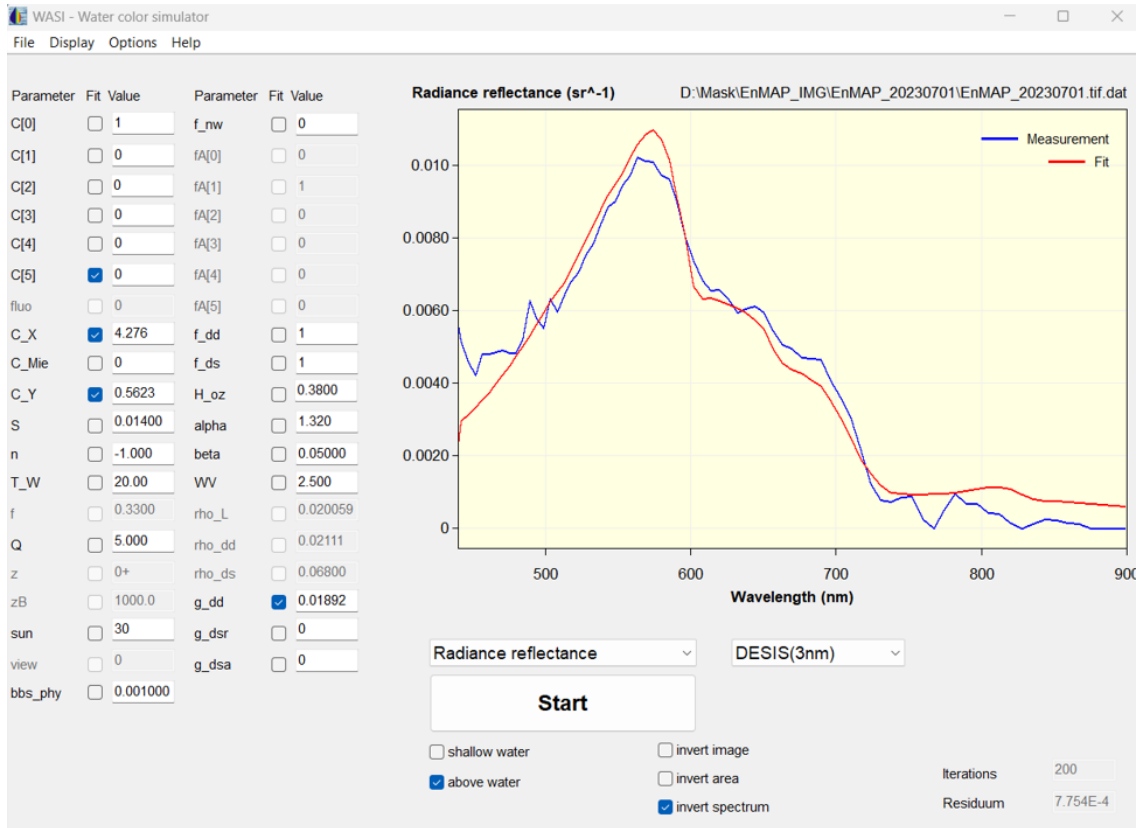


Figure 146: EnMAP image date 2023-07-01 parameter data setup.

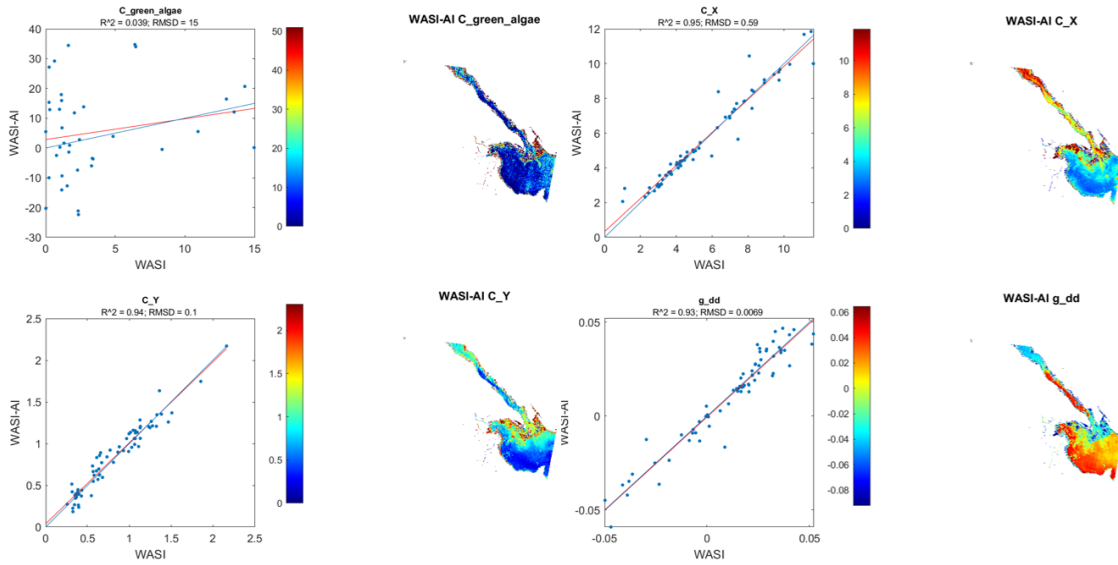


Figure 147: EnMAP image date 2023-07-01 process results.

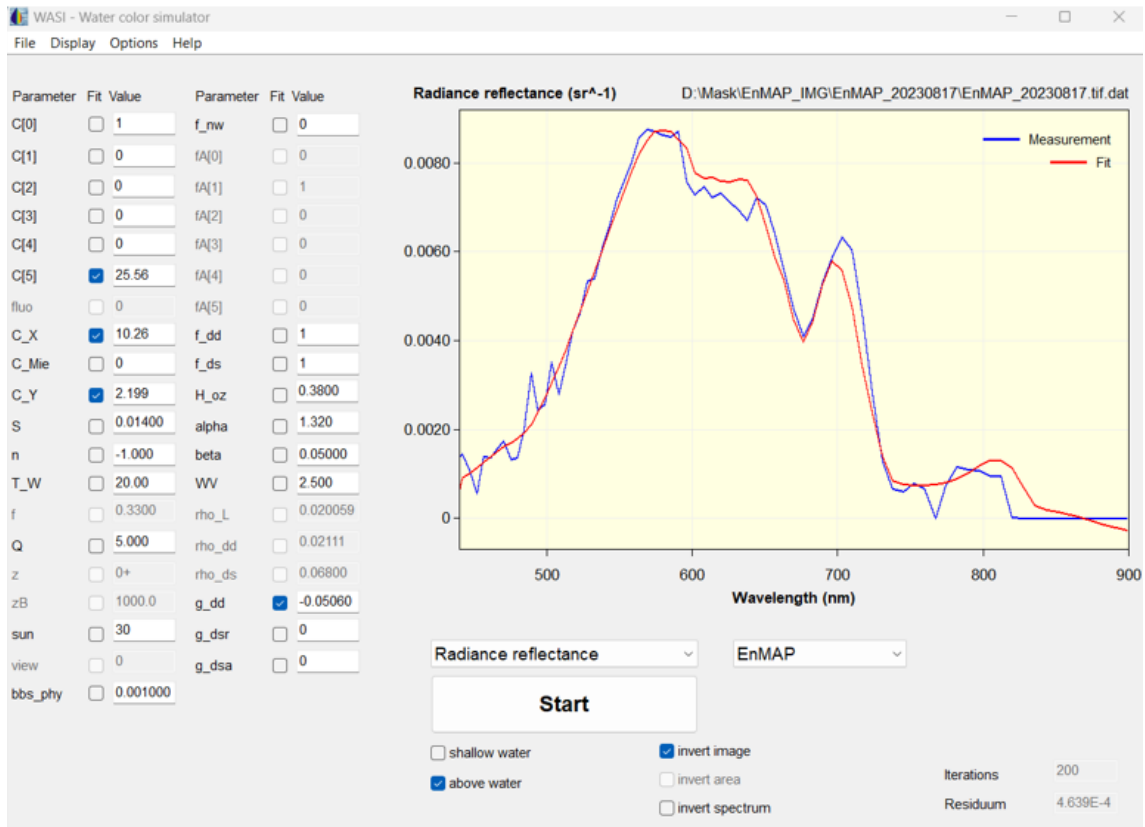


Figure 148: EnMAP image date 2023-06-17 parameter data setup.

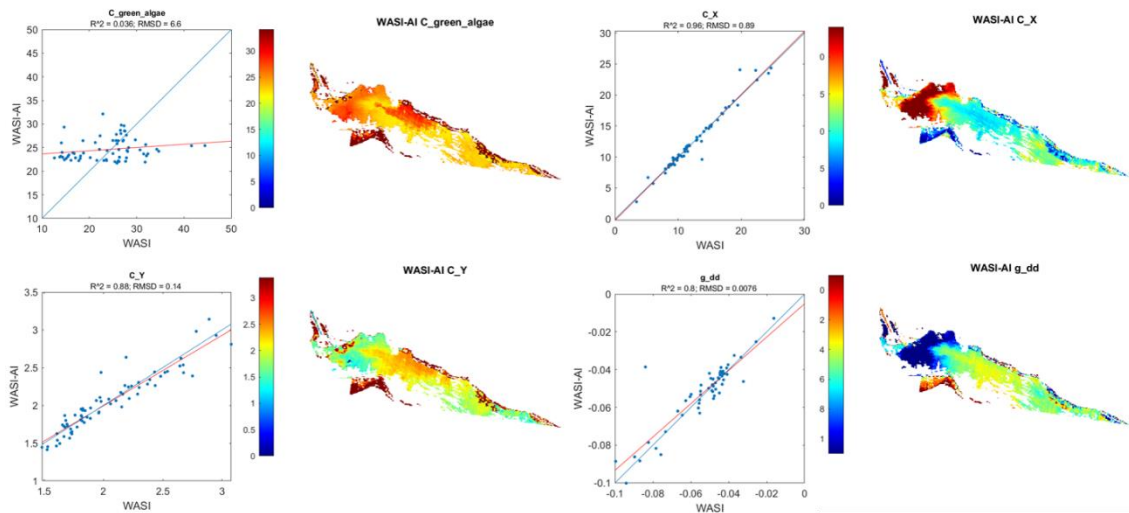


Figure 149: EnMAP image date 2023-06-17 process results.

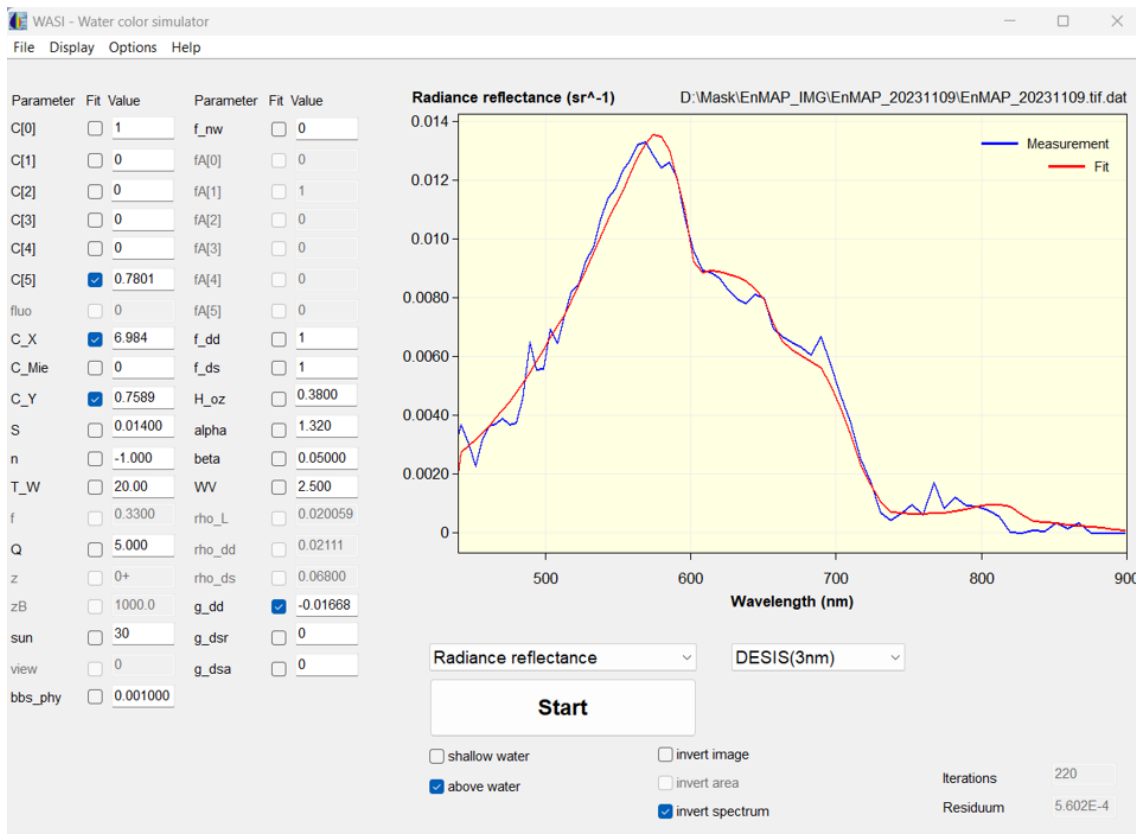


Figure 150: EnMAP image date 2023-11-09 parameter data setup.

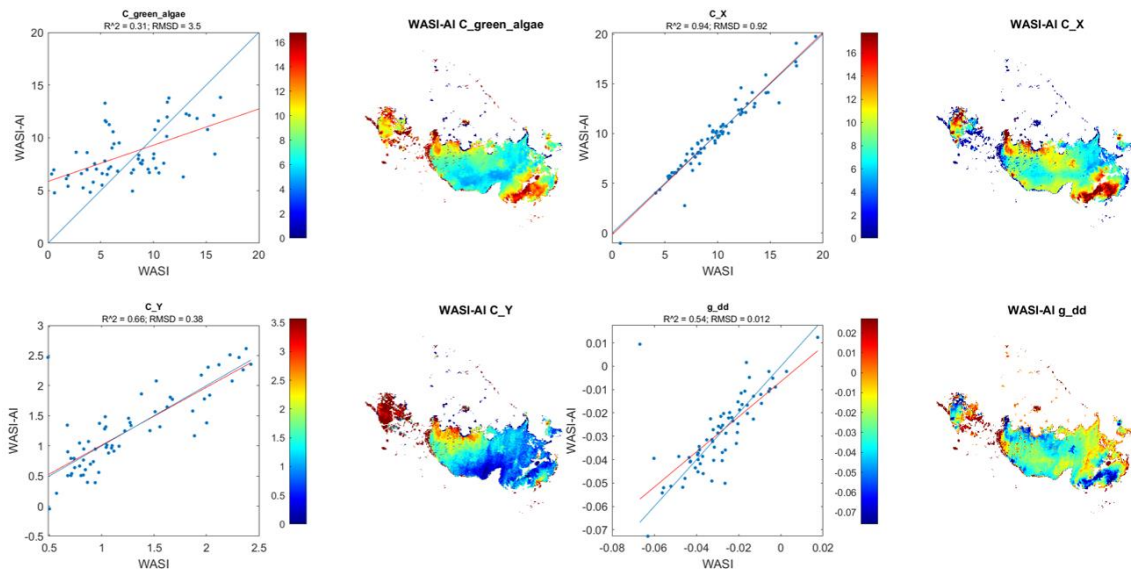


Figure 151: EnMAP image date 2023-11-09 process results.

10 IMAGE RESULTS FROM WASI PITXEL DISTRIBUTION OF THE PROCESS IMAGES DESIS AND ENMAP (BAR CHART)

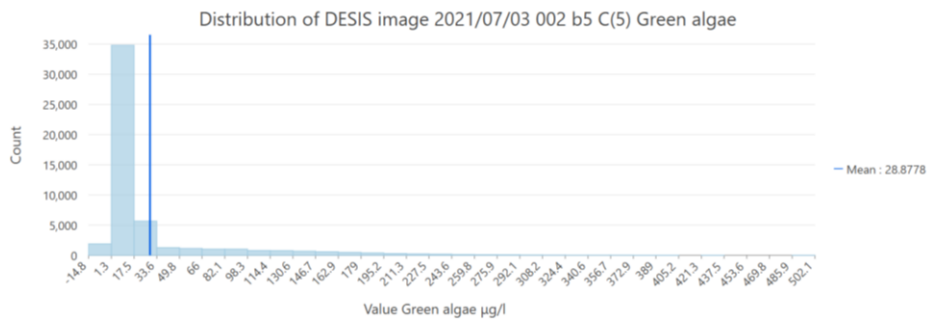


Figure 152: Bar chart result pixel distribution of DESIS 2021/07/03 002 b5 C(5) Green algae.

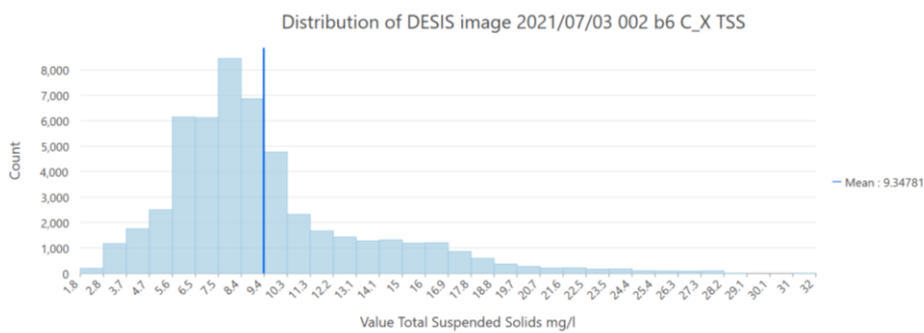


Figure 153: Bar chart result pixel distribution of DESIS 2021/07/03 002 b6 C_X TSS.

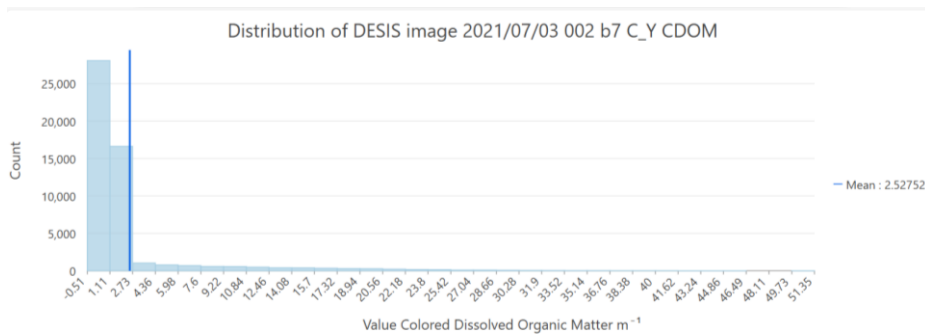


Figure 154: Bar chart result pixel distribution of DESIS 2021/07/03 b7 C_Y CDOM.

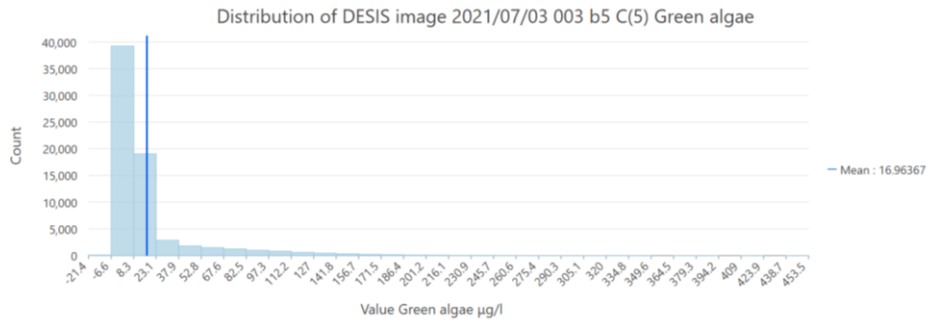


Figure 155: Bar chart result pixel distribution of DESIS 2021/07/03 002 b5 C(5) Green algae

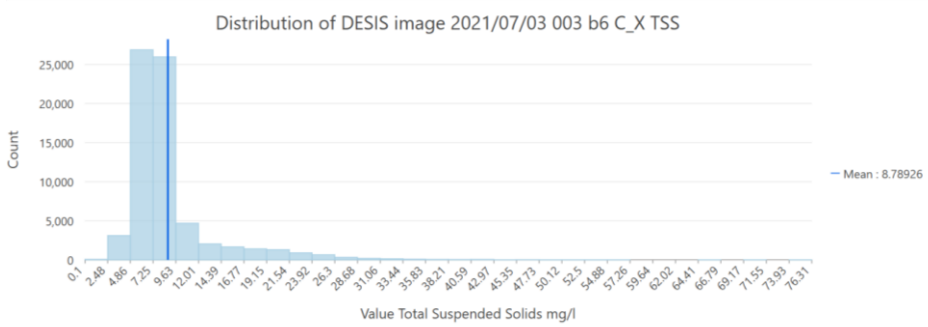


Figure 156: Bar chart result pixel distribution of DESIS 2021/07/03 003 b6 C_X TSS.

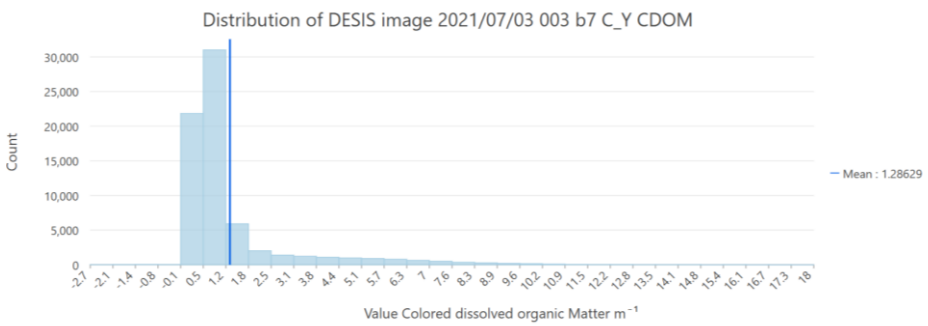


Figure 157: Bar chart result pixel distribution of DESIS 2021/07/03 003 b7 C_Y CDOM

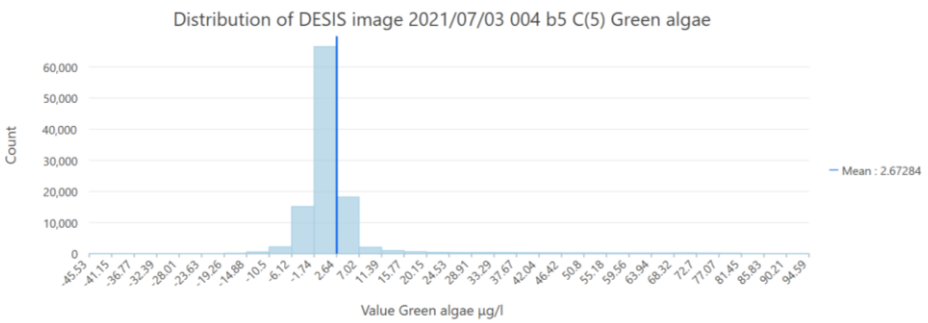


Figure 158: Bar chart result pixel distribution of DESIS 2021/07/03 004 b5 C(5) Green algae.

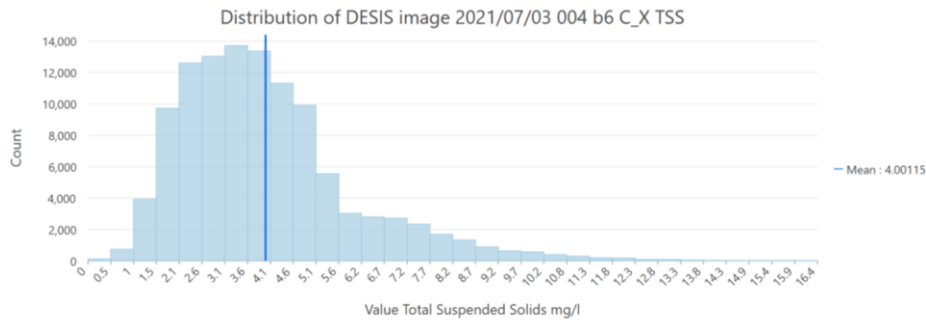


Figure 159: Bar chart result pixel distribution of DESIS 2021/07/03 004 b6 C_X TSS.

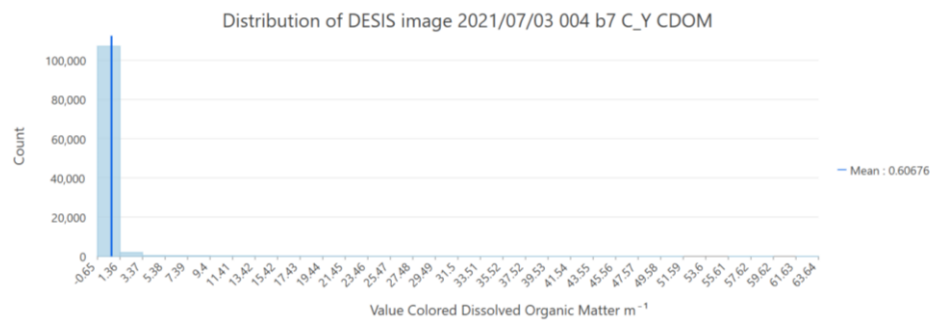


Figure 160: Bar chart result pixel distribution of DESIS 2021/07/03 004 b6 C_Y CDOM.

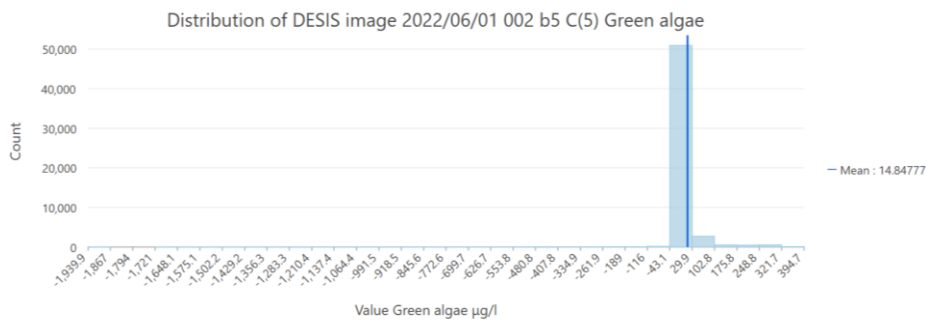


Figure 161: Bar chart result pixel distribution of 2022/06/01 002 b5 C(5) Green algae.

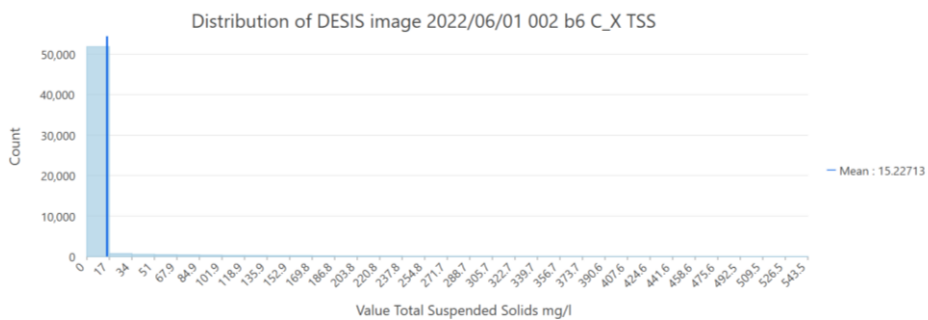


Figure 162: Bar chart result pixel distribution of DESIS 2022/06/01 002 b6 C_X TSS.

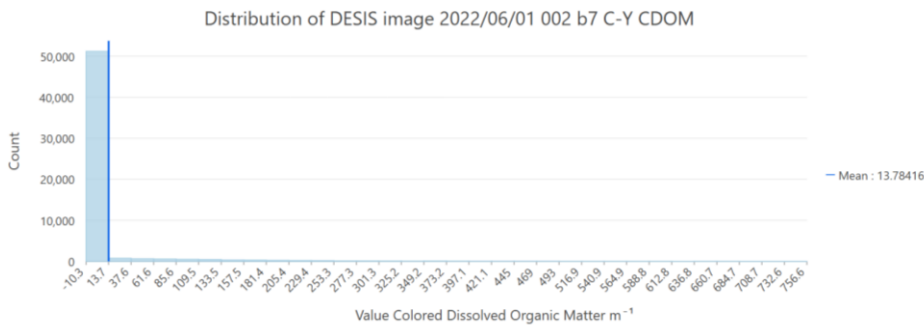


Figure 163: Bar chart result pixel distribution of DESIS 2022/06/01 002 b7 C_Y CDOM.

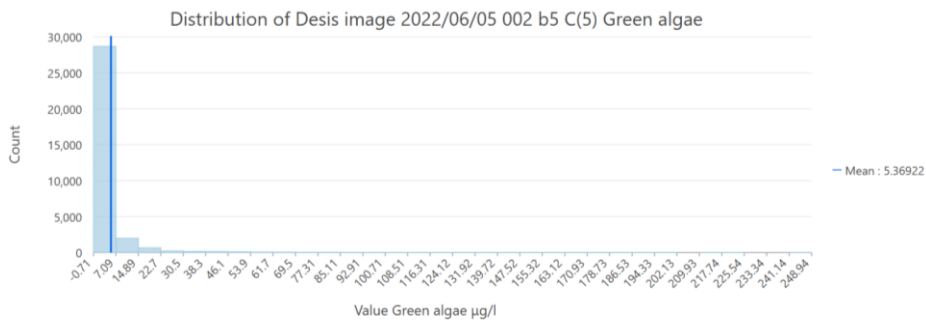


Figure 164: Bar chart result pixel distribution of DESIS 2022/06/05 002 b5 Green algae.

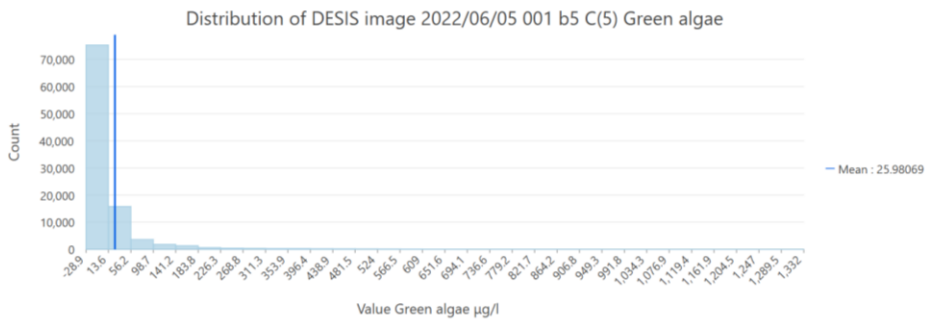


Figure 165: Bar chart result pixel distribution of DESIS 2022/06/05 001 b5 C(5) Green algae.

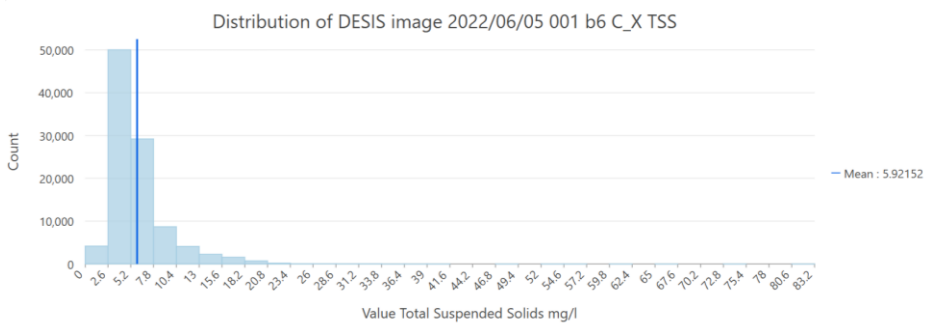


Figure 166: Bar chart result pixel distribution of DESIS 2022/06/05 001 b6 C_X TSS.

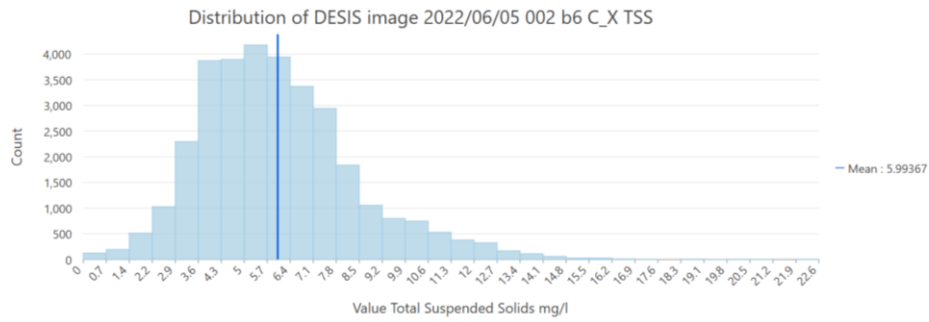


Figure 167: Bar chart result distribution of DESIS 2022/06/05 002 b6 C_X TSS.

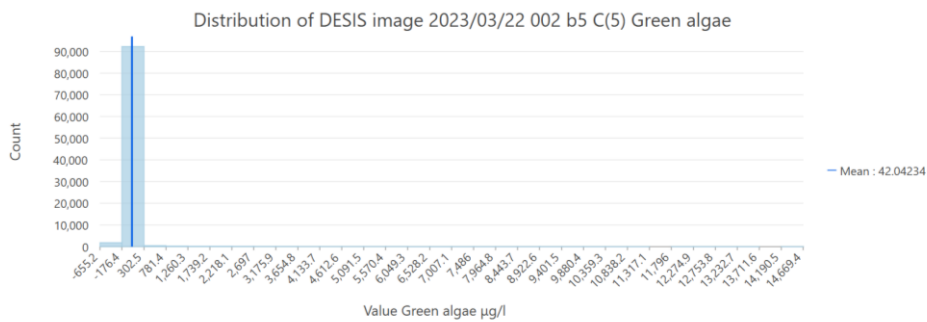


Figure 168: Bar chart result pixel distribution of DESIS 2023/03/22 002 b5 C(5) Green algae.

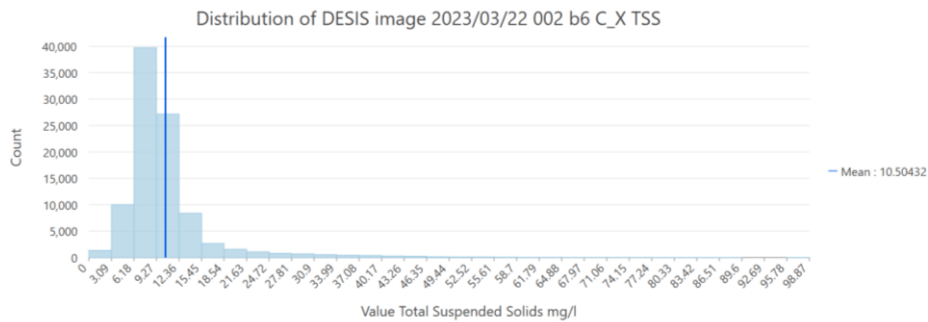


Figure 169: Bar chart result pixel distribution of DESIS 2023/03/22 002 b6 C_X TSS.

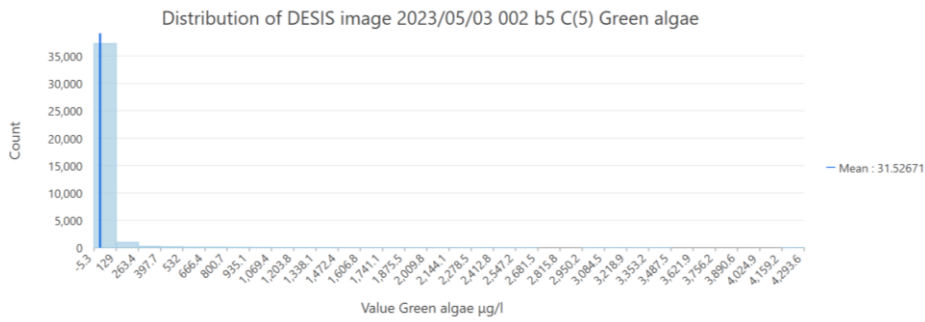


Figure 170: Bar chart result pixel distribution of DESIS 2023/05/03 002 b5 C(5) Green algae.

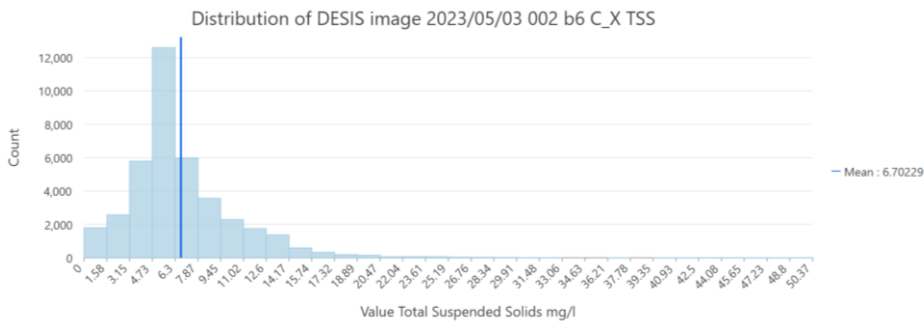


Figure 171: Bar chart result pixel distribution of DESIS 2023/05/03 002 b6 C_X TSS.

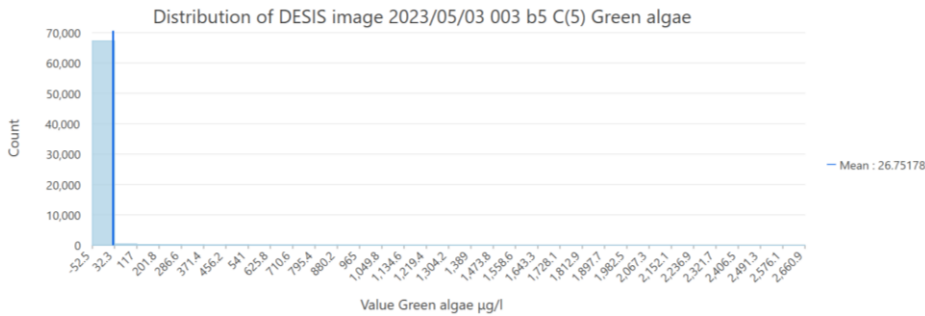


Figure 172: Bar chart result pixel distribution of DESIS 2023/05/03 003 b5 C(5) Green algae.

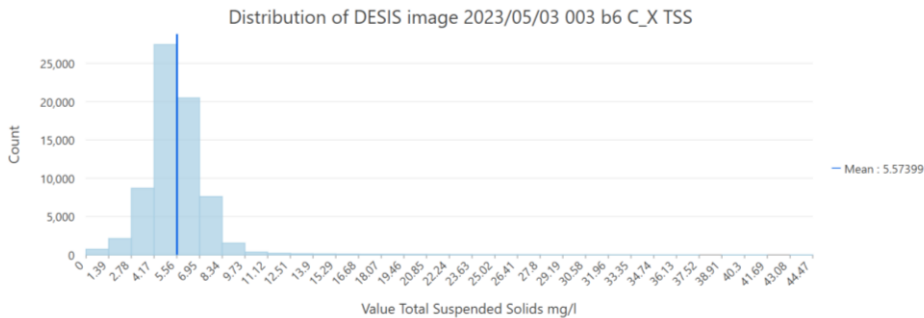


Figure 173: Bar chart result pixel distribution of DESIS 2023/05/03 003 b6 C_X TSS.

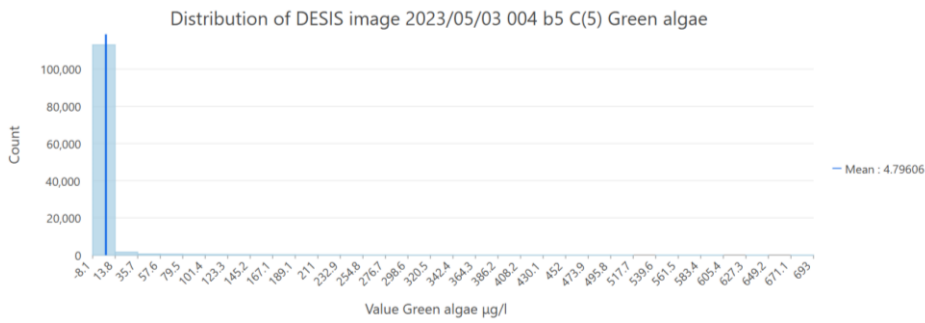


Figure 174: Bar chart result pixel distribution of DESIS 2023/05/03 004 b5 C(5) Green algae.

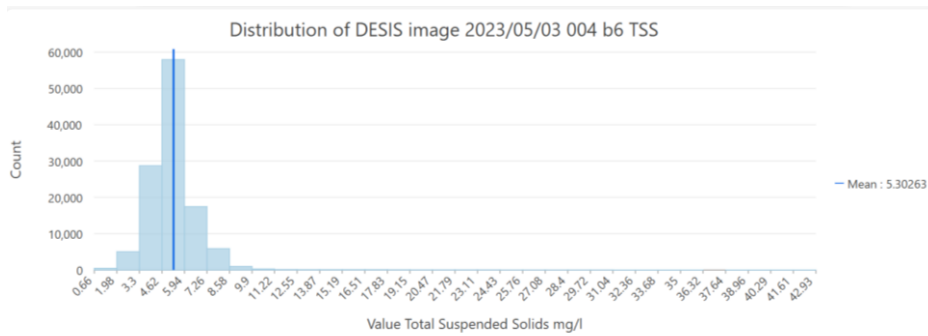


Figure 175: Bar chart result pixel distribution of DESIS 2023/05/03 004 b6 TSS.

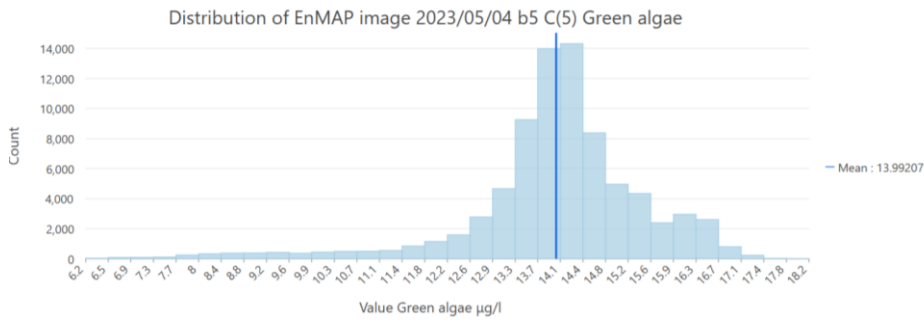


Figure 176: Bar chart result pixel distribution of EnMAP 2023/05/04 b5 C(5) Green algae.

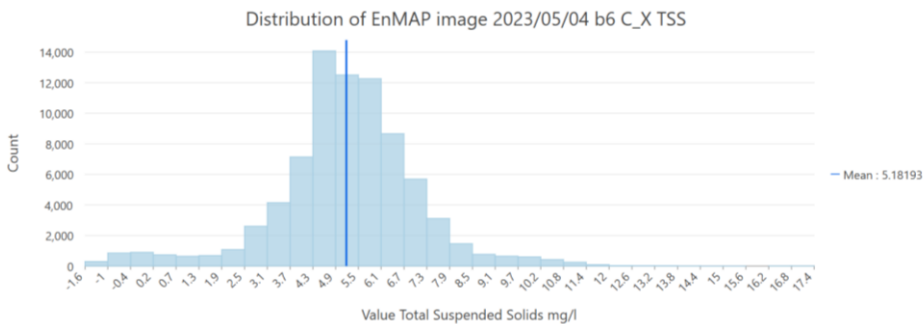


Figure 177: Bar chart result pixel distribution of EnMAP 2023/05/04 b6 C_X TSS.

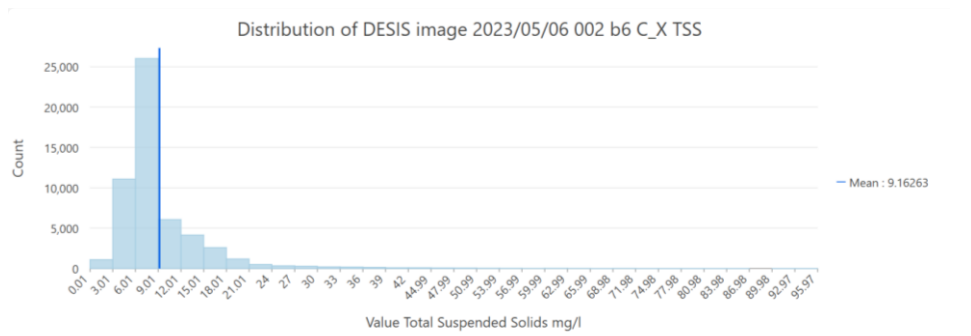


Figure 178: Bar chart result pixel distribution of DESIS 2023/05/06 002 b6 C_X TSS.

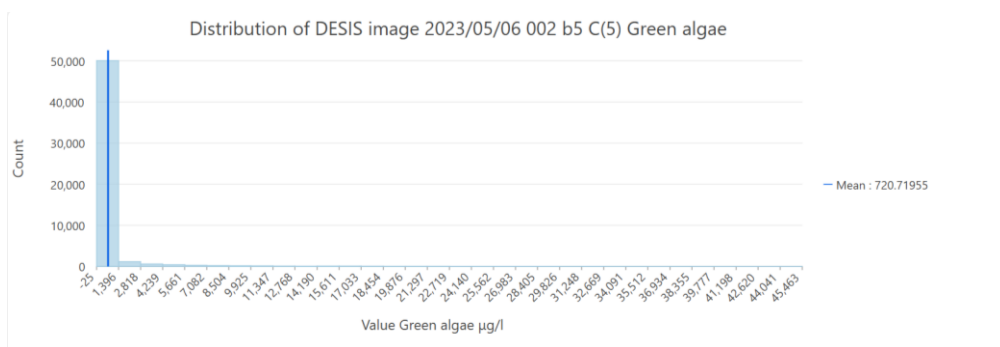


Figure 179: Bar chart result pixel distribution of DESIS 2023/05/06 002 b5 C(5) Green algae.

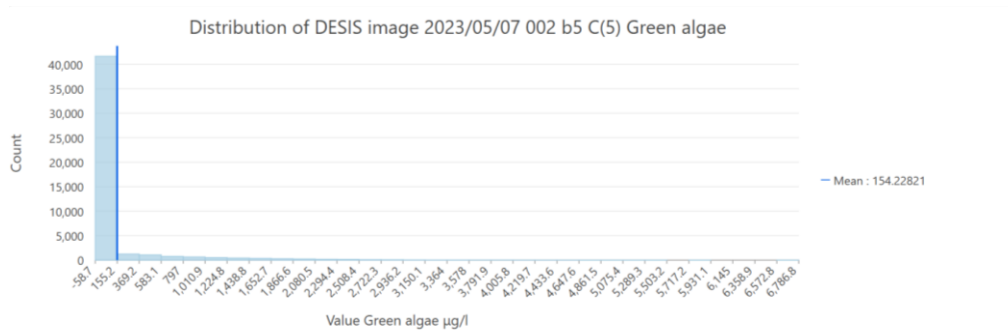


Figure 180: Bar chart result pixel distribution of DESIS 2023/05/07 002 b5 C(5) Green algae.

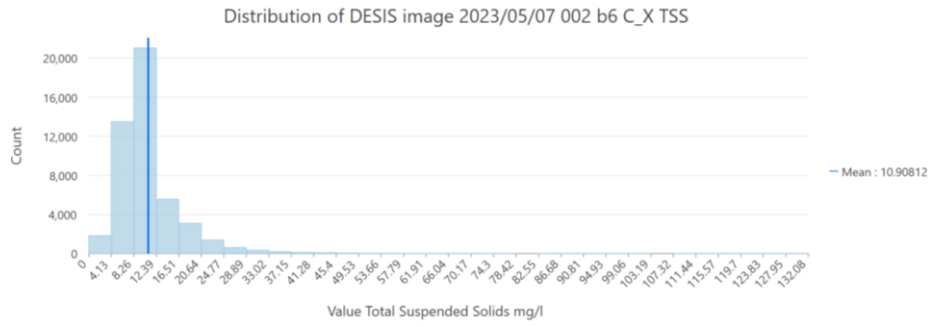


Figure 181: Bar chart result pixel distribution of DESIS 2023/05/07 002 b6 C_X TSS.

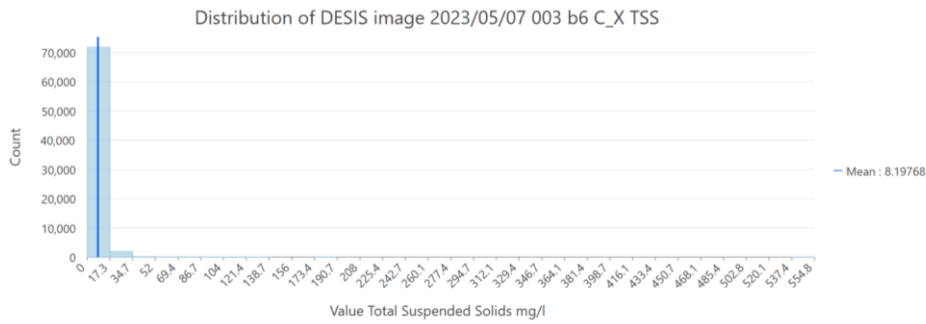


Figure 182: Bar chart result pixel distribution of DESIS 2023/05/07 003 b6 C_X TSS.

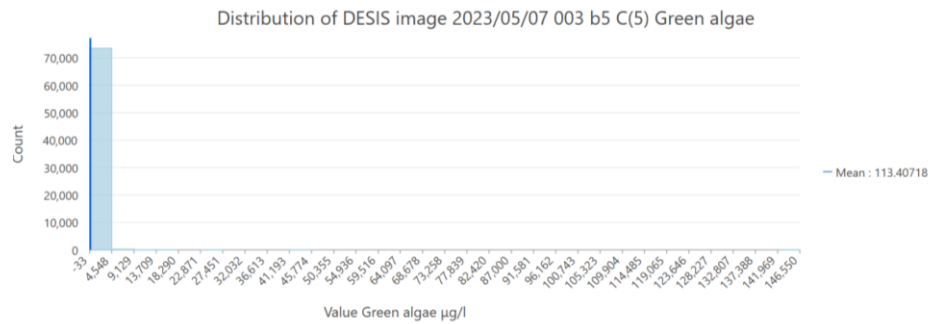


Figure 183: Bar chart result pixel distribution of DESIS 2023/05/07 003 b5 C(5) Green algae.

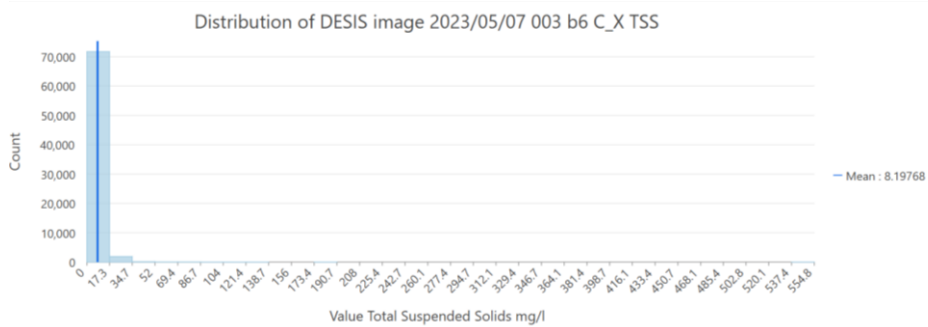


Figure 184: Bar chart result pixel distribution of DESIS 2023/05/07 003 b6 C_X TSS.

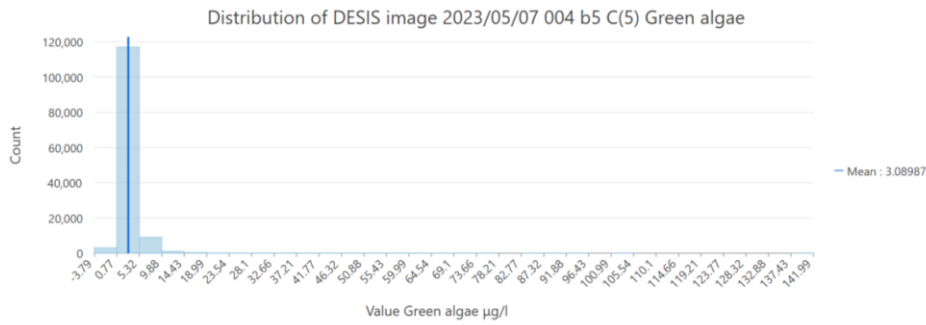


Figure 185: Bar chart result pixel distribution of DESIS 2023/05/07 004 b5 C(5) Green algae.

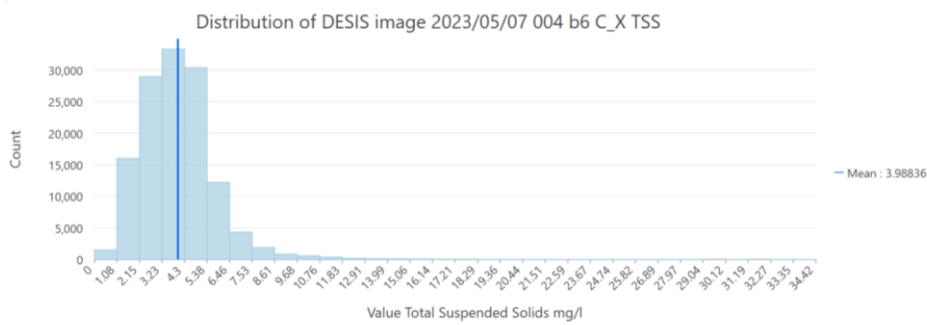


Figure 186: Bar chart result pixel distribution of DESIS 2023/05/07 004 b6 C_X TSS.

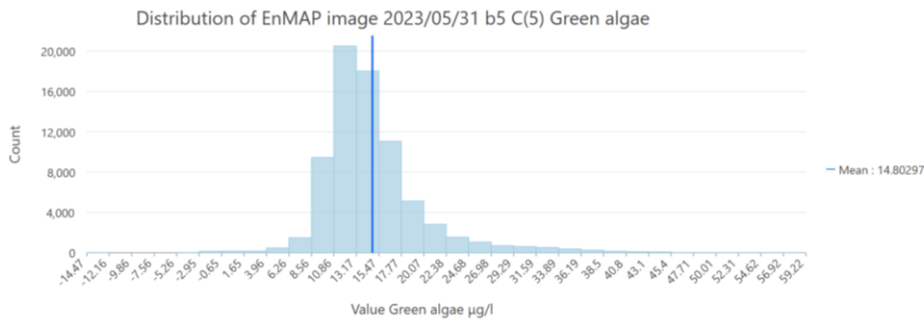


Figure 187: Bar chart result pixel distribution of EnMAP 2023/05/31 b5 C(5) Green algae.

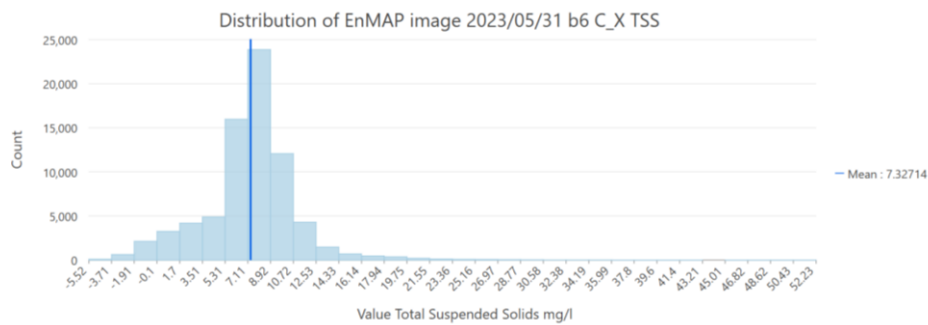


Figure 188: Bar Chart result pixel distribution of EnMAP 2023/05/31 b6 C_X TSS.

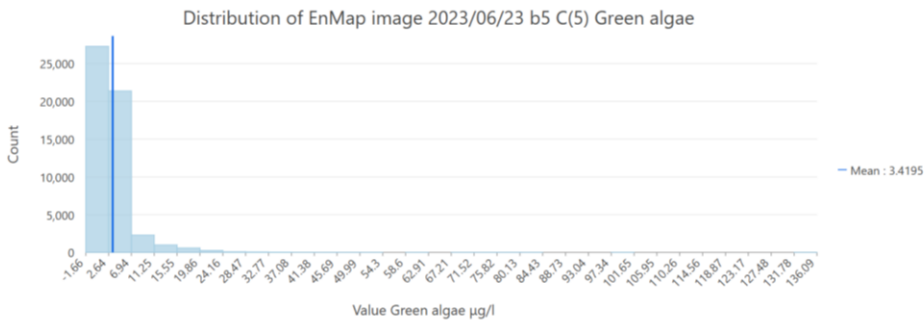


Figure 189: Bar chart result pixel distribution of EnMAP 2023/06/23 b5 C(5) Green algae.

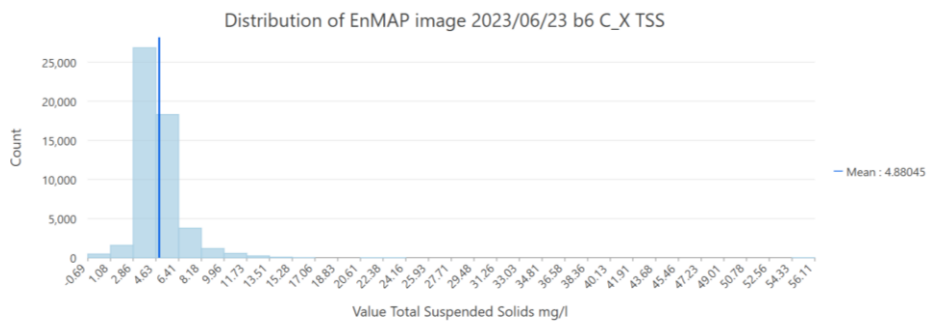


Figure 190: : Bar chart result pixel distribution of EnMAP 2023/06/23 b6 C_X TSS.

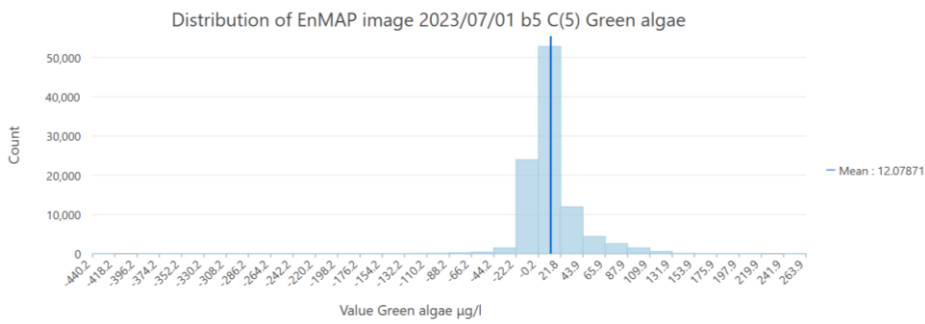


Figure 191: Bar chart result pixel distribution of EnMAP 2023/07/01 b5 C(5) Green algae.

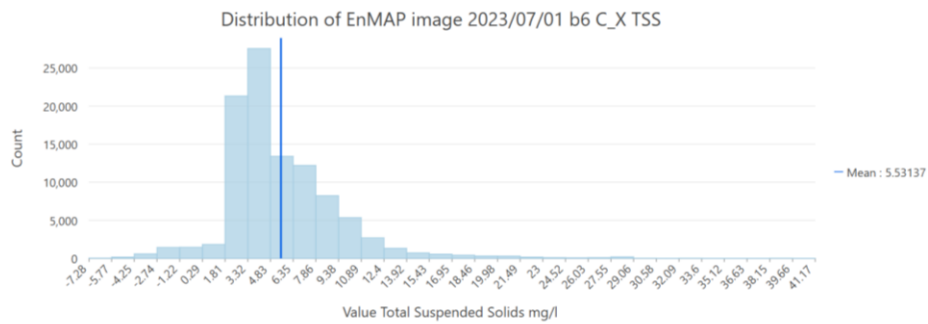


Figure 192: Bar Chart result pixel distribution of EnMAP 2023/07/01 b6 C_X TSS.

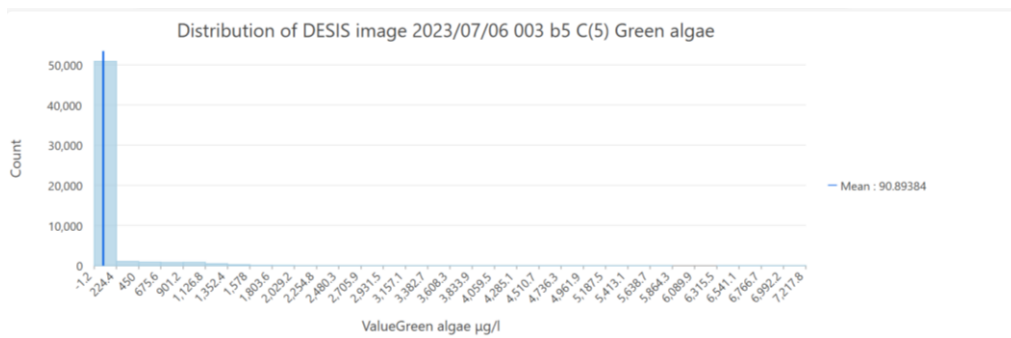


Figure 193: Bar chart result pixel distribution of DESIS 2023/07/06 003 b5 C(5) Green algae.

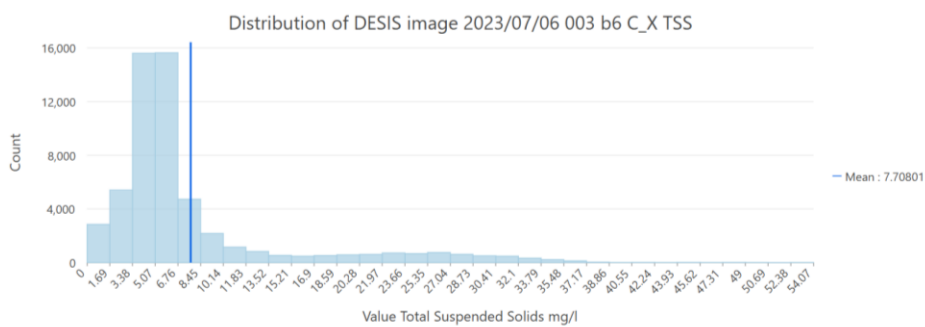


Figure 194: Bar chart result pixel distribution of DESIS 2023/07/06 003 b6 C_X TSS.

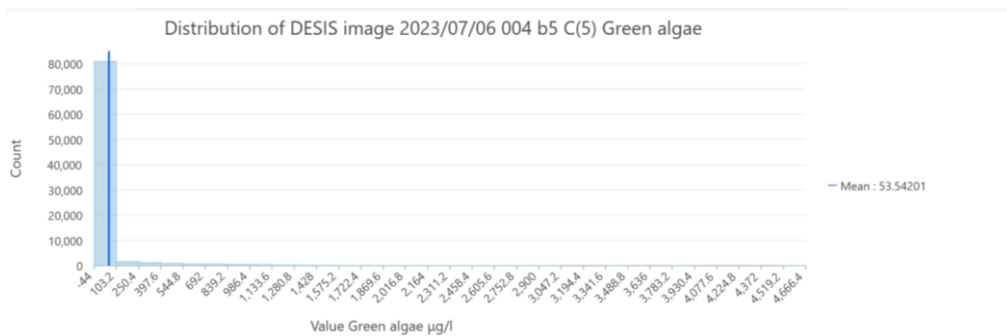


Figure 195: Bar chart result pixel distribution of DESIS 2023/07/06 004 b5 C(5) Green algae.

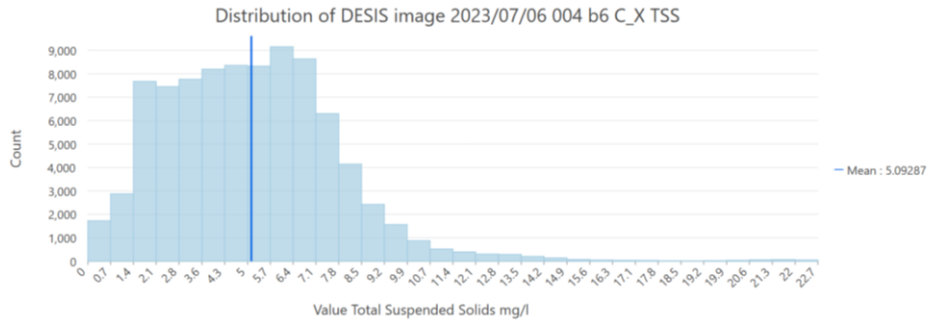


Figure 196: Bar chart result pixel distribution of DESIS 2023/07/06 004 b6 C_X TSS.

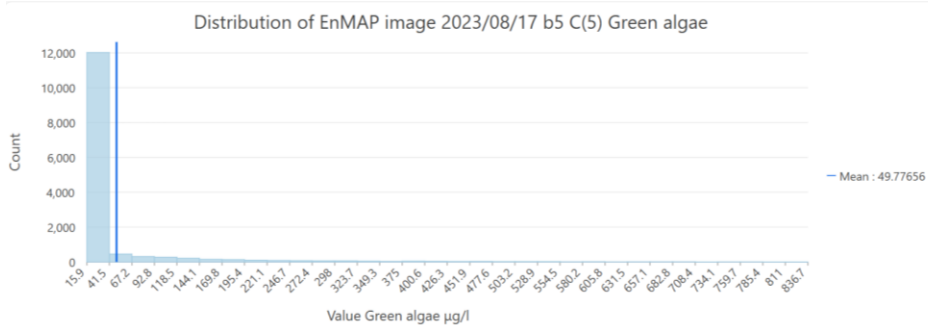


Figure 197: Bar chart result pixel distribution of EnMAP 2023/08/17 b5 C(5) Green algae.

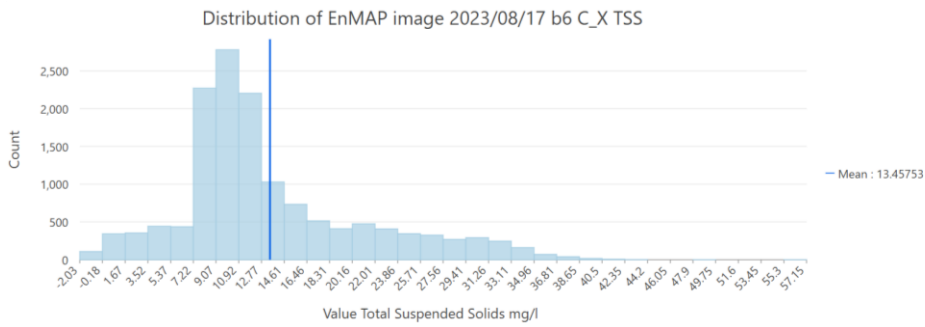


Figure 198: Bar chart result pixel distribution of EnMAP 2023/08/17 b6 C_X TSS.

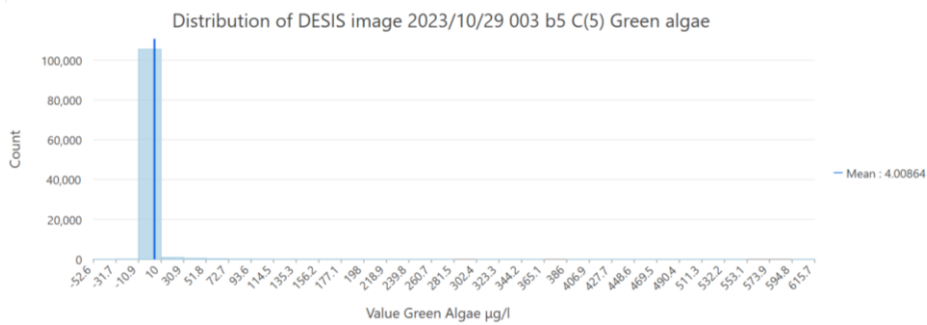


Figure 199: Bar chart result pixel distribution of DESIS 2023/10/29 003 b5 C(5) Green algae.

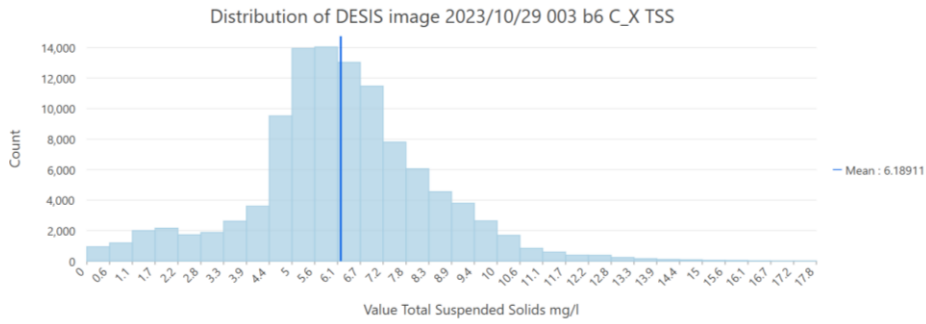


Figure 200: Bar chart result pixel distribution of DESIS 2023/10/29 003 b6 C_X TSS.

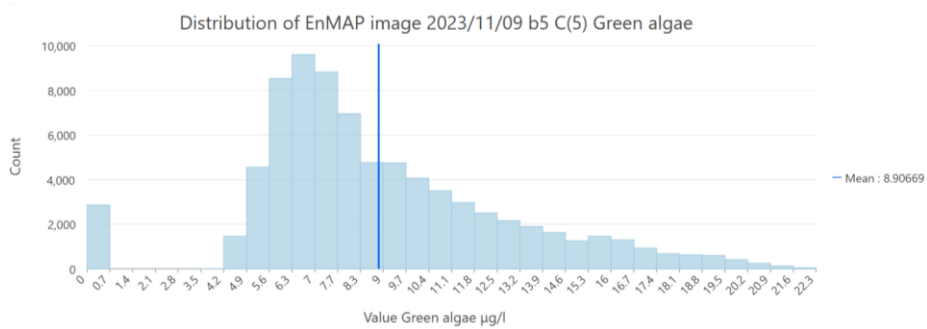


Figure 201: Bar chart result pixel distribution of EnMAP 2023/11/09 b5 C(5) Green algae.

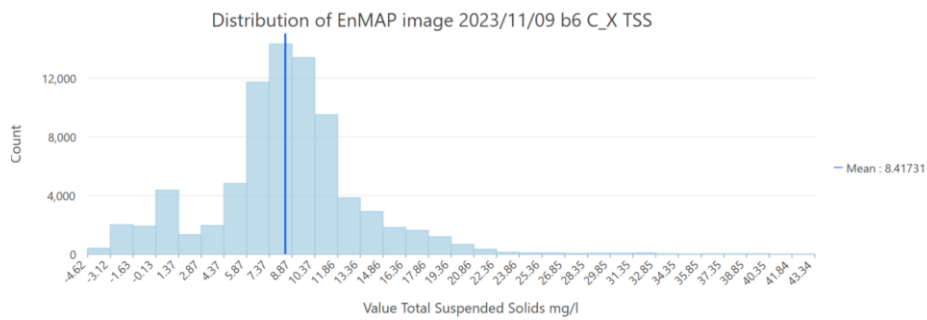


Figure 202: Bar chart result pixel distribution of EnMAP 2023/11/09 b6 C_X TSS.

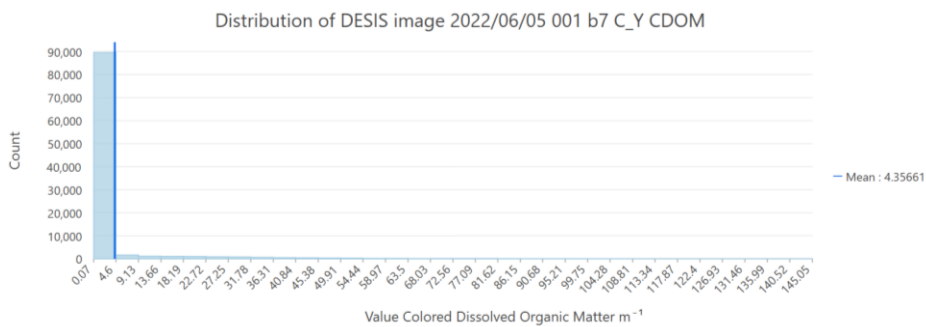


Figure 203: Bar chart result pixel distribution of DESIS 2022/06/05 001 b7 C_Y CDOM.

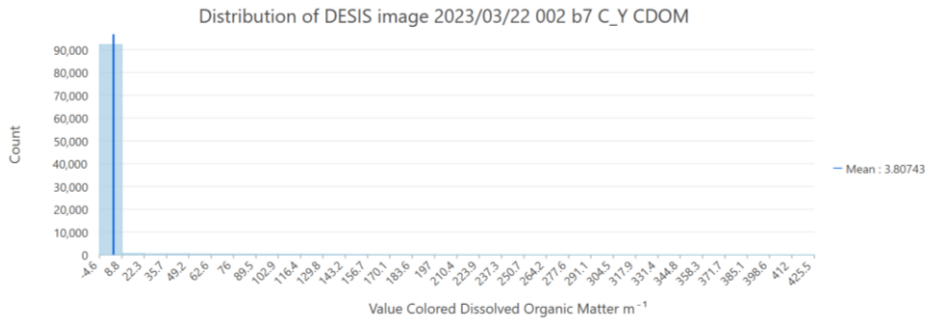


Figure 204: Bar chart result pixel distribution of DESIS 2023/03/22 002 b7 C_Y CDOM.

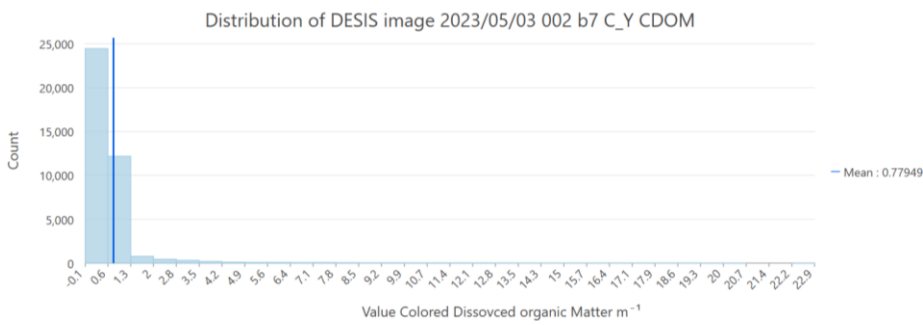


Figure 205: Bar chart result pixel distribution of DESIS 2023/05/03 002 b7 C_Y CDOM.

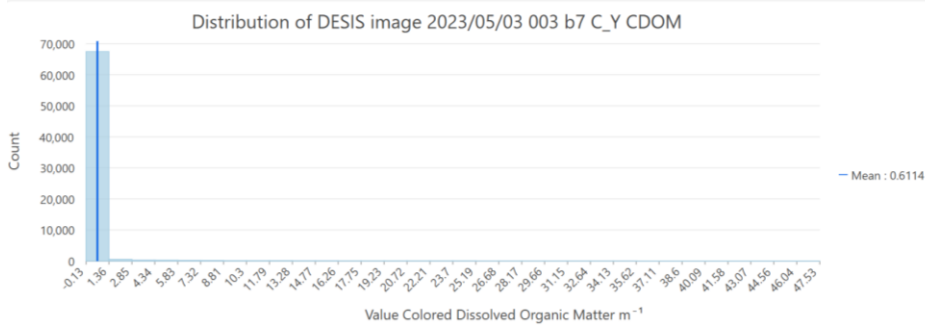


Figure 206: Bar chart result pixel distribution of DESIS 2023/05/03 003 b7 C_Y CDOM.

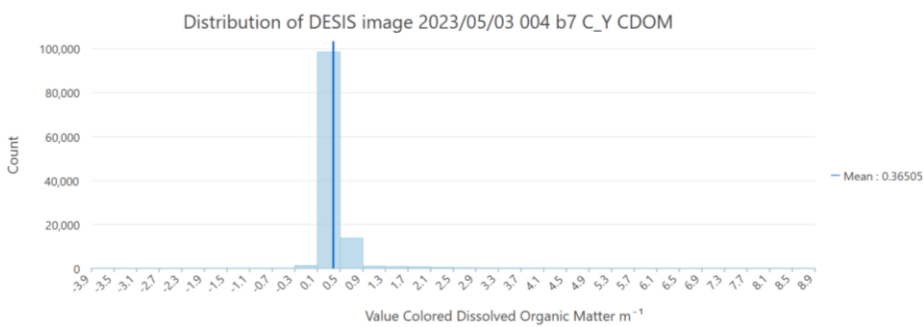


Figure 207: Bar chart result pixel distribution of DESIS 2023/05/03 004 b7 C_Y CDOM.

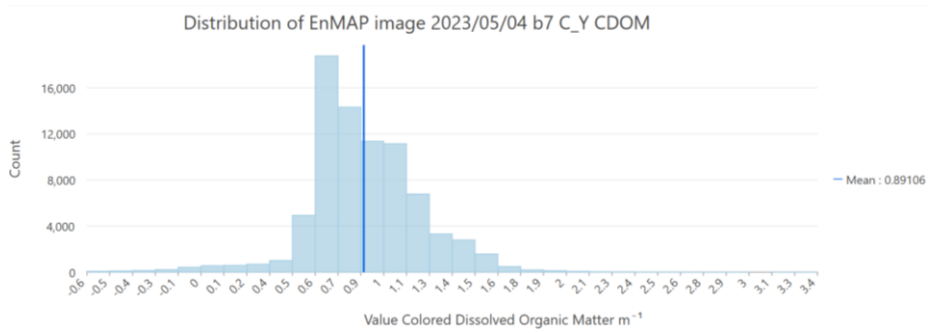


Figure 208: Bar chart result pixel distribution of EnMAP 2023/05/04 b7 C_Y CDOM.

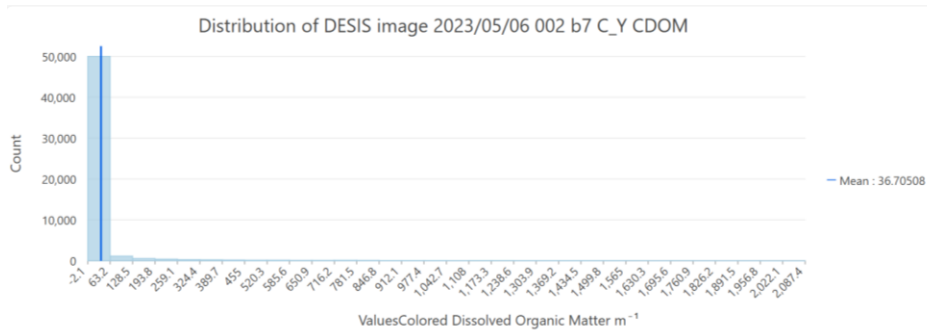


Figure 209: Bar chart result pixel distribution of DESIS 2023/05/06 002 b7 C_Y CDOM.

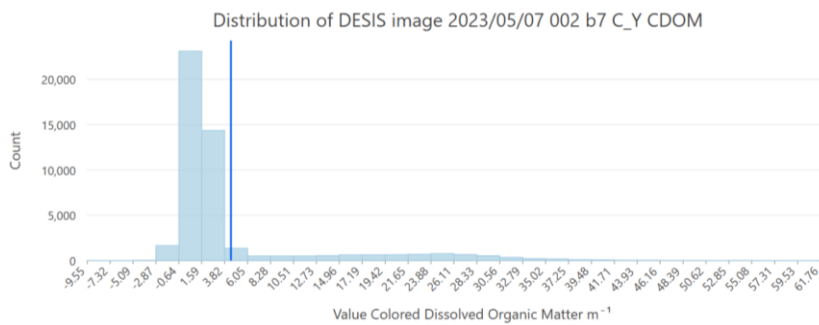


Figure 210: Bar chart result pixel distribution of DESIS 2023/05/07 002 b7 C_Y CDOM.

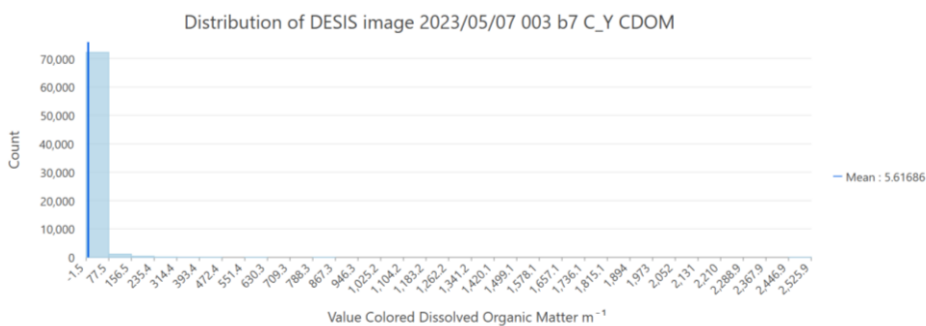


Figure 211: Bar chart result pixel distribution of DESIS 2023/05/07 003 b7 C_Y CDOM.

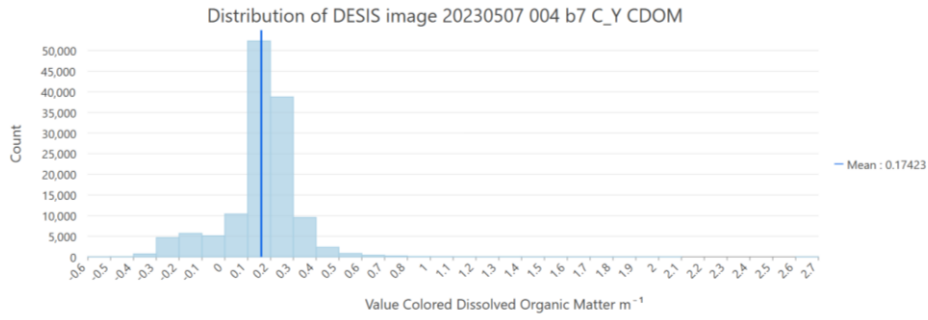


Figure 212: Bar chart result pixel distribution of DESIS 203/05/07 003 b7 C_Y CDOM.

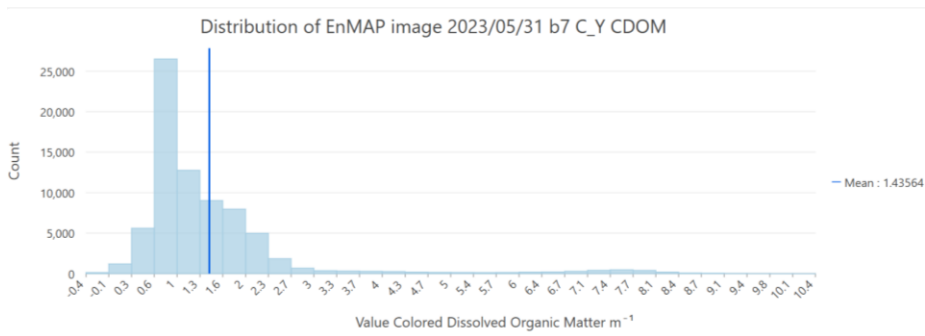


Figure 213: Bar chart result pixel distribution of EnMAP 2023/05/31 b7 C_Y CDOM.

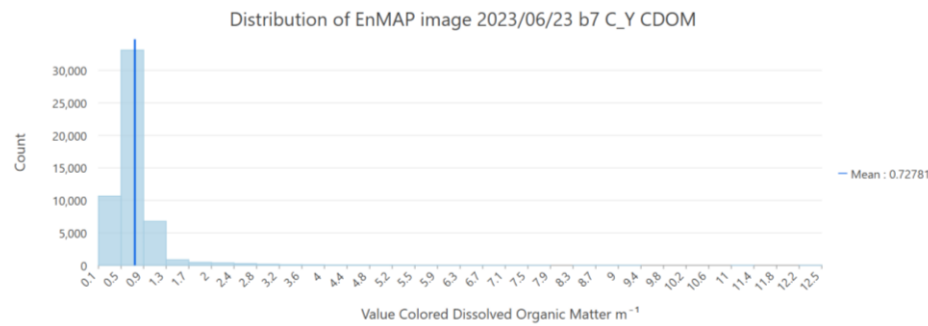


Figure 214: Bar chart result pixel distribution of EnMAP 2023/06/23 b7 C_Y CDOM.

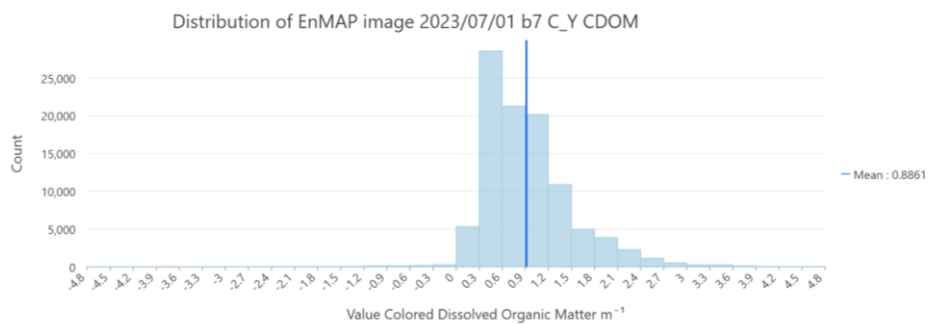


Figure 215: Bar chart result pixel distribution of EnMAP 2023/06/23 b7 C_Y CDOM.

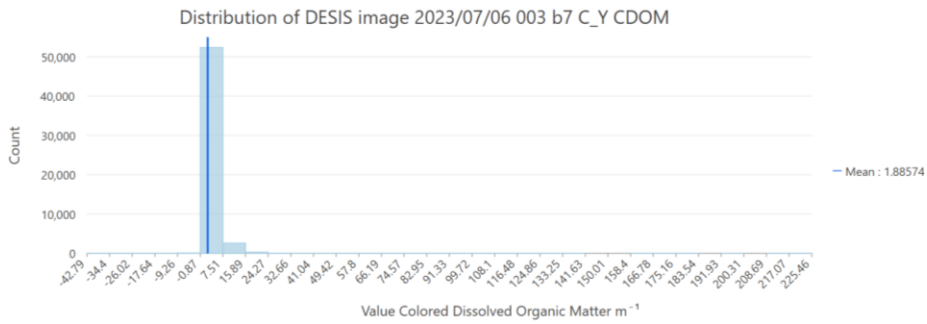


Figure 216: Bar chart result pixel distribution of DESIS 2023/07/06 003 b7 C_Y CDOM.

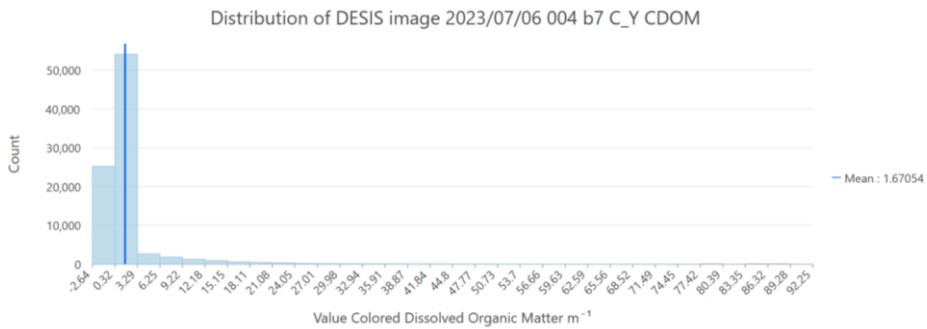


Figure 217: Bar chart result pixel distribution of DESIS 2023/07/06 004 b7 C_Y CDOM.

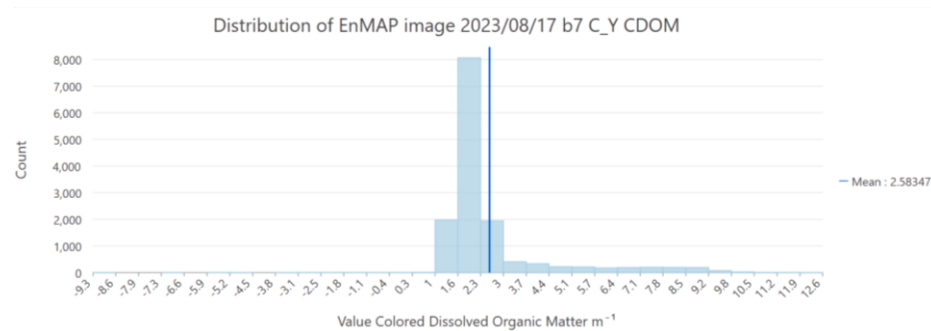


Figure 218: Bar chart result pixel distribution of EnMAP 2023/08/17 b7 C_Y CDOM.

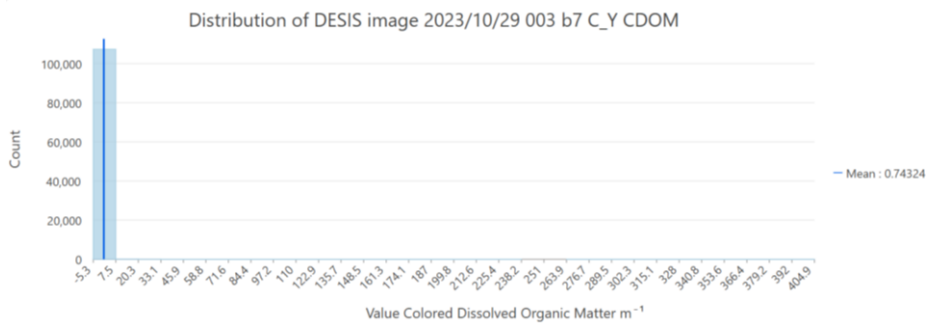


Figure 219: Bar chart result pixel distribution of DESIS 2023/10/29 003 b7 C_Y CDOM.

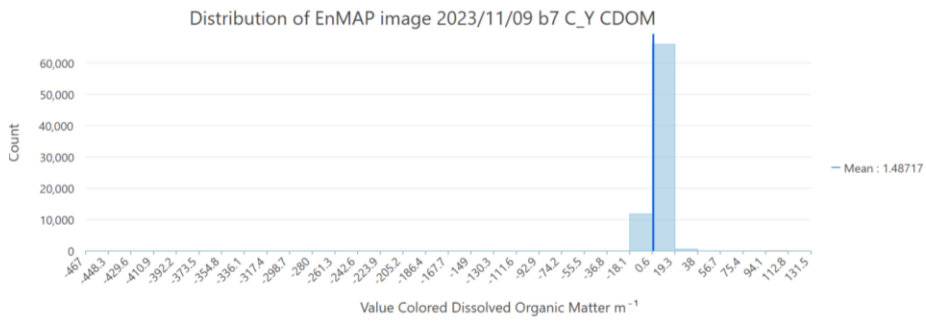


Figure 220: Bar chart result pixel distribution of EnMAP 2023/1109 b7 C_Y CDOM.

11 SUMMARY FROM HEXAGON IMAGE RESULTS DISTRIBUTION OF THE IMAGE SUMMERY (BAR CHART)

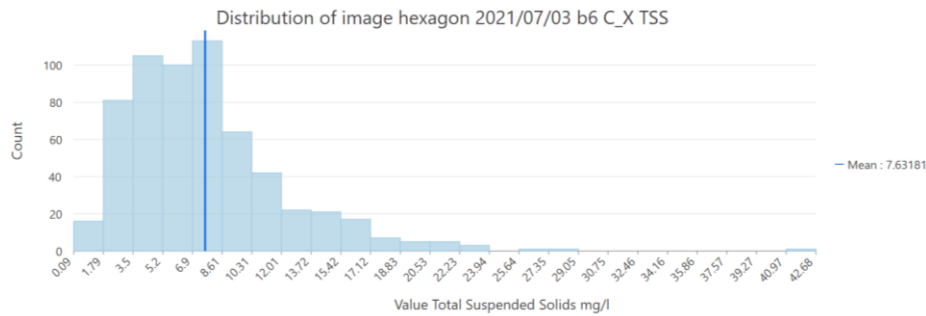


Figure 221: Bar chart result distribution of hexagon 2021/07/03 b6 C_X TSS.

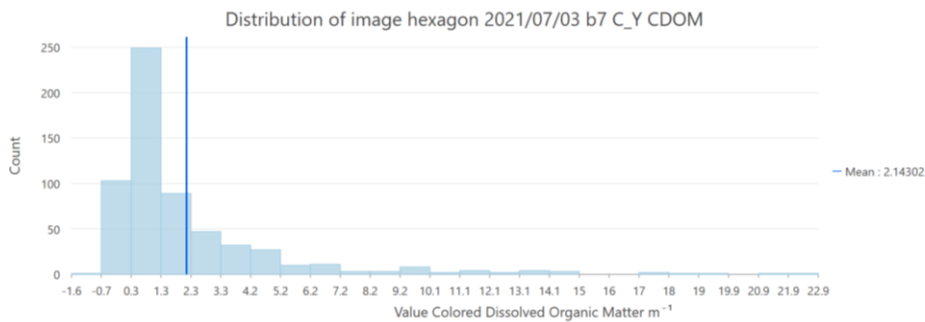


Figure 222: Bar chart result distribution of hexagon 2021/07/03 b7 C_Y CDOM.

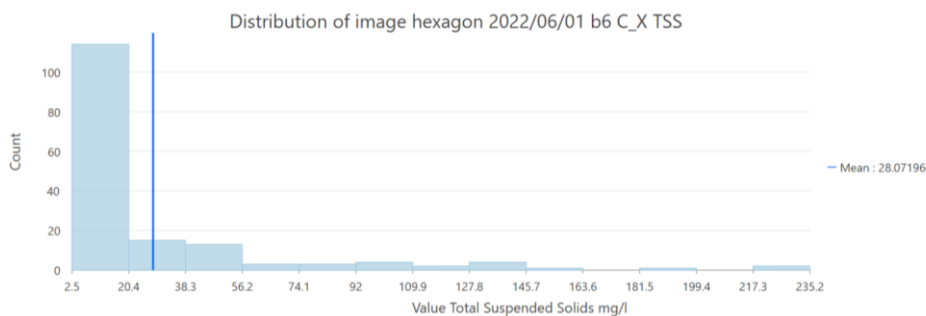


Figure 223: Bar chart result distribution of hexagon 2022/06/01 b6 C_X TSS.

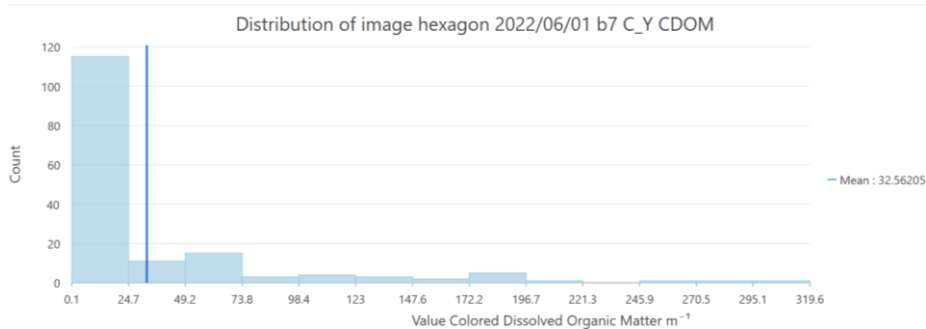


Figure 224: Bar chart result distribution of hexagon 2022/06/01 b7 C_Y CDOM.

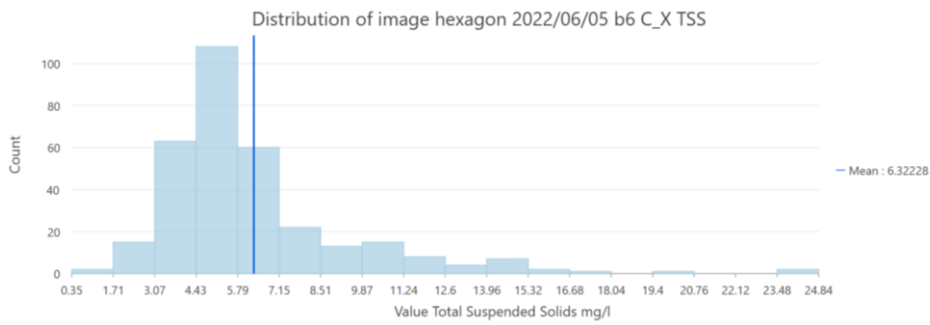


Figure 225: Bar chart result distribution of hexagon 2022/06/05 b6 C_X TSS.

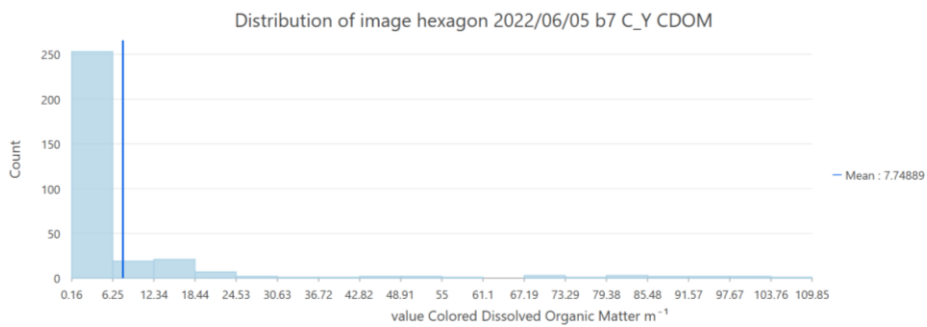


Figure 226: Bar chart result distribution of hexagon 2022/06/05 b7 C_Y CDOM.

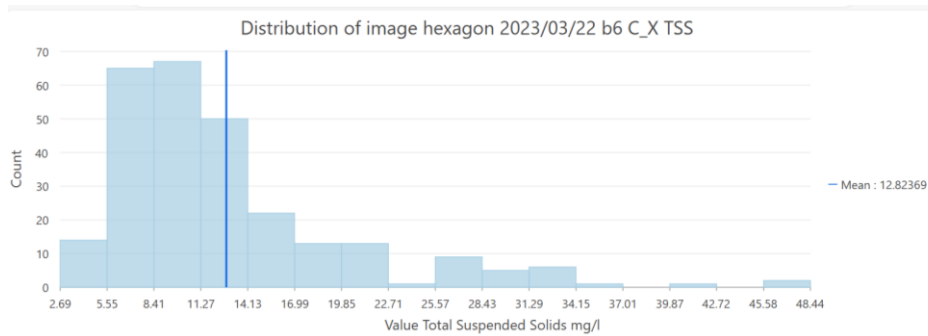


Figure 227: Bar chart result distribution of hexagon 2023/03/22 b6 C_X TSS.

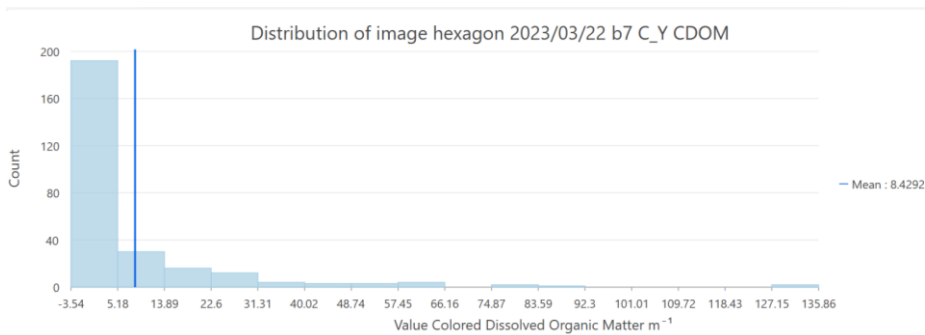


Figure 228: Bar chart result distribution of hexagon 2023/03/22 b7 C_Y CDOM.

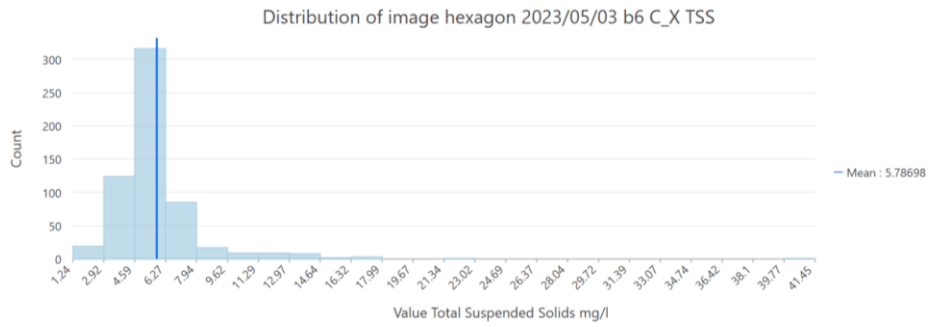


Figure 229: Bar Chart result distribution of hexagon 2023/05/03 b6 C_X TSS.

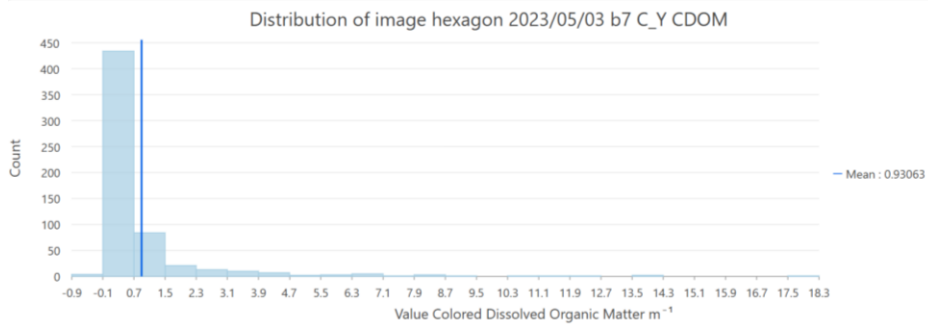


Figure 230: Bar chart result distribution of hexagon 2023/05/03 b7 C_Y CDOM.

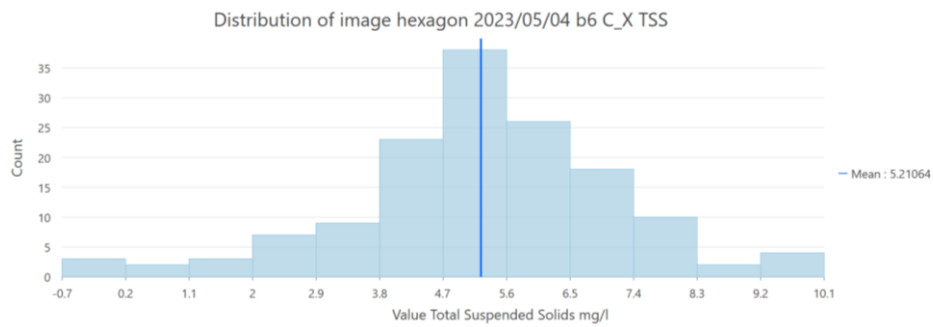


Figure 231: Bar chart result distribution of hexagon 2023/05/04 b6 C_X TSS.

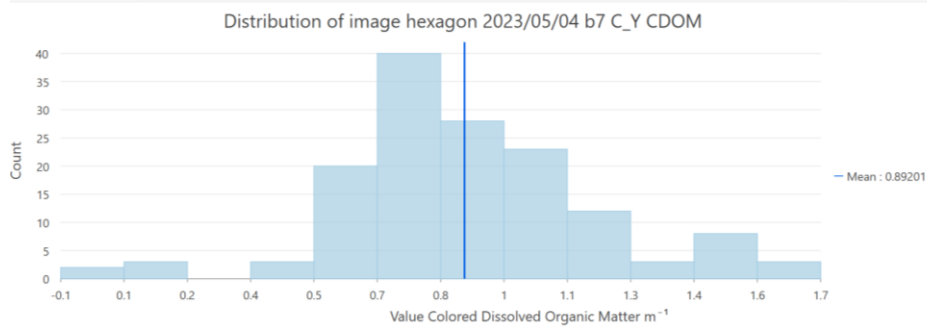


Figure 232: Bar chart result distribution of hexagon 2023/05/04 b7 C_Y CDOM.

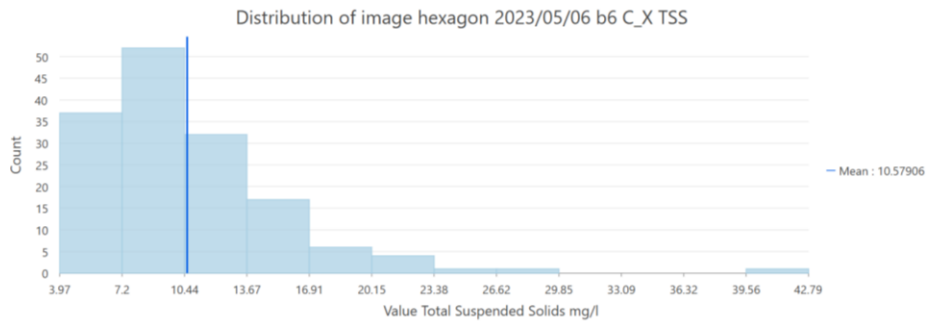


Figure 233: Bar chart result distribution of hexagon 2023/05/06 b6 C_X TSS.

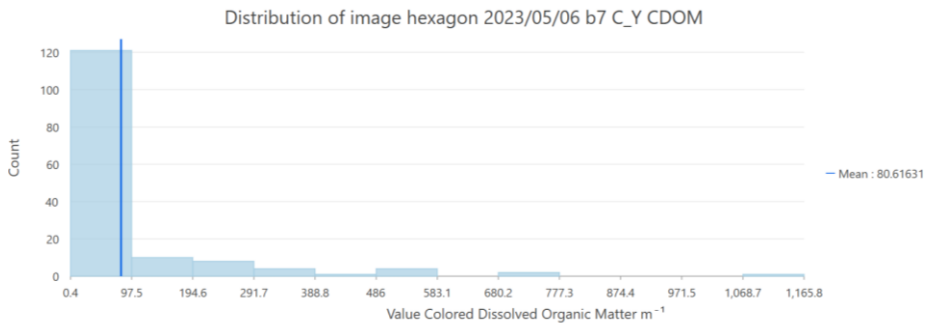


Figure 234: Bar chart result distribution of hexagon 2023/05/06 b7 C_Y CDOM.

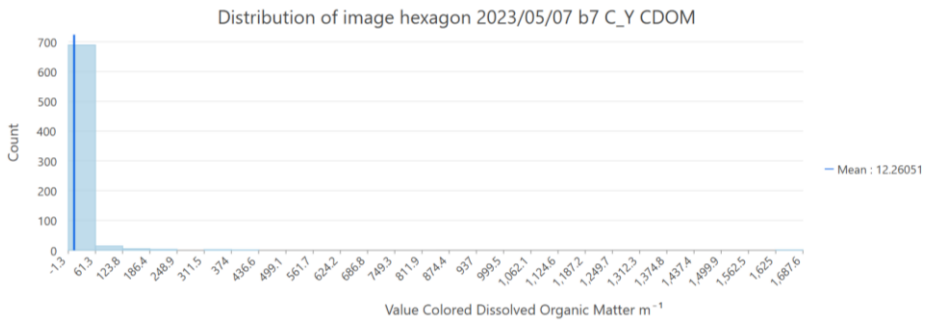


Figure 235: Bar chart result distribution of hexagon 2023/05/07 b7 C_Y CDOM.

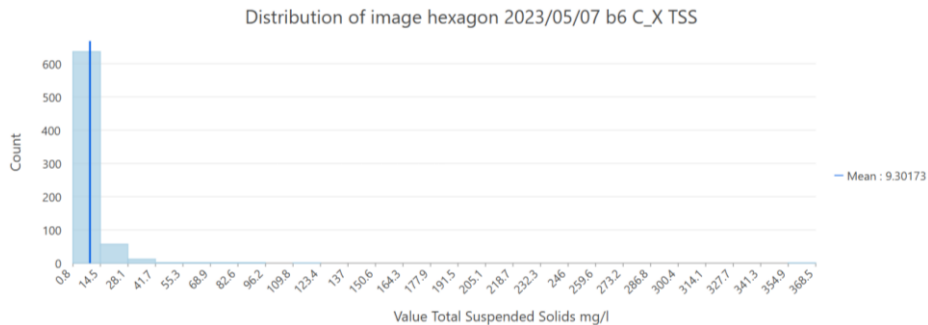


Figure 236: Bar chart result distribution of hexagon 2023/05/07 b6 C_X TSS.

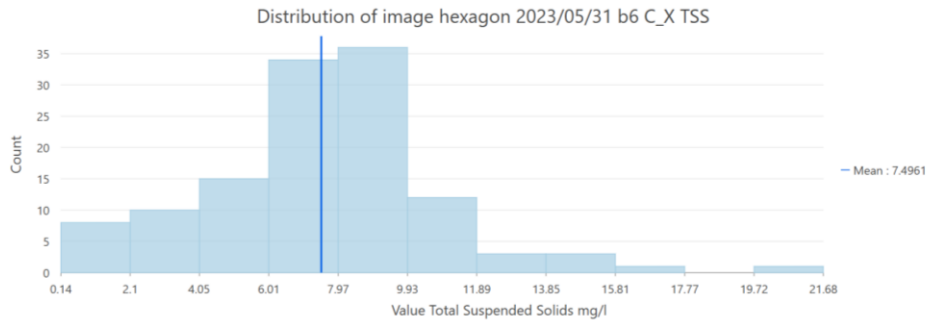


Figure 237: Bar chart result distribution of hexagon 2023/05/31 b6 C_X TSS.

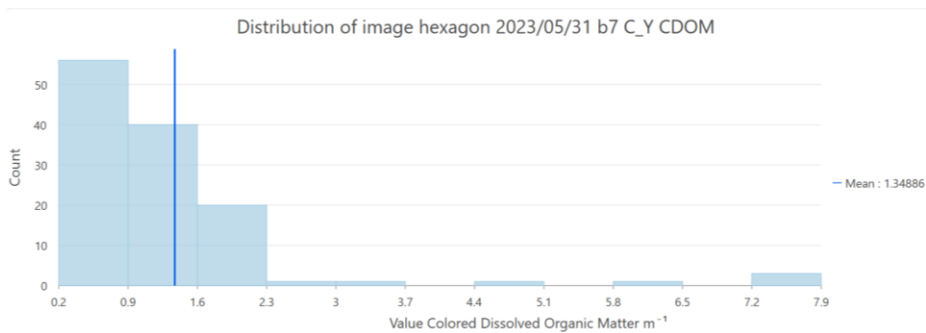


Figure 238: Bar chart result distribution of hexagon 2023/05/31 b7 C_Y CDOM.

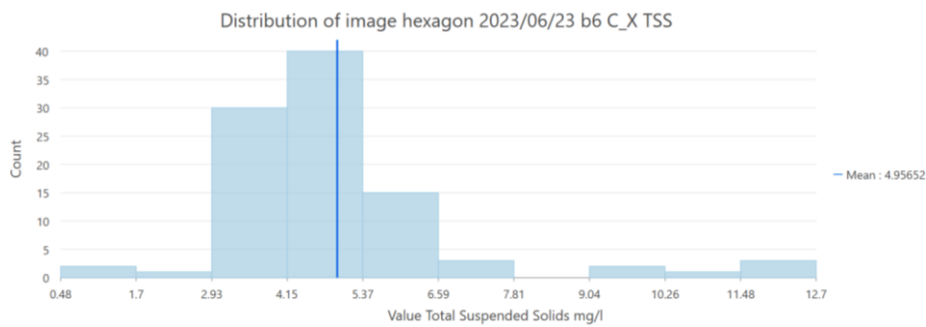


Figure 239: Bar chart result distribution of hexagon 2023/06/23 b6 C_X TSS.

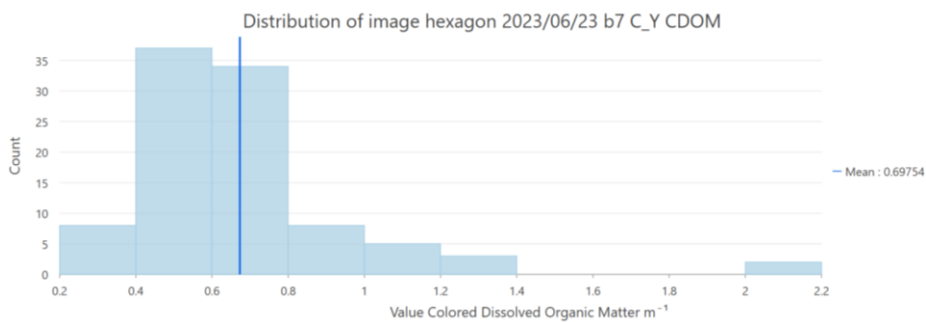


Figure 240: Bar chart result distribution of hexagon 2023/06/23 b7 C_Y CDOM.

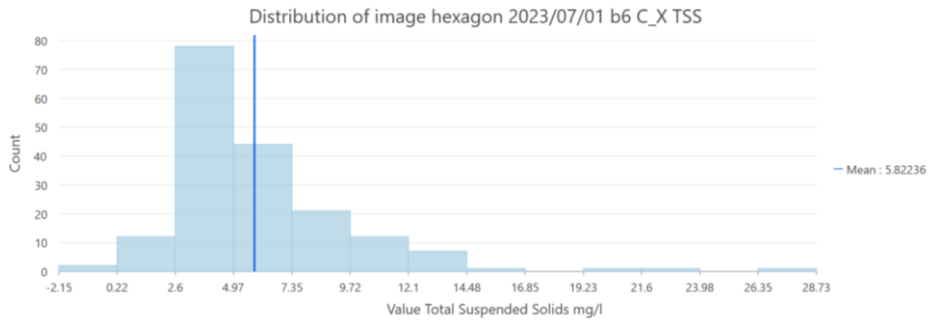


Figure 241:: Bar chart result distribution of hexagon 2023/07/01 b6 C_X TSS.

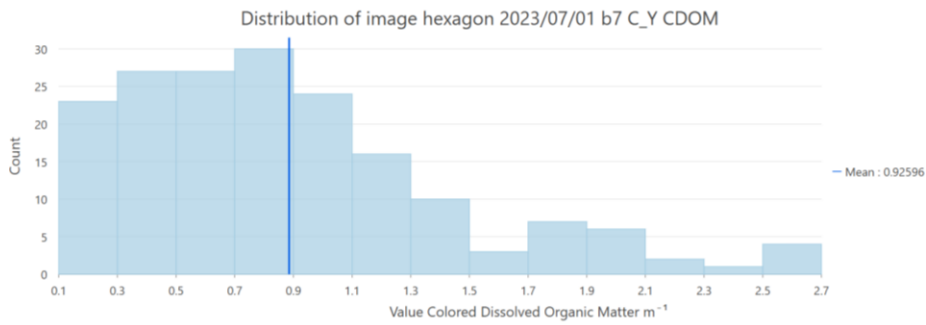


Figure 242: Bar chart result distribution of hexagon 2023/07/01 b7 C_Y CDOM.

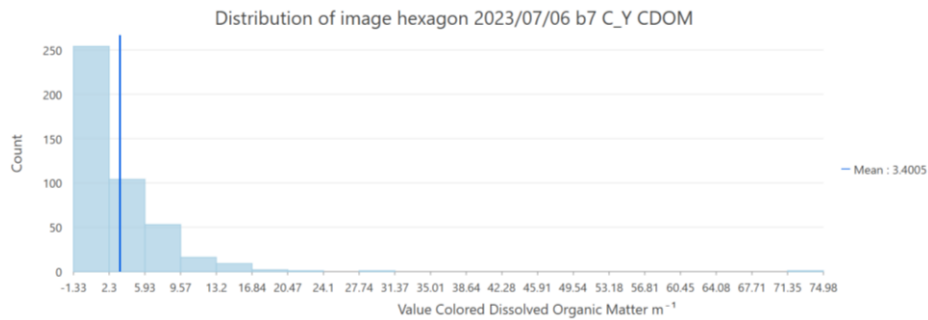


Figure 243: Bar chart result distribution of hexagon 2023/07/06 b7 C_Y CDOM.

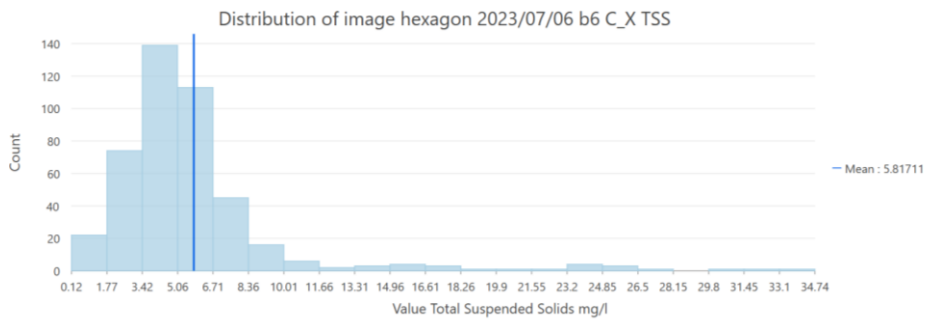


Figure 244:: Bar chart result distribution of hexagon 2023/07/06 b6 C_X TSS.

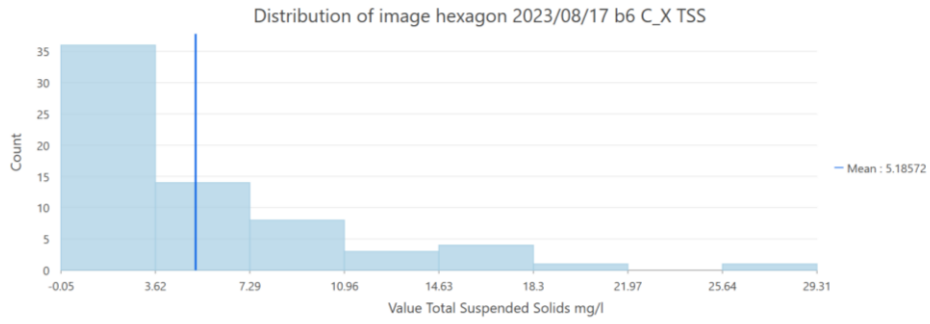


Figure 245: Bar chart result distribution of hexagon 2023/08/17 b6 C_X TSS.

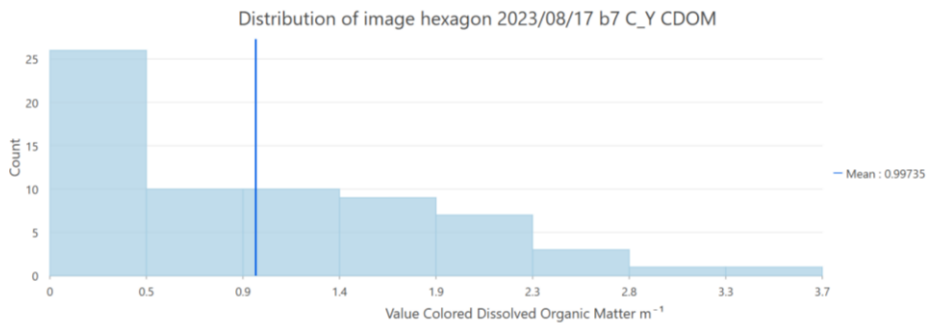


Figure 246: Bar chart result distribution of hexagon 2023/08/17 b7 C_Y CDOM.

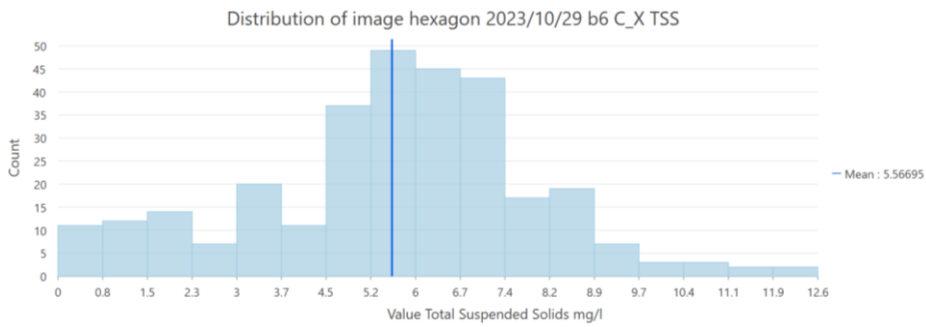


Figure 247: Bar chart result distribution of hexagon 2023/10/29 b6 C_X TSS.

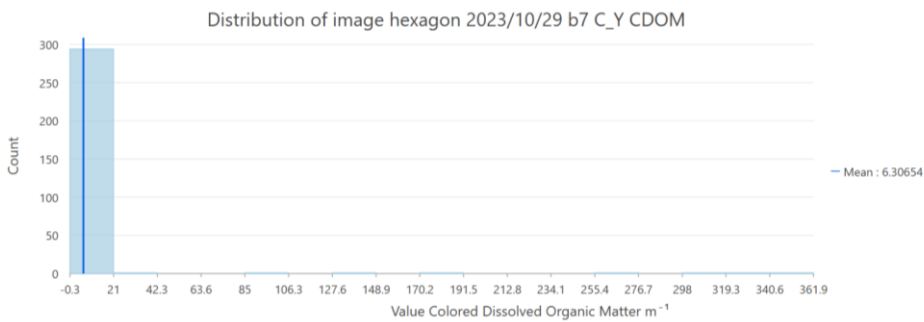


Figure 248: Bar chart result distribution of hexagon 2023/10/29 b7 C_Y CDOM.

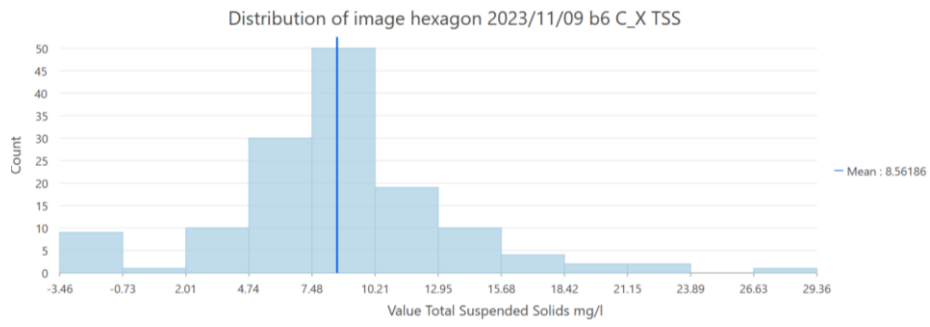


Figure 249: Bar chart result distribution of hexagon2023/11/09 b6 C_X TSS.

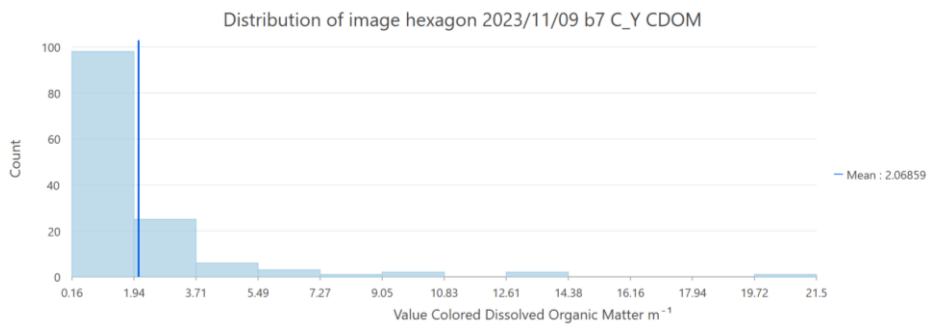


Figure 250: Bar chart result distribution of hexagon 2023/11/09 b7 C_Y CDOM.

12 GRAPH FOR COMPARING IN-SITU AND SATELLITE DATA

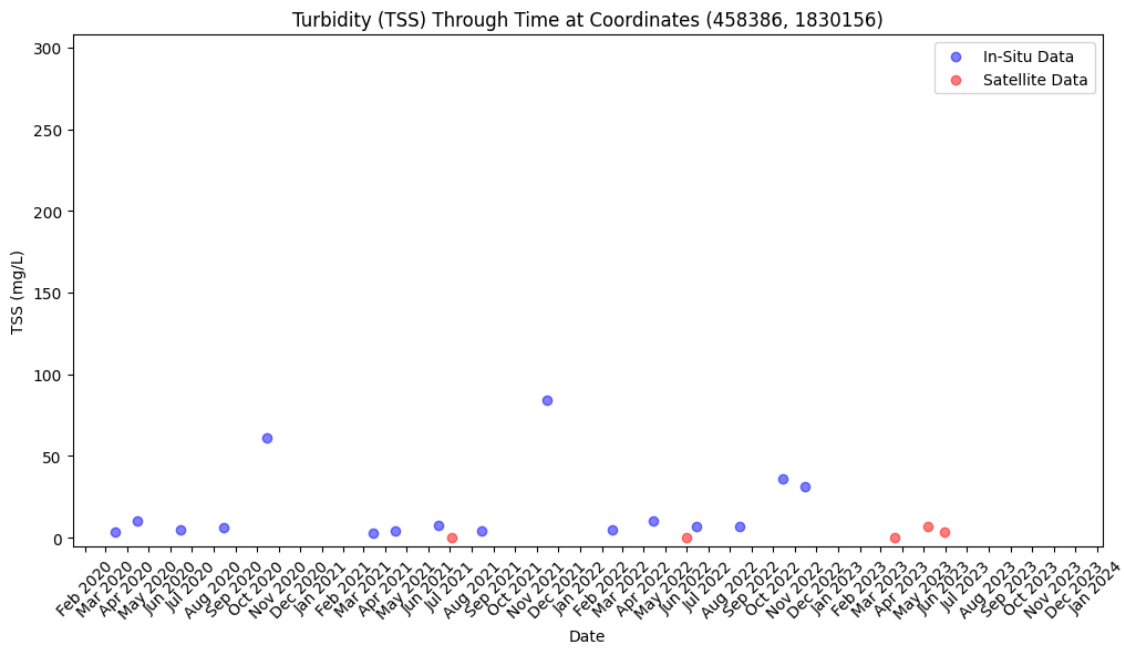


Figure 251: Point sample data of In-situ and satellite point id NSH7 coordinates 458386 1830156.

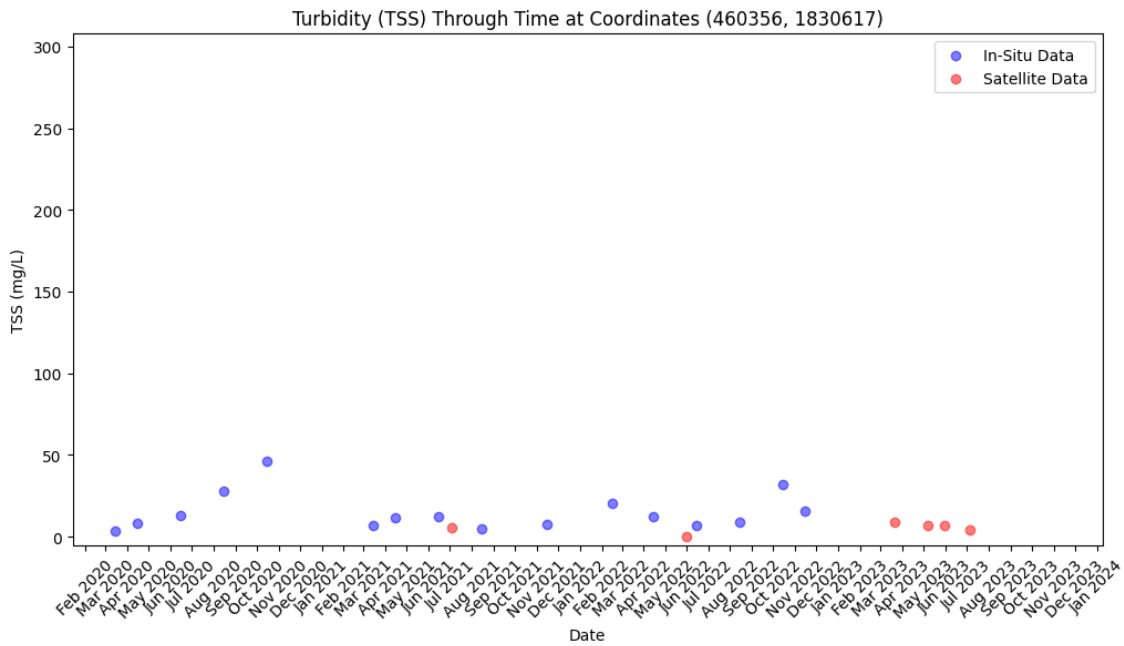


Figure 252: Point sample of In-situ and satellite point id NSH9 coordinates 460356 1830617.

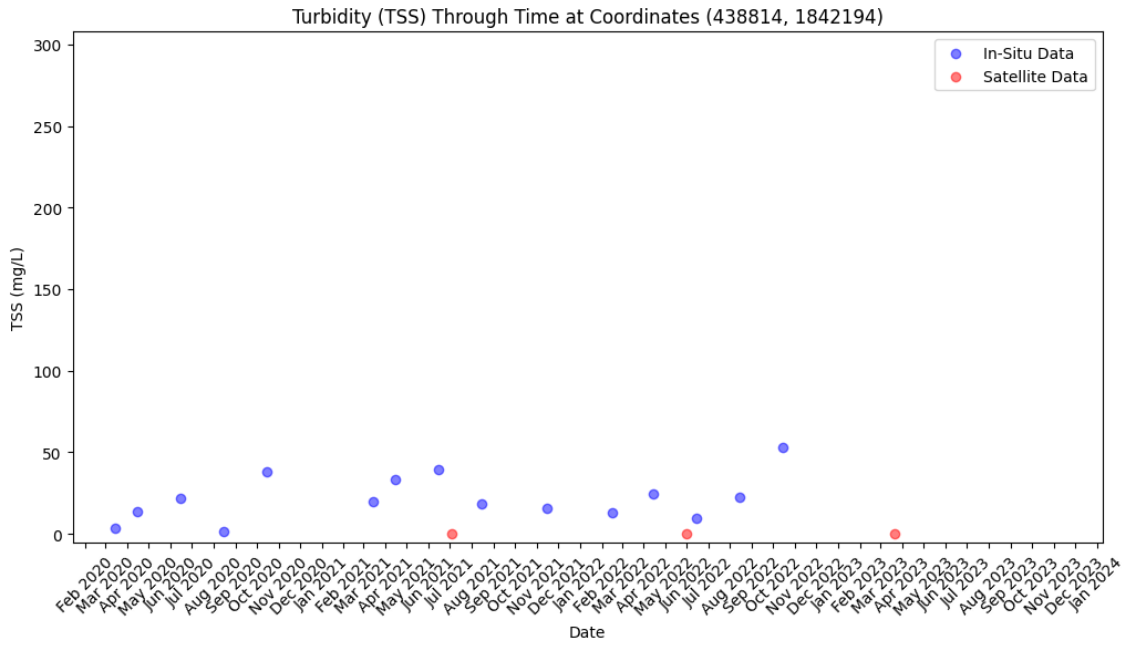


Figure 253: Point sample data of In-situ and satellite point id NPTG1 coordinates 438814 1842194.

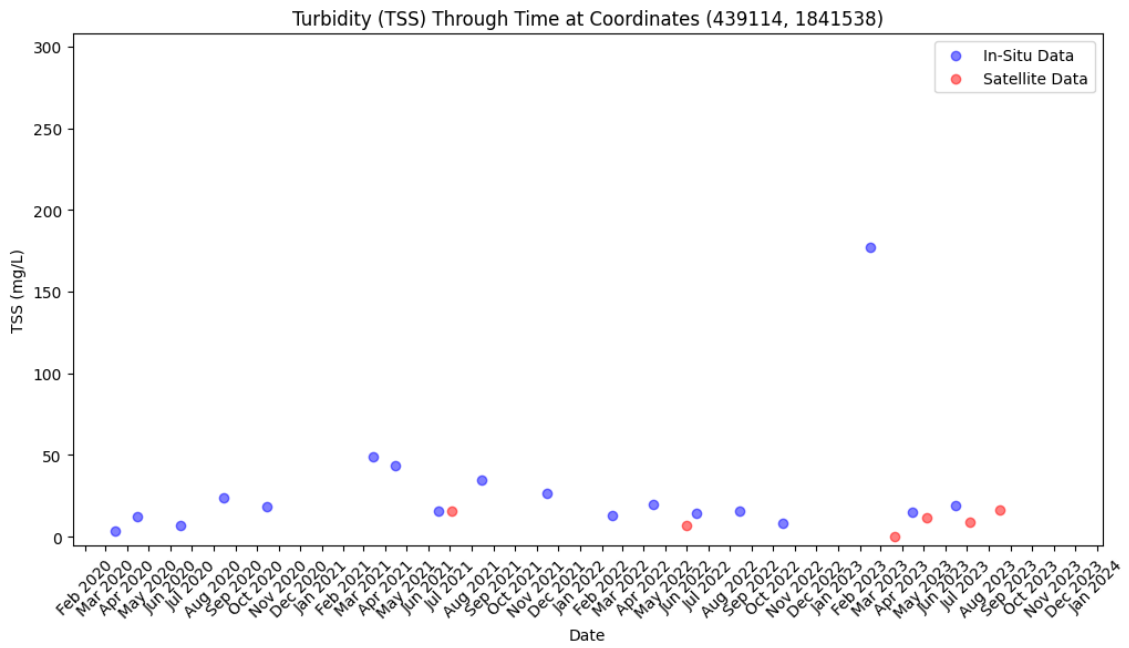


Figure 254: Point sample data of In-situ and satellite point id NPTG3 coordinates 439114 1841538.

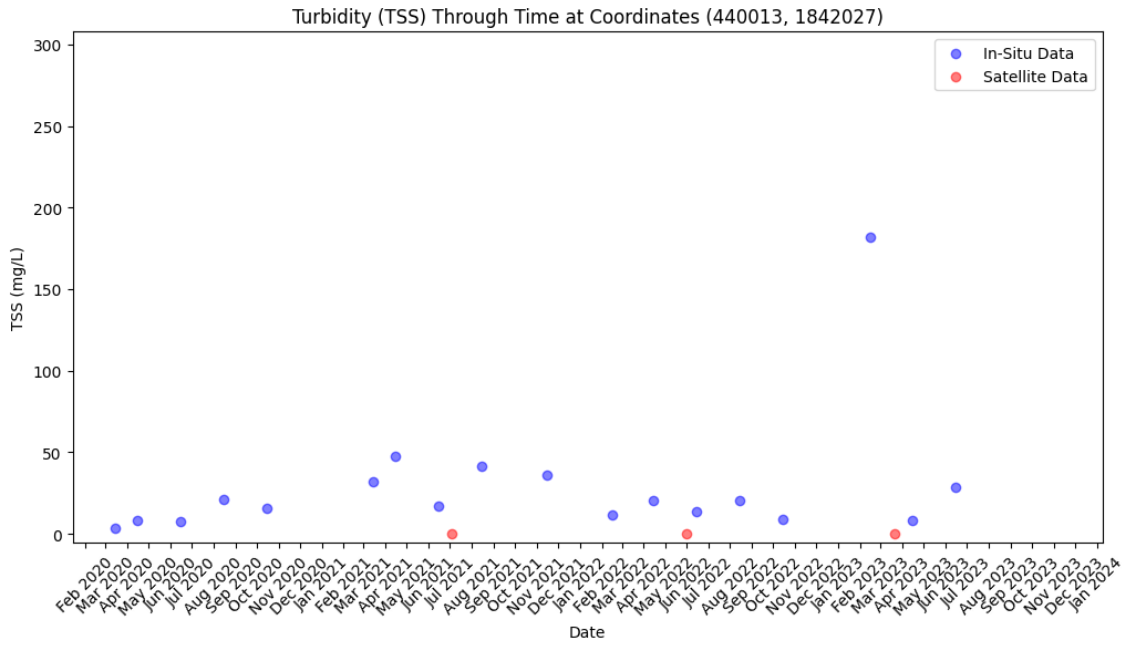


Figure 255: Point sample data of In-situ and satellite point id NPTG4 coordinates 440013 1842027.

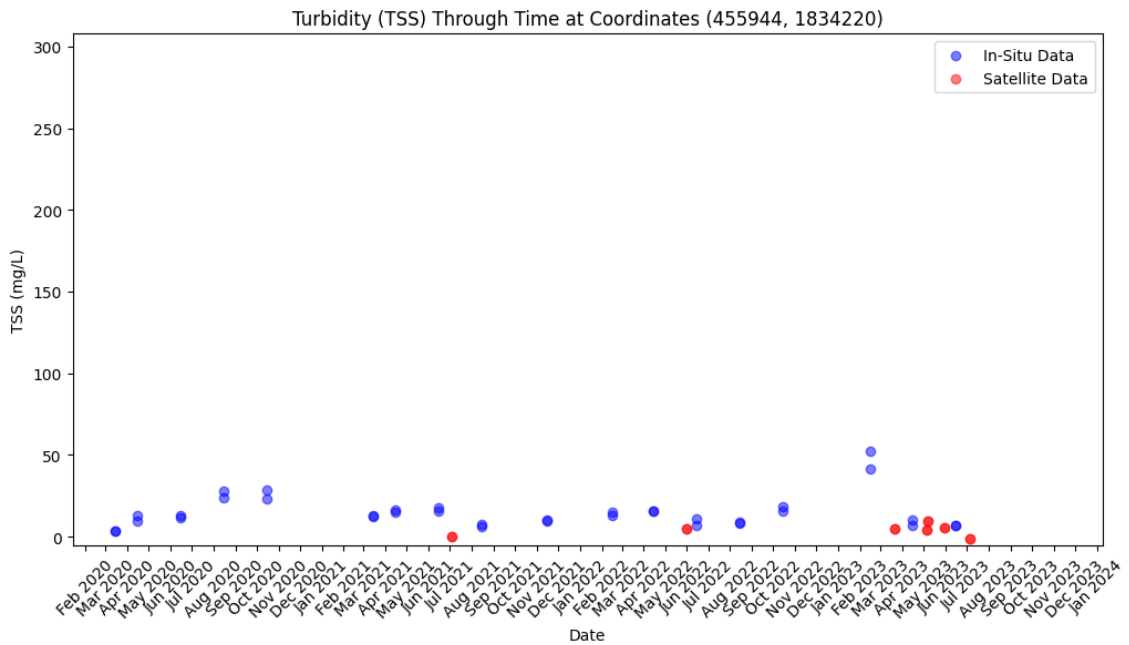


Figure 256: Point sample data of In-situ and satellite point id NPTG5 coordinates 455944 1834220.

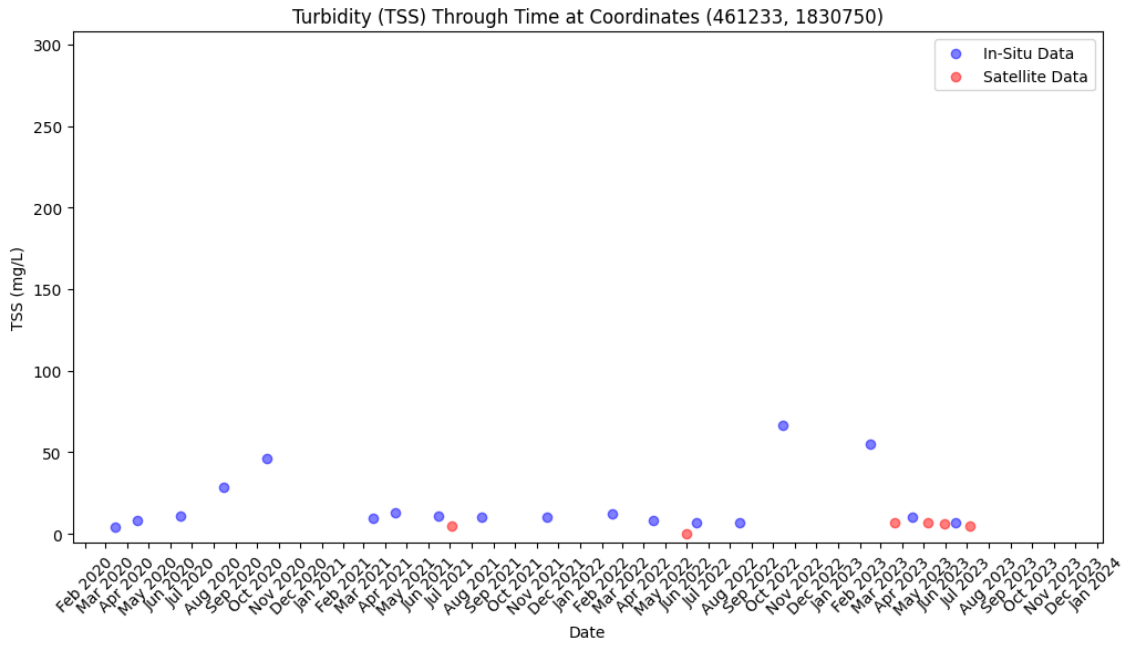


Figure 257: Point sample data of In-situ and satellite point id NPTG7 coordinates 461233 1830750.

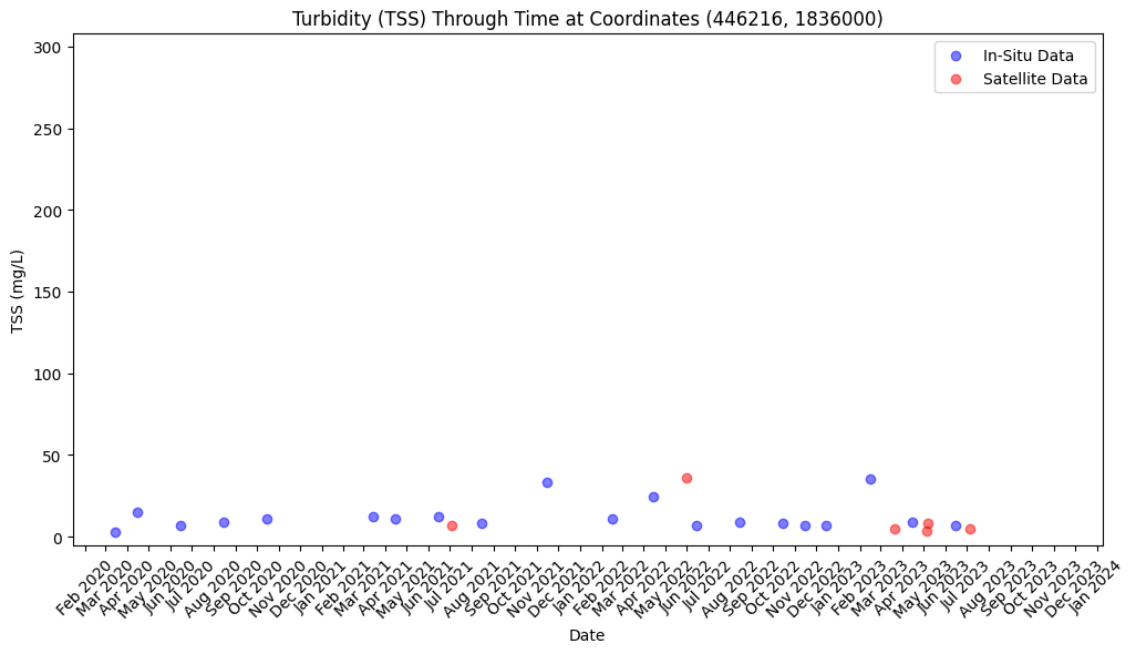


Figure 258: Point sample data of In-situ and satellite point id NPTG8 coordinates 446216 1836000.

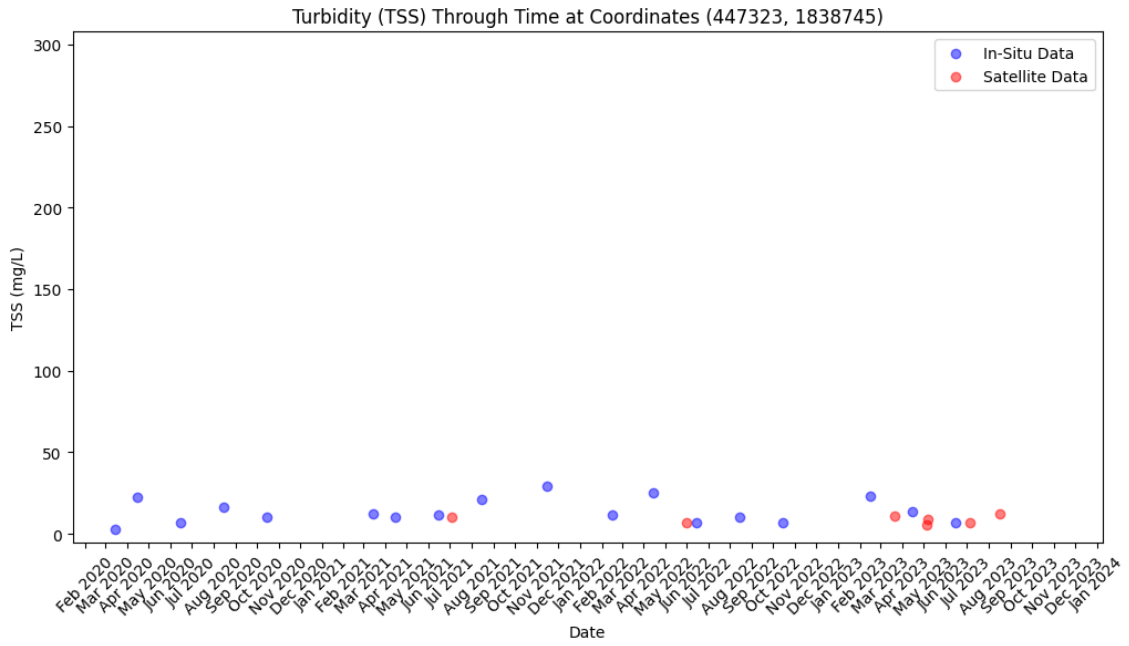


Figure 259: Point sample data of In-situ and satellite point id NPTG9 coordinates 447323 1838745.

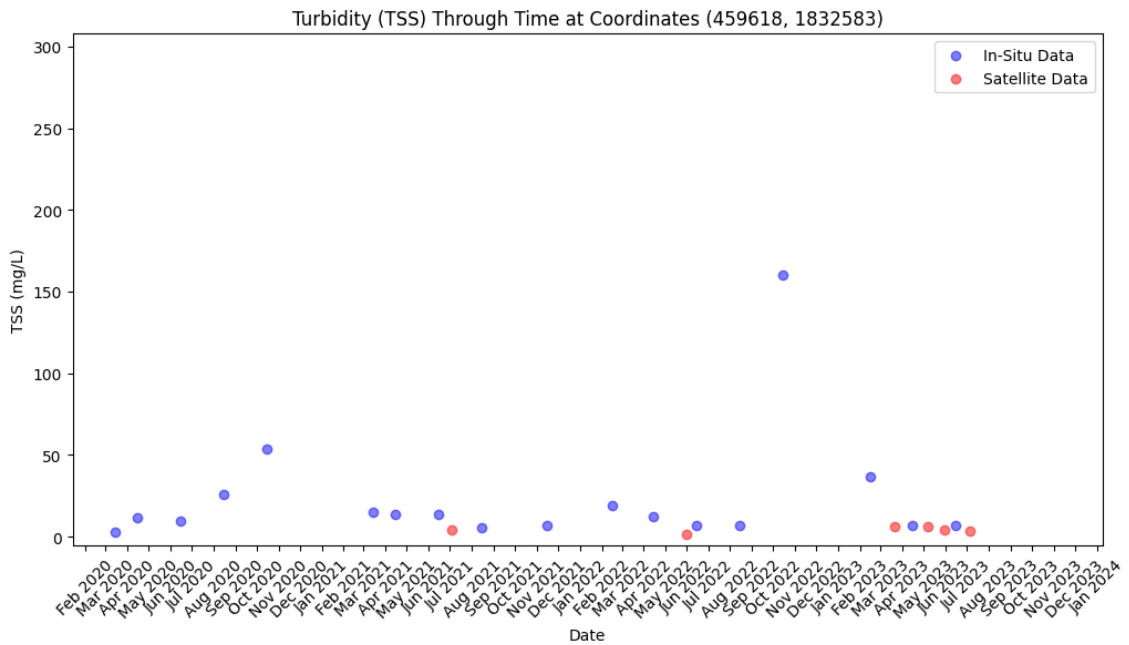


Figure 260: Point sample data of In-situ and satellite point id NPTG10 coordinates 459618 1832583.

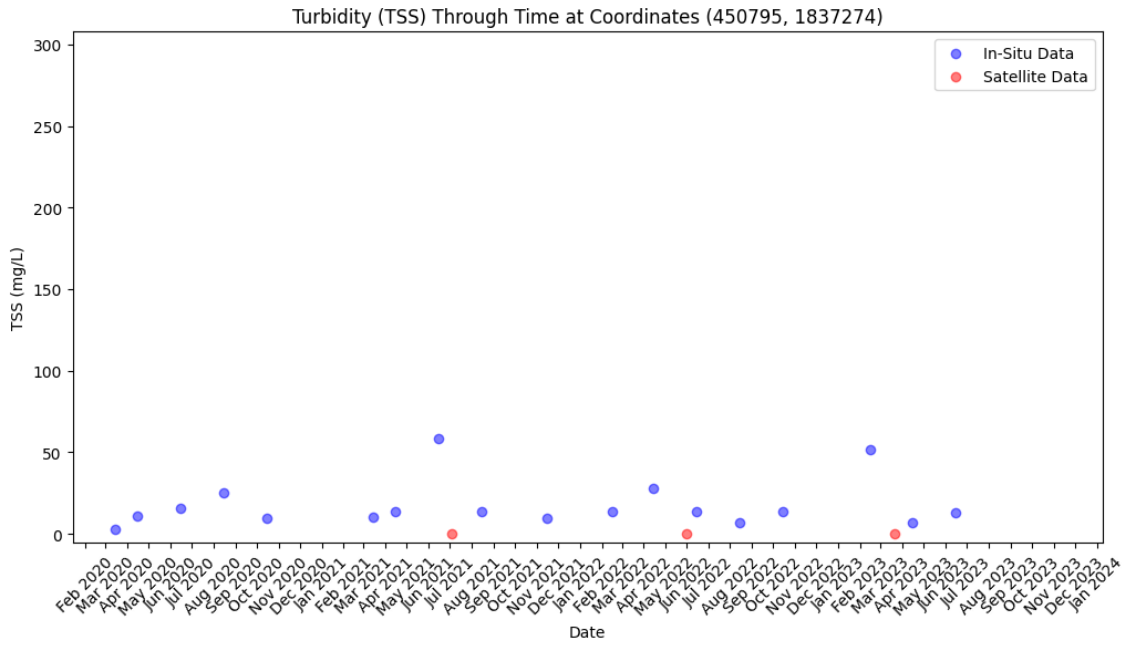


Figure 261: Point sample data of In-situ and satellite point id NPTG11 coordinates 450795 1837274.

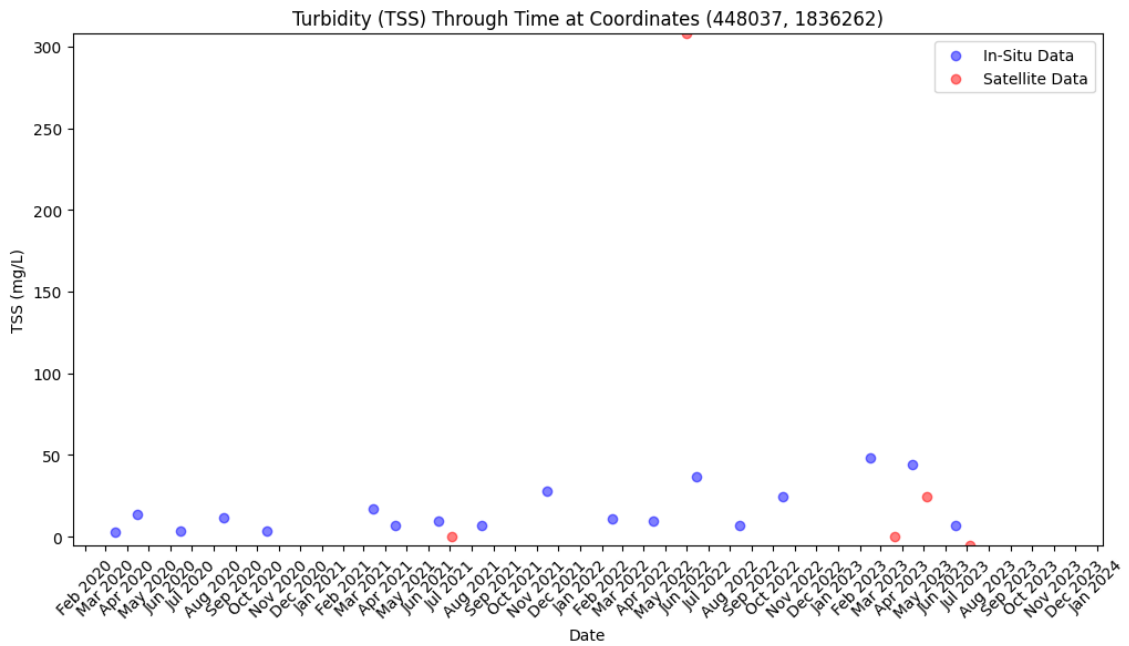


Figure 262: Point sample data of In-situ and satellite point id NPTG12 coordinates 448037 1836262.

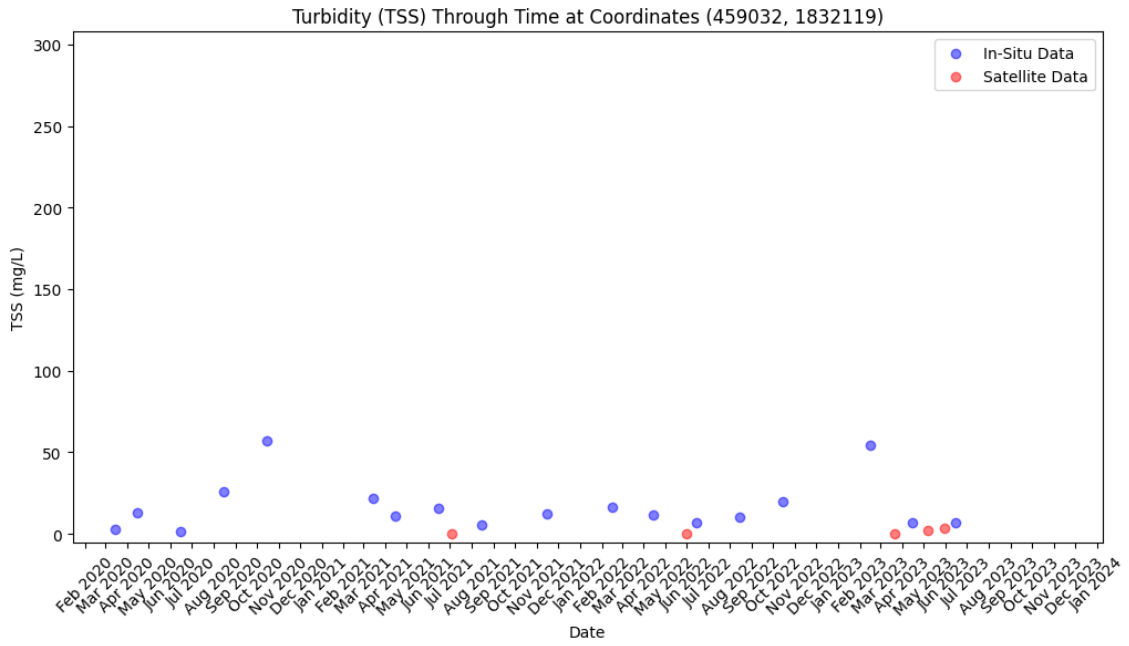


Figure 263: Point sample data of In-situ and satellite point id NPTG13 coordinates 459032 1832119.

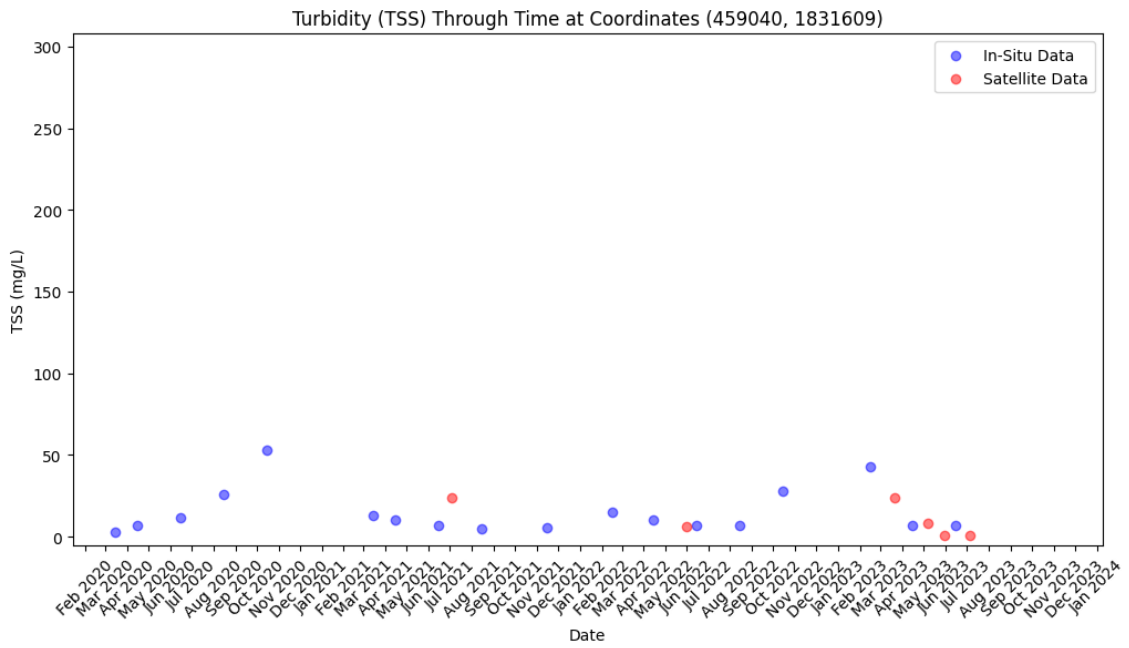


Figure 264: Point sample data of In-situ and satellite point id NPTG14 coordinates 459040 1831609.

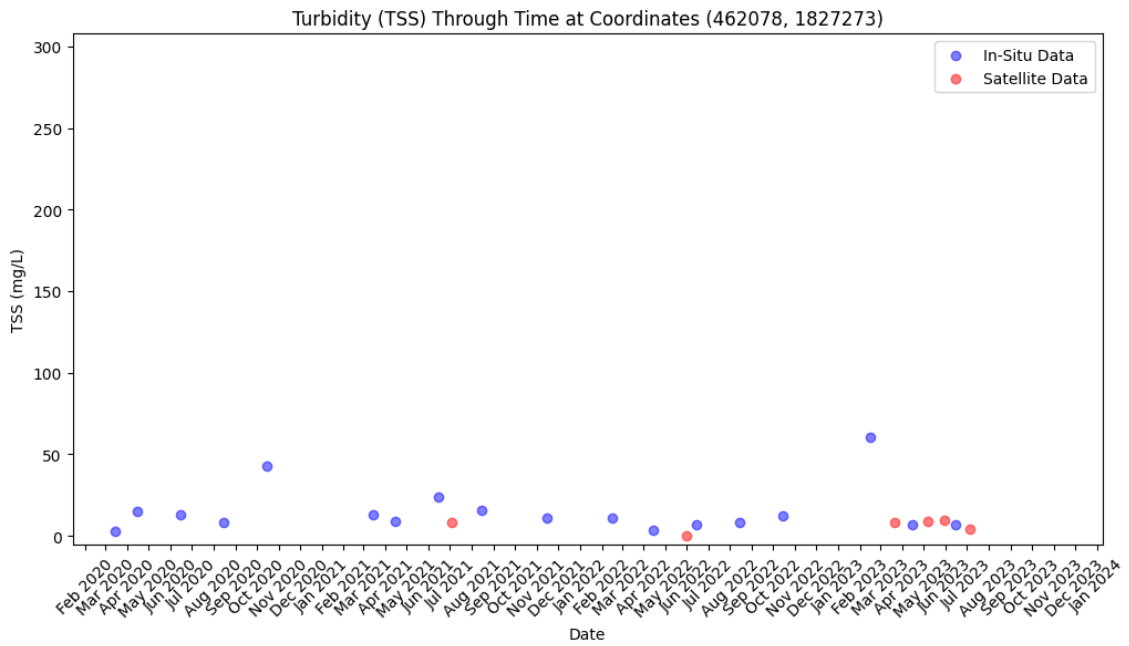


Figure 265: Point sample data of In-situ and satellite point id NÄDTL1 coordinates 462078 1827273.

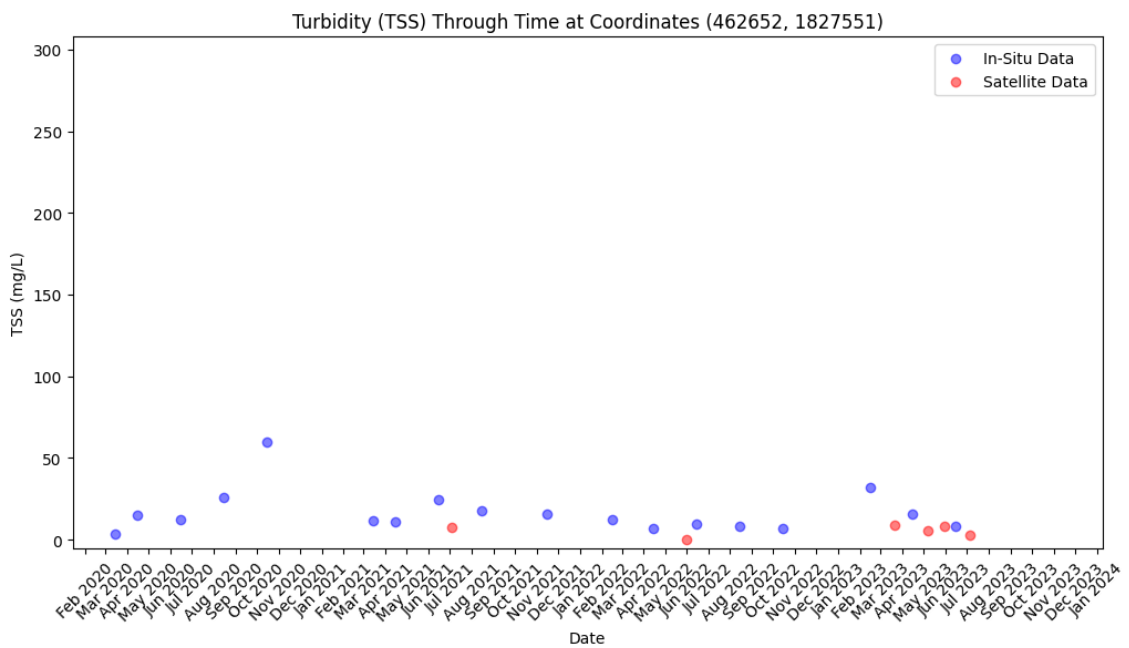


Figure 266: Point sample data of In-situ and satellite point id NÄDTL2 coordinates 462652 1827551.

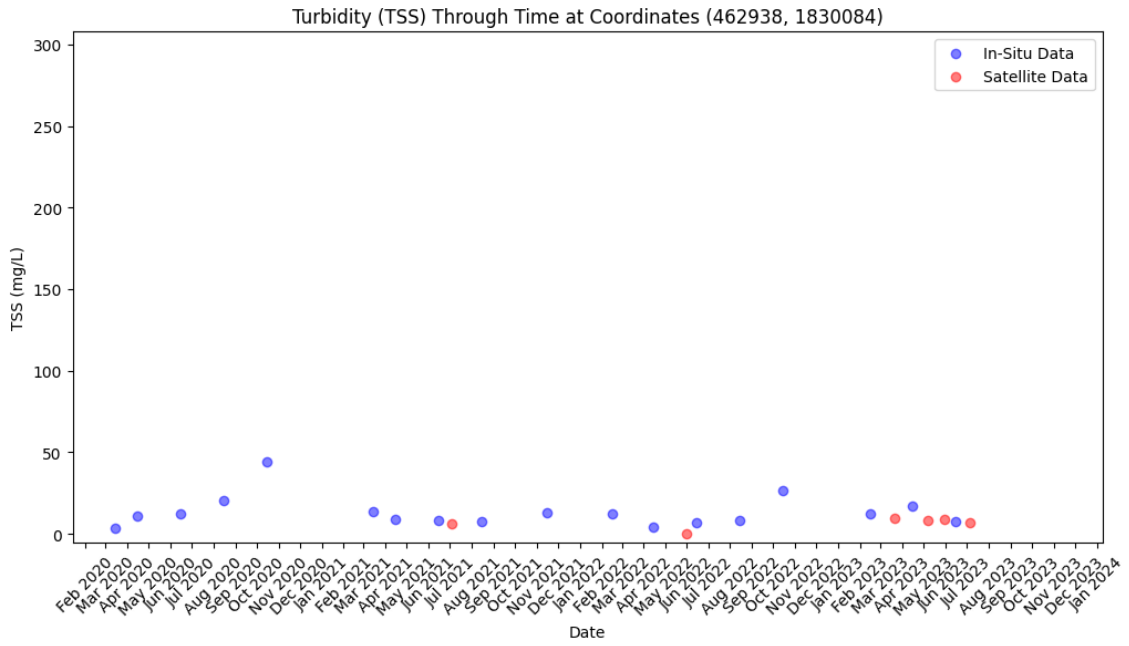


Figure 267: Point sample data of In-situ and satellite point id NÄDTL3 coordinates 462938 1830084.

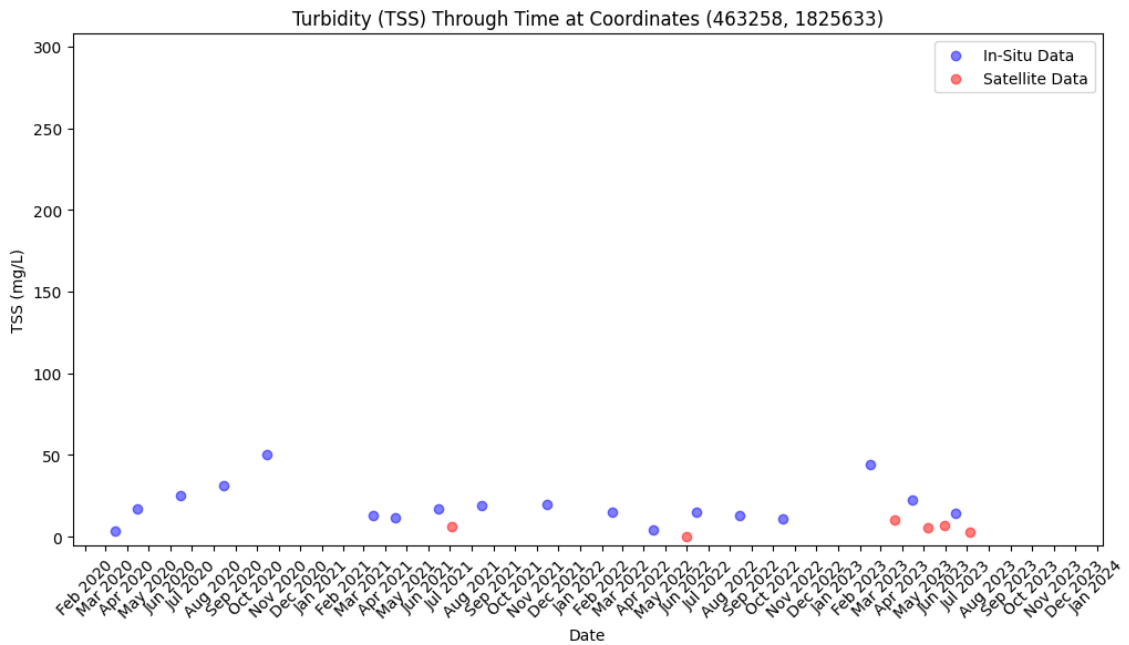


Figure 268: Point sample data of In-situ and satellite point id NÄDTL4 coordinates 463258 1825633.

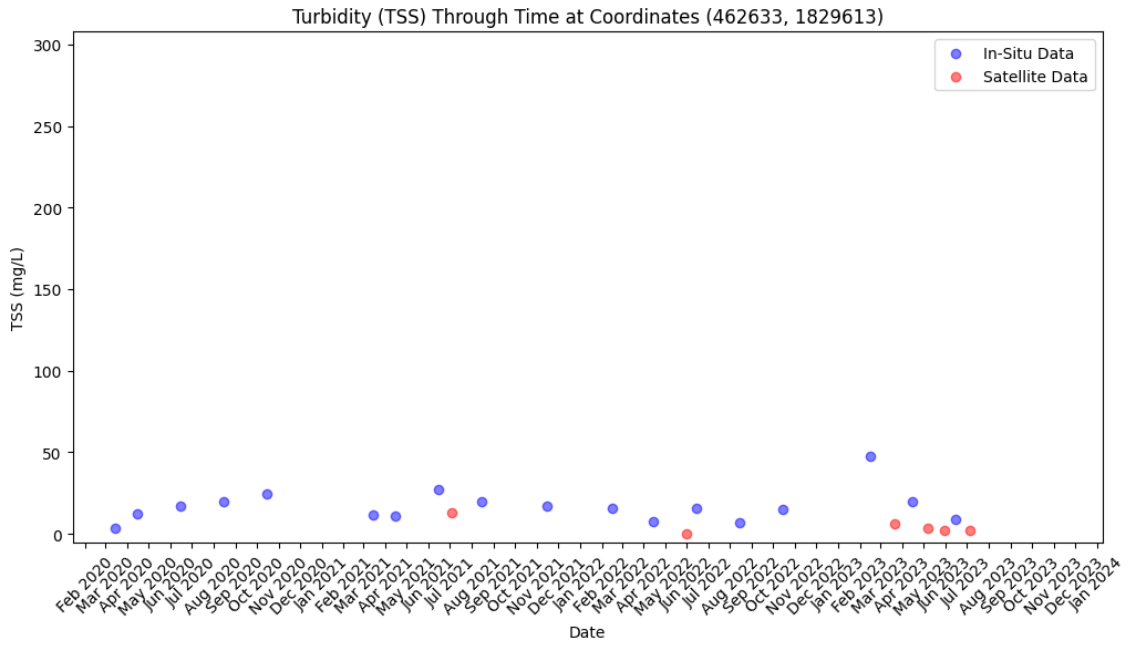


Figure 269: Point sample data of In-situ and satellite point id NÄDTL5 coordinates 462633 1829613.

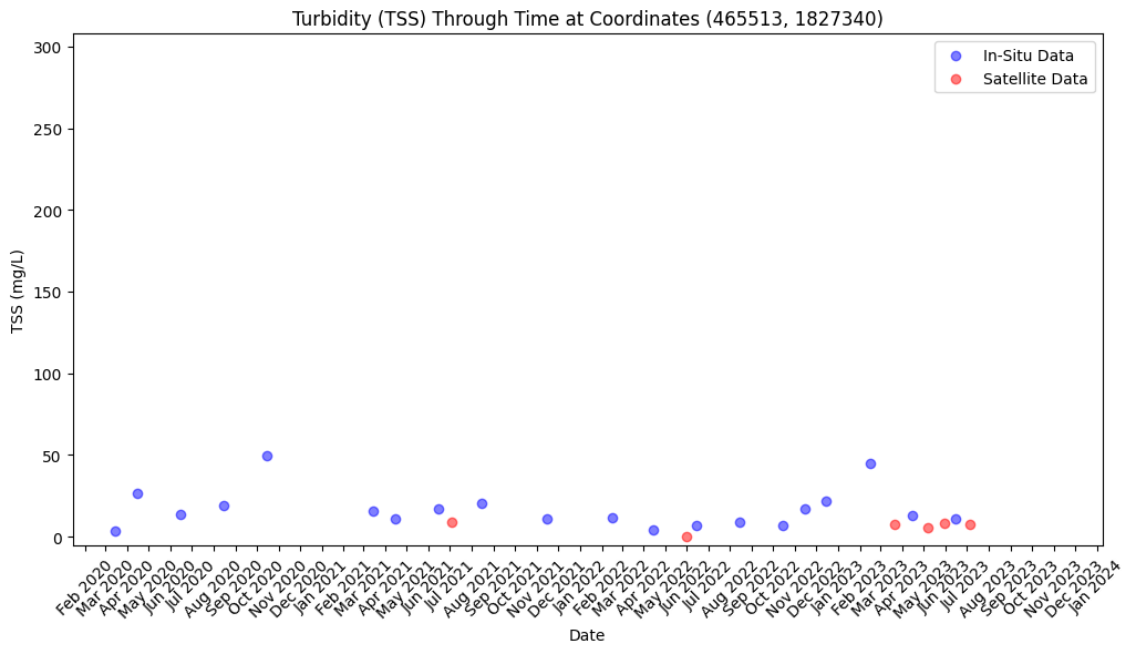


Figure 270: Point sample data of In-situ and satellite point id NÄDTL6 coordinates 465513 1827340.

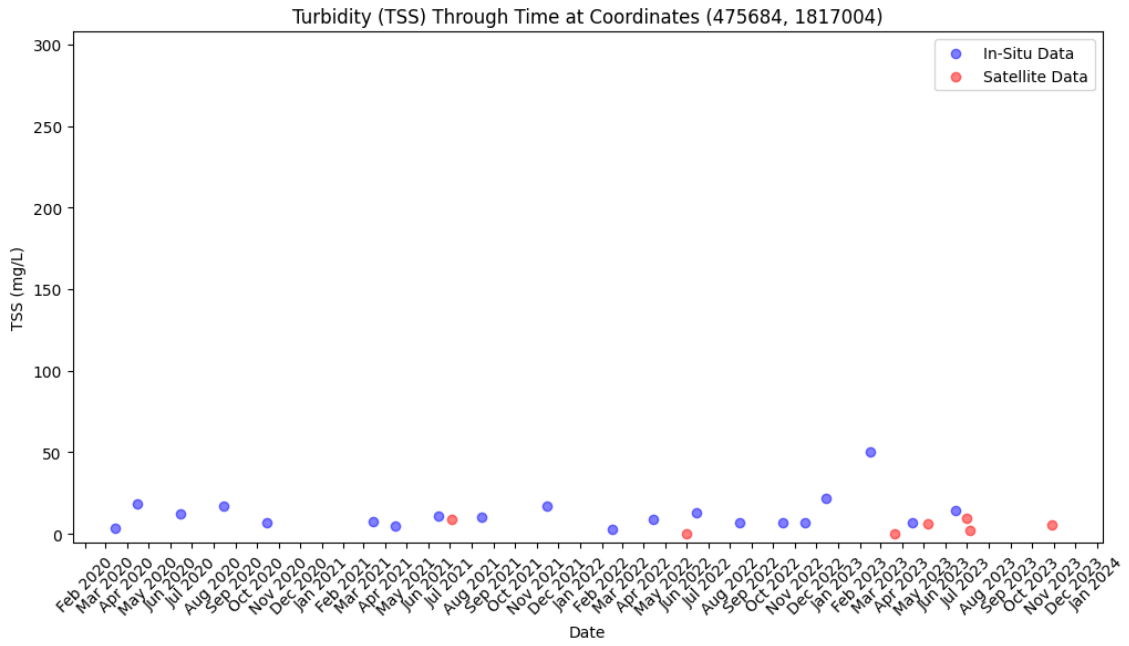


Figure 271: Point sample data of In-situ and satellite point id NÄDTT1 coordinates 475684 1817004.

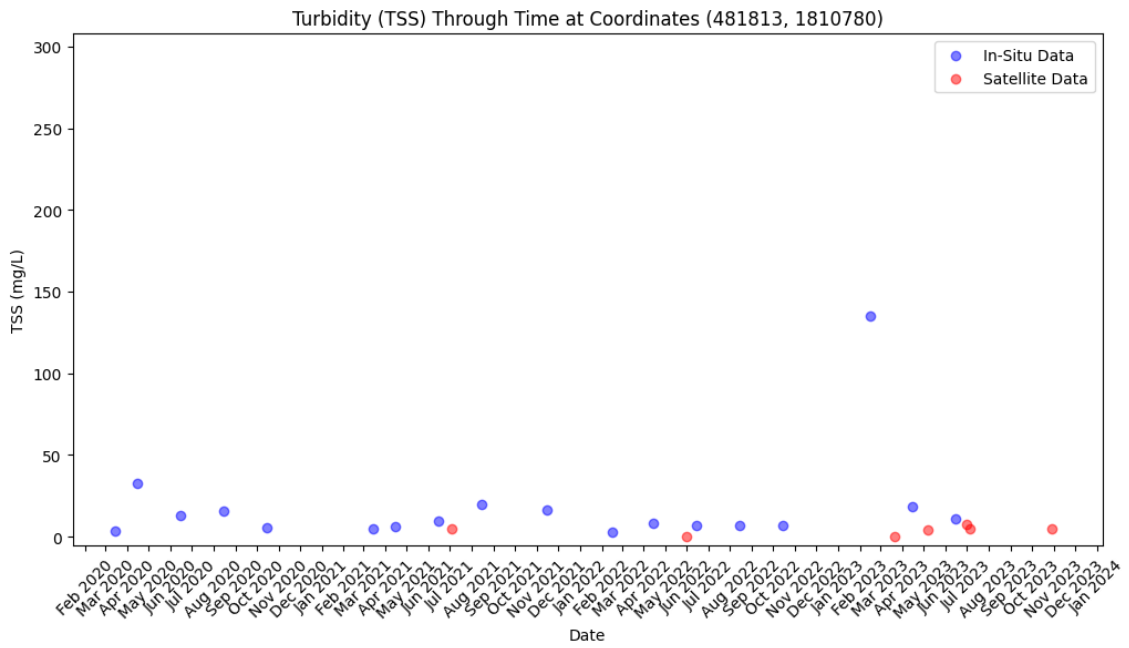


Figure 272: Point sample data of In-situ and satellite point id NÄDTT2 coordinates 481813 1810780.

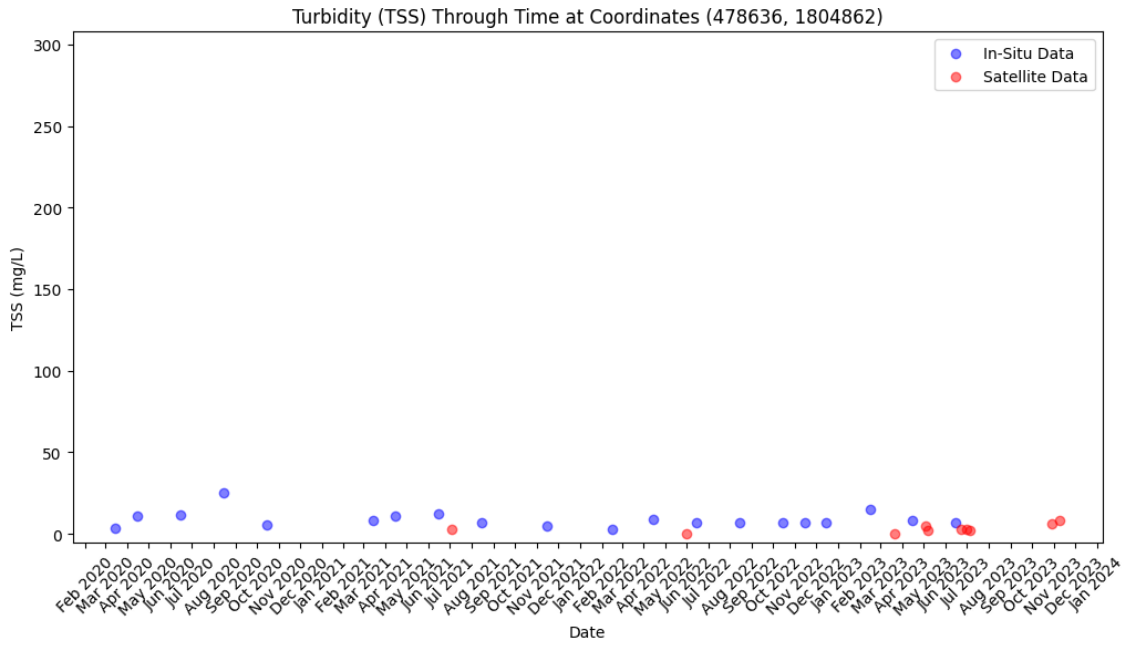


Figure 273: Point sample data of In-situ and satellite point id NDCH1 coordinates 478636 1804862.

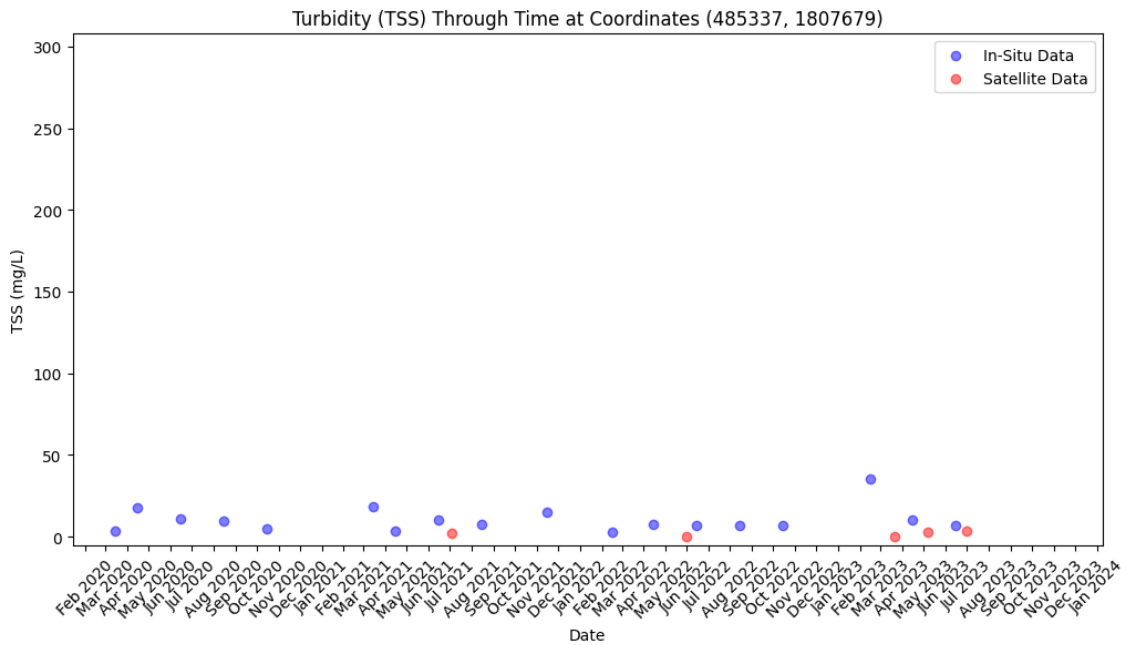


Figure 274: Point sample data of In-situ and satellite point id NDCH2 coordinates 485337 1807679.

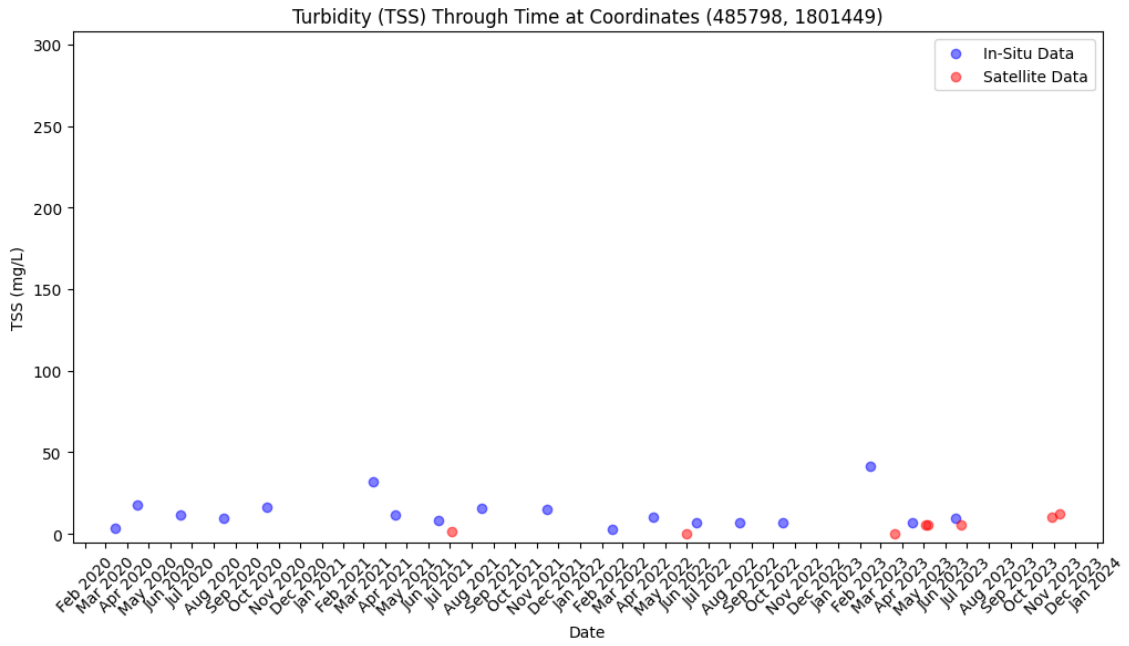


Figure 275: Point sample data of In-situ and satellite point id NDCH3 coordinates 485798 1801449.

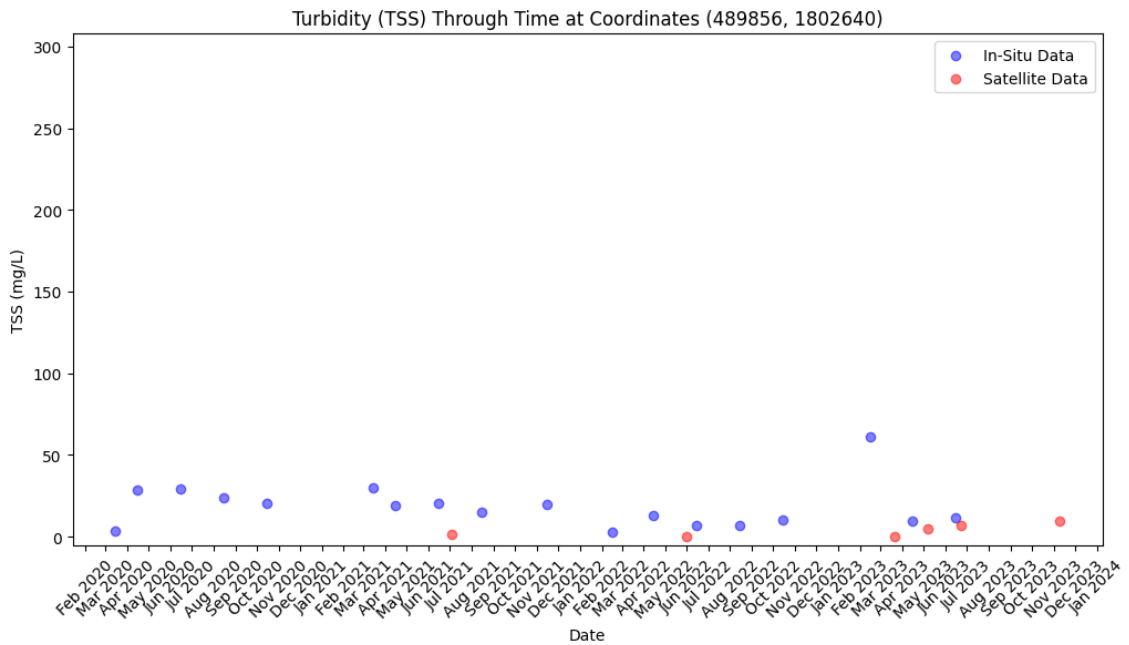


Figure 276: Point sample data of In-situ and satellite point id NDCH4 coordinates 489856 1802640.

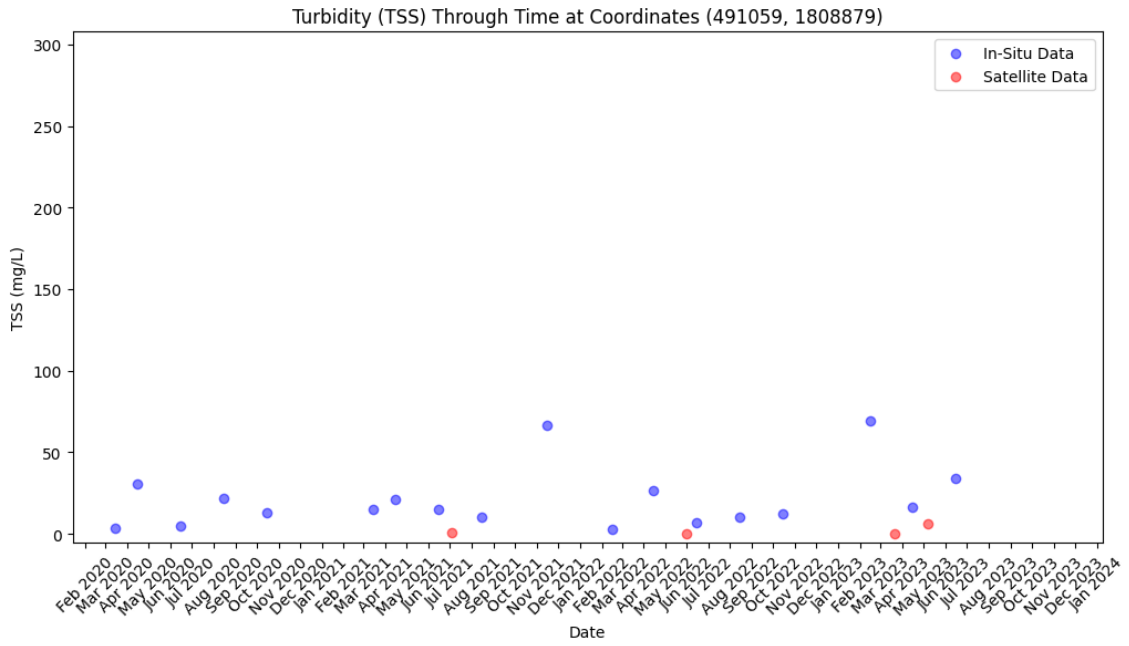


Figure 277: Point sample data of In-situ and satellite point id NÄDCH5 coordinates 491059 1808879.

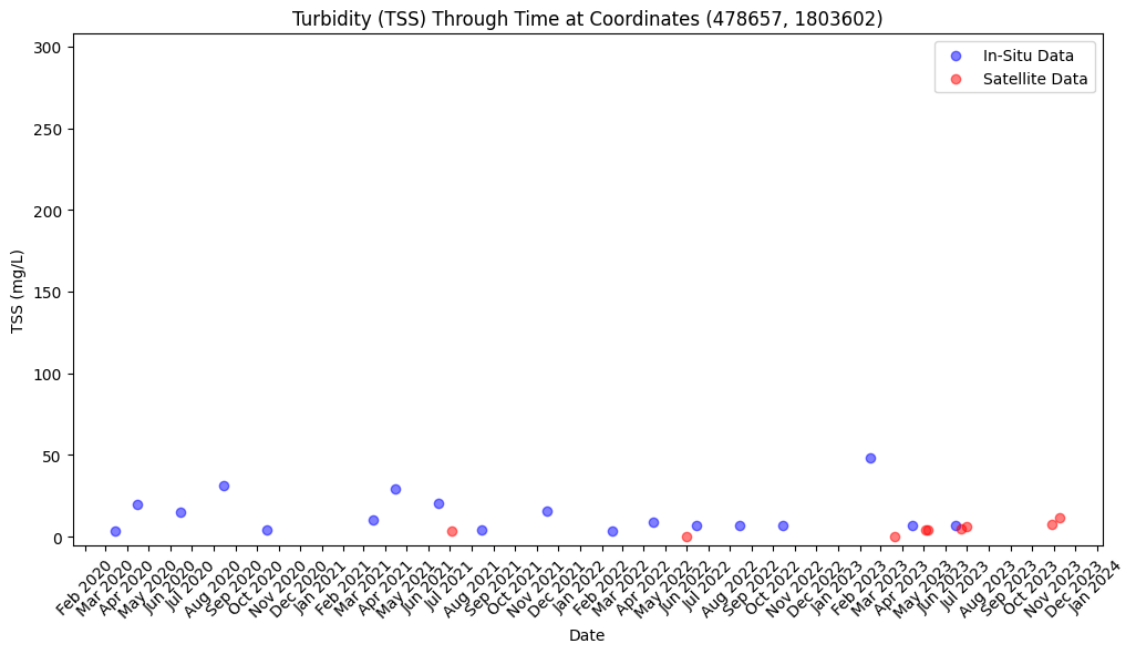


Figure 278: Point sample data of In-situ and satellite point id NÄDCH6 coordinates 478657 1803602.

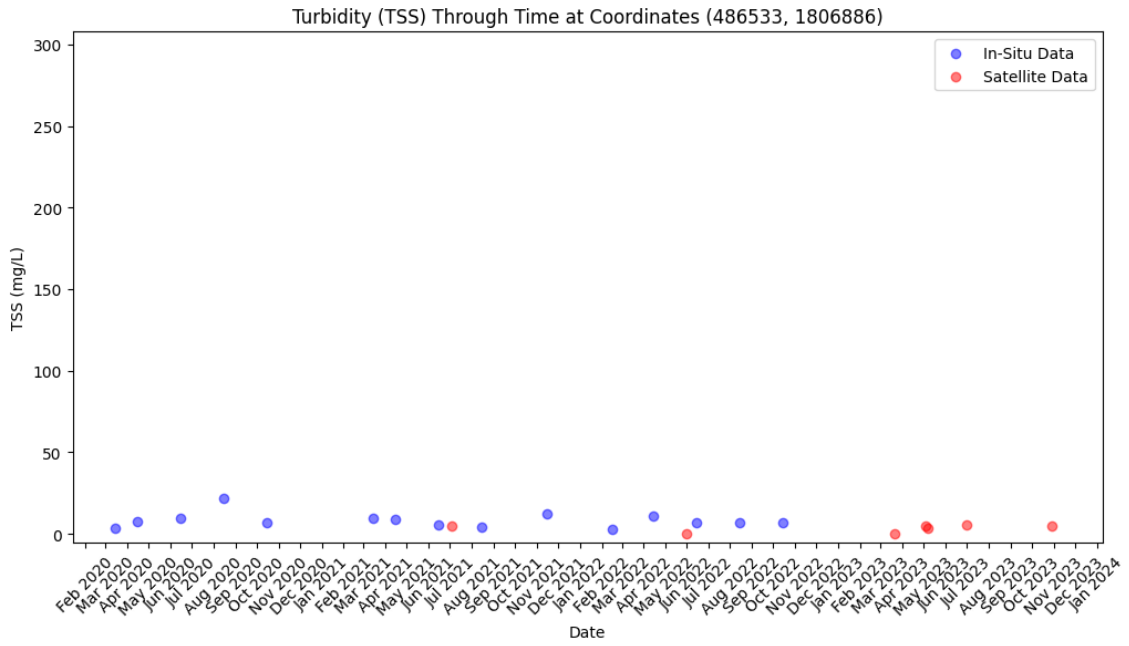


Figure 279: Point sample data of In-situ and satellite point id NÄDCH7 coordinates 486533 1806886.

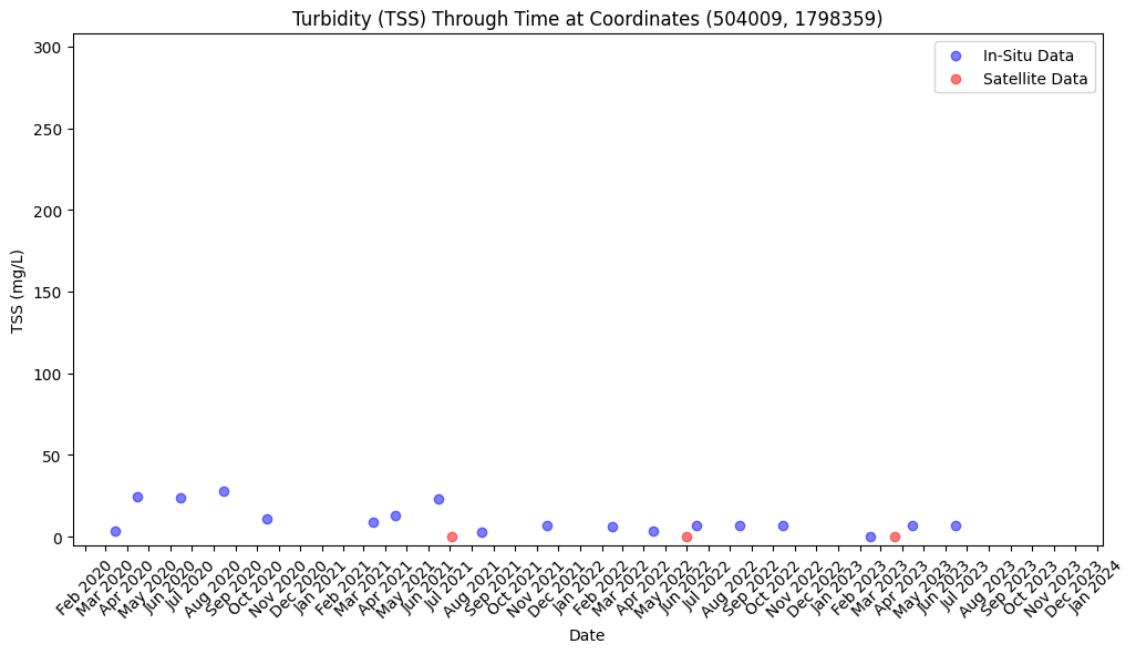


Figure 280: Point sample data of In-situ and satellite point id NÐLC1 coordinates 504009 1798359.

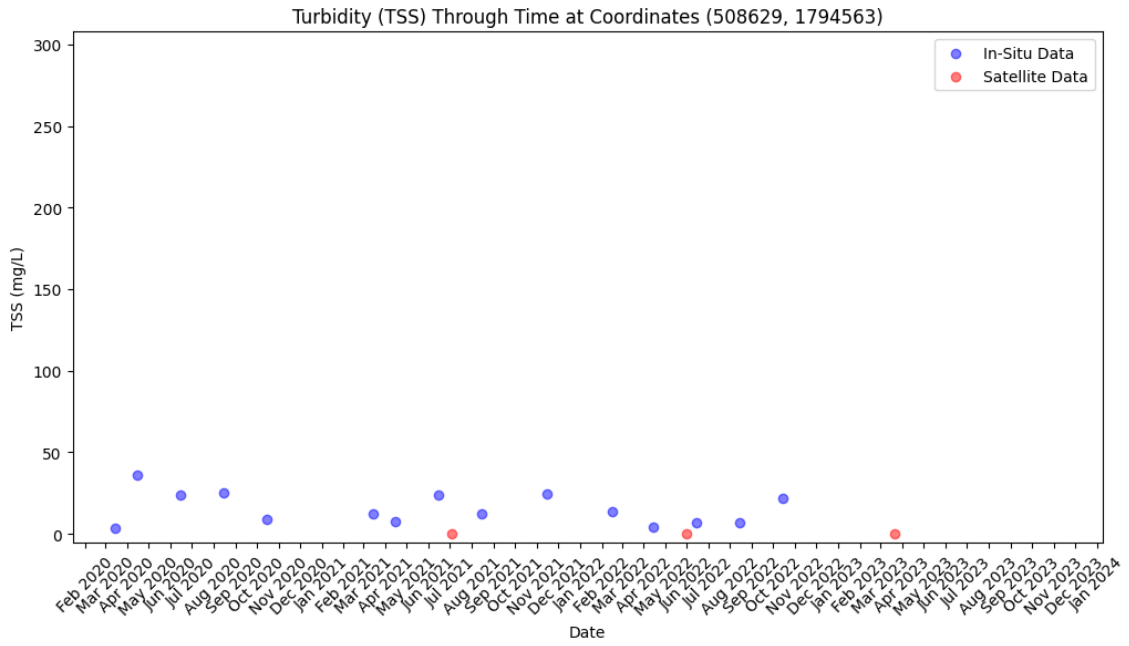


Figure 281: Point sample data of In-situ and satellite point id NDL2 coordinates 508629 1794563.

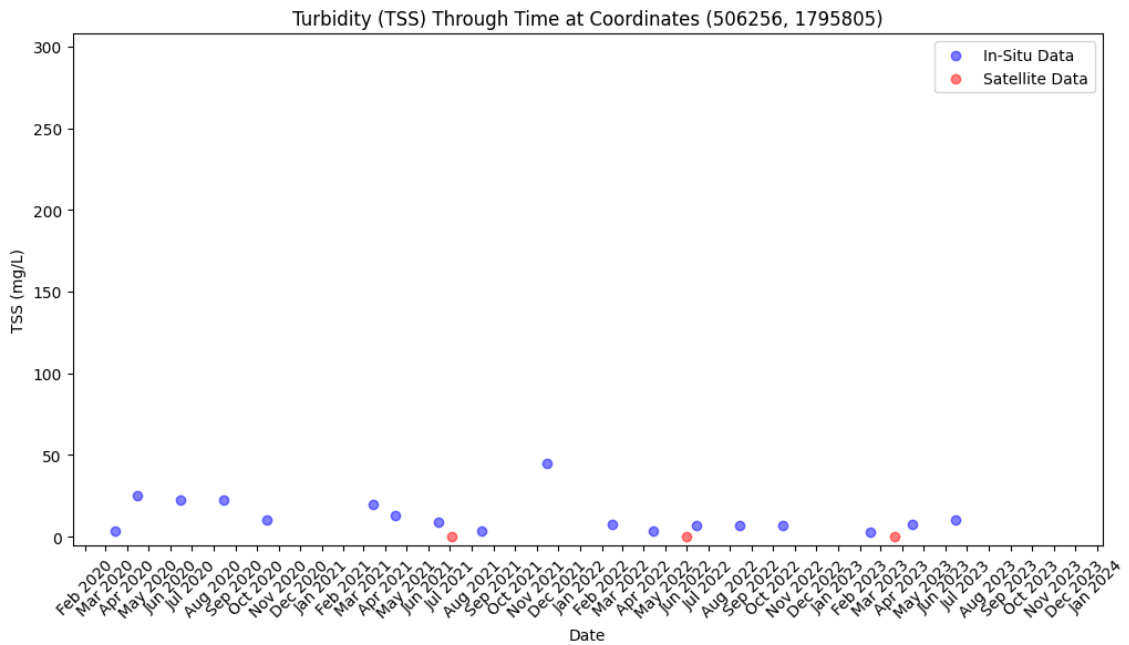


Figure 282: Point sample data of In-situ and satellite point id NDL3 coordinates 506256 1795805.

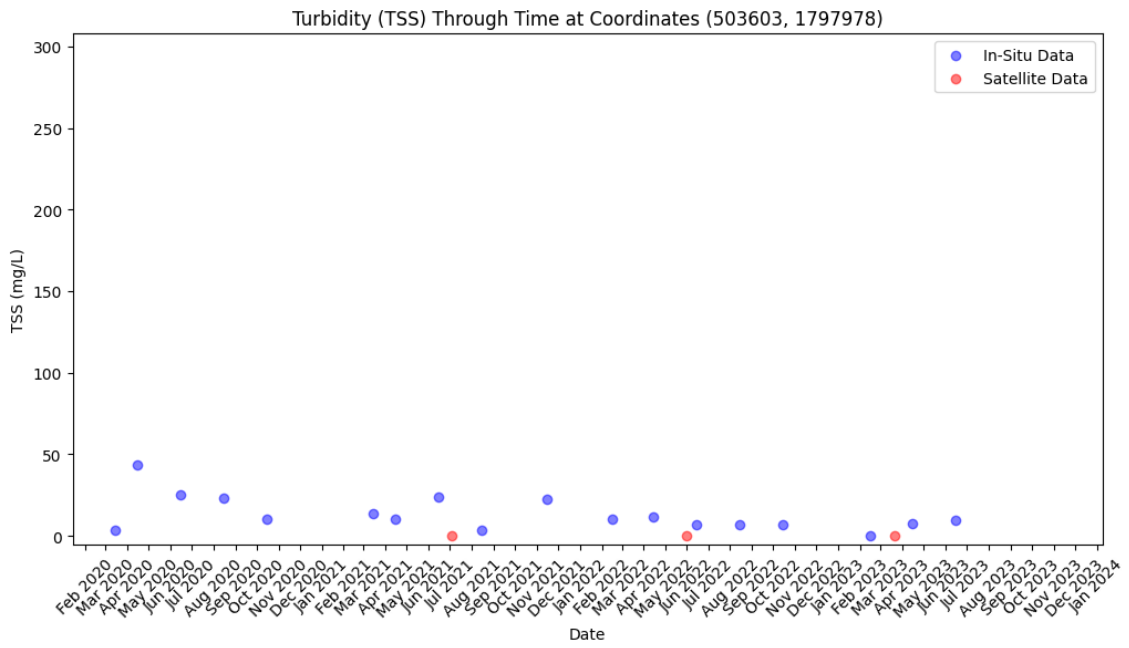


Figure 283: Point sample data of In-situ and satellite point id NDL4 coordinates 503603 1797978.

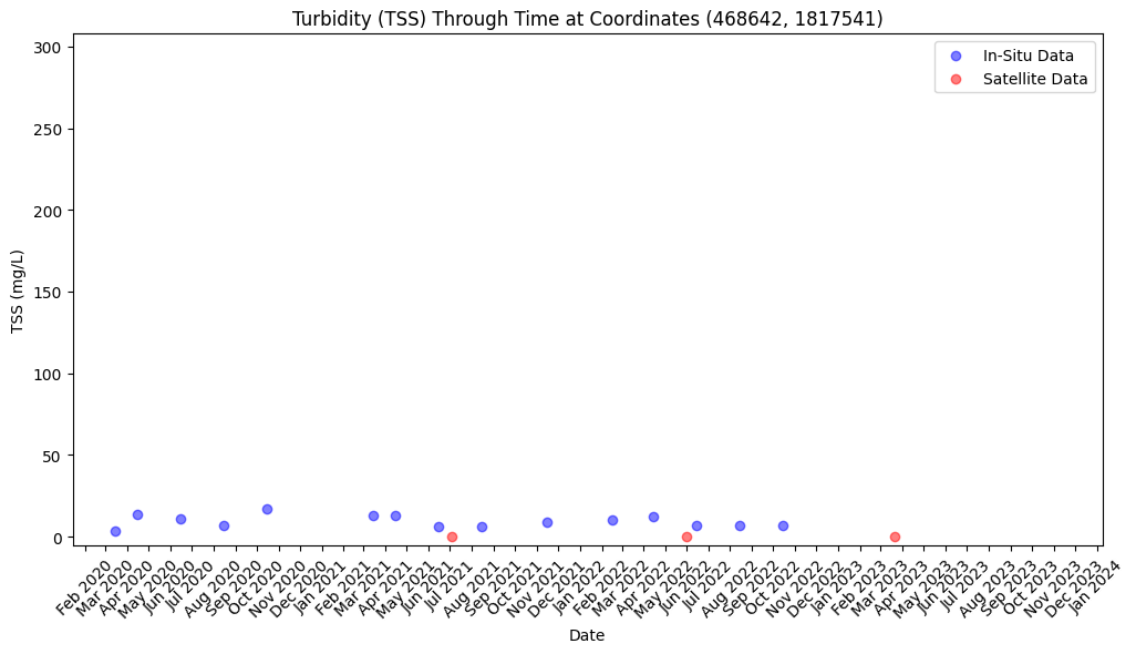


Figure 284: Point sample data of In-situ and satellite point id NSADG1 coordinates 468642 1817541.

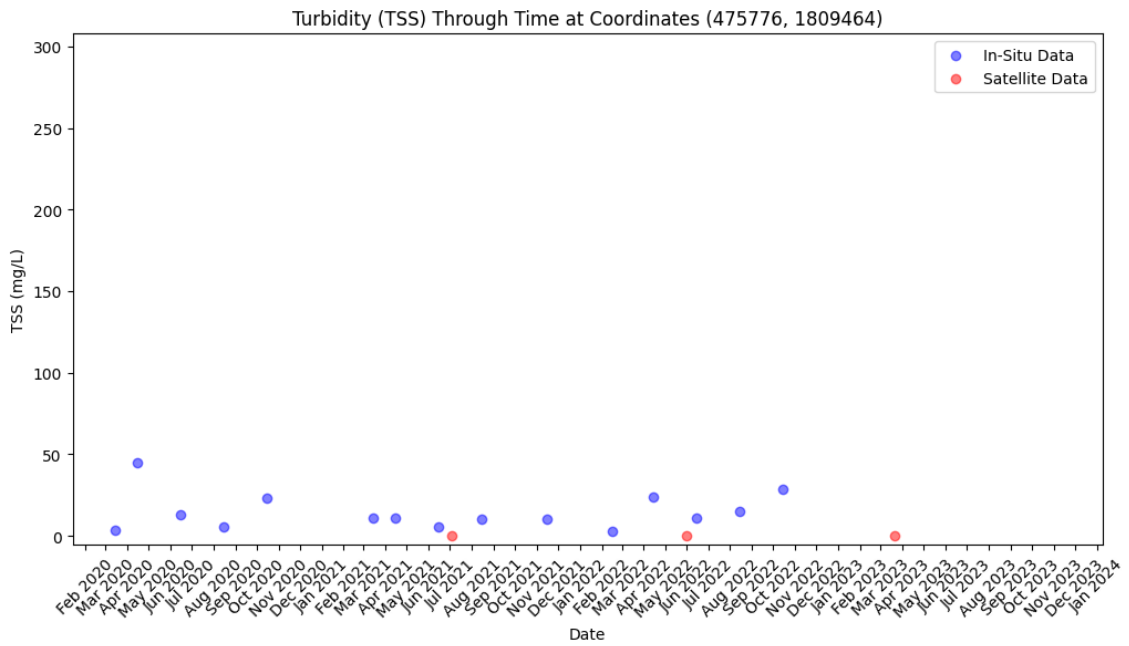


Figure 285: Point sample data of In-situ and satellite point id NSDG2 coordinates 475776 1809464.

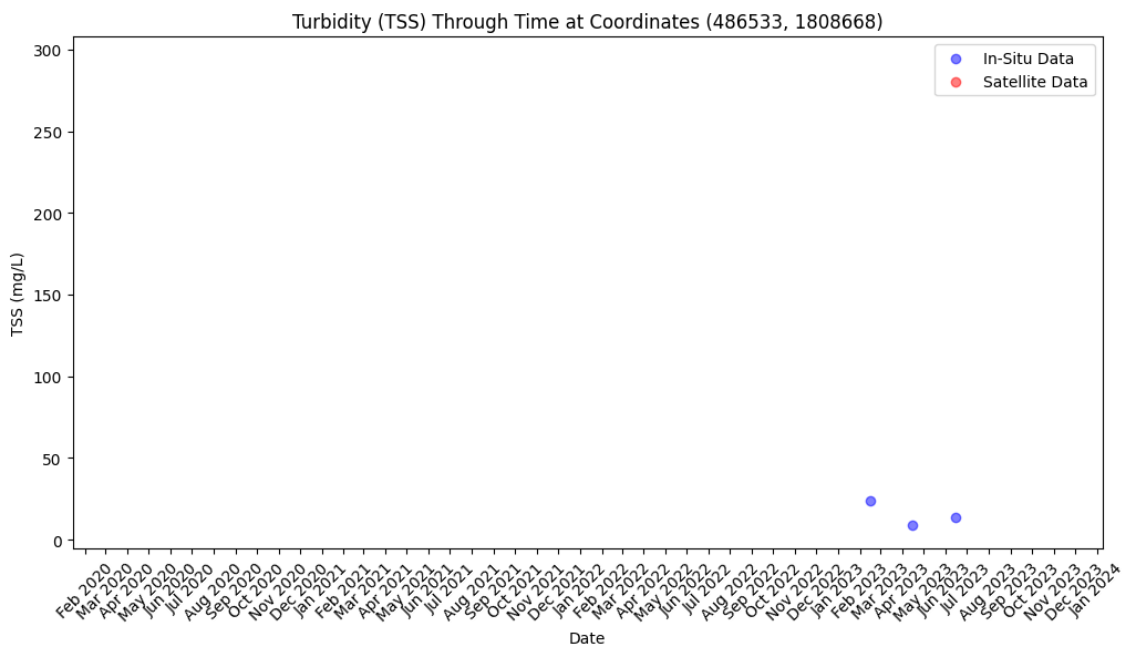


Figure 286: Point sample data of In-situ and satellite point id NÄDCH7 coordinates 486533 1808668.

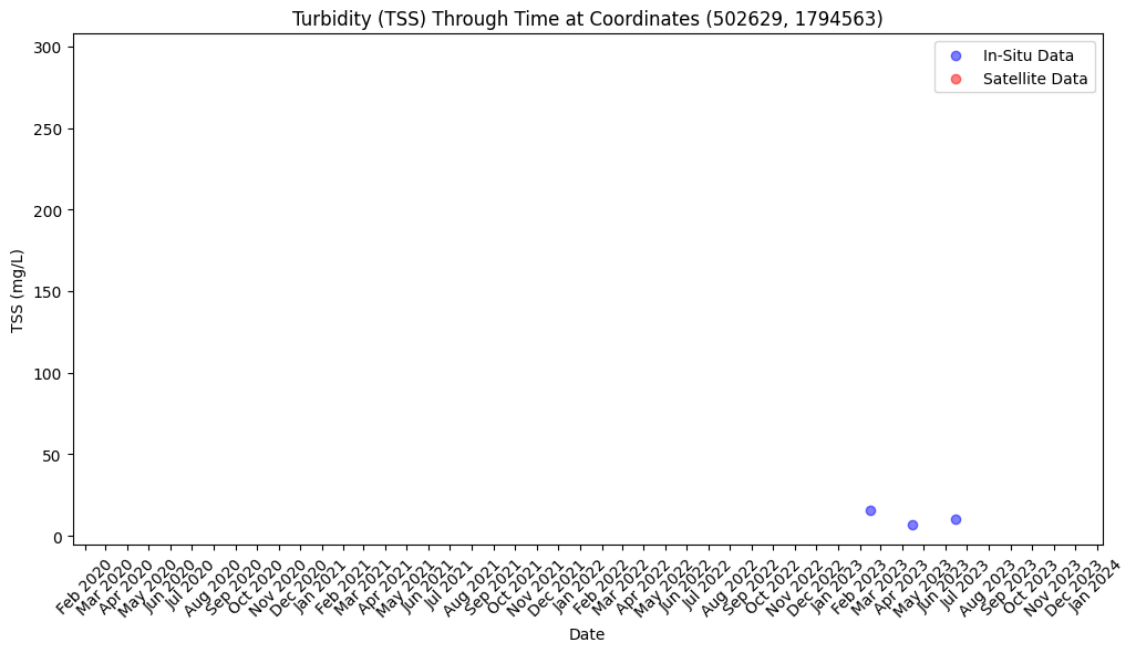


Figure 287: Point sample data of In-situ and satellite point id NADLC2 coordinates 502629 1794563.